



HAL
open science

Multiphysics coupling for cardiovascular surgery application

Giulia D'ambrogio

► **To cite this version:**

Giulia D'ambrogio. Multiphysics coupling for cardiovascular surgery application. Electronics. INSA de Lyon, 2022. English. NNT : 2022ISAL0122 . tel-04416343

HAL Id: tel-04416343

<https://theses.hal.science/tel-04416343>

Submitted on 25 Jan 2024

HAL is a multi-disciplinary open access archive for the deposit and dissemination of scientific research documents, whether they are published or not. The documents may come from teaching and research institutions in France or abroad, or from public or private research centers.

L'archive ouverte pluridisciplinaire **HAL**, est destinée au dépôt et à la diffusion de documents scientifiques de niveau recherche, publiés ou non, émanant des établissements d'enseignement et de recherche français ou étrangers, des laboratoires publics ou privés.



N°d'ordre

NNT : 2022ISAL0122

**THESE de DOCTORAT DE L'INSA LYON,
membre de l'Université de Lyon**

**Ecole Doctorale N° ED 162 MEGA
Mécanique, Energétique, Génie civil et acoustique**

**Spécialité/ discipline de doctorat :
Acoustique**

Soutenue publiquement le **15/12/2022**, par :

Giulia D'Ambrogio

**Multiphysics coupling for cardiovascular
surgery application**

Devant le jury composé de :

Nom, prénom grade/qualité établissement/entreprise GUIFFARD, Benoit Professeur des Universités / Nantes Université	Président
BARRAU, Sophie Maître de Conférence HDR / Université de Lille - UMET	Rapporteure
COLIN, Annie Professeur des Universités / ESPCI Paris - PSL	Rapporteure
LIANG, Zhiyong (Richard) Professor / Florida State University	Examinateur
COTTINET, Pierre-Jean Maître de Conférence HDR /INSA-LYON	Directeur de thèse
CAPSAL, Jean-Fabien Maître de Conférence HDR /INSA-LYON	Co-directeur de thèse
DELLA SCHIAVA, Nellie Praticienne Hospitalière HDR / HCL Hôpital Edouard Herriot	Invitée
DIETSCH, Hervé Directeur de Recherche, Docteur / Société MICHELIN	Invité

Département FEDORA – INSA Lyon - Ecoles Doctorales

SIGLE	ECOLE DOCTORALE	NOM ET COORDONNEES DU RESPONSABLE
CHIMIE	CHIMIE DE LYON https://www.edchimie-lyon.fr Sec. : Renée EL MELHEM Bât. Blaise PASCAL, 3e étage secretariat@edchimie-lyon.fr	M. Stéphane DANIELE C2P2-CPE LYON-UMR 5265 Bâtiment F308, BP 2077 43 Boulevard du 11 novembre 1918 69616 Villeurbanne directeur@edchimie-lyon.fr
E.E.A.	ÉLECTRONIQUE, ÉLECTROTECHNIQUE, AUTOMATIQUE https://edeea.universite-lyon.fr Sec. : Stéphanie CAUVIN Bâtiment Direction INSA Lyon Tél : 04.72.43.71.70 secretariat.edeea@insa-lyon.fr	M. Philippe DELACHARTRE INSA LYON Laboratoire CREATIS Bâtiment Blaise Pascal, 7 avenue Jean Capelle 69621 Villeurbanne CEDEX Tél : 04.72.43.88.63 philippe.delachartre@insa-lyon.fr
E2M2	ÉVOLUTION, ÉCOSYSTÈME, MICROBIOLOGIE, MODÉLISATION http://e2m2.universite-lyon.fr Sec. : Bénédicte LANZA Bât. Atrium, UCB Lyon 1 Tél : 04.72.44.83.62 secretariat.e2m2@univ-lyon1.fr	Mme Sandrine CHARLES Université Claude Bernard Lyon 1 UFR Biosciences Bâtiment Mendel 43, boulevard du 11 Novembre 1918 69622 Villeurbanne CEDEX sandrine.charles@univ-lyon1.fr
EDISS	INTERDISCIPLINAIRE SCIENCES-SANTÉ http://ediss.universite-lyon.fr Sec. : Bénédicte LANZA Bât. Atrium, UCB Lyon 1 Tél : 04.72.44.83.62 secretariat.ediss@univ-lyon1.fr	Mme Sylvie RICARD-BLUM Institut de Chimie et Biochimie Moléculaires et Supramoléculaires (ICBMS) - UMR 5246 CNRS - Université Lyon 1 Bâtiment Raulin - 2ème étage Nord43 Boulevard du 11 novembre 1918 69622 Villeurbanne Cedex Tél : +33(0)4 72 44 82 32 sylvie.ricard-blum@univ-lyon1.fr
INFOMATHS	INFORMATIQUE ET MATHÉMATIQUES http://edinfomaths.universite-lyon.fr Sec. : Renée EL MELHEM Bât. Blaise PASCAL, 3e étage Tél : 04.72.43.80.46 infomaths@univ-lyon1.fr	M. Hamamache KHEDDOUCI Université Claude Bernard Lyon 1 Bât. Nautibus 43, Boulevard du 11 novembre 1918 69 622 Villeurbanne Cedex France Tél : 04.72.44.83.69 hamamache.kheddouci@univ-lyon1.fr
Matériaux	MATÉRIAUX DE LYON http://ed34.universite-lyon.fr Sec. : Yann DE ORDENANA Tél : 04.72.18.62.44 yann.de-ordenana@ec-lyon.fr	M. Stéphane BENAYOUN Ecole Centrale de Lyon Laboratoire LTDS 36 avenue Guy de Collongue 69134 Ecully CEDEX Tél : 04.72.18.64.37 stephane.benayoun@ec-lyon.fr
MEGA	MÉCANIQUE, ÉNERGÉTIQUE, GÉNIE CIVIL, ACOUSTIQUE http://edmega.universite-lyon.fr Sec. : Stéphanie CAUVIN Tél : 04.72.43.71.70 Bâtiment Direction INSA Lyon mega@insa-lyon.fr	M. Jocelyn BONJOUR INSA Lyon Laboratoire CETHIL Bâtiment Sadi- Carnot9, rue de la Physique 69621 Villeurbanne CEDEX jocelyn.bonjour@insa-lyon.fr
ScSo	ScSo* https://edsciencessociales.universite-lyon.fr Sec. : Mélina FAVETON INSA : J.Y. TOUSSAINT Tél : 04.78.69.77.79 melina.faveton@univ-lyon2.fr	M. Bruno MILLY Université Lumière Lyon 286 Rue Pasteur 69365 Lyon CEDEX 07 bruno.milly@univ-lyon2.fr

Cette thèse est accessible à l'adresse : <https://theses.insa-lyon.fr/publication/2022ISAL0122/these.pdf>

*ScSo : Histoire, Géographie, Aménagement, Urbanisme, Archéologie, Science politique, Sociologie, Anthropologie

Alle mie care nonna Gianna e zia Marisa,
vi porto sempre nel mio cuore

“ Έτσι, δεν γνωρίζω ”
Socrate

“Memento audere semper”
G. D’Annunzio

ABSTRACT

Blood clotting is a natural process that happens in the human body to repair leaking blood vessels and to prevent the outflow of blood. However, even contact with artificial surfaces, for instance those of vascular or cardiac prostheses, can trigger coagulation. This raises important issues about the choice of materials used in vascular grafts, as a thrombus that forms on the duct's inner surface inhibits blood flow which can be fatal if not treated soon, and about the need of reliable prosthetic monitoring techniques. In this thesis, we focus on the development of a novel class of smart vascular prosthetics able to detect the event of thrombosis and hinder the coagulation response. *In vivo* and *ex vivo* coagulation monitoring systems are developed with the goal of designing antithrombogenic and self-monitoring grafts. First, we focus on *in vivo* monitoring: blood pressure monitoring can be employed to determine whether coagulation is happening on the prosthesis. Thus, we develop piezoelectric composites that can be integrated into vascular prosthesis, to act as blood pressure sensors. These composites are produced using the dielectrophoresis structuring (DEP) technique, which involves applying an alternating electric field to the mixture (polymer and fillers) before and during the curing steps, which rearranges the fillers into columnar structures along the electric field lines. This process results in an anisotropic material whose piezoelectric properties are enhanced along the structuration axis. In this work we design composites with biocompatible piezoelectric fillers (BaTiO_3 and NaNbO_3) in polydimethylsiloxane matrix, a thermosetting polymer known for its flexibility and biocompatibility. Through in-situ microscopy we study the process parameters such as electric field frequency and amplitude, and shape of the filler, from particles to fiber-shaped, with the aim of optimizing the process. Dielectric and piezoelectric analyses are performed, and the results are compared with physical models and Finite Element analysis. Furthermore, X-ray diffraction (XRD), differential scanning calorimetry (DSC) and dynamic mechanical analysis (DMA) are carried out to study the effect of DEP structuring on the materials' properties. Pressure sensors made of structured piezo-composites are suitable for a variety of medical care approaches for blood pressure monitoring, for instance smart catheters used in fractional flow reserve measurement (FFR) and smart self-monitoring vascular prostheses, as proven by two different proofs of concept developed during this research using a cardiovascular simulator. Secondly, we concentrate on *ex vivo* monitoring: a new technique to assess surface contact coagulation by blood impedance spectroscopy is developed. Through impedance characterization of recalcified human blood, it is possible to identify significative biomarkers related to the main coagulation's steps, which are then validated through comparison with confocal microscopy and rotational thromboelastometry test (Rotem®). The developed technique gives rise to a comprehensive and evolving picture of coagulation, allowing for real-time monitoring of the entire process. Furthermore, it is used to test surfaces with different wettability, proving to be able to characterize materials for antithrombogenic cardiovascular prosthetics, whose properties can be monitored *in situ* and/or online using effective biomarkers. Finally, we present a preliminary study related to charge/cells interaction. One way to improve vascular grafts while preventing body rejection and lowering the danger of thrombosis is to cover the prosthesis with endothelial cells, which are the natural cells that line the inner layer of a human vessel. To accomplish so, innovative methods able of accelerating and improving cell culture are needed. For that purpose, we study the interaction between cells and charged surfaces, by using the charge developed by photo-capacitive composites ($\text{ZnS:Cu/PVDF-TrFE-CFE}$), able to develop a charge in response to a light. The results are promising, showing good response of cells adhesion to both positive and negative charges and paving the way for new tissue vascular engineered grafts.

Acknowledgments

Above all, I express my gratitude to Dr. Pierre-Jean Cottinet, my thesis supervisor, and Dr. Jean-Fabien Capsal, my thesis co-supervisor, for their immense assistance and significant contributions to this work. Their unwavering dedication to this project over the past three years has been exceptional, consistently providing me with valuable feedback and support, inspiring me to always strive for excellence. Throughout these years, I have gained a wealth of knowledge from both of them, and I appreciate it greatly.

I would also like to thank the co-advisers of this thesis, Pr. Patrick Lermusiaux and Dr. Nellie Della Schiava, whom I hold in high esteem and whose suggestions and comments allowed me to achieve interesting results inherent to the world of cardiovascular medicine, enabling me to understand phenomena outside of my area of expertise. Along with my advisers, I would like to express my gratitude to Pr. Claude Richard for his genuine interest and constructive criticism of my work.

Furthermore, I want to thank: Dr. Guilhem Rival, whose knowledge has been very helpful to me over the last year, Dr. Minh-Quyen Le for all of her guidance and support over these years and Marine Bordet, whose help was fundamental in developing vascular prosthetics.

During this project I collaborated with several teams from different laboratories: at the Carmen Iris laboratory in Lyon, I was able to work with Dr. Yves Gouriou, whom I thank for all the help he gave me in trying to perform confocal microscopy. It was really fun learning this new technique with such a friendly person. At the Laboratory of Human movement Sciences (LIBM), I was able to work with Dr. Vincent Pialoux and Laurie Josset, who helped me immensely in the study of blood coagulation. I really appreciated all their support. At the Centre microélectronique de Provence of the Ecole des mines Saint-Etienne (Gardanne), I was able to work with Dr. Mohamed Saadaoui and Dr. Xavier Boddaert, from whose collaboration I learnt a lot. I want to express my gratitude to everyone of them for their time, which was crucial to the completion of this work.

I want to thank Prof. Richard Liang and all the team of HPMI of Florida State University, for welcoming me to their lab and helping me greatly in understanding my composites, I have a lot of esteem for all of you.

Thanks also to personnel and colleagues at the LGEF laboratory, Mr. Frederic Deformerie, Dr. Laurence Seveyrat, Ms. Veronique Perrin and Ms. Evelyne Dorieux for their assistance in fixing problems with my experimental setup as well as bureaucracy issues and for giving me with accessibility to the lab's resources.

I would like to thank all the guys from LGEF: Foamy for her incredible kindness, who welcomed me to the lab with joy and enthusiasm, I am very glad that I could share these years with such a funny friend; Angela, my dear intern, who brought a bit of Italian spirit and a lot of fun for a few months; and then Amaury, Gaspard and Giulia, Eliot, Leopold, Van, Shurui, Yan, Zhyn and Xiaoting, and all the others that I may have

forgot, it was very nice to meet all of you and get to share funny experiences during these years.

I appreciate each and every member of my family for their support over the years. Despite the pain of being apart, they recognized the significance of this project to me and stood behind me every step of the way. Their constant encouragement and attentive ears, displaying a genuine attempt to understand, will forever remain etched in my mind.

Last but not least, I would want to express my heartfelt gratitude to Omar, whose assistance and ongoing scientific and spiritual support have been essential in making this project a reality. **Working together has been an amazing journey.**

Table of Contents

Table of Contents	I
List of Figures	VI
List of Tables.....	XIII
Nomenclature	XIV
Le résumé de la thèse en français.....	1
Purpose of this thesis.....	7
Chapter I Vascular bypass grafting: state of the art	8
1. Cardiovascular diseases.....	8
2. Preoperative risk evaluation	11
3. Prosthetic bypass grafting	12
3.1 Poly (ethylene terephthalate) Dacron® vascular grafts.....	13
3.2 Polytetrafluoroethylene (PTFE) grafts	14
3.3 Polyurethanes (PU) grafts	15
3.4 Scaffold - based tissue engineered vascular grafts (TEVGs)	16
3.4.1 Biodegradable polymer based TEVGs	17
3.4.2 Natural Biomaterials	18
4. <i>In Vivo</i> and Clinical Applications	18
4.1 Peripheral Bypass Graft	19
4.2 Carotid Artery Bypass Grafts	20
4.3 Coronary Artery Bypass Grafts.....	20
5. Problematic of vascular prosthetics.....	21
5.1 Compliance issues.....	22
5.2 Poor hemodynamics	22
5.3 Infections.....	23
5.4 Thrombogenicity	23
5.5 Contact coagulation.....	24
6. Improving endothelialization and reducing thrombogenicity	25
7. Purpose of this work: developing new vascular grafts.....	26
7.1 Self-monitoring smart grafts	26

7.2 <i>In vitro</i> dynamic test system for thrombogenicity evaluation of medical devices and biomaterials	27
7.3 Scaffold for fast cells seeding.....	28
Chapter II Structured piezoelectric composites for biosensor applications.....	30
<i>Summary</i>	30
Introduction	30
1. Piezoelectricity: concept and models	31
1.1 Piezoelectric materials.....	31
1.2 Analytical formulation of piezoelectricity and figure of merit (FoM)	33
1.3 Pyroelectric and Ferroelectric ceramics	35
1.4 Ferroelectric polarization.....	37
1.5 Antiferroelectric ceramic materials	38
1.6 Piezoelectric composites	39
1.7 Fillers: Biocompatible ferroelectric BaTiO ₃ and antiferroelectric NaNbO ₃	43
1.8 The matrix	44
1.9 Connectivity	44
1.10 Dielectrophoresis (DEP) structuring	49
1.11 Polarization of particles under non-homogeneous electric fields.....	50
1.12 Dielectrophoresis model.....	51
1.13 Parameters affecting the dielectrophoresis structuring	54
2. Material and methods	55
2.1 Materials.....	55
2.1.1 Polydimethylsiloxane (PDMS).....	56
2.1.2 Barium titanate	56
2.1.3 Sodium niobate.....	58
2.1.4 Hydrothermal synthesis of NaNbO ₃	59
2.2 Fabrication procedure.....	60
2.2.1 BT/PDMS piezocomposites	60
2.2.2 NN/PDMS composites fabrication	62
2.3 Method of Characterization.....	62
2.3.1 DEP process analysis.....	62
2.3.2 Optical Microscopy	63

2.3.3 Scanning Electron microscopy (SEM) characterization.....	63
2.3.4 Dielectric spectroscopy	64
2.3.5 Poling procedure and piezoelectric characterization	64
2.3.6 Thermal stability of the piezoelectric response	65
2.3.7 X-ray diffraction.....	65
2.3.8 Dynamic mechanical Analysis (DMA)	66
2.3.8 Differential Scanning Calorimetry (DSC).....	66
2.3.9 Broadband dielectric spectroscopy in temperature.....	67
3. Improving piezoelectric particle-composites via DEP: BaTiO ₃ /PDMS.....	69
3.1 Introduction	69
3.2 Finite Element Analysis (FE) of BT/PDMS.....	69
3.3 Experimental results and discussion.....	72
3.3.1 Dielectrophoresis optimization.....	72
3.3.2 Optical microscopy and Scanning electron microscopy.....	74
3.3.3 Dielectric spectroscopy	75
3.3.4 Piezoelectric characterization.....	78
3.3.5 Thermal stability and XRD analysis	80
3.3.6 Dynamic mechanical analysis (DMA)	82
3.3.7 Differential Scanning Calorimetry	85
3.3.8 Broadband dielectric spectroscopy.....	89
3.4 Conclusions	92
4. The effect of the aspect ratio: connectivity improvement via DEP structuring of fiber composites. 95	
4.1 Introduction	95
4.2 DEP on high aspect ratio filler: a model description.....	96
4.3 Simulation based on finite element (FE) analysis	98
4.4 Experimental results and discussion.....	102
4.4.1 X-ray Diffraction.....	102
4.4.2 Scanning electron microscopy (SEM).....	102
4.4.3 Dielectric spectroscopy	105
4.4.4 Piezoelectric analysis	111
4.4.5 Dynamic Mechanical Analysis (DMA).....	115
4.4.6 DSC	119

4.5 Comparing piezoelectric materials	121
4.6 Conclusions	122
Chapter III Piezoelectric sensors for blood pressure monitoring	124
<i>Summary</i>	124
1. Developing Fractional Flow Reserve Catheters: a proof of concept.....	124
2. Fractional flow reserve: state of art.....	124
3. Experimental section	127
3.1 Dynamic mechanical excitation	127
3.2 FFR simulation	127
4. Results and discussions	128
4.1 FFR simulation	128
5. Smart Vascular Grafts for Thrombosis detection: a proof of concept.....	130
5.1 Introduction	130
6. Experimental section	131
6.1 Smart graft demonstrator.....	131
7. Results and discussion.....	134
7.1 Smart graft pressure sensor	134
8. Conclusions	138
Chapter IV <i>In vitro</i> thrombosis monitoring via impedance characterization	142
<i>Summary</i>	142
1. Introduction	142
2. The mechanism of coagulation.....	143
3. <i>In vitro</i> blood test	145
4. Bioimpedance characterization of biological systems.....	148
5. Materials and methods.....	152
5.1. Materials.....	152
5.2 Blood clot preparation.....	152
5.3. Impedance magnitude spectroscopy	153
5.4 Impedance phase angle.....	154
5.5 Confocal microscopy.....	154
5.6 Rotem® characterization.....	154
5.7 Coagulation time and wettability.....	155

6. Results and discussion.....	155
6.1 Impedance spectroscopy	155
6.2 Confocal microscopy.....	158
6.3 Rotem® characterization.....	161
6.4 Coagulation and wettability	165
7. Conclusions and perspectives.....	167
Chapter V A preliminary study on self-endothelialized tissue engineered vascular grafts	170
<i>Summary</i>	170
1. Introduction	170
2. Cell-surface charge interaction.....	172
3. Photo-capacitive ZnS:Cu/Terpolymer.....	173
4. Materials and methods	174
4.1 Material development.....	174
4.2 Electrical characterization	175
4.3 Wettability test	176
4.4 Cells preparation	177
4.5 Charge stimulated epithelial cells adhesion test.....	178
5. Results and discussion.....	179
5.1 Electrical characterization and wettability investigation.....	179
5.2 Cell's adhesion on charged surfaces	182
6. Conclusions	184
Chapter VI Conclusions and Perspectives.....	187
Bibliography.....	192

List of Figures

Figure 1 2016 disability adjusted life-years (DALYs) by country, global cardiovascular disease (CVD) DALYs per 100,000 inhabitants, 2016 [4].	9
Figure 2 a) Deaths per year associated with different diseases in the world; CVDs are the highest cause of death accounting for 18 million death per year. b) CVDs risk factors.	9
Figure 3 Representative image of clogged vessel and bypass grafting.	11
Figure 4 Drawing of FFR catheter equipped with pressure sensor.	11
Figure 5 Drawing representing an artificial graft. Anastomosis indicates the points of connection between the graft and the human vessels.	12
Figure 6 Representation of human artery structure. There are three layers, tunica intima media and externa. The inner surface of the vessel, named intima or lumen is covered in endothelial cells (ECs), while the tunica media is composed of smooth muscle cells (SMCs). Created with BioRender.com.	13
Figure 7 a) Picture of Dacron [®] aorto-bifemoral graft (Albograft [®])[32]. b) SEM pictures of internal and external surface of the graft.	14
Figure 8 a) Picture of ePTFE vascular graft produced by B Braun [®] [43]. b) SEM pictures of internal and external surface of the graft.	15
Figure 9 Drawing representing the most common Peripheral bypass grafting. Created with BioRender.com.	20
Figure 10 Scheme displaying coronary artery disease. Created with BioRender.com.	21
Figure 11 Cross section of an artificial vascular graft with intima hyperplasia, i.e., excessive growth of endothelial cells.	22
Figure 12 Development of thrombosis in the intima of the graft due to poor hemocompatibility of synthetic materials.	23
Figure 13 Coagulation cascade. There are two possible paths for triggering the coagulation, the intrinsic and the extrinsic. While the extrinsic is activated due to contact with Tissue Factor, present in the outside of the vessels, the intrinsic pathway is triggered by the activation of the protein named fXII, which may be activated by a trauma as well as contact with artificial surface. Both the pathways continue with a common pathway involving platelet activation, that ends with the formation of fibrin.	24
Figure 14 Schematic representation of a self-monitoring vascular graft, able to communicate with a point-of-care device. Created with BioRender.com.	27
Figure 15 Drawing of endothelial seeding stimulated by an electroactive material, to fast cover a cardiovascular graft.	28
Figure 16 Conceptual representation of the piezoelectric effect.	31
Figure 17 Representation of 33 and 31 transduction modes [1].	34
Figure 18 a) Cubic unit cell of perovskitic Barium titanate above the Curie temperature; b) below the Curie temperature the unit cell is tetragonal with Ba ²⁺ and Ti ⁴⁺ displaced with respect to O ²⁻ , and consequently the center of positive charge does not coincide with the center of negative discharge.	36
Figure 19 a) Typical bipolar polarization curve; b) dipole orientation in a multiple domain system before, during, and after poling.	38
Figure 20 Typical antiferroelectric material's double hysteresis.	39
Figure 21 Comparisons between FoM of different piezoelectric composites and polymers described in the literatures [131,138–143].	41

Figure 22 Number of publications on piezocomposites from 1970 to 2020.	41
Figure 23 Example of the variety of applications that piezocomposites cover.	42
Figure 24 Fundamental parameters in designing piezocomposites.	43
Figure 25 All the possible connectivity described by Newnham et al. for a diphasic composite [161].	45
Figure 26 Schematic drawing of 0-3 and quasi 1-3 connectivity in 2D.	46
Figure 27 Figure displaying the electrical model proposed by Bowen et al. to describe the behavior of quasi 1-3 composites [164].	48
Figure 28 Schematic representation of the dielectrophoretic structuring. At zero applied field the particles are homogeneously dispersed. Under external AC electric field, dipole-dipole interactions occur, causing the orientation in columns[172].	50
Figure 29 a) Effect of the electric field on the interaction potential vs. s , the center particles distance; b) effect of Θ on the interaction potential [173,177].	53
Figure 30 Interaction between two particles in function of Θ [177].	53
Figure 31 a) Scanning electron microscopy of the Barium Titanate filler used in this research; b) histogram of the distribution of the BaTiO ₃ diameter, with an average size of 569 nm.	55
Figure 32 Silicone repeating unit.	56
Figure 33 Crystalline unit cells at different temperature for BaTiO ₃ and variation of the cube root of the volume of the cell with temperature for various phases of BaTiO ₃ [191].	57
Figure 34 a) Orthorhombic Pbcm NaNbO ₃ visualized with Vesta [®] . b) Crystallographic phases of NaNbO ₃ depending on the Temperature (°C).	58
Figure 35 a)-i) All the steps for hydrothermal synthesis of fibers of Sodium Niobate.	60
Figure 36 Setup designed to fabricate the composites.	61
Figure 37 a)-h) Step by step procedure followed to produce 0-3 and quasi 1-3 composites.	61
Figure 38 a) Set up developed to perform in-process microscopy; b) detail of the sample holder where the blend was placed during the observation.	63
Figure 39 Set up used to pole the composites.	65
Figure 40 Schematic drawing representing the direction of stretching during the DMA test with respect to the alignment direction for 1-3 composites.	66
Figure 41 Thermal cycle for DSC measurements of PDMS, BaTiO ₃ -based and NaNbO ₃ -based composites.	67
Figure 42 a) and b) FE simulation of fillers' electric field distribution in 0-3 and quasi 1-3 connectivity respectively under external electric field of $E_z=30 \text{ V } \mu\text{m}^{-1}$. c) and d) FE simulation of electric field distribution in 0-3 and quasi 1-3 connectivity composites, respectively, under an external electric field $E_y= 30 \text{ V } \mu\text{m}^{-1}$	70
Figure 43 FE simulation of a) 0-3 connectivity composites and b) quasi 1-3 connectivity composites under compressive stress of 10 kPa applied in the z direction. The color map indicates the voltage developed across the sample.	71
Figure 44 In process microscopy results: left pictures represent the results from the study of electric field amplitude: three frames from the in-situ microscopy analysis taken 10 minutes after structuration at a) $1 \text{ V } \mu\text{m}^{-1}$ and 1 Hz, b) $2 \text{ V } \mu\text{m}^{-1}$ and 1 Hz and c) $3 \text{ V } \mu\text{m}^{-1}$ and 1 Hz. Right pictures represent the study of frequency effect on dielectrophoresis: three frames from the in-situ microscopy analysis taken 10 minutes after structuration at d) $3 \text{ V } \mu\text{m}^{-1}$ and 1000 Hz, e) $3 \text{ V } \mu\text{m}^{-1}$ and 100 Hz and f) $3 \text{ V } \mu\text{m}^{-1}$ and 1 Hz. All the tests were performed at room temperature.	74

Figure 45 Optical microscopy in transmission mode of the cross section of 1-3 BT/PDMS 2.4%v..... 75

Figure 46 SEM pictures in BSE mode of a) 0-3 BT/PDMS 2.4%v and b) 1-3 BT/PDMS 2.4%v..... 75

Figure 47 Relative permittivity real at room temperature for a) PDMS and 0-3 BT/PDMS with 2.4%v, 12%v and 24%v and b) PDMS and 1-3 BT/PDMS with 2.4%v, 12%v and 24%v..... 77

Figure 48 Loss tangent at room temperature for a) PDMS and 0-3 BT/PDMS with 2.4%v, 12%v and 24%v and b) PDMS and 1-3 BT/PDMS with 2.4%v, 12%v and 24%v..... 77

Figure 49 Relative dielectric permittivity real vs. filler volume content for 0-3 and 1-3 BT/PDMS at 1 kHz and measured at room temperature, fitted with the models presented in subsection 1.9. 78

Figure 50 a) d_{33} vs. filler volume content and b) g_{33} vs. filler volume content for 0-3 and 1-3 BT/PDMS. All the data are fitted with the models presented in subsection 1.9..... 80

Figure 51 Normalised d_{33} vs. annealing temperature for 0-3 and 1-3 BT/PDMS at 24%v..... 81

Figure 52 X-ray diffraction of 0-3 BT/PDMS (left side) and 1-3 BT/PDMS (right side) at 25,100, 130 and 150°C..... 82

Figure 53 a) Storage modulus and b) Loss modulus for 0-3 BT/PDMS at all the volume contents produced examined at 25°C. 83

Figure 54 a) Storage modulus and b) Loss modulus for 1-3 BT/PDMS at all the volume contents produced examined at 25°C. 83

Figure 55 Y vs. volume fraction for 0-3 and 1-3 BT/PDMS..... 84

Figure 56 Heat flow (mW/mg) from [-150°C to 15°C] measured with DSC for a) 0-3 BT/PDMS from 0%v to 24%v and b) 1-3 BT/PDMS from 0%v to 24%v. The red arrow indicates the inflection point of the glass transition, while the red circle is surrounding the melting peak at ~-48°C. The black arrows are indicating the glass transitions that appears in 1-3 24%v BT/PDMS..... 86

Figure 57 a) Zoom over the glass transition for 0-3 BT/PDMS from 0%v to 24%v of filler and b) zoom over the glass transition for 1-3 BT/PDMS from 0%v to 24%v of filler. c) Tg (°C) variation with filler content for 0-3 (black dots) and 1-3 (red dots) BT/PDMS composites. D) Variation of the ΔT_g (°C) for 0-3 and 1-3 BT/PDMS in function of the volume content. 87

Figure 58 a) Variation of ΔC_p with volume content and connectivity; b) melting enthalpy for 0-3 BT/PDMS 24%v and 1-3 BT/PDMS with 12%v and 24%v of filler..... 87

Figure 59 Heat flow vs. Temperature for pure PDMS, 0-3 and 1-3 BT/PDMS 24%v..... 88

Figure 60 $\tan\delta$ vs. Temperature from 100 mHz to 1 MHz for a) pure PDMS, b) 0-3 BT/PDMS 24%v and c) 1-3 BT/PDMS 24%v 90

Figure 61 $\tan\delta$ vs. temperature for 1-3 BT/PDMS 24%v (red lines), 0-3 BT/PDMS (green lines) and pure PDMS (blue lines) for 100 mHz, 1kHz and 1MHz as indicated in the graphs..... 90

Figure 62 ϵ'_r vs. Temperature at 100 mHz (black curves), 1kHz (red curves) and 1MHz (green curves), for pure PDMS (continuous line), 0-3 BT/PDMS 24%v (dash and dot lines) and 1-3 BT/PDMS 24%v (dash lines). 91

Figure 63 Arrhenius plot reporting the relaxation time τ (s) vs $1000/T$ (K^{-1}) for pure PDMS, 0-3 and 1-3 BT/PDMS 24%v. The x axis is reversed so that the high temperature is on the right side and the lower one on the left. The data are fitted with the VTF law, showing two relaxations associated with glass transition..... 92

Figure 64 COMSOL® FE simulation of spherical filler composites with a) 0-3 and b) quasi 1-3 connectivity. For each configuration, the electric field inside the fillers is displayed, when an external field of $30 \text{ V } \mu\text{m}^{-1}$ is applied to the entire system in the z direction..... 99

Figure 65 COMSOL® FE simulation of fibers composites with a) 0-3 connectivity, b) perfectly aligned fibers and c) slightly tilted fibers. For each configuration, the electric field inside the fillers is displayed, when an external field of $30 \text{ V } \mu\text{m}^{-1}$ is applied to the entire system in the z direction.	100
Figure 66 Voltage distribution in response to an external compressive stress of 10 kPa simulated using COMSOL® for a) 0-3 particle based composite and b) quasi 1-3 particle based composite.....	100
Figure 67. Voltage distribution in response to an external compressive stress of 10 kPa simulated using COMSOL® for a) 0-3 fiber composite, b) composite with perfectly aligned fibers and c) composite with slightly tilted fibers.	101
Figure 68 X-ray diffraction at 25°C of NaNbO ₃ fibers and particles after 4h annealing at 600°C	102
Figure 69 SEM images depicting a) Na ₂ Nb ₂ O ₆ fibers produced via hydrothermal synthesis prior to annealing, b) NaNbO ₃ fibers annealed for 4 hours at 600°C, c) NaNbO ₃ particles produced via hydrothermal synthesis and annealed for 4 hours at 600°C. Near to each picture the distribution in length (for fibers) or diameter (for particles), computed via ImageJ®, is reported.	104
Figure 70 Images acquired by SEM of a) 1%v NN_MF/PDMS with 0-3 connectivity, b) 1%v NN_MF/PDMS with quasi 1-3 connectivity, c) unstructured NN_MF/PDMS 3%v, d) structured NN_MF/PDMS 3%v, e) unstructured NN_MF/PDMS 5%v, f) structured NN_MF/PDMS 5%v, g) 0-3 NN_MP/PDMS 5%v, h) 1-3 NN_MP/PDMS 5%v.....	105
Figure 71 Relative permittivity real for a) PDMS and 0-3 NN_MF/PDMS with 1, 3 and 5%v and b) PDMS and 1-3 NN_MF/PDMS with with 1, 3 and 5%v.	106
Figure 72 Loss tangent for a) PDMS and 0-3 NN_MF/PDMS with 1%v, 3%v and 5%v and b) PDMS and 1-3 NN_MF/PDMS with with 1%v, 3%v and 5%v.	107
Figure 73 a) Relative permittivity real part and b) dielectric loss tangent for PDMS and NN_MP/PDMS 5%v with 0-3 and 1-3 connectivity.	107
Figure 74 Real part of dielectric constant (ϵ'_r) versus fiber volume content for a) 0-3 and 1-3 NN_MF/PDMS structured with $6 \text{ V } \mu\text{m}^{-1}$ b) 1-3 NN_MF/PDMS structured with $4 \text{ V } \mu\text{m}^{-1}$ and $6 \text{ V } \mu\text{m}^{-1}$	109
Figure 75 ϵ'_r for 5%v NN_MP/PDMS and NN_MF/PDMS composites in both 0-3 and quasi 1-3 connectivity. The arrows indicate the increasing rate of ϵ'_r achieved by DEP structuration, and the increase of ϵ'_r related to the shape of the filler in quasi 1-3 composites.	111
Figure 76 Saturation of poling field for non-structured and structured composites (4 and $6 \text{ V } \mu\text{m}^{-1}$) with a) 1%v of NN fibers, b) 3%v of NN fibers, c) 5%v of NN fibers and d) 5%v of NN particles.	112
Figure 77 a) Piezoelectric charge coefficient (d_{33}) plotted as function of fibers volume content for unstructured and structured ($6 \text{ V } \mu\text{m}^{-1}$) NN_MF/PDMS composites. b) d_{33} vs. filler content for NN_MF/PDMS composites structured with 4 and $6 \text{ V } \mu\text{m}^{-1}$	113
Figure 78 d_{33} of 5%v NN_MP/PDMS and NN_MF/PDMS in 0-3 and quasi 1-3 connectivity ($6 \text{ V } \mu\text{m}^{-1}$). The arrows indicate the increasing rate in d_{33} achieved by structuring for both particle and fiber composites, and the rise in d_{33} from structured NN_MP/PDMS to structured NN_MF/PDMS.....	114
Figure 79 a) g_{33} in function of fibers volume content for 0-3 non-structured composites and quasi 1-3 composites structured with 4 and $6 \text{ V } \mu\text{m}^{-1}$; b) g_{33} of 5%v NN_MP/PDMS and NN_MF/PDMS in 0-3 and quasi 1-3 connectivity ($6 \text{ V } \mu\text{m}^{-1}$). The arrows indicate the increasing rate in g_{33} achieved by structuring for both particle and fiber composites, and the rise in d_{33} from structured NN_MP/PDMS to structured NN_MF/PDMS.	115

Figure 80 a) Storage modulus and b) Loss modulus for 0-3 NN_MF/PDMS at all the volume contents produced and pure PDMS. 116

Figure 81 a) Storage modulus and b) Loss modulus for 1-3 NN_MF/PDMS at all the volume contents produced and pure PDMS. 116

Figure 82 a) Y vs. volume fraction for 0-3 and 1-3 NN_MF/PDMS. b) Comparison of the experimental results with the Halpin-Tsai model, which evaluate the Young's modulus as function of the angle θ ($^{\circ}$ deg), which is the inclination of the fiber with respect to the applied stress. Dots and squares are the experimental values for 0-3 and 1-3 NN_MF/PDMS composites..... 118

Figure 83 a) Storage modulus and b) Loss modulus for 0-3 and 1-3 NN_MP/PDMS at 5% v..... 119

Figure 84 Y for pure PDMS, 0-3 and 1-3 NN_MP/PDMS. 119

Figure 85 a) Heat flow (mW/mg) vs. Temperature measured via Differential Scanning Calorimetry for particles and fibers-based composite at 5%v of filler with 0-3 and 1-3 connectivity; b) Glass transition temperature for the four composites NaNbO₃-based under investigation. 120

Figure 86 Piezoelectric charge coefficient (g_{33}) versus the reciprocal of the Young's modulus($1/Y$) for the composite developed in this research compared to other piezoelectric materials reported in the literatures [138,151,202,222,229–231]..... 122

Figure 87 Representation of FFR sensor implemented inside the vessel. P_a is the proximal coronary pressure while P_d is the distal coronary pressure..... 125

Figure 88 a) Optical FFR catheter COMET™ II produced by Boston Scientific [248]. b) St. Jude Medical's New FFR Measuring Pressure Wire [249]. 126

Figure 89 Schematic drawing of the set up used to study the piezoelectric behavior of the film under dynamic mechanical excitation simulating an arterial pulse shape stress. 127

Figure 90 a) Picture representing the cardiac simulator arm. b) Detail of piezoelectric sensor applied on the catheter to perform the simulation..... 128

Figure 91 Typical architecture of FFR sensor made of piezoelectric composite. 128

Figure 92 d_{33} at different volume contents for BT/PDMS 0-3 and quasi 1-3; For pressure sensors the most performing is 1-3 at 24%v, indicated by the red arrow. 129

Figure 93 Performance of the developed piezoelectric sensor: a) Force input applied on the sensor with the set-up represented in Figure 89 a to simulate FFR measurement; b) charge output response of the sensor; and c) computed voltage output response. 129

Figure 94 a) Charge response of sensor developed in this study integrated in a catheter during the simulation setup shown in Figure 90-b, compared with b) FFR measurement carried out with a pressure wire available in the market [253]..... 130

Figure 95 a) Illustrative sketch of the setup simulating the cardiovascular system, where is inserted an artificial graft together with the developed piezoelectric sensor. b) Cross section of the tube when the clip is inserted and is open (0%), is clicked once (5%) and is clicked twice (25%)..... 132

Figure 96 Picture of the setup simulating the cardiovascular system used to perform the proofs of concept. 133

Figure 97 Detail of the ePTFE graft incorporated with the smart sensor made of piezoelectric composite. 133

Figure 98 a) Picture of the evolution of the blood pressure measured by the blood pressure monitor of the cardiovascular simulator. b) Evolution of the open-circuit voltage generated by the smart graft which follows the systolic-diastolic pressure variation when the clips are open. 134

Figure 99 Schematic drawing of the smart graft integrated sensor, where two clips are applied prior and after the graft and individually closed to simulate the presence of a clot occlusion.	135
Figure 100 Evolution of the piezoelectric response on the graft sensor following the systolic-diastolic pressure for: a) occlusion applied before the sensor, where the amplitude of the signal decreases with an increasing % of occlusion (from 0% to 25%); b) an occlusion applied after the sensor, where the increasing the % of occlusion induces an increase in the pressure sensed in the graft, leading to an increase of the output signal from the sensor. All the values are reported as normalized voltage, meaning that the voltage measured was normalized over the maximum voltage developed at 0%.....	135
Figure 101 Linear variation of the voltage amplitude vs. the % of occlusion variation for the before-clip and after-clip, respectively; in the graph are also reported pictures of the cross section of the tube for ground state, i.e., 0%, 5% and 25%.....	136
Figure 102 Normalized losses versus frequency for the LC system with the liquid passing through it: the shift of the resonance frequency due to the partial closure of the clip applied before a) and after b) the sensor (from 0% to 5% to 25%)......	137
Figure 103 Resonance frequency of the filter vs. the occlusion's degree for before clip and after clip, respectively.	138
Figure 104 Drawing representing the primary and secondary hemostases occurring after vessel's damage.	144
Figure 105 Scheme displaying the coagulation cascade. The blue path is the intrinsic pathway, the green one is the extrinsic pathway and the red one is the common pathway.....	145
Figure 106 Schematic representation of a) TEG [®] technology; b) Rotem [®] technology; c) Sonoclot [®] technology.....	146
Figure 107 Typical signature of a) TEG [®] , b) Rotem [®] . c) Illustration of the phenomena related with the TEG [®] and Rotem [®] indicators; d) Sonoclot [®] signature.....	148
Figure 108 a) P-L-P structure of the membrane of the cells. b) Electrical model of the system made of ECF, ICF and membrane.....	149
Figure 109 Electric field distribution for a) low frequency voltage, b) high frequency voltage.	150
Figure 110 a) Broadband dielectric spectroscopy (relative permittivity real part) of whole blood [289]. b) Dielectric broadband spectroscopy (real permittivity) of whole blood normalized over the value at MHz, performed in this work at 37°C.....	151
Figure 111 a) Two-electrodes and b) four-electrodes bioimpedance configuration.....	152
Figure 112 a) Sample-holder used for blood impedance magnitude spectroscopy. b) Complete set-up employed in $ Z $ measurements.	153
Figure 113 Time evolution of normalized impedance ($ Z / Z_{t=0} $) measured at 10 kHz for the whole blood and recalcified blood.	156
Figure 114 Evolution in time of normalized impedance magnitude during coagulation at 100 Hz, 1 kHz, 10 kHz, 100 kHz and 1 MHz.....	157
Figure 115 a) Retracting blood impedance magnitude analysis at 10 kHz with respective picture of retracted blood clot; b) non-retracting blood impedance magnitude analysis with picture of non-retracted clot.....	157
Figure 116 a) Impedance phase angle (Φ) as function of time for recalcified blood; the red arrows indicate the value of Φ before and after the steep increase. b) Impedance phase broadband spectroscopy (100 Hz-1MHz) of clot and serum separated after retraction.....	158

Figure 117 a)-l) Confocal microscopy frames at different times since the addition of calcium solution. The red arrow in figure a) indicates the dark shadow of a red cell. The green fibers correspond to the fibrin network labeled using fibrinogen from human plasma Alexa Fluor™ 488 conjugate. 160

Figure 118 a)-l) Detail of a of fibrin branch from its appearance through the different moment of the contraction. On each frame the length of the fibrin is measured in pixels using ImageJ® software. .. 161

Figure 119 Impedance magnitude test of clotting blood from the same donor as that tested via confocal microscopy. 161

Figure 120 a) Impedance magnitude test and b) Rotem® analysis of recalcified blood from the same donor without TF..... 162

Figure 121 Box graph computed over 9 different blood samples (recalcified without TF) representing clotting time by impedance magnitude spectroscopy and Rotem® (black and red boxes, respectively). 163

Figure 122 a) Impedance magnitude test and b) Rotem® analysis of recalcified blood from the same donor with TF..... 163

Figure 123 Box graph computed over 6 different blood samples (recalcified with TF) representing clotting time by impedance magnitude spectroscopy and Rotem® (green and blue boxes, respectively). 164

Figure 124 Drop of blood on the four different surfaces pictured by means of Contact Angle Goniometer. 166

Figure 125 Coagulation impedance test at 25°C carried out simultaneously on a) PET and PET treated with UV-ozone b) PVDF positive and negative sides. 167

Figure 126 Concept behind tissue engineered vascular grafts covered in endothelial cells. 170

Figure 127 Stages of cells culture. 171

Figure 128 Typical steps of Stem cells culture..... 171

Figure 129 a) Picture of the photo-capacitive sample based on ZnS:Cu/PVFD-TrFE-CFE; b) architecture of the photo-capacitive device developed. 175

Figure 130 Set-up used to examine the charge produced by the sample when exposed to blue light. In this image, the connection is made in a way to measure the charge developed on the surface directly enlightened. 176

Figure 131 Set-up used for water/ITO contact angle. In this drawing we report the case where ITO is positively charged..... 177

Figure 132 Class II hood used to perform all the cells manipulation. 178

Figure 133 Drawing of the cells sample holder with detail of the geometry..... 179

Figure 134 Charge per unit of surface when the photo-capacitive sample is lit by a blue light. The black curve is the positive charge coming from the face that is directly facing the light, while the negative one is described by the red curve and is the side not facing the light. 179

Figure 135 a) Relative permittivity real part vs. frequency and b) dielectric losses ($\tan\delta$) vs. frequency (0.1-10⁶Hz) at 25°C without (black curve) and with light (red curve). 181

Figure 136 Drop of pure water on ITO a) uncharged, b) positively charged and c) negatively charged. 181

Figure 137 Normalized Contact angle (°deg) of pure water in contact with ITO in three different situations: 1) no charge; 2) negative surface charge; 3) positive surface charge. The real value for the

contact angle is reported in the graph at the top of the picture; the test is repeated on two different slides of ITO/glass (test 1 and test 2).	182
Figure 138 Percentage of HBEPc-p cells variation adhered on ITO substrate charge positively, negatively with respect to uncharged sample (control) depending on the amount of charge per unit of surface. The test analysis performed via optical microscope, was done after 6h of incubation at 37°C.	183
Figure 139 Epithelial cells (HBEPc-p) adhered onto a)-c) ITO positively charged (106 pC.cm ⁻²), d)-f) ITO negatively charged (160 pC.cm ⁻²), g)-i) ITO without charge. The imaging, taken via optical microscopy in light transmission was carried out after 6h of incubation.	184
Figure 140 Human bronchial epithelial cells from a) Biotrend® [314] and b) Sigma Aldrich® [315].	184

List of Tables

Table 1 Voltage, g_{33} D, ϵ'_r and d_{33} for 0-3 and 1-3 BT/PDMS 5% v simulated using COMSOL®.	72
Table 2 Relative dielectric permittivity (real part) for 0-3 and 1-3 BT/PDMS at 2.4% v, 12% v and 24% v, compared to pure PDMS.	78
Table 3 d_{33} and g_{33} for 0-3 and 1-3 BT/PDMS at 2.4% v, 12% v and 24% v, compared to pure PDMS.	79
Table 4 Values of the Young's Modulus evaluated at 1 Hz at room temperature for all the composites of BT/PDMS with 0-3 and 1-3 connectivity and pure PDMS.	84
Table 5 Voltage, g_{33} D, ϵ'_r pre-poling and after poling, and d_{33} for 0-3 and 1-3 NN_MF/PDMS and NN_MP/PDMS with 5% v, simulated using COMSOL®.	101
Table 6 Real part of dielectric permittivity at 1 kHz, for all the composite of NN_MF/PDMS and NN_MP/PDMS.	108
Table 7 Comparison between experimental permittivity and FE permittivity at 5% v for fiber and particle-based composites with 0-3 and quasi 1-3 connectivity.	109
Table 8 d_{33} for 0-3 and 1-3 NN_MF/PDMS and NN_MP/PDMS composites developed in this work.	112
Table 9 g_{33} for 0-3 and 1-3 NN_MF/PDMS and NN_MP/PDMS developed in this work.	114
Table 10 Comparison between the experimental results and the FE analysis for particle and fiber-based composites at 5% v of filler (0-3 and 1-3 connectivity).	115
Table 11 Y for 0-3 and 1-3 NN_MF/PDMS and NN_MP/PDMS developed in this work.	118
Table 12 ΔC_p and ΔT_g associated with the glass transition for 0-3 and 1-3 NN_MP/PDMS and 0-3 and 1-3 NN_MF/PDMS 5% v.	120
Table 13 Statical data related to $CT_{Impedance}$ and CT_{Rotem} for recalcified samples with and without TF.	
6.4 Wettability and blood coagulation.	165
Table 14 Contact angle of blood on PET non-treated, PET UV-treated, PVDF positive and negative sides.	165
Table 15 Capacitance for the photo-capacitive samples without and with light excitement.	180
Table 16 Water contact angle (°deg) with ITO in absence of charge and with negative and positive charge.	181

Nomenclature

α = Dielectric relaxation amorphous phase	∇ = Nabla
α' = Dielectric relaxation constrained amorphous phase	
α = Polarizability	a = Electrodes thickness
α_j = Polarizability along the j axis	ACT = Activated clotting time
α_f = Dilatation coefficient of free volume	AFE = Antiferroelectric
α = alpha angle TEG/Rotem	
β = Dielectric relaxation	BaTiO ₃ = Barium Titanate
γ = Dielectric relaxation	BDS = Broadband dielectric spectroscopy
δ = Poling ratio	Bi ₄ Ti ₃ O ₁₂ = Bismuth titanate
ΔC = Capacitance variation	BNT = Ternary compositions BaO-TiO ₂ -Nd ₂ O ₃
ΔC_p = Heat capacity changes	BSE = Back scattered electrons
ΔQ = Charge variation	BT/PDMS = Barium titanate / PDMS composite
ΔT_g = Glass transition temperatures step	
ϵ_0 = Vacuum permittivity (8.85×10^{-12} F m ⁻¹)	C = Capacitance
$\epsilon_{0-3 M-G}$ = Permittivity Maxwell - Garnett model	C_f = Capacitance of the filter
$\epsilon_{0-3 Yamada}$ = Permittivity Yamada's model	C_M = Membrane capacitance
ϵ_{1-3} = Parallel Mixing rule for permittivity 1-3 composites	C_p = Specific heat
ϵ_f = Permittivity of the filler	CAD = Coronary artery disease
ϵ'_f = Filler real dielectric permittivity	CABG = Coronary artery bypass grafting
ϵ''_f = Filler imaginary dielectric permittivity	CFT = Clot formation time
ϵ^*_f = Filler complex dielectric permittivity	CM = Clausius-Mossotti Factor
ϵ_r = Relative dielectric permittivity	CR = Clot rate
ϵ^{T_r} = dielectric constant at constant Temperature	CT = Clotting time
ϵ_m = Permittivity of the matrix	CT _{Impedance} = Clotting time measured via impedance magnitude test
ϵ'_m = Matrix real dielectric permittivity	CT _{Rotem} = Clotting time measured via Rotem
ϵ''_m = Matrix imaginary dielectric permittivity	CVD = Cardiovascular disease
ϵ^*_m = Matrix complex dielectric permittivity	
$\epsilon_{quasi 1-3}$ = Bowen's model for permittivity of quasi 1-3 composites	D = Dielectric displacement
η = Viscosity	D = Fragility coefficient
θ = Angle of inclination of the fibers with respect to the x axe	d = Diameter sphere
θ = Orientation angle of the particles	DALY = Disability adjusted life-years
ν_{LT} = Poisson ratio	DMA = Dynamic mechanical analysis
π = Mathematical constant (3.14159)	DSC = Differential scanning calorimetry
σ_m = Matrix conductivity	$d_{ij} = d_{ij}$ = Piezoelectric charge coefficient
σ_f = Fillers conductivity	d_{ij} = dielectric charge coefficient
ρ = Angle of a fiber with respect to the electric field	d_{33} = Piezoelectric charge coefficient 33 direction
σ = Stress	$d_{33 Yamada} = d_{33}$ Yamada's model
$\tau(T)$ = Relaxation time	$d'_{33} = d_{33}$ for the ceramic inclusions
τ_0 = Preexponential factor Arrhenius law	$d^{m_{33}} = d_{33}$ for the matrix
τ_{0a} = Preexponential factor VTF law	$d_{33 1-3}$ = Parallel Mixing rule for d_{33} 1-3 composites
φ_{Cr} = Volume fraction of crystalline phase	$d_{33 quasi 1-3}$ = Van den Ende's model for d_{33} of quasi 1-3 composites
φ = Particles volume fraction	D_i = Dielectric displacement in the i direction
Φ = Impedance angle	
Φ_{Blood} = Blood impedance phase angle	E = Electric field
Φ_{Serum} = Serum impedance phase angle	e = Eccentricity ellipsoid
Φ_{clot} = Clot impedance phase angle	E_0 = Applied electric field
ψ = Angular velocity of the fibers	$E_{0 RMS}$ = Root mean square applied electric field
ω = Pulsation ($= 2 \pi f$)	E_2 = Local electric field coefficient
	E_a = Activation energy
	E_c = Coercitive electric field

E_f = Electric field threshold
 E_i = Electric field in the i direction
 E_{pol} = Poling electric field
 E_s = Electric field of saturation on poling
 E_z = Electric field z direction
EC = Endothelial cells
ECF= Extracellular fluids
ECM = Extracellular matrix

f_{VII} = Protein factor VII
 f_{VIIa} = Activated protein factor VII
 f_X = Protein factor X
 f_{Xa} = Activated protein factor X
 f_{XI} = Protein factor XI
 f_{XIa} = Activated protein factor XI
 f_{XII} = Factor XII
 f_{XIIa} = Activated protein factor XII
 $F_{DEP}(t)$ = DEP force
 F_{drag} = Drag force
 $F_{Drag\ i}$ = i -th Drag force component
 f_r = Resonance frequency
FDA = US Food and drug administration
FE = Finite element
FFR = Fractional Flow Reserve
FoM = Figure of Merit

g_{33} = Piezoelectric voltage coefficient 33 direction
 $g_{33\ Yamada}$ = g_{33} Yamada's model
 g_{ij} = Piezoelectric voltage coefficient
 G_{LT} = Shear modulus

HBEpC-p= Epithelial brochial human cells
HBS= Hepes buffered solution
HEK293T= Embryonic kidney cells
HepG2= Human hepatocellular carcinoma cells

i = Imaginary vector
 I = Current
ICF= Intracellular fluids
 Im = Imaginary part
IQR= Interquartile range
ITA = Internal thoracic artery
ITO= Indium tin oxide

j = a, b and c axis for ellipsoidal particle
 K^*_j = Complex polarizability
 $K^*_{//}$ = Parallel complex polarizability
 K^*_{\perp} = Perpendicular complex polarizability
KNbO₃ = Potassium Niobate
KNN = Potassium sodium niobate

L = Fiber's length
 L_f = Inductance of the filter
 LC = Inductance-capacitance filter
LiNbO₃ = Lithium niobate
LI60= Lysis 60 minutes after MFC
LY30= Lysis 30 minutes after MA

M= Membrane
 $M_{//}$ = Depolarization factor parallel direction
 M_{\perp} = Depolarization factor perpendicular direction
 M_j = Depolarization factor along the axis j
MA= Maximum amplitude
MCF= Maximal clot firmness
MEK= Methyl Ethyl Cetone
MEMS = Micro-Electro-Mechanical Systems
 MF = Micro-fibers
 MP = Micro- particles

N = Number of segments
 n = Depolarization factor
NaNbO₃ = Sodium Niobate
 $NaOH$ = Sodium hydroxide
NaTaO₃ = Sodium tantalate
 Nb_2O_5 = Niobium pentoxide
 Nb_6O^{8-19} = Intermediate compound
NIH3T3= Mouse embryofibroblast
NN_MF/PDMS = Sodium niobate microfibers/PDMS
NN_MP/PDMS = Sodium niobate microparticles / PDMS

P = Polarization
 \mathbf{p}^* = Dipole moment
 P_s = Saturation Polarization
 P_r = Remnant polarization
 $P2_1ma$ = Ferroelectric Crystalline space group
PA = Polyamide
PA11 = Polyamide
PAD = Periphery artery disease
Pbcm= Antiferroelectric Crystalline space group
PbNb₂O₆ = Lead meta niobate
PBS= Phosphate buffered saline
PCL = Polycaprolactone
PDMS = Polydimethylsiloxane
PDS = Polydioxanone
PE = Paraelectric Phase
PET = Polyethylene terephthalate
PG910 = Polyglactin (Vicryl®)
PGA = Polyglycolic acid
PHA = Polyhydroxyalkanoate
PLA = Polylactic acid
P-L-P= Protein-lipid-protein structure
PMMA = Polymethyl methacrylate
PTFE = Polytetrafluoroethylene
PVDF = Polyvinylidene fluoride
P(VDF)-TrFE = Poly(vinylidene fluoride-trifluoroethylene)
PVDF-TrFE-CFE= Vinylidene fluoride-trifluoroethylene-chlorofluoroethylene terpolymer
PZT = Lead zirconate titanate

Q = Charge
 Q = Mechanical quality factor
 Q_1 = 25th percentile
 Q_2 = 50th percentile

Q₃= 75th percentile
QDC= Quartile coefficient of dispersion

R =Radius
ℜ= Starting fibrin formation TEG®
℞= Perfect gas constant
r = Average size of the particle-interparticle distance ratio
R1= Rate of fibrin formation Sonoclot®
R2= Second shoulder Sonoclot®
R3= Fibrinolysis shoulder Sonoclot®
R_{ICF}= Intracellular fluids resistance
R_{E_{CF}}= Extracellular fluids resistance
RBC= Red blood cell
Re = Real part
Rotem®= Rotational thromboelastometry

S= Surface
s = Distance between two particles
S_I = Strain in the I direction
s^{E_{ij}} = Mechanical compliance at constant electric field
s^{f₃₃} = Filler elastic compliance in 33 direction
s^{m₃₃} = Matrix elastic compliance in 33 direction
SE = Secondary electrons
SEM= Scanning electron microscopy
SV = Saphenous vein
SMC = Smooth muscle cells
T= Penetration depth
t = Thickness
t₁ = Average size of the particle
t₂ =Interparticle distance
T^o = Temperature of the diffractometer
T_∞ = Homogeneous constant VTF law
T_c = Curie temperature

T_g= Glass transition temperature
T_J=Stress in the J direction
T_{REAL} = Desired temperature in XRD chamber
tan δ = Dielectric losses
TEG®= Thromboelastogram

V= Voltage
v= Volume filler
v= Filler speed
v_{//} = Parallel velocity of the fiber
v_⊥ = Perpendicular velocity of the fiber
v_i= i-th velocity of the fiber component
VTF = Vogel -Tamman - Fulcher

w= Electrodes distance

X_M= Capacitive reactance membrane
XRD = X-ray diffraction

Y= Young's modulus
Y'= Storage component Young's modulus
Y''= Dissipation component Young's modulus
Y₃₃ = Elastic moduli of the filler in 33 direction
Y_f= Fiber Young's modulus
Y_L= Longitudinal modulus
Y_m= Matrix Young's modulus
Y_T= Transversal modulus

Z= Impedance
Z_{cell}= Cell impedance
ZnO = Zinc oxide
ZnS= Zinc sulfide

Le résumé de la thèse en français

Ce projet de recherche vise à mettre au point de nouvelles technologies pour les greffes vasculaires qui permettent un suivi in vivo du dispositif et son intégration complète dans le corps humain. Cette thèse est structurée en quatre phases, impliquant différents domaines scientifiques tels que l'ingénierie des matériaux, le biomédical, l'électricité et la bioélectronique. La combinaison de tous ces domaines nous a permis d'apporter des innovations dans le domaine des dispositifs cardiovasculaires. Dans ce résumé de thèse, le contenu de chaque chapitre sera expliqué étape par étape afin de donner un aperçu général mais détaillé du projet.

Le **Chapitre I** présente la procédure chirurgicale du bypass vasculaire, qui consiste à ajouter un greffe vasculaire pour rediriger le flux sanguin lorsque les propres veines ou artères du patient sont obstruées. La solution optimale pour cette procédure serait d'utiliser les propres veines du patient (veine saphène par exemple), car cela permettrait une intégration optimale du greffon. Cependant, il arrive souvent que cela ne soit pas possible et qu'il soit nécessaire d'intervenir avec des prothèses artificielles. Aujourd'hui, les prothèses artificielles les plus utilisées sont en polyéthylène téréphtalate (PET) appelé Dacron® ou en polytétrafluoroéthylène expansé (ePTFE). Ces prothèses sont utilisées depuis des années dans diverses procédures de pontage telles que le pontage de l'artère carotide, le pontage périphérique et le pontage de l'artère coronaire et sont limitées à des diamètres <6mm. De récents développements ont vu l'émergence de prothèses en polyuréthane PU. Cependant, ils ont créé beaucoup de problèmes car une fois insérés dans le corps, ils créaient des sous-produits nocifs pour les humains. Récemment, plusieurs études ont porté sur le développement de TEVG, c'est-à-dire de greffons vasculaires issus de l'ingénierie tissulaire, mais ceux-ci n'ont pas encore été utilisés dans des cas cliniques. Un TEVG se compose d'un support, de cellules qui y ont étéensemencées et de signaux environnementaux appropriés (tels que des hormones de croissance et une stimulation physique) pour encourager le développement de nouveaux tissus. Le principal avantage des TEVG, qui les rend très intéressants pour les pontages, est leur excellente compatibilité tissulaire, qui prévient le rejet et maintient une perméabilité à long terme après la transplantation. Il existe des développements récents sur le TEVG avec des substrats biodégradables. Cette classe de greffons comprend des polymères artificiels biodégradables (PLA, PGA, etc.) qui sont capables de se dégrader avec le temps tout en stimulant la croissance d'un tissu de cellules qui établiront un nouveau conduit, ou des polymères naturels comme l'élastine ou le chitosan. En général, toutes ces prothèses présentent des limites considérables qui nécessitent des solutions urgentes.

Parmi les principaux problèmes rencontrés, on trouve une tendance à la formation de thrombus due à l'interaction entre le sang et les surfaces artificielles, un décalage entre les propriétés mécaniques des greffons et des vaisseaux humains, une mauvaise hémodynamique pouvant induire une hyperplasie intimale, c'est-à-dire l'accumulation de cellules endothéliales dans la zone de jonction entre la veine et le greffon, et enfin des infections.

Compte tenu de tous les problèmes soulevés, il est essentiel de mettre au point de nouvelles prothèses en utilisant des technologies susceptibles d'augmenter leur intégrabilité et d'éviter

des situations dangereuses pour la santé. C'est pourquoi la recherche actuelle s'est concentrée sur l'optimisation des greffons de plusieurs points de vue. Dans ce travail, nous nous focalisons sur la question de la thrombogénicité des greffons; en effet, le fait que le sang coagule au contact d'une surface artificielle est un phénomène connu depuis longtemps et est associé à la mauvaise hémocompatibilité des matériaux synthétiques. Cela peut entraîner un grave danger pour le patient, car la présence d'un thrombus réduit le flux sanguin vers les organes et, dans le pire des cas, peut provoquer une embolie ou une crise cardiaque. La conception de nouveaux greffons peut être abordée sous plusieurs aspects pour résoudre le problème de la coagulation. Tout d'abord, malgré les récents développements, les greffons actuellement utilisés continuent de développer des sténoses et de coaguler, mettant en danger la vie des patients. Un diagnostic rapide de la thrombose dans le greffon est crucial pour remplacer la prothèse avant que des conséquences mortelles ne surviennent. Il est donc essentiel de développer un dispositif non invasif de surveillance de la coagulation qui puisse alerter rapidement l'utilisateur lorsqu'un blocage commence à se former à l'intérieur du greffon. Deuxièmement, pour mieux comprendre les facteurs qui déclenchent la formation de thrombus, il est nécessaire d'approfondir la recherche sur l'hémocompatibilité des matériaux. Pour cela, il faut développer de nouvelles méthodes de test qui permettent d'examiner rapidement et simplement chaque surface. Enfin, il est essentiel de poursuivre les recherches sur les TEVGs, en accordant une attention particulière au potentiel d'ensemencement endothélial, afin de développer des greffons manufacturés hautement hémocompatibles. Nous pouvons résumer les principaux objectifs de ce travail comme suit : Développement de greffons autosurveillés capables de signaler la présence d'un caillot ; Développement d'un système de test dynamique in vitro pour l'évaluation de la thrombogénicité des dispositifs médicaux et des biomatériaux ; Conception de prothèses hybrides capables de favoriser l'endothélialisation.

Dans le **Chapitre II**, nous nous concentrons sur le développement de capteurs à intégrer dans les prothèses vasculaires afin de les surveiller in vivo. Le besoin de capteurs de pression flexibles et facilement adaptables aux prothèses nous a conduits à choisir des composites piézoélectriques pour ce projet. Ces matériaux, composés d'une charge piézoélectrique et d'une matrice polymérique, possèdent la capacité de développer une charge électrique en réponse à un stimulus mécanique externe et sont donc adaptés à la surveillance de la pression sanguine. Toutefois, l'une des principales limites de ces matériaux est qu'ils nécessitent souvent une teneur élevée en charges pour atteindre des niveaux de sensibilité optimaux. En effet, les composites courants présentent une connectivité 0-3, c'est-à-dire que la charge est dispersée de manière aléatoire dans la matrice. De plus, le fort taux de charge de ces composites 0-3 altère de manière importante la souplesse de ces matériaux.

L'une des façons d'améliorer leurs propriétés électroactives et mécaniques est d'augmenter leur connectivité dans une direction, ce qui permet de construire des composites à connectivité *quasi* 1-3, sans qu'il soit nécessaire d'augmenter la teneur volumétrique en charge au détriment des propriétés mécaniques. Cette connectivité implique que les charges soient disposées de manière à former des colonnes le long d'une direction préférée, dans le but de minimiser la distance entre les charges dans cette direction. Pour créer ce type de

connectivité, nous avons utilisé la technique de structuration par diélectrophorèse (DEP-structuration), qui consiste à appliquer un champ électrique Alternatif basse fréquence au matériau avant et pendant sa polymérisation. Celle-ci interagit avec les particules diélectriques, qui se redistribuent pour former des colonnes denses le long des lignes de champ électrique. Il en résulte des matériaux anisotropes dont les propriétés piézoélectriques sont renforcées dans une direction spécifique.

Dans un premier temps, les concepts fondamentaux de la piézoélectricité, du ferro/anti-ferroélectricité, des composites piézoélectriques, de la connectivité et de la diélectrophorèse sont exposés. Ensuite, des composites avec des particules de titanate de baryum (BaTiO_3) dans une matrice de polydiméthylsiloxane (PDMS), appelés BT/PDMS, sont développés et caractérisés. Après avoir analysé les paramètres optimaux du processus de structuration DEP en termes de fréquence et d'amplitude du champ électrique (1Hz , $3\text{ V } \mu\text{m}^{-1}$), les composites BT/PDMS sont préparés avec une connectivité 0-3 et 1-3 et trois contenus volumiques différents ($2,4\%v$, $12\%v$ et $24\%v$). Les résultats confirment avec succès une amélioration de ϵ'_r , d_{33} et g_{33} apportée par la structuration DEP. Par rapport au composite non structuré ($24\%v$), le 1-3 BT/PDMS présente une permittivité diélectrique supérieure de 70% , un coefficient de charge piézoélectrique (d_{33}) amélioré de plus de 3 fois, ainsi qu'une augmentation de 1.6 fois pour le coefficient de tension piézoélectrique (g_{33}). L'étude sur la stabilité thermique piézoélectrique met en évidence que le composite quasi 1-3 conserve de bonnes propriétés piézoélectriques dans une large gamme de température ($T \sim 100^\circ\text{C}$). Les valeurs expérimentales sont en accord avec les modèles physiques (Bowen, Yamada et Van den Ende) et l'analyse par éléments finis (FE) reproduite dans ce travail. L'analyse XRD menée à différentes températures ($25\text{-}150^\circ\text{C}$) confirme également la stabilité structurale des deux configurations de matériaux, qui commencent à perdre leurs propriétés piézoélectriques aux alentours de 130°C . L'analyse DMA prouve que la structuration DEP affecte légèrement les propriétés mécaniques du composite en augmentant la rigidité dans la direction perpendiculaire de l'alignement. Enfin, l'analyse DSC permet de comprendre l'effet de la teneur en phase inorganique et de la connectivité sur la température de transition vitreuse, indiquant que la structuration à $24\%v$ de charge affecte la polymérisation des chaînes, induit une seconde transition vitreuse liée à la phase amorphe contrainte et l'apparition d'un pic de fusion à -48°C , lié au PDMS non polymérisé. La présence d'une phase amorphe contrainte et l'empêchement partiel de la polymérisation constatée par DSC peuvent justifier l'augmentation des pertes diélectriques ainsi que le renforcement mécanique constaté pour le 1-3 BT/PDMS avec $24\%v$ de charge. La spectroscopie diélectrique à large bande en température, et en particulier $\tan\delta$ vs température dans la gamme $100\text{mHz} - 1\text{MHz}$, a permis de confirmer l'observation faite par DSC. En conclusion, le 1-3 BT/PDMS conçu dans ce travail montre une bonne combinaison de propriétés mécaniques et piézoélectriques. Dans le chapitre III, l'échantillon structuré développé ici sera testé comme biocapteur pour la surveillance de la pression sanguine, intégré sur un cathéter FFR.

Ensuite, une deuxième classe de composites est développée à base de Niobate de Sodium (NaNbO_3) dans une matrice PDMS. Dans cette partie du projet, nous souhaitons comprendre l'effet du facteur de forme sur les composites structurés. Des fibres et des particules de

NaNbO₃ sont préparées par synthèse hydrothermale et utilisées pour produire des composites avec une connectivité 0-3 et *quasi* 1-3. Les composites avec fibres (NN_MF/PDMS) sont produits avec des charges de 1%v, 3%v et 5%v, tandis que les composites avec particules (NN_MP/PDMS) sont produits avec des charges de 5%v, à des fins de comparaison. La structuration du NaNbO₃ en général, qu'il s'agisse de fibres ou de particules, permet d'obtenir une amélioration par rapport à ses homologues à connectivité 0-3.

En outre, le d_{33} du 1-3 NN_MF/PDMS est ~ 3 fois plus élevé que celui du 1-3 NN_MP/PDMS. De même, la permittivité et le g_{33} du composite à base de fibres dépassent tous les autres composites produits. Cette amélioration remarquable est due au fait que l'utilisation de fibres au lieu de particules permet une plus grande connectivité le long de l'axe de structuration, en effet le rapport dimension de filler-distance inter-filler est significativement plus élevé. L'analyse FE est en bon accord avec les résultats expérimentaux rapportés. Les résultats de l'analyse mécanique montrent que tous les composites ont un module d'Young similaire, ce qui indique que la structuration modifie les propriétés mécaniques dans une mesure limitée, ce qui est en bon accord avec les modèles rapportés par Halpin-Tsai pour les composites à fibres courtes.

Enfin, contrairement au composite BT, la DSC ne montre aucun changement discernable entre 0-3 et 1-3 ou entre les fibres et les particules. Les résultats révèlent clairement que le NN_MF/PDMS avec une très faible teneur en charge de 5%v présente le meilleur compromis entre les caractéristiques piézoélectriques (~ 10 pC N⁻¹) et l'extensibilité ($Y \sim 4.5$ MPa). Dans l'ensemble, les deux composites préparés, quasi 1-3 BT/PDMS 24%v et quasi 1-3 NN_MF/PDMS 5%v, semblent très appropriés pour les capteurs de pression sanguine.

Dans le **Chapitre III**, nous décrivons des preuves de concept où les capteurs développés sont intégrés dans des dispositifs de mesure de la pression vasculaire et testés dans des simulateurs du système cardiovasculaire. Tout d'abord, le BT/PDMS 24%v 1-3 intégré à un cathéter vasculaire est utilisé comme capteur *Fractional Flow Reserve* (FFR) dans un simulateur endovasculaire. Il s'avère être approprié pour mesurer la pression sanguine afin de déterminer le coefficient FFR. Cette approche est très importante pour les contrôles préopératoires des pontages, mais elle est également prometteuse pour les contrôles postopératoires. Deuxièmement, le NN MF/PDMS 5%v 1-3 est inclus dans un greffon et testé comme capteur de pression dans un simulateur vasculaire. Le composite se comporte parfaitement comme un détecteur de pression sanguine, démontrant une grande précision dans la mesure de la pression systolique et diastolique, ainsi que la capacité d'identifier la présence d'obstructions dans le flux qui, dans des scénarios réels, peuvent être produites par des thrombus. Dans cette expérience, le capteur a été connecté à une bobine inductive pour créer un filtre résonant LC. En cas d'obstruction, la fréquence de résonance du filtre changeait, signalant le développement d'un caillot sur la prothèse. Le système développé pourrait être implanté dans le corps humain pour fournir des informations en temps réel sur l'état de la greffe. Ce chapitre conclut la partie sur le développement des capteurs pour le contrôle des prothèses vasculaires.

Le **Chapitre IV** aborde le second objectif de ce travail, notamment le développement d'un système de test in-vitro pour évaluer la thrombogénicité des dispositifs médicaux et des biomatériaux. Dans ce chapitre, une nouvelle technique de surveillance de la coagulation basée sur la magnitude de l'impédance du sang pendant la coagulation est développée. Le dispositif se compose de deux électrodes qui peuvent être utilisées sur tout type de surface et garantissent une mesure fiable du sang, permettant d'identifier son hémocompatibilité. Le test consiste à envoyer un signal (tension) à l'échantillon de sang et à recueillir le courant de réponse. A partir de ces signaux, la magnitude de l'impédance peut être calculée. Deux marqueurs significatifs sont identifiés, c'est-à-dire liés à la formation de fibrine (le 1er marqueur) et à la contraction du caillot (le 2ème marqueur). L'étude de la phase d'impédance (Φ) confirme la signification du 2ème marqueur, révélant une augmentation du comportement résistif pendant la contraction causée par l'expulsion du sérum du caillot. Ensuite, l'imagerie par microscopie confocale fournit le temps de début de la polymérisation de la fibrine ainsi que le début de la contraction du caillot, fournissant la signification physique des deux marqueurs d'impédance. En outre, la caractérisation de l'impédance comparée à l'analyse de référence "ROTEM®" permet de renforcer la signification du 1er marqueur. Le test de magnitude d'impédance donne un aperçu du temps de coagulation qui pourrait être utilement utilisé comme un indicateur efficace des troubles d'hypo/per coagulabilité. Le test proposé dans cette étude est non seulement fiable en termes d'identification du temps de coagulation, mais il permet également de détecter le début de la rétraction du caillot, habituellement non accessible par les tests courants. En effet, si la contraction n'a pas lieu ou est retardée, le test ne devrait pas montrer le 2ème marqueur suivi d'une forte augmentation. Cette technologie, qui repose sur la caractérisation de l'impédance électrique du sang, permet un suivi en temps réel de la coagulation qui, autrement, est inaccessible avec les techniques actuelles (analyse Rotem®). L'originalité de ce travail réside dans le développement d'une technique simple et efficace, adaptable à la surface de plusieurs matériaux pour analyser leurs interactions avec le sang. L'approche proposée permet d'étudier le temps de coagulation lié à la mouillabilité.

Les résultats d'un test d'impédance de coagulation sur quatre surfaces à mouillabilité variable (PET, PET traité aux UV, PVDF côtés positif et négatif) révèlent que plus la mouillabilité est élevée, plus le temps de coagulation est rapide. Ceci prouve que le test d'impédance de coagulation est adapté à la détermination de la thrombogénicité des matériaux afin d'identifier les candidats les plus hémocompatibles. L'étude de la thrombogénicité des matériaux est cruciale car l'une des principales limites des prothèses cardiovasculaires est leur tendance à induire une thrombose une fois en contact avec le sang. Il existe donc un besoin urgent de matériaux capables de retarder ou d'éviter la coagulation, afin de prévenir les patients de graves problèmes de santé tels que l'ischémie, la crise cardiaque ou l'embolie. La caractérisation du sang par impédance peut donc ouvrir la voie à une nouvelle génération de matériaux intelligents qui pourraient surmonter le verrou technologique actuel des prothèses cardiovasculaires où la coagulation est un problème sérieux. Les perspectives d'avenir de cette étude incluent le développement de dispositifs intégrables dans une vraie greffe pour effectuer un suivi in vivo en temps réel.

Enfin, le **Chapitre V** aborde le dernier objectif de ce travail, à savoir la conception de prothèses hybrides capables de favoriser l'endothélialisation. Ce chapitre présente une étude préliminaire de l'interaction des cellules avec les surfaces chargées positivement et négativement par rapport aux surfaces non chargées. Grâce à cette étude, nous sommes en mesure de présenter des résultats préliminaires sur l'interaction charge/cellules humaines. L'intérêt pour cette question découle du fait que les prothèses humaines, en particulier les prothèses vasculaires au cœur de cette thèse, bénéficieraient énormément d'un revêtement de cellules endothéliales, c'est-à-dire les cellules qui tapissent la lumen des conduits vasculaires. Ce travail est réalisé sur des cellules épithéliales, car elles sont plus pratiques pour réaliser une première série de tests, mais les projets futurs incluront l'étude de l'interaction entre les cellules souches/endothéliales et la charge du substrat. La charge est générée par des échantillons photo-capacitifs basés sur des charges semi-conductrices ZnS:Cu dans une matrice ferro-relaxor P(VDF-TrFE-CFE) déposée sur des lames d'ITO/verre, qui sont capables de générer une charge de surface en réponse à une source lumineuse à une longueur d'onde de 470 nm. L'échantillon éclairé subit une augmentation de capacité de 40%, produisant une charge de surface de 90 pC/cm². La face du composite éclairée par la source lumineuse génère une charge positive, tandis qu'une charge négative est générée sur la face opposée à la lumière. Le système photo-capacitif (composite sur lame d'ITO/verre) est couplé électriquement à une autre lame d'ITO/verre non recouverte, ce qui permet de véhiculer des charges positives ou négatives selon le côté connecté, et un test de mouillabilité à l'eau pure est effectué. En présence d'une charge positive, la goutte d'eau présente une réduction de ~15% de l'angle de contact par rapport à l'ITO/verre non chargé, tandis que la réduction est de ~20% avec une charge négative, ce qui indique l'influence de la charge sur la surface. Enfin, des tests d'adhésion de cellules épithéliales sur des surfaces chargées positivement et négativement à différents niveaux de charge sont réalisés en comparaison avec des surfaces non chargées ; les résultats révèlent que la charge positive et négative surpasse le substrat à charge nulle. Il semble donc que l'effet des charges positives et négatives soit la clé de l'accélération de l'adhésion. Ces résultats sont prometteurs, néanmoins l'association entre la quantité de charge et l'adhésion ainsi que l'impact de la charge sur la croissance (temps de test >24h) nécessitent des tests supplémentaires. En outre, il pourrait être utilisé pour induire *ex vivo* la prolifération des cellules endothéliales sur les prothèses vasculaires avant qu'elles ne soient implantées dans le corps. Cependant, des tests supplémentaires sont nécessaires pour comprendre si ce phénomène est reproductible sur les cellules endothéliales. Toutefois, l'interaction démontrée des cellules épithéliales avec une surface dont la charge électrique est induite par la lumière présente des retombées prometteuses pour le développement de patch permettant une cicatrisation accélérée.

Enfin, ce projet permet de franchir des étapes intéressantes dans la direction de greffons vasculaires intelligents issus de l'ingénierie tissulaire, capables à la fois de s'auto-surveiller et de s'intégrer au corps humain sans induire de réactions négatives, ouvrant ainsi la porte à une nouvelle classe de greffons vasculaires intelligents issus de l'ingénierie tissulaire.

Purpose of this thesis

This thesis seeks to create novel technologies to enhance the functionality of vascular prostheses, mainly grafts. These devices, in reality, have various drawbacks, the most serious of which is that they promote blood clotting, resulting in thrombi, which are exceedingly dangerous to the patient. In this work we address the issue of thrombosis on three levels:

- The first point is based on an engineering approach that involves developing blood pressure sensors that, once embedded within the vascular graft, can monitor blood flow and detect the presence of a thrombus. Furthermore, they must be able to quickly transmit the occurrence via wireless network with point-of-care devices.
- The second point comprises two combined engineering and scientific methods for examining the interaction of blood with different surfaces via the development of a novel bioimpedance coagulation technique. This enables the evaluation of a surface's thrombogenicity, meaning tendency to induce blood to coagulate.
- Finally, the third point is investigating the interaction of charged scaffolds and cells. In fact, in order to optimize vascular prosthesis implantation, strategies that promote cellular coverage must be considered (endothelial cells). To do this, new procedures capable of stimulating the entire cell culture process must be developed in order to decrease the time of coverage and risk of infection. A possible approach appears to be the use of positively charged surfaces (photo-capacitive or piezoelectric materials).

Finally, the combination of these three distinct aspects of the research may enable the development of new generations of vascular prosthesis that can integrate into the circulatory system and self-monitor without inducing thrombogenic reactions.

Under the direction of thesis director Dr. Pierre-Jean Cottinet and co-director Dr. Jean-Fabien Capsal, this project was executed at the Laboratoire de Génie Electrique et Ferroélectricité (LGEF) of INSA de Lyon in collaboration with the cardiovascular department of the Hospices Civils de Lyon with Prof. Patrick Lermusiaux and Dr. Nellie della Schiava.

Chapter I

Vascular bypass grafting: state of the art

Summary

The state-of-the-art of vascular prostheses (grafts) used in vascular bypass surgeries is covered in this chapter. First, cardiovascular diseases (CVDs), the disorders that require bypass grafting, are introduced. Following that, the various types of synthetic and hybrid vascular grafts and the procedures in which they can be employed are explained. The primary issues associated with the usage of synthetic materials are reviewed, including compliance mismatch, lumen thrombogenicity, infection, and poor fluid hemodynamics. A review of the approaches presented to date in response to these issues is provided, with a focus on biodegradable polymers and hybrid grafts (Tissue Engineered Vascular Grafts). This study's approach, which aims to optimize vascular prosthesis, may be summed up as follows:

- *Development of vascular prostheses capable of self-monitoring and determining the reduction in blood flow, usually due to thrombosis or hyperplasia;*
- *Development of new techniques to study blood coagulation in contact with synthetic materials;*
- *Development of novel techniques that will allow for the rapid and safe coating of prostheses in endothelial cells (endothelialization of the grafts).*

1. Cardiovascular diseases

Nowadays cardiovascular disease (CVD) is one of the leading causes of death globally, accounting for 18 million deaths per year, of which 85% are due to heart attack and stroke [1,2]. CVDs, in general, are associated with a build-up of fatty deposits inside the arteries (atherosclerosis) and an increased risk of blood clots. Their occurrence grew in the past century due to changes in lifestyle and lengthening of the average lifespan. Previously, most deaths were linked to other circumstances such as plagues and malnutrition; however, these factors have continuously declined as food availability, cleanliness standards, and public health (vaccines and antibiotics) have improved. The average life expectancy has risen far above 50 years, and excessive consumption of fast food, alcohol, and tobacco has ushered in the so-called noncommunicable disease era, among which CVDs have outpaced mortality from infectious illnesses and hunger. Due to a variety of social and economic reasons, the prevalence of CVDs is not consistent around the world. Eastern Europe and Central Asia continue to have the greatest per capita burden of CVDs globally. In 2016 the highest overall burden of CVD was in East Asia (78.1 million CVD disability adjusted life-years [DALYs] and South Asia (65.6 million CVD DALYs), being associated to their large and aging populations [3,4]. These countries are followed by low- and middle-income nations with populations of more than 100 million, where the CVD burden rate is increasing year by year (**Figure 1**).

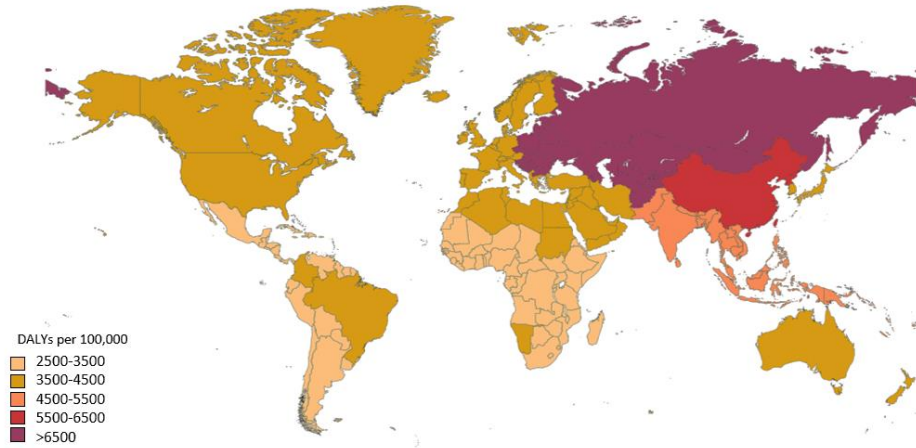


Figure 1 2016 disability adjusted life-years (DALYs) by country, global cardiovascular disease (CVD) DALYs per 100,000 inhabitants, 2016 [4].

Unhealthy eating, inactivity, usage of tobacco, and abusing alcohol are the main behavioral risk factors for heart diseases and stroke. Individuals may experience elevated blood pressure, elevated blood glucose, elevated blood lipids, as well as overweight and obesity because of those behavioral factors. There are other additional underlying factors that contribute to CVDs incidence, for instance urbanization, pollution, population aging, and globalization related to social, economic, and cultural change. Poverty, stress, and inherited factors are other important CVD risk factors (Figure 2 a-b) [1,5].

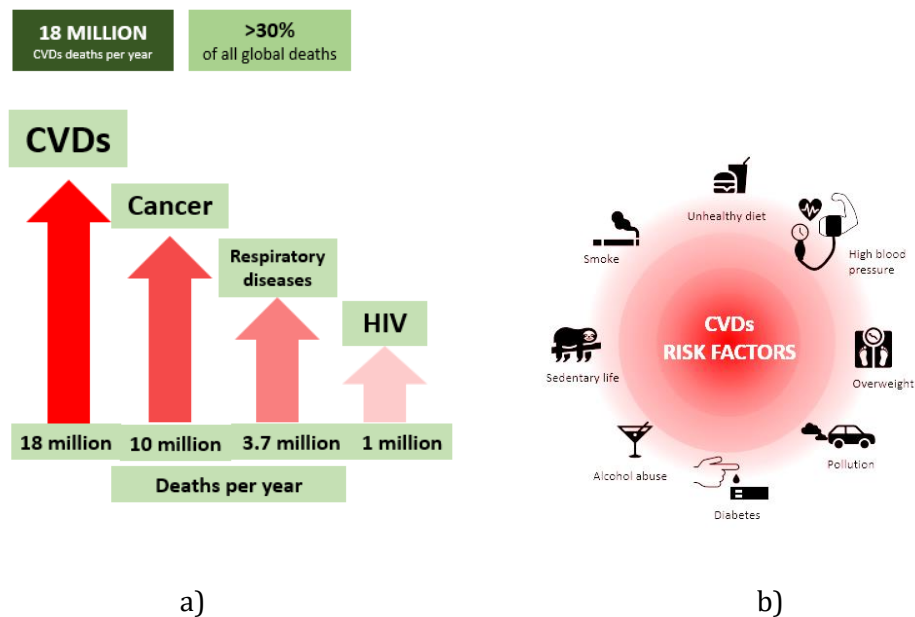


Figure 2 a) Deaths per year associated with different diseases in the world; CVDs are the highest cause of death accounting for 18 million death per year. b) CVDs risk factors.

CVDs are generally associated with narrowing or obstruction of blood vessels, resulting in reduced blood flow to the organs, which may not receive sufficient oxygen and nutrients. The consequences could be life-threatening, as in the case of cardiac attacks, when there is insufficient blood flow to the heart, or ischemic strokes, when the brain does not receive adequate flux of blood [2].

CVDs include

- Coronary artery disease (CAD), which is the buildup of plaque in the arteries that supply oxygen-rich blood to the heart [6];
- Peripheral artery disease (PAD), which is associated with reduced blood supply to the limbs due to clogged arteries [7];
- Cerebrovascular disease, a group of conditions that affect blood flow and blood vessels in the brain due to narrowing of vessels (stenosis), clot formation (thrombosis), blockage of arteries (embolism), or rupture of blood vessels (hemorrhage)[8];
- Deep vein thrombosis, occurring when a blood clot (thrombus) forms in one or more of the deep veins in the body, usually in the legs [9,10];
- Rheumatic heart disease – damage to the heart muscle and heart valves from rheumatic fever, caused by streptococcal bacteria [11];
- Congenital heart disease – birth defects that affect the normal development and functioning of the heart caused by malformations of the heart structure from birth [12].

Except for the last two points, CVDs are associated with vascular occlusion. The most effective way to revascularize a clogged vessels is through bypass grafting, especially for patients with a life expectancy of more than two years (**Figure 3**) [13]. Bypass grafting involves diverting the normal path of blood by adding a piece of blood vessel taken from the patient or using an artificial graft. More than 400,000 artery bypass procedures are performed per year in the United States [13]. Generally, it is preferable to use autologous vessels¹ for such a purpose, including the internal thoracic artery (ITA), radial artery and especially the saphenous vein (SV). This procedure is called autografting bypass [14–16]. However, it often happens that autologous vessels have limited availability, or their extraction may cause donor site morbidity. It is estimated that about 20% of patients who need bypass grafting cannot proceed with autografting [17]. Additionally, the quality of autologous blood vessels can deteriorate over time, and the likelihood of postoperative complications increases. It is crucial, from a clinical standpoint, to develop artificial vascular prosthetics that can act as blood vessels in order to replace damaged blood vessels and restore blood flow around obstructions, when autologous vessels are not available [18].

A suitable choice is to use artificial grafts, usually made of polyethylene terephthalate (PET), also known as Dacron® and polytetrafluoroethylene (PTFE). Synthetic grafts are suitable for

¹ A vessel (vein or artery) extracted from the patient during surgery to be utilized as a bypass transplant. The most common are the saphenous vein and the internal thoracic artery.

bypassing large and medium-sized arteries, *i.e.*, >8mm or between 6-8mm in diameter, while, to this day, they are not used for smaller vessels, with a diameter lower than 6mm. Typical artificial bypass grafts are applied on carotid or femoral artery replacement, aortoiliac replacements, peripheral artery grafting, aorto-bifemoral grafting [7]. Biodegradable polymers and natural materials have also been proposed for the development of synthetic grafts, although their use has been limited as they are currently under investigation. Finally, tissue-engineered vascular grafts (TEVGs) are recently gaining a lot of attention being very promising for vascular grafts of small dimensions [18].

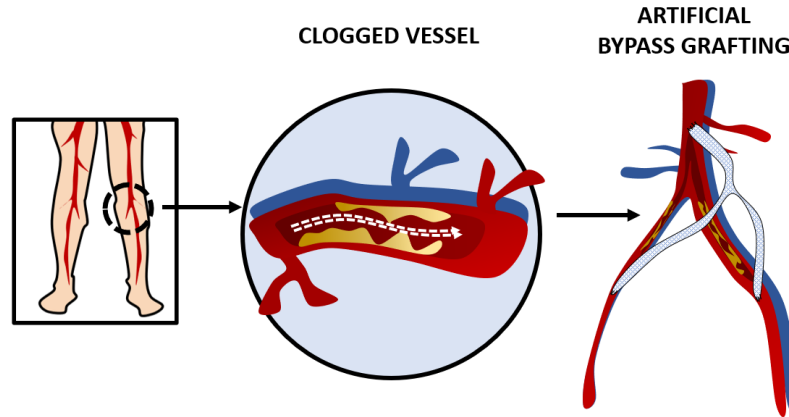


Figure 3 Representative image of clogged vessel and bypass grafting.

2. Preoperative risk evaluation

A preoperative risk assessment must be performed before proceeding with bypass revascularization. Coronary angiography and fractional flow reserve (FFR) method are the procedures used to perform this examination. Coronary angiography employs X-Rays and a specific dye (contrast material) to examine how blood flows through the arteries, whereas FFR uses a vascular catheter equipped with sensors to detect blood pressure within the vessel. In contrast to FFR, which can clearly define the degree of stenosis in terms of a pressure drop across a coronary lesion, the angiography might be subjective and cannot always predict the functional importance of an occlusion to the flow. A severe stenosis is commonly defined as having an FFR \leq 0.75. Revascularizations guided by the FFR have been linked to considerably better outcomes. FFR is often executed with vascular catheters supplied with a pressure sensor capable of monitoring and transmitting blood pressure in the vicinity of an obstruction (**Figure 4**) [19,20].

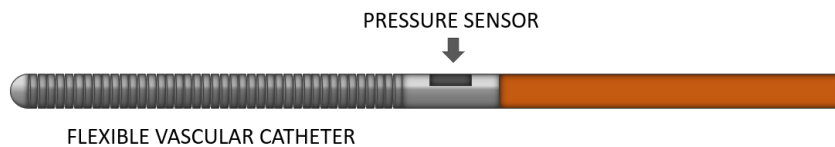


Figure 4 Drawing of FFR catheter equipped with pressure sensor.

3. Prosthetic bypass grafting

Artificial vascular grafts are now manufactured using a variety of materials, including synthetic polymers, natural materials, or a combination of sorts. Dacron®, PTFE and expanded PTFE are the materials most frequently employed in vascular prostheses [21]. Dacron® grafts are mainly used for large diameter aortic and peripheral vessels being stiffer, while PTFE and ePTFE grafts, already used for heart valves, are employed in lower limb bypasses [21,22]. There are several clinical studies reporting the efficiency of artificial grafts, which however remain less compatibles than autologous ones. For instance, a three-years research pursued by Post *et al.* reported a 65% primary patency for Dacron® bypass grafting and a 61% primary patency for PTFE grafts, while Jensei *et al.* found a 2-years patency of 70% and 57% respectively [23,24]. Prager *et al.* studied the 5 years patency of expanded PTFE grafts employed for aorto-iliac bypass, proving their functionality in the 90% of the cases [25]. For smaller vessels, artificial grafts were proven to be inadequate at the actual state, showing a 2 year patency of 32% compared to 90% of SV autologous grafts [23]. **Figure 5** represents an artificial graft, where anastomoses are the connection points of the graft with the human vessels.

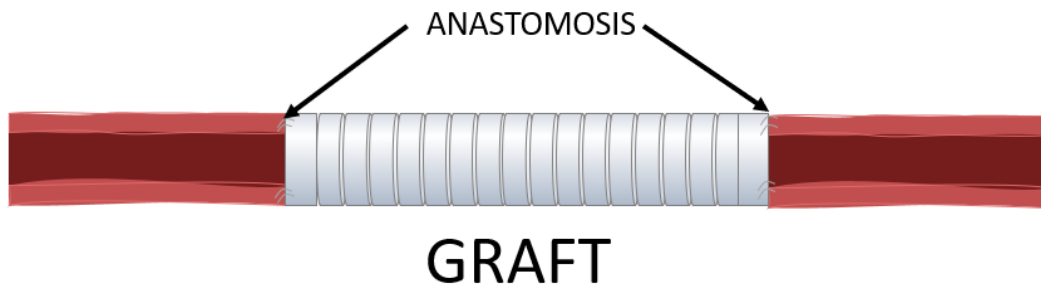


Figure 5 Drawing representing an artificial graft. Anastomosis indicates the points of connection between the graft and the human vessels.

The ideal artificial vascular graft should exhibit strong hemocompatibility and biocompatibility that would last till reendothelialization is complete, and it should match the mechanical properties of the vessel that is bypassing [18,21]. Human arteries are composed of three different structural layers: tunica intima, medium, and externa (or adventitia) (**Figure 6**). This structure is directly connected to blood vessel physiological functions. The most promising materials should mimic it and facilitate *in vivo* tissue regeneration with long-term patency as well as provide mechanical support comparable to autogenous blood arteries to support blood pressure load. There are several requirements depending on the size of the vessel; for example, non-thrombogenic intima is crucial for small vessels while mechanical properties are more relevant for large vessels [18]. Other features, such as biodegradation, can be advantageous; however, this phenomenon must be carefully monitored since it might result in irreversible changes in the graft properties [26]. Other than Dacron® and PTFE, there are variety of materials with interesting qualities that enable good adaptability to the human body [7]. The existing types of grafts, their usage in vascular surgery, the primary drawbacks and issues that still need to be resolved and the future prospective will be covered in detail in the paragraphs that follow.

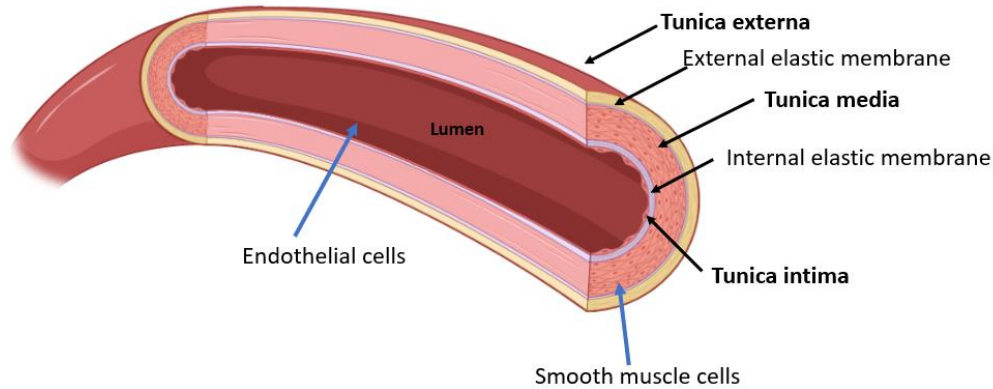


Figure 6 Representation of human artery structure. There are three layers, tunica intima media and externa. The inner surface of the vessel, named intima or lumen is covered in endothelial cells (ECs), while the tunica media is composed of smooth muscle cells (SMCs). Created with BioRender.com.

3.1 Poly (ethylene terephthalate) Dacron® vascular grafts

Dacron® is the DuPont® trademark for PET, a highly durable polyester thermoplastic polymer that can be processed into synthetic fibers (**Figure 7-a**). DeBakey introduced the first knitted Dacron® prosthesis in 1957; it is produced in strands that are either woven or knitted together to shape a graft. Knitted grafts feature larger pores that allow better tissue ingrowth and are more compliant than woven grafts[18,27]. **Figure 7-b** displays scanning electron microscopy of inner and outer surfaces of a knitted Dacron® graft. Knitted Dacron® grafts must be pre-clotted with albumin, gelatin, or even blood prior to use, especially in high pressure conduits like the aorta, due to the larger pore sizes. The inner albumin or gelatin coating fades over 2 to 3 months. As for the mechanical properties, Dacron® is robust, with a tensile strength of 170 MPa to 180 MPa, a tensile modulus of 14,000 MPa, and a highly crystalline nature [28]. Dacron® grafts are nonbiodegradable (complete resorption within 30 years), although they do have a propensity to swell over time. Currently, Dacron® is mostly employed with certain success in aortic and large diameter peripheral bypass grafts (>6mm)[18,29,30]. Since 1957, studies have demonstrated that Dacron® large-diameter grafts (7-9 mm) have a 5-year patency rate of 93% in aortic bypass grafts. However, this percentage reduces noticeably with lower artery diameters (7mm) [28]. Dacron® grafts' primary drawback is thrombogenicity²[31]; To this end, several type of Dacron® grafts in therapeutic settings has been authorized. Grafts coated with bioactive heparin³ or passivated with fluoropolymers to lessen surface thrombogenicity have been developed. Immobilized heparin may also lessen the hydrophobicity of Dacron® in addition to improving the performance of heparin-binding proteins. Femoro-popliteal bypass grafts with heparin-bonded Dacron® had a three-year patency rate of 55% compared to 43% for the untreated type [26]. In spite of heparin's biological effects, this shift in surface chemistry may affect the proteins at the interface and the biocompatibility. A Dacron® graft with silver coating has also been recently developed to lessen the likelihood of graft infection [28]. To ascertain if these improvements enhance the patency, extensive follow-up research is needed.

² Thrombogenicity refers to the tendency of a material in contact with the blood to produce a thrombus, or clot.

³ Anticoagulant used to prevent and treat thrombotic events such as deep vein thrombosis, pulmonary embolism, and atrial fibrillation.

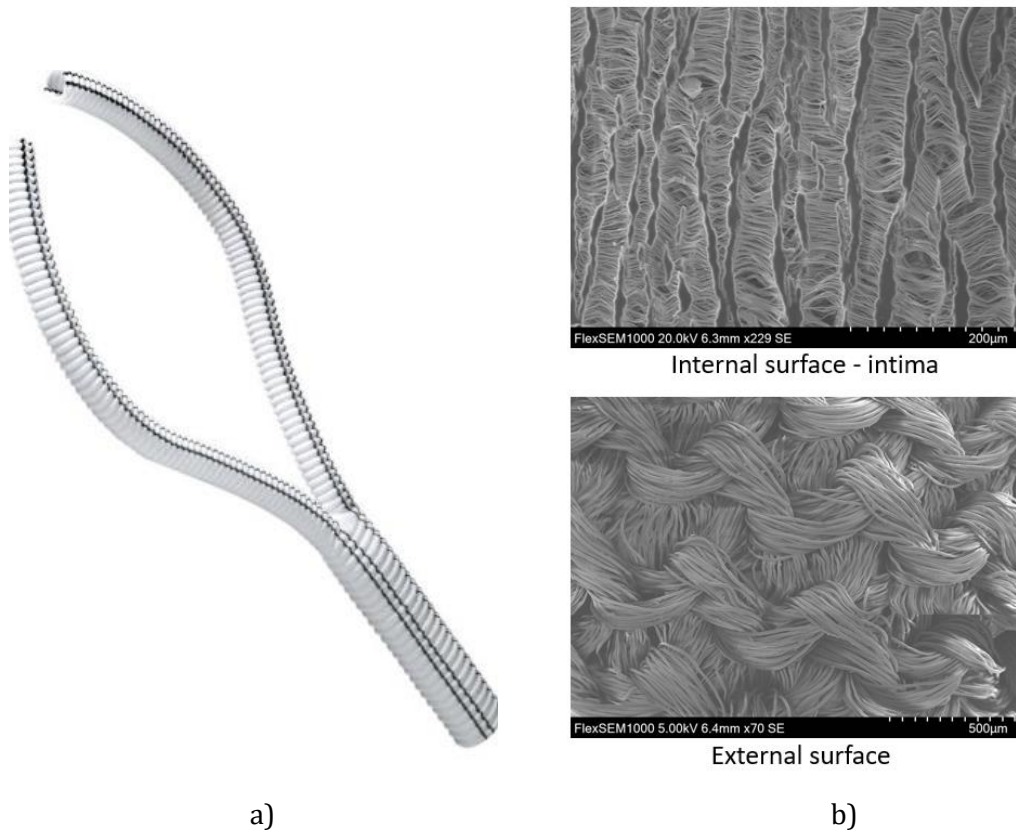


Figure 7 a) Picture of Dacron® aorto-bifemoral graft (Albograft®)[32]. b) SEM pictures of internal and external surface of the graft.

3.2 Polytetrafluoroethylene (PTFE) grafts

DuPont® registered the fluoropolymer PTFE under the Teflon® trademark in the late 1930s. It is hydrophobic, physically robust, and chemically inert and non-biodegradable [33]. PTFE is highly crystalline (>90%), has a stiffness of 0.5 GPa, and a tensile strength of 14.0 MPa. Being PTFE biostable, it won't degrade biologically once in the human body [28]. It was first utilized as fibers in textile-based grafts. PTFE grafts have been gradually substituted by expanded ePTFE (Gore-tex®), patented by Gore® in 1969 [26]. The process of stretching, heating, and extruding the expanded polymer results in a microporous substance that is more suited for firm tissue attachment. In 1972, ePTFE grafts were inserted for the first time in animals, and in 1976, Campbell *et al.* reported their first clinical application. The advantage of using ePTFE is its microporosity that enhances cells adhesion compared to plain PTFE and it is now widely used as lower limb bypass grafts (7–9 mm) with excellent results [34]. **Figure 8-a** displays a typical ePTFE graft from B|Braun® while **Figure 8-b** represents the inner and outer surface of an ePTFE graft pictured using scanning electron microscopy. The porosity of ePTFE is around 30µm, nonetheless several studies on animals suggest that an increase to 90 µm could enhance the reendothelialization [35]; Clinical studies proved that at five years, more than 90% of aorto-iliac ePTFE grafts are still functional, whereas only 45% of femoro-popliteal bypass grafts are still functional, compared to 77% of autologous vein grafts [36]. An advantage of PTFE and ePTFE grafts is the electronegative luminal face, which in principle

enhances antithrombogenicity. Nonetheless, its applicability in vessels smaller than 7 mm is limited by the adherence of materials to its surface leading to thrombosis. Efforts are being undertaken to modify ePTFE for this purpose. The electronegativity can be improved via carbon-coating, as it has antiplatelet effect [37]. Heparin impregnation have been applied also on ePTFE grafts to improve hemocompatibility, nonetheless there are some concerns on the release rate of heparin from the graft [28,38]. Biodegradable elastomers based on citric acid have also been considered as ePTFE coating materials [39]. They were discovered to be biocompatible in porcine carotid artery circulation and did not enhance the risk of thrombosis, restenosis, or inflammation [40]. These results are significant because they might be at the basis of a drug-eluting⁴ vascular graft. The relative stiffness of ePTFE grafts is a well-known drawback since it results in a compliance mismatch between the prosthesis and host artery, which might exacerbate anastomotic intimal hyperplasia⁵ [41]. The patency rates of Dacron[®] and ePTFE grafts are comparable, despite some data indicating that platelet deposition and complement activation are lower on ePTFE prostheses than on Dacron[®] ones [42].

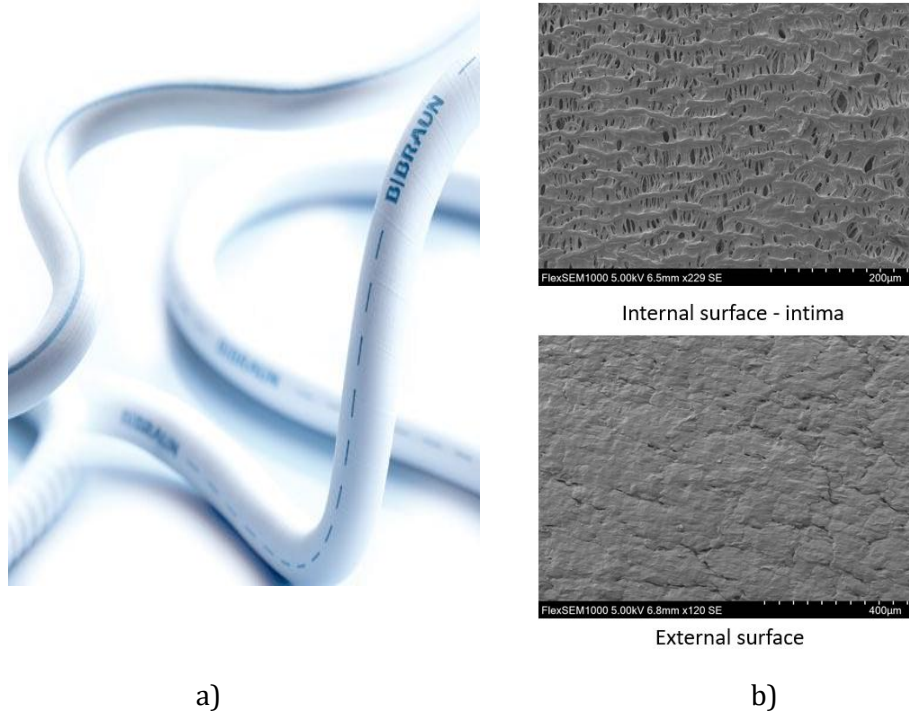


Figure 8 a) Picture of ePTFE vascular graft produced by B|Braun[®] [43]. b) SEM pictures of internal and external surface of the graft.

3.3 Polyurethanes (PU) grafts

The goal to eliminate compliance mismatches between artificial and human vessels drove the design of a new class of polyurethane vascular prostheses. Before being used for grafts,

⁴ Slow-release medication to help prevent blood clots from forming in a graft.

⁵ Thickening of arteries at graft anastomoses (e.g., junction) due to excessive cell population increase.

polyurethane has been employed as a polymeric coating for several medical devices and implants, for instance pacemaker leads, breast implants, and barrier films for cutaneous wounds [18,22,28]. Polyurethane is a copolymer composed of three monomers: a diisocyanate hard domain, a chain extender, and a diol soft domain. The soft domains give flexibility at physiological temperatures, whereas the hard domains provide strength [22]. The mechanical properties of polyurethane prosthesis may be adjusted by varying the composition of the monomer repeat units. Tensile strength varies from 20 MPa to 90 MPa with a tensile modulus of 5 MPa to 1150 MPa, depending on the ratio of its hard and soft segments [28]. Intimal hyperplasia (IH), an abnormal accumulation of cells in the vascular tunica intima at the anastomotic sites should occur less often, thanks to PU mechanical properties, which gives rise to a new generation of radially compliant polymers. This together with biocompatibility make it an interesting choice for vascular grafts. Nonetheless, the first generation of PU grafts revealed a big problematic related to *in vivo* degradation of the polyol soft segments, which may eventually induce a buildup of materials causing graft occlusion [44]. In response to this problematic polyether-based PU grafts were developed, solving the problem of polyol degradation, nonetheless, were susceptible to oxidative degradation [45]. Thoratec® Laboratories' polyetherurethaneurea grafts were another promising solution to the issue of degradation, however they exhibited major graft elongation issues, which led to an increase in intimal hyperplasia [46]. A new generation of PU grafts based on polycarbonate is emerging. This class of grafts is more stable from oxidation and biodegradation point of view. Additionally, in some clinical studies it proved faster reendothelialization, early stabilization of ECs proliferation as well as thinner neointima⁶ compared with ePTFE grafts[26]. There are several contradictory researches studying the tissue response to PU grafts. This is a consequence of the variety of existing PU compositions, graft manufacturing, porosity, and surface changes which all have an impact on the graft performances. It is hard to predict whether PU grafts would work better than ePTFE or Dacron® grafts until further data are released. The possible carcinogenic effects of PU grafts' degradation products are one of the main concerns preventing the choice of PU for grafts [33]. *In vitro* and animal investigations have shown that the most recent generation of polyurethanes based on polycarbonate are inert to both hydrolysis and oxidation [47].

3.4 Scaffold - based tissue engineered vascular grafts (TEVGs)

A tissue engineered vascular graft (TEVG) consists of a scaffold, cells that have seeded into it, and the right environmental signals (such as growth hormones and physical stimulation) to encourage the development of new tissue [18,48]. The key benefit of TEVGs, which make them very appealing for bypass grafting, is their excellent tissue compatibility, which prevents rejection and maintains long-term patency after transplantation. The scaffold is usually manufactured using synthetic and organic biodegradable components [13,49]. High porosity and a microstructure capable of supplying, orienting, and supporting cell connections are two crucial requirements. It is important to provide hemocompatibility, stenosis resistance, and mechanical qualities that match those of the autologous vessels. The scaffold initially offers

⁶ Neointima is a term used to describe scar tissue that develops inside tubular anatomical systems like blood veins.

structural stability to the TEVG's as well as the framework for cell attachment and remodeling and it may be made of biodegradable polymers or natural biomaterials[18].

3.4.1 Biodegradable polymer based TEVGs

TEVG made of biodegradable polymer is an alternative to the synthetic grafts mentioned above. After being placed into the body, the graft progressively becomes covered in human tissue and starts to degrade. Only human tissue will remain after total degradation, guaranteeing the same function of autologous vessels. A fundamental aspect of bioresorbable grafts is that they must regenerate a tissue with adequate strength prior to loss of prosthetic integrity to decrease the potential of aneurysmal dilatation⁷[13,22]. The biodegradable polymers' rate of breakdown is influenced by several variables, for instance pore size. According to Matsuda *et al.*, reendothelialization is most effective in pores with a diameter of 18 to 50 μm [50]. Smaller pores would trigger an inflammatory response, whereas those that are excessively big may permit excessive blood leakage. Radial compliance of vessels is also improved by increasing pore diameters and porosities. It is possible to classify single component and multiple components biodegradable grafts. Single components grafts are temporary scaffolds for vessels being gradually replaced by human tissue composed by only one polymer. Examples of materials are polylactic acid (PLA), polyglycolic acid (PGA), polydioxanone (PDS) and polyhydroxyalkanoate (PHA). Multiple components are grafts constructed by at least two bioresorbable polymers or a bioresorbable polymer with a non-resorbable one [28]. They have the advantage of combining different resorption rates, and they can be designed to completely disappear when the regenerated tissue is strong enough. An example is polyglactin (Vicryl®) (PG910) a copolymer of polyglycolic and polylactic acid. Vicryl® dissolves in two months, hence it has been coupled with slower degrading polymers to delay absorption and allow for arterial regeneration. In the rabbit aorta model, researchers developed composite polymeric grafts of Vicryl® (PG910) and PDS (74%:26%) capable of 100% patency at 1 year [51]. The aortoiliac arteries of dogs were implanted with partially resorbable grafts made of 70% PDS and 30% polypropylene or 69% PG910 and 31% polypropylene [52]. For up to a year, there were no aneurysms and an overall patency rate of 90% for PG910/polypropylene and 86% for PDS/polypropylene. PDS took four months to completely resorbed, while PG910 took two months. Tissue ingrowth was induced by both grafts, and it remained histologically stable for 4 months to 1 year [22]. The main limitation of this class of prosthetics is that the vessel reconstruction strongly depends on a delicate balance between the host cells' invasion, the degradation of the materials, and the replacement by human tissue. If the pace of decomposition of the degradable substance does not coincide with the rate of vascular tissue regeneration, aneurysms or even vascular rupture may occur. Another relevant problem is the possibility of over-proliferating cells, leading to restenosis in the latter post-implantation phase while the endodermis⁸ of the artificial blood vessel grafts is not fully developed [18]. These problems make it difficult for

⁷ A 50% increase over the normal diameter of the vessel is considered aneurysmal dilatation.

⁸ The endodermis is a thin layer of tightly packed cells that acts as an impermeable barrier or water repellent layer through which water can only go in one direction, toward the root system's core.

grafts to adequately maintain biocompatibility *in vivo* and fully realize vascular tissue regeneration. Nowadays mainly polycaprolactone (PCL) is used for tissue engineered scaffolds as the US Food and drug administration (FDA) approved it [18,53]. It is possible to conclude that while synthetic polymers (Dacron®, ePTFE and PU) guarantee strength of the graft, they come with poor cellular compatibility as well as thrombogenicity. Biodegradable materials may be a better solution as they gradually disappear leaving behind only humans' cells, nonetheless they are still under study, being biodegradation extremely complicated to control.

3.4.2 Natural Biomaterials

TEVGs can be also based on organic biomaterials. Natural elastin, for instance, has been widely used to produce TEVGs' scaffolds. It is the main component of the extracellular matrix, which provides the compliance to the vessels. It is unsolvable and challenging to work with when building scaffolding. For these reasons few scaffolds are created entirely of elastin, while it is rather added to scaffolds already consisting of other supporting materials [48]. For instance, with a two-layer scaffold made of an outer layer of PCL and an inner layer of recombinant human tropoelastin, Wise *et al.* have reported successful results in a rabbit model [54]. Although these grafts appear promising, more research is essential to ascertain their scaffolding qualities. Chitosan, a natural polymer derived from shellfish, has also been employed in the design of TEVGs, being porous, antibacterial, and exhibiting high mechanical properties. It has already been successfully used to replace bones and cartilage. Because of its large pore diameters, quickly dissolving chitosan is supposed to facilitate cell invasion and neovascular remodeling when incorporated into a scaffold [55]. Finally, it is worth mentioning tissue decellularization. This technique consists in decellularizing animals' arteries, for instance swine and bovine or human umbilical arteries. All the cellular and nuclear material is removed from these arteries so that only the extracellular matrix (ECM), which is in the media of the vessel, is left intact [48,56]. Using this scaffold helps to suppress the immunological responses. Additionally, the acellular scaffold promotes cells adhesion, differentiation, and proliferation, as well as ensure good mechanical matching with the autologous arteries. These grafts are promising, nonetheless the complete removal of tissue antigens is a huge problematic. Additionally, during a decellularization process, ECM components may be subjected to physical and chemical stress, which could negatively impact an ECM's biomechanical capabilities [48,57]. The inability to change an ECM's composition and structure, the varying quality of donor materials, and the possibility of viral transmission from animal tissues are all drawbacks of decellularized materials. As a result, they are still under assessment and not being used in therapeutic treatments.

4. *In Vivo* and Clinical Applications

As was previously mentioned, not all vascular conduits can accommodate artificial bypass grafting using the prostheses that are now available. Moreover, the right graft should be selected according on the flow and pressure circumstances. Following the typical bypass grafting involving artificial grafts are presented.

4.1 Peripheral Bypass Graft

Peripheral artery disease (PAD) is a consequence of the blocked blood vessels due to plaque builds up on the arterial walls (atherosclerosis). The obstruction restricts normal blood flow that usually gives oxygen and nutrients to the body's lower extremities, and this causes the cells and tissues of the legs and feet to die. In the worst circumstances, this might result in gangrene in the limbs and subsequent amputation since normal cells growth and repair cannot occur. More than two hundred million individuals are estimated to have PAD globally, with symptoms ranging from mild to severe [58]. The frequency of PAD grows with age and affects a significant fraction of the elderly population (>20% in adults >80 years old), despite being very uncommon in younger people [58]. A peripheral vascular bypass, also known as a lower extremity bypass, is a minimally invasive treatment that uses general anesthesia and tiny incisions that are ~5-7 cm long and the insertion of a graft to redirect blood flow around a blocked blood artery. The graft establishes a new path for the blood flow. Peripheral vascular bypasses are classified by the arteries that will be bypassed and the artery that will receive the diverted blood (**Figure 9**) [59]. For instance, aorto-bifemoral refers to a bypass that reroutes blood from the abdominal aorta to the two femoral arteries in the groin, femoro-popliteal from the femoral to the popliteal arteries above or below the knee, and femoro-tibial from femoral artery to the tibial artery. Dacron® has been widely used for peripheral bypass grafting for large diameter grafts of 7-9mm, showing 3 years patency rates of 93%. ePTFE grafts have been often selected for smaller diameter grafts >7mm in femoro-popliteal bypass procedures [60]. Postoperative results of autologous vein and ePTFE grafts were examined in one research including 75 infrainguinal bypasses. The primary patency rates at 4 years were 82% for veins and 80% for ePTFE grafts, respectively, with no statistically significant difference between these groups [61]. Most clinical investigations show that femoro-popliteal bypass grafts made of Dacron® or ePTFE are acceptable. Smaller diameter infrapopliteal artificial grafts, however, have not performed as well at lower pressures. ePTFE showed a 12% primary patency at 4 years for infrapopliteal bypass grafting for instance [61]. A patency rate of 23% for ePTFE in tibial artery bypass grafts after 5 years post-surgery indicates that the performance must still be optimized [61]. Several techniques have been attempted to improve the patency rate of artificial grafts, such as endothelialization of ePTFE grafts, *i.e.*, coating the graft with autologous endothelial cells, demonstrating a significant improvement in patency rates; The 5-year patency rate in infrapopliteal grafts was 76% in a 9-year randomized clinical study employing endothelialized 6-mm ePTFE grafts [62]. Autologous vein grafts reinforced with prosthesis were employed by other surgeons [63]. Studies are now being conducted on endothelialized PU bypass grafts for lower extremity revascularization treatments. They are resistant to deterioration and show similar natural compliance, according to preliminary *in vivo* research. Additionally, PU grafts are less thrombogenic than ePTFE or Dacron®. Endothelialized polyurethane grafts have been assessed in canine femoral artery model remaining 4 weeks after implantation with minimal to no thrombus development [28].

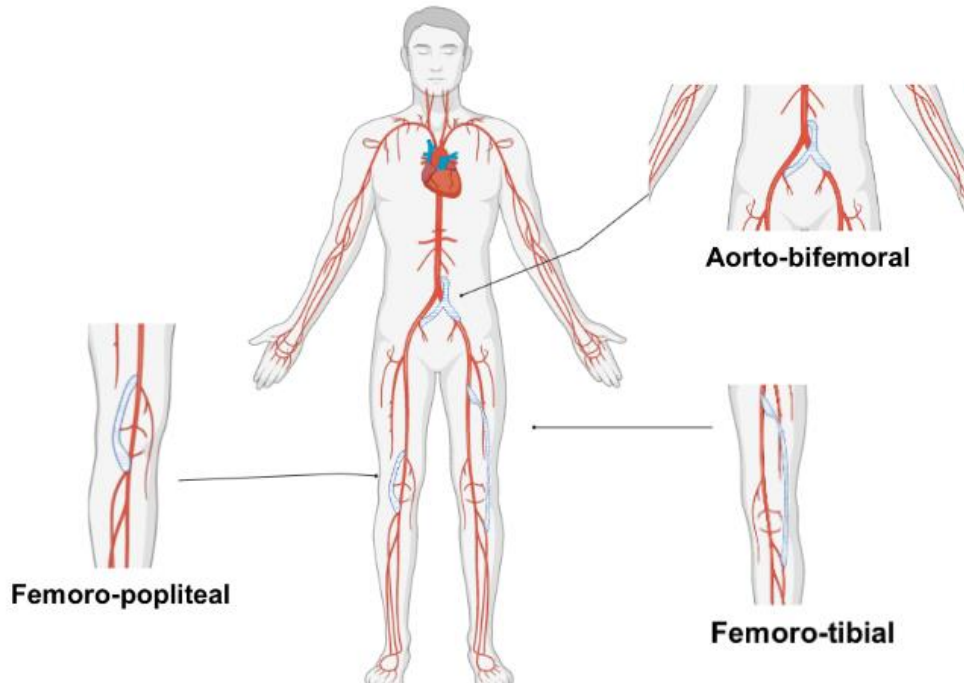


Figure 9 Drawing representing the most common Peripheral bypass grafting. Created with BioRender.com.

4.2 Carotid Artery Bypass Grafts.

Carotid artery surgery is a procedure to treat carotid artery disease. The carotid artery supplies the brain with vital blood. When fatty substance, *i.e.*, plaque, partially or completely obstruct blood flow in this artery a stroke may occur (**Figure 10**). Surgery on the carotid arteries is performed to get the brain's blood flow back to normal. At three years after implantation, carotid artery bypass grafting using autologous vein grafts has been demonstrated to have patency rates above 80% [28]. However, within a year following the surgery, some of these vein grafts tend to stenose. At one year after carotid bypass grafting, 6-mm-diameter ePTFE and autologous vein grafts were compared and the result was that ePTFE stenosed less than autologous vein, proving that ePTFE grafts are at least as effective as autologous vein grafting. Porous 5-mm polyurethane vascular grafts with a 38% patency rate have been used in experiments on sheep carotid arteries [64]. This low patency was a result of the hydrolysis-induced biodegradation of polyurethanes with an ester structure.

4.3 Coronary Artery Bypass Grafts.

Coronary artery bypass graft surgery (CABG) is performed to treat coronary artery disease (CAD). The blood channels that feed the heart with oxygen and nutrients are called the coronary arteries. When these arteries get congested due to fatty deposits, the amount of oxygen-rich blood that can reach the heart muscle is reduced and this leads to CAD. Bypass grafting is performed to revascularize those vessels. The majority of CABGs are conducted using autologous vein [65]. Only a small percentage of all procedures employs synthetic polymeric grafts, when utilizing autologous veins is contraindicated. This is because, as

compared to autologous veins, prosthetic cardiac bypass has much lower patency rates. Vein grafts have a reported 86% one-year patency rate, compared to just 59% for ePTFE grafts [66]. On the other side, Dacron® has been employed in a few case reports as a polymeric graft (3–4 mm) with patent vessels at 17 months. Longer term outcomes, however, are not yet available. It may be preferable to use polymers that are more flexible, like PU. For instance, 1.5 mm electro sprayed polyurethane-polydimethylsiloxane grafts (Cardiothane 51) were implanted in a rat aorta model [21]. The importance of porosity for long-term graft patency is highlighted by the fact that at 3 months after implantation, of small porosity grafts were occluded while those with medium porosity had a 76% patency rate with no intimal hyperplasia and full end. Clearly, before being applied clinically, these results will need to be replicated in humans [28].

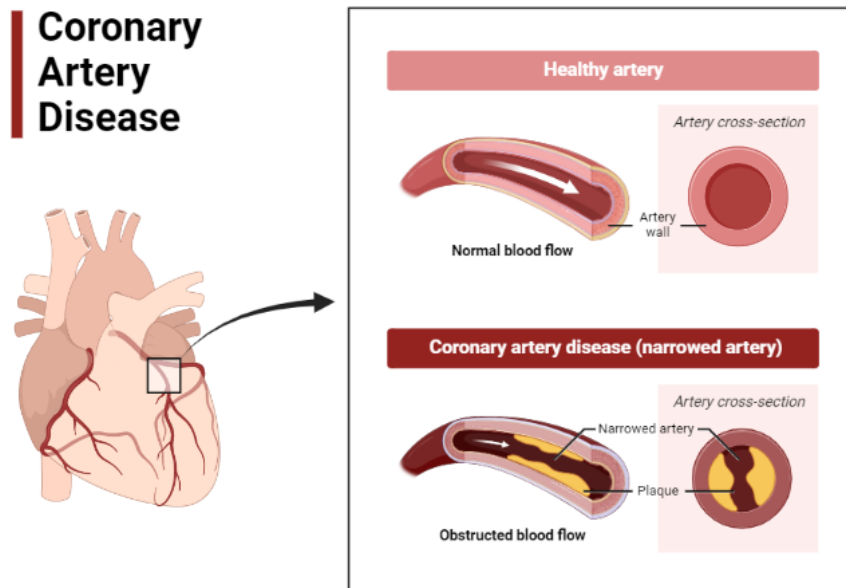


Figure 10 Scheme displaying coronary artery disease. Created with BioRender.com.

5. Problematic of vascular prosthetics

Vascular prosthesis can fail for a variety of causes, as described in the previous sections, while discussing current grafts state and bypass grafting procedures. The major cause is the difficult mechanical and biochemical replication of the essential properties of vascular conduits. Grafts failure is associated to restenosis and clots formation often consequence of poor hemodynamics, poor endothelialization, poor hemocompatibility of the intima of the graft and insufficient compliance matching between the graft and human tissue. These issues are magnified for small diameters, making it challenging to execute synthetic bypass surgery below 6 mm in diameter [13,67]. In most cases, graft failure during the first month of insertion is the result of technical difficulties during surgery or the patient's thrombophilia. The primary issues between six months and three years later are usually related to thrombus

development and abnormal cell accumulation leading to intimal anatomical hyperplasia. Infection of prosthetic devices is uncommon, although it does occur sometimes due to bacteria's proclivity to thrive on synthetic polymers [18,68].

5.1 Compliance issues

The percentage change in diameter of a vessel between diastolic and systolic⁹ pressure is defined as compliance. A compliance mismatch between a somewhat extensible host vascular conduit and a stiffer graft results in an area of excessive mechanical stress, which may contribute to anastomotic intimal hyperplasia (**Figure 11**) and give rise to subtle arterial wall injuries [69]. A particular feature of human conduits is their dynamic compliance inversely related to blood pressure. This means that at low physiological pressure, natural arteries may be better equipped to conserve pulsatile energy and maximize flow than non-compliant prosthetic grafts. In comparison to a native artery (0.059%/mm Hg) and vein (0.044%/mm Hg), Dacron® (0.019%/mm Hg) and ePTFE (0.016%/mm Hg) grafts are considerably noncompliant, whereas polyurethane grafts show compliance comparable to the host artery [22,70]. Many researches showed a favorable association between compliance and patency rates. However, the two most often used prosthetic materials, ePTFE and Dacron®, are very stiff across the physiological pressure range [22]. Additionally, compliance of synthetic grafts may decrease after implantation due to the creation of a fibrous capsule around the graft, which stiffens the graft's wall. As a result, determining the influence of early compliance on long-term patency may be challenging.

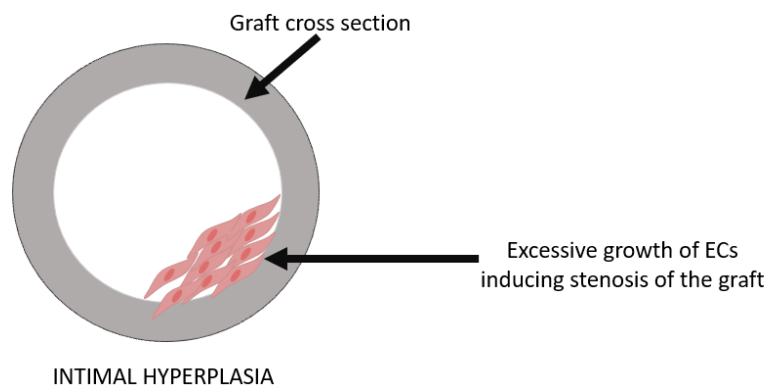


Figure 11 Cross section of an artificial vascular graft with intima hyperplasia, i.e., excessive growth of endothelial cells.

5.2 Poor hemodynamics

Poor hemodynamics often induce anastomotic intimal hyperplasia (IH), which is a frequent cause of prosthetic graft failure, owing to changes in wall shear stress and local flow disruptions (e.g., flow separation, recirculation, reattachment, stasis, and reflux). Indeed, endothelial cell (EC) function may be modulated by local flow conditions [18,70]. For instance, in disrupted flow at anastomosis, endothelial cells may become activated and prothrombotic.

⁹ Systolic blood pressure indicates how much pressure the blood is exerting against the artery walls when the heart beats, while diastolic blood pressure indicates the pressure of blood on the artery walls while the heart is resting between beats.

Activated endothelium, in turn, stimulates vascular smooth muscle cell (SMC) proliferation and migration, as well as matrix protein synthesis. Thrombus production may also be aided by zones of stasis caused by low blood velocity and high shear rates, which activate platelets locally [71].

5.3 Infections

Graft infections are more likely to happen with synthetic implants because foreign bodies can be colonized by bacteria. These infections cause persistent inflammation in which bacteria produce toxins that interfere with graft healing [72]. A bacterial biofilm develops on the graft surface, protects germs from antibody and cell-mediated assault and affects the efficacy of antibiotics. Graft infection occurs at a rate of 1% to 6%, and infection is linked with a 50% amputation rate and a 25% to 75% death rate [70]. Attempts have been made to reduce bacterial infection by binding rifampicin¹⁰, silver, and other antibacterial substances to the luminal surface of grafts [22,73]. However, it has been difficult to determine the efficacy of rifampicin-coated or silver-coated grafts.

5.4 Thrombogenicity

Beyond compliance mismatch, thrombogenicity is the main factor contributing to the failure of artificial grafts and it remains the one of most difficult problems solve in grafts design (**Figure 12**). Thrombogenicity of vascular grafts can lead to serious health risks for patients, as the blood clots developed on the inner surface of the conduct decrease its sectional area, as consequence blood flow is reduced, and embolisms and fatal strokes may occur [67,74].

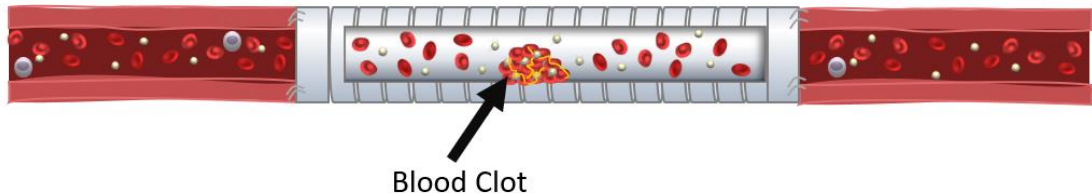


Figure 12 Development of thrombosis in the intima of the graft due to poor hemocompatibility of synthetic materials.

This is mainly related to blood/material interaction, and it can be worsened by poor hemodynamic often induced by compliance mismatches [75]. This problem is somewhat connected to every issue mentioned in the preceding subsections. In general, coagulation is a typical defensive mechanism that activates nearly instantly in response to damage and serves as a prelude to the inflammatory reactions that comprise the healing process. Numerous lipids, proteins, and cells work together in the coagulation reactions to cause localized amplification. The propagation and termination of these reactions are controlled by several negative feedback mechanisms. Because many of these antithrombotic feedbacks are exclusive to the endothelium, existing artificial prostheses are not able to reproduce them, and this often leads to graft failure [31,70,75]. In order to understand the dynamic of contact surface induced coagulation, the structure of the coagulation cascade must be introduced. In

¹⁰ Rifampicin (rifampin) is an antibiotic used to treat a variety of bacterial infections.

this section this matter will be briefly described, and more details will be given in Chapter IV. The coagulation cascade is a chain of reactions that ends with the formation of a stable clot. A stable clot is made of activated platelets, red cells, and fibrin. Platelets and red cells are already present in the blood, while fibrin is the product of the coagulation cascade [76]. The cascade comprises two possible pathways for triggering blood clotting, extrinsic and intrinsic (**Figure 13**). The extrinsic pathway is activated by the contact of blood with Tissue Factor (TF), produced by endothelial cells outside the lumen when the vessel is present of damaged. The intrinsic pathway occurs through the activation of a protein called factor XII (*fXII*) after exposure to subendothelial collagen. Both pathways, through consecutive reactions, lead to the common pathway, where prothrombin activates in thrombin which converts fibrinogen to fibrin, ending with the formation of the a network around platelets and reds cells [76-78]. This happens when a vessel is injured. Nonetheless activation can be triggered by synthetic surfaces as well, as described in the next subsection.

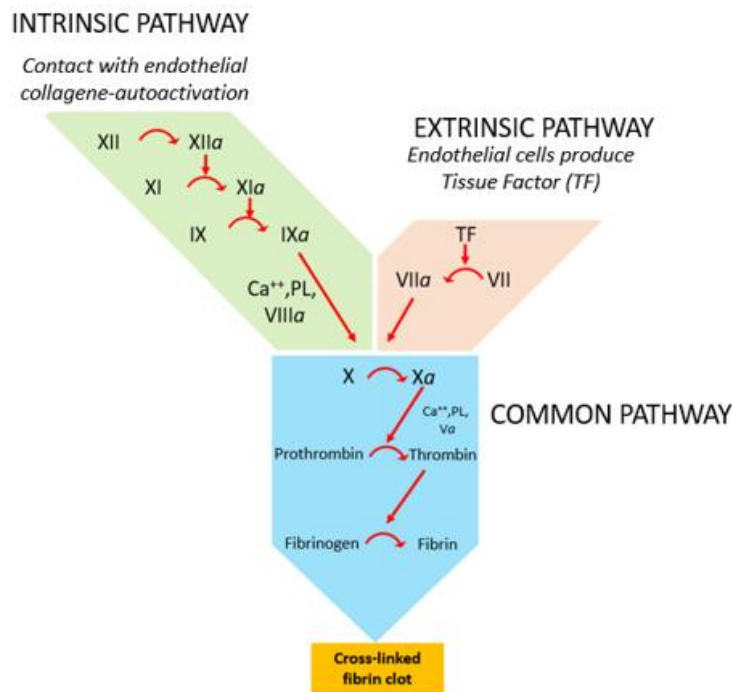


Figure 13 Coagulation cascade. There are two possible paths for triggering the coagulation, the intrinsic and the extrinsic. While the extrinsic is activated due to contact with Tissue Factor, present in the outside of the vessels, the intrinsic pathway is triggered by the activation of the protein named *fXII*, which may be activated by a trauma as well as contact with artificial surface. Both the pathways continue with a common pathway involving platelet activation, that ends with the formation of fibrin.

5.5 Contact coagulation

Blood contains several cells, for instance, platelets, white cells, and red cells, as well as numerous proteins. The adsorption of proteins is one of the first events that take place when blood meets an artificial surface. The structure of the adsorbed protein layer directly influences the thrombotic response, through the activation of the coagulation cascade [67,75]. The protein's size, charge, and structure, as well as surface physiochemical factors including

topography and chemical composition, heavily influence the adsorption process. It's still difficult to prevent thrombogenic proteins from adhering *in vivo*. Proteins are transported to a surface both by convection and diffusion. Blood velocity and flow profile affect convective transfer. However, protein transport mostly happens through diffusion very close to the surface, in an area known as a boundary layer [70]. The attraction of bound proteins to the surface depends on several other factors, including surface charge and wettability, a protein's propensity to unfold, and protein charges [70]. The composition of the protein layer changes in time, this dynamic variation is referred to as "Vroman effect". The equilibrium surface composition of the adsorbed species is determined subsequently by unique binding affinities and exchange interactions with other proteins present in the blood [74]. After adsorption, proteins unfold and reveal a region that in some way set off processes that lead to thrombosis. Depending on the surface type, different proteins will adsorb determining the starting of coagulation through two possible different mechanisms. Negatively charged and hydrophilic surfaces initiate the intrinsic pathway with the activation of *fXII*, while hydrophobic surfaces support the adsorption of fibrinogen and a conformational change that positively correlates with platelet adhesion and activation [74,79]. In each case, the process ends with the formation of fibrin and the generation of a stable clot [79]. The blood flow may influence contact coagulation, for instance at an anastomosis, locally disturbed flow or eddies may produce recirculation regions where clotting factors are concentrated.

6. Improving endothelialization and reducing thrombogenicity

In vascular graft applications, especially in small-diameter or low-flow artery bypass, thrombosis is a non-negligible cause of restenosis. As result a suitable non-thrombogenic luminal surface is required. The surface may be synthetic, cellular or biochemical, but it must prevent protein and cell adsorption, stop blood coagulation from occurring when it comes into touch with the intima of the graft, and hinder platelet adhesion and activation to prevent thrombosis in the arterial system [31]. To address this issue, for instance, heparinized grafts have been recently produced: heparin, immobilized on the surface of the graft, hamper the adherence and activation of platelets as well as fibrinogenesis, preventing clotting [80]. However, a significant problem in the development of heparinized grafts is the release and stability of heparin [28]. Another solution to prevent thrombosis and maintain patency is to induce fast endothelialization of the intima of the graft; indeed, endothelial cells (ECs) offer a proper interface between blood and surrounding tissue guaranteeing antithrombogenicity as well as deterring intimal hyperplasia [18,74]. A method to promote *in situ* endothelialization of vascular grafts is trans-anastomotic ingrowth of the endothelium of the innate arteries; in this process, the host intima responds to the damage caused by the implantation operation by growing ECs from the anastomosis sites towards the center of the graft, *i.e.*, there is a migration of endothelial cells from the anastomosis to the graft intima [81]. Another technique to exploit the effect of endothelial cells is prosthetic graft seeding, consisting in ECs coverage of the graft intima prior to its insertion into the human body [29,82]. This biohybrid graft may improve the biocompatibility and patency rates of prostheses. One of the

technological limitations is the low seeding density of these cells to current biomaterials, particularly once they are exposed to arterial flow.

7. Purpose of this work: developing new vascular grafts

Given all the issues raised, it is essential to develop new prostheses using technologies that can extend their patency rates and avert health-threatening circumstances. Therefore, current research has centered on graft optimization from several points of view. In this work we focus on the issue of grafts' thrombogenicity; Novel graft design may be approached from several aspects to address the coagulation problem. First, despite recent developments, grafts that are now in use continue to develop stenosis and clotting, endangering the life of the patients. A timely diagnosis of thrombosis within the graft is crucial for replacing the prosthesis before deadly consequences arise. Therefore, it is essential to develop a non-invasive coagulation monitoring device that can promptly alert the user when a blockage begins to form inside the graft. Secondly, to better understand the factors that trigger the formation of thrombi, it is necessary to further research of materials' hemocompatibility. To achieve this, new testing methods that make it quick and simple to examine each surface must be developed. Finally, it is essential to keep researching on TEVGs, paying close attention to the potential of endothelial seeding, to develop high hemocompatible engineered grafts. We can summarize the main objectives of this work as follow:

- Development of self-monitoring grafts capable of signaling the presence of a clot;
- Developing an *in vitro* dynamic test system for thrombogenicity evaluation of medical devices and biomaterials;
- Design of hybrid prostheses capable of promote endothelialization.

7.1 Self-monitoring smart grafts

Clot development in contact with the surface is one of the most common reactions to the implantation of a foreign, synthetic material into the human body, as previously discussed. However, once a vascular prosthesis is implanted, it is impossible to access it directly to determine eventual thrombosis, without resorting to somewhat intrusive procedures. New measurement tools that enable instantaneous thrombosis recognition are demanded so that timely intervention may be taken. An interesting approach may be to monitor blood flow and pressure; indeed, a clot alters the blood pressure due to the change in the cross-sectional area of the duct. The monitoring of blood pressure is therefore an indication of the state of the graft. The integration of pressure sensors within the prosthesis, would allow daily graft condition monitoring. Since there is a demand for a circuit-free, sensitive, and long-term stable system that could be easily integrated into the conduit design while maintaining the mechanical properties of the prosthesis, electroactive materials are a viable option. Being able to generate an electrical charge in response to an external pressure, they could easily be inserted into grafts and perform *in vivo* monitoring of blood flow. Once integrated they could detect any change in blood pressure. Additionally, the sensor should include an RFID system and be able to interact with point-of-care devices, so that to be comfortably used at home by the patient to get easily fast diagnostic results (**Figure 14**).

In this work we propose ferro/piezoelectric composite based pressure sensors: this class of materials is gaining a lot of attention in the field of sensors as they possess the piezoelectric capabilities of the ceramic filler with the mechanical behavior of the polymer matrix, as it is suited for a wide range of applications. Being easily processed, soft, and requiring a lower poling field¹¹, piezoelectric composites present noticeable advantages compared to other ferroelectric materials such as the electroactive polymers PVDF and P(VDF-TrFE) [83,84]. In light of these factors, we focus a part of this study on developing high-performance piezoelectric composites for in-vivo blood pressure monitoring.

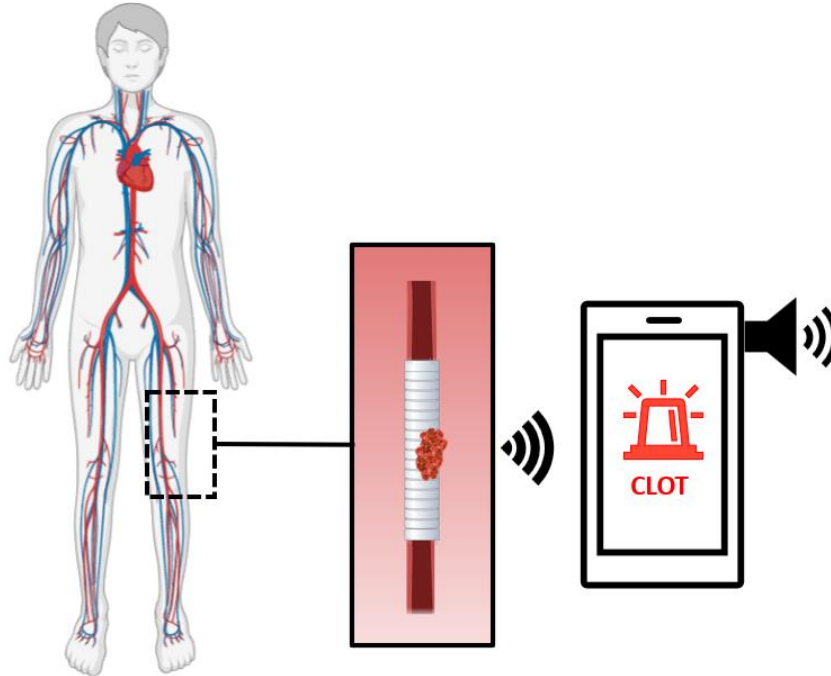


Figure 14 Schematic representation of a self-monitoring vascular graft, able to communicate with a point-of-care device. Created with BioRender.com.

7.2 *In vitro* dynamic test system for thrombogenicity evaluation of medical devices and biomaterials

The examination of the hemocompatibility of various surfaces is a crucial aspect. It is important to have a quick and simple method for studying the materials' hemocompatibility *in vitro*. As matter of fact, *in vitro* coagulation tests are usually based on viscosity measurements, which do not enable testing of different surfaces [85]. In this study, we propose a novel method for determining the thrombogenicity of a graft by measuring the impedance magnitude of blood during coagulation. This method is simple to use on various surfaces and provides access to the clotting time. In the future, this method may be integrated in grafts in order to track *in vivo* coagulation-related impedance changes and advance *in vivo* monitoring in addition to pressure monitoring.

¹¹ Every ferroelectric material requires the poling field in order to trigger the sensing activity and become piezoelectric.

7.3 Scaffold for fast cells seeding

Various studies have now shown that cell adherence may be improved by charge stimulation. Depending on the kind of cell, a positive or negative charge could enhance cell adhesion and growth, speeding up seeding and encouraging thicker cell layers on the scaffold. Fastening cells culture would also be advantageous in reducing bacterial contamination, linked to prolonged culture durations. Indeed, a faster culture has a better chance of surviving [86]. In this regard, using the charge produced by electroactive materials to fasten cell culture could be a suitable choice. Electroactive materials capable of generating surface charge in response to an external input may promote cells' layers development (**Figure 15**). In the final part of this work we will focus on the effect of charge on cells adhesion.

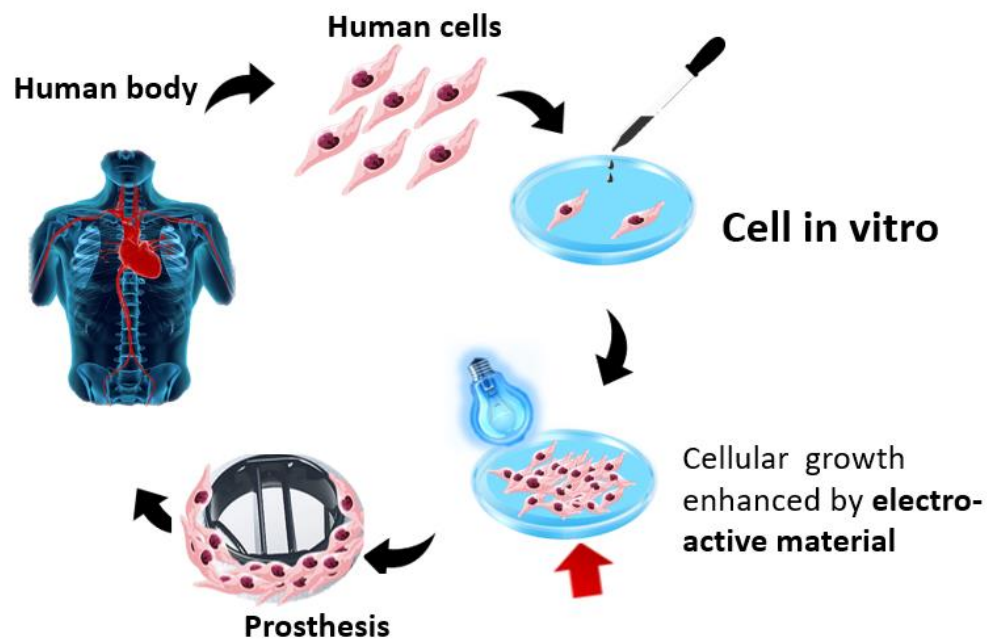


Figure 15 Drawing of endothelial seeding stimulated by an electroactive material, to fast cover a cardiovascular graft.

Chapter II

Structured piezoelectric composites for biosensor applications

Summary

This chapter discusses the development of high-performance piezoelectric composites produced through a technique known as dielectrophoresis structuring (DEP). BaTiO₃ (particles) and NaNbO₃ (fibers and particles) are selected as electroactive fillers, while the chosen matrix is Polydimethylsiloxane (PDMS). BaTiO₃-based composites, named BT/PDMS are produced in three volume concentrations (2.4%v, 12%v and 24%v) with 0-3 and quasi 1-3 connectivity. The first connectivity simply indicates composites with fillers randomly dispersed in the matrix, while the second is the result of DEP structuring and describes fillers arranged in columns along the thickness of the sample. This is obtained by applying an alternate electric field across the blend before and during the polymerization. NaNbO₃ fibers composites (named NN_MF/PDMS) are then produced in 0-3 and quasi 1-3 connectivity with three filler concentrations (1%v, 3%v and 5%v). In order to compare the effect of the form factor, NaNbO₃ particles-based composites (NN_MP/PDMS) with 5%v filler are developed as well with 0-3 and quasi 1-3 connectivity and compared with their equivalents with fibers. NaNbO₃ fillers are manufactured via a hydrothermal synthesis process. Finite element (FE) simulation as well as dielectric and piezoelectric characterizations prove that DEP structured composites outperform 0-3 composites regardless of filler or form factor. Furthermore, using fibers instead of particles allows for even greater piezoelectric coefficients. The effects of filler content and connectivity on mechanical properties and degree of crosslinking are studied using dynamic mechanical analysis (DMA), differential scanning calorimetry (DSC) and broadband dielectric spectroscopy in temperature (BDS).

Introduction

In this chapter the fabrication of a new class of piezoelectric composites for blood pressure sensors is presented; their production involves a technique named dielectrophoresis structuring (DEP), which allows the fillers to arrange in aligned columns under the effect of an external electric field. This structure, known as *quasi 1-3* connectivity, provides for a significant increase in piezoelectric sensitivity over composites with randomly dispersed fillers, *i.e.*, with 0-3 connectivity. First composites made of BaTiO₃ in Polydimethylsiloxane matrix (named BT/PDMS) with 0-3 and *quasi 1-3* connectivity are fabricated and characterized at different volume contents; Secondly, composites with NaNbO₃ fillers (fibers and particles) in PDMS matrix (named NN_MF/PDMS and NN_MP/PDMS) with 0-3 and *quasi 1-3* connectivity are developed varying the volume content and characterized. The goal is to examine and understand the effect of connectivity and form factor over dielectric, piezoelectric, and mechanical properties. The experimental results are supported by physical models and Finite Element analysis, performed via COMSOL®. Additionally, this research

focuses on determining the best DEP settings to induce perfect alignment. The developed piezocomposites are chosen for biosensor applications because of their high sensing potential, biocompatibility, and stretchability. Indeed, as thoroughly explained in the previous chapter, there is a need for pressure sensors that can be integrated into cardiovascular devices to perform *in vivo* blood monitoring. In the next sections, the theories of piezoelectricity, ferroelectricity, antiferroelectricity, dielectrophoresis and piezocomposites will be fully covered in order to provide foundation for the science underpinning the materials developed in this work. Later on, the materials and techniques used in this work will be described, followed by the results and discussion. The implementation of the sensors in real vascular devices will be discussed in Chapter III.

1. Piezoelectricity: concept and models

1.1 Piezoelectric materials

Piezoelectricity, from the greek $\pi\acute{\epsilon}\iota\theta\omega$ and $\eta\lambda\epsilon\kappa\tau\rho\upsilon\nu$, which means electricity produced by pressure, is defined as the ability of some crystalline bodies to develop an electric charge as consequence of a mechanical stress (direct piezoelectric effect) and vice versa is the mechanical deformation developed under the action of an electric field (reverse piezoelectric effect); the reciprocal relationship is referred to as the piezoelectric effect [87]. Pierre and Paul Jacques Curie discovered the direct piezoelectric effect while exploring quartz properties in 1880, and only later, in 1881, they demonstrated the reverse effect predicted by Gabriel Lippman. The piezoelectric effect is a linear and reversible mechanism: a stress causes a linear change of the internal polarization and thus the development of an electrical field across the material boundaries (**Figure 16**) [87-91]. Materials exhibiting direct effect always show the reverse piezoelectric effect. Because of this feature, piezoelectric materials are well suited for sensors, actuators, transducers, and energy harvesters.

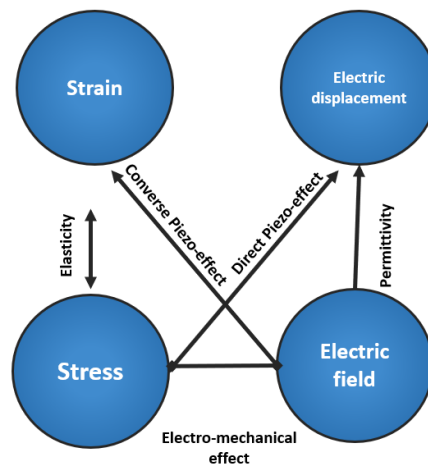


Figure 16 Conceptual representation of the piezoelectric effect.

Piezoelectricity has been observed in inorganic ceramics as well as organic polymers. The source of the piezoelectricity in ceramics can be attributed to the non-centrosymmetric crystalline structures, which leads to the production of electric dipoles as a result of mechanical distortion. Twenty-one of the thirty-two crystal classes into which all crystalline materials can be classified have non-centrosymmetric structure and twenty of them can exhibit piezoelectricity. When a distortion is established on the piezoelectric crystal, electric dipole moments are generated due to the lack of a center of symmetry [91,92]. This does not happen in centrosymmetric structures because when the crystal is strained, all of the generated dipoles annihilate each other, leaving the net dipole at zero [90-92]. Often, piezoelectric ceramics are ferroelectrics that require a polarization to display piezoelectric activity, which involves poling technique [87,92,93]. The piezoelectric activity is quantified in charge created per unit of force (pC N^{-1}), named piezoelectric charge coefficient d_{ij} . For instance, piezoceramics exhibit outstanding piezoelectric characteristics (hundreds of pC N^{-1}). Among them, Lead-Zirconate-Titanate (PZT) is a major piezo-ceramic that is widely employed for energy harvesting and storage applications. Other ceramics include Barium Titanate (BaTiO_3) and Potassium Niobate (KNbO_3) [87,94,95]; Temperature has an impact on piezoelectric behavior of inorganic materials. Indeed, each piezoelectric crystal has a specific temperature, known as the Curie Temperature (T_c), above which piezoelectric activity is lost. Above this temperature, the crystal structure transforms from non-centrosymmetric to centrosymmetric, resulting in a non-piezoelectric paraelectric material [83].

Piezoelectric behavior can also be observed in materials different from crystalline ceramics, for instance in organic electroactive polymers. This class of materials possesses piezoelectric properties due to the presence of dipoles in the molecular structure of the polymer that can be oriented in a preferential direction by poling process [88,96]. Especially worth mentioning are semicrystalline electroactive polymers, including the well-known polyvinylidene fluoride (PVDF) and its copolymers (P(VDF-TrFE)), polyamides, and parylene-C. This class behaves similarly to inorganic materials, as being semi-crystalline, they have microscopic crystals distributed in the amorphous part. The crystalline domains are responsible for piezoelectric activity since they contain dipoles that, when properly oriented, impart piezoelectricity [88]. PVDF and its copolymers are among the most well-known, showing high piezoelectric constants (-20 to -28 pC N^{-1}) which make them superior to other bulk piezopolymers. PVDF is synthesized via polymerization of $\text{H}_2\text{C}=\text{CF}_2$ monomers. When two CF_2 or CH_2 groups link, a flaw in the polymer chain arises. The polarity of the polymer is linked to these imperfections, and the more faults there are, the higher the piezoelectricity. This material is typically copolymerized with trifluoro ethylene TrFE, which improves its piezoelectric properties significantly [88,97-99]. Parylene-C, which has molecular dipoles due to the solitary chlorine atom in the benzene ring, is another bulk electroactive polymer. It exhibits, however, a modest piezoelectric constant of -2 pC N^{-1} [88,100]. Polyimide falls within the amorphous group of electroactive bulk polymers, although it always exhibits lower piezoelectric constants (-3 pC N^{-1}) [88,101]. Both parylene-C and polyimide are mostly used in MEMS. Other electroactive polymers worth of mention are polyamides (PAs) (1.1 pC N^{-1}) and poly lactic acids (PLA) (-1.58 pC N^{-1}) [96,102,103]. As well as piezo-ceramics, electroactive organic polymers feature

a Curie limit temperature at which their piezoelectric capabilities deteriorate, which usually is lower than those of inorganic piezoelectric materials [104].

Finally, among piezoelectric materials it is worth to mention piezoelectric composites, made of a polymeric matrix and an inorganic piezoelectric filler. Such a combination enables good piezoelectric activity with the appropriate mechano-electric characteristics [83,88]. Tuning the phases is possible to get a wide range of piezoelectric composites, such as PZT/Epoxy, BaTiO₃/Epoxy, PA11/BaTiO₃ or ZnO/PMMA to name a few [93,105-107]. Generally, the piezoelectricity range extends from the unit to tens of pC N⁻¹.

In conclusion, piezo-materials can be classified in the three main classes reported: ceramic, polymers and composites; each one presents characteristics that make it more suitable for a determined set of applications. As stated in the introductory paragraphs, piezo-composites were found to be the best solution for the problematic presented in this project, therefore, more information on piezoelectric composites will be provided in the next sections. The thermodynamic formulation of piezoelectricity, which applies to all the above categories of piezoelectric, will be discussed in the following paragraphs. Following that, the concepts of pyroelectric and ferroelectric materials, a subclass of piezoelectric inorganics, will be introduced as these materials were chosen as fillers in the composites designed in this work, thus it is important to discuss the physics that regulates their piezoelectric activity.

1.2 Analytical formulation of piezoelectricity and figure of merit (FoM)

Based on the thermodynamic theory it is possible to define the mathematical coefficients and relationships describing the piezoelectric effect. Considering temperature and entropy as constants, the relationships are between stress (T_j), strain (S_j), electric field (E_i) and electric displacement (D_i), where I and J are indices with values from 1 to 6, i and j from 1 to 3, thus D and E are (3x1) tensors and T and S are (6x1) tensors. Concerning the direct piezoelectric effect, when a stress is imposed to a piezoelectric material, the electrical polarization changes, and an electric charge develops on the material's surfaces. Taking into consideration the elastic properties of the material, the direct effect can be described by the following relationship[91,92,108]:

$$D_i = \varepsilon_0 \varepsilon_r^T E_i + d_{ij} T_j \quad (1)$$

where ε_0 is the permittivity of the free space and ε_r^T is the dielectric constant of the material at constant stress. d_{ij} is the coefficient that represents the direct proportionality between force and charge. It is a tensor of rank 3 and is defined as piezoelectric charge coefficient. For the direct piezoelectric effect, considering the external electric field, E , equal to zero, it is expressed in coulomb/Newton as follows:

$$d_{ij} = \frac{D_i}{T_j} \quad (2)$$

Piezoelectric reverse effect describes a deformation produced by and applied electrical field and for an elastic material can be expressed as:

$$S_I = d_{Ij}E_j + s_{IJ}^E T_j \quad (3)$$

where s_{IJ}^E is the material's mechanical compliance matrix at constant electric field and d_{ij} is the coefficient which defines the direct proportionality between the applied electric field and the generated strain. It is a tensor of rank 3 and has the same value of the piezoelectric charge coefficient measured for the direct piezoelectric effect. For reverse piezoelectricity in unstrained conditions, *i.e.*, T equal to zero, the piezoelectric strain coefficient is expressed in meters/volt and is computed as [91,92,108]:

$$d_{Ij} = S_I/E_j \quad (4)$$

d_{ij} denotes the electric polarization generated in direction i per unit of mechanical stress of index J , and d_{Ij} represents the mechanical strain in I direction per unit electric field applied in direction j . The piezoelectric charge coefficient and the piezoelectric strain coefficient are equals. d_{ij} is essential for evaluating piezoelectric materials, and it is especially useful for actuators. Depending on the direction i of the charge displacement and J of stress application it is possible to define 18 operating modes; If stress and electric polarization are in the same direction (d_{11} , d_{22} and d_{33}), the mode is defined as longitudinal. The transverse mode is when a change in electric polarization is perpendicular to the mechanical load (d_{12} , d_{13} , d_{21} , d_{23} , d_{31} and d_{32}) while longitudinal shear mode is when a shear stress is applied and induces an electric polarization change perpendicular to the plane of shearing stress (d_{14} , d_{35} and d_{36}). Finally the transverse shear mode is related to a change in polarization in the plane of the applied shearing stress (d_{15} , d_{16} , d_{24} , d_{26} , d_{34} and d_{35}) [108]. The most used piezoelectric charge coefficients are d_{31} and d_{33} , which represent respectively the transverse coefficient and the longitudinal coefficient (**Figure 17**) [91,92,108].

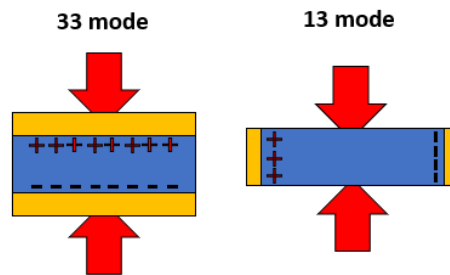


Figure 17 Representation of 33 and 31 transduction modes [1].

Another relevant coefficient used to describe the piezoelectric behavior of a material is the piezoelectric voltage coefficient, g_{ij} , defined as follow [83]

$$g_{ij} = \frac{d_{ij}}{\epsilon_0 \epsilon_r} \quad (5)$$

It represents the electric field generated by a piezoelectric material per unit of mechanical stress applied or, alternatively, the mechanical strain experienced by a piezoelectric material per unit of electric displacement applied. It is a tensor of rank 3 and its unit of measure is $V\ m\ N^{-1}$. It is crucial in understanding a material's suitability for sensing (sensor) applications [83,108]. Figures of merit (FoMs) are a valuable indicator for identifying optimal piezoelectric materials based on the application. For instance, in the case of transducers, sensors, and energy storage devices, the most effective FoM is the product of the piezoelectric charge and voltage coefficients ($d_{ij} * g_{ij}$). The higher the FoM, the stronger the electromechanical coupling, defined as the ratio of stored electrical energy to applied mechanical energy or vice versa. On the other side, $d_{ij} * Q$ is useful for evaluating high power piezoelectrics operating at their resonance frequency, being Q the mechanical quality factor associated with the vibration [83].

1.3 Pyroelectric and Ferroelectric ceramics

In the opening section the causal relationship between non-centrosymmetric crystalline structure and piezoelectricity was introduced. As mentioned, due to a lack of center of symmetry in the crystal structure, twenty of the thirty-two crystalline classes display piezoelectric activity [109]. Among these it is possible to identify an additional subclass of ten crystalline structures, named pyroelectric materials. These materials are classified as piezoelectric pyroelectrics, as opposed to other crystalline types that just exhibit piezoelectricity. All pyroelectrics are piezoelectric but not vice-versa [91,92]. This subclass of piezoelectrics is characterized by the presence of a single polar axis under non-stress conditions, resulting in a net electric dipole.

A discrepancy in the centers of positive and negative charges in a unit cell causes the dipole to form. At rest, however, the internal dipole is neutralized by the charges on the crystal faces. When this material is subjected to stress or uniform heat, the spontaneous polarization of the material changes, causing a change in the strength of the dipole and surface charges to develop at the crystal's end [90,91]. This external charge, consequence of a change in the net internal dipole, is called polarization, and is measured as charge per unit of area. In summary, such materials differ from the other piezoelectric materials since they display spontaneous polarization at rest, additionally electrical charge develops not only in response to stress but also to uniform heating. This occurs because temperature variations can slightly alter the locations of atoms inside the crystal structure, changing the material's polarization [110,111]. Non-pyroelectric piezoelectric crystals, on the other hand, have all their dipoles displaced in such a way that they counterbalance each other when unstrained, thus there is no net crystal dipole in the absence of external stress. When a stress is applied, one of the dipoles' directions is preferred, and a net crystal dipole is formed. Because uniform heat does not cause variations in the dipole, they are not pyroelectric. Quartz is an example of non-pyroelectric piezoelectric [90,91].

Finally, a subclass of materials known as ferroelectric materials may be distinguished within the pyroelectric one. Ferroelectrics are pyroelectrics that have a net dipole that can be reversed by applying an external electric field. Being pyroelectrics, the polarity of ferroelectrics resides in a non-centrosymmetric crystalline structure with a singular polar axis in non-stress conditions [90-92,111]. However, not all pyroelectrics are ferroelectric: the poling field, which is required to reverse polarity, may be greater than the material

breakdown of some pyroelectrics, or some pyroelectrics simply have an irreversible asymmetrical arrangement of atoms [91]. The crystallographic structures of ferroelectric ceramics are perovskite, tungsten bronze, layer bismuth and pyrochlore structures [83,112,113]. Perovskite is the most important among them, being highly piezoelectric. Such a structure, which is displayed in **Figure 18**, is characterized by an ABO_3 structure, where the A (metal) site is placed on the corner of a cubic cell, B smaller cation (metal) in the center and oxygens O in the center of the faces [90,92,114].

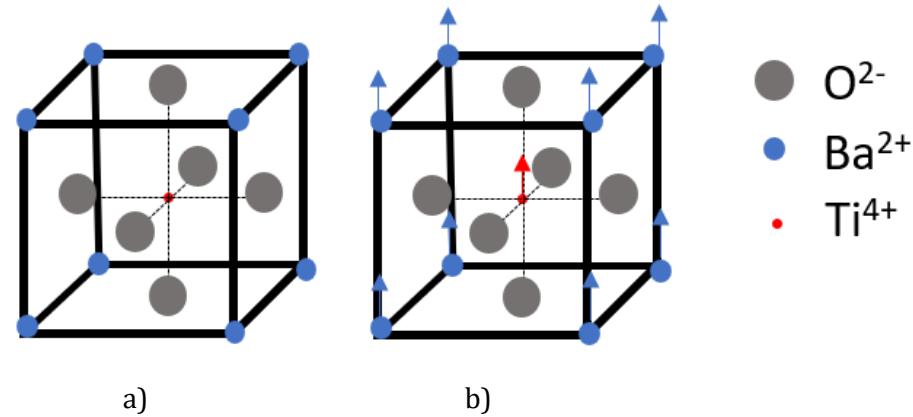


Figure 18 a) Cubic unit cell of perovskitic Barium titanate above the Curie temperature; b) below the Curie temperature the unit cell is tetragonal with Ba^{2+} and Ti^{4+} displaced with respect to O^{2-} , and consequently the center of positive charge does not coincide with the center of negative discharge.

Being the piezoelectric, the ferroelectric materials have a characteristic Curie temperature, T_c . For $T > T_c$ there is a paraelectric phase, where the cubic symmetry of the unit cell is in equilibrium. Below this T_c , the unit cell deforms, and the metal cations are displaced from their symmetry sites relative to the oxygen anions, resulting in an electrical dipole moment, which is associate to the ferroelectric behavior. Among all the ferroelectrics, perovskite piezoelectric materials offer high dielectric and piezoelectric properties and a relatively high Curie Temperature, that must be taken into account for high temperature applications [115]. Furthermore, it is possible to distinguish lead based and lead-free ferroelectric ceramics. Barium Titanate ($BaTiO_3$), for instance, is a lead-free ceramic with a Curie temperature of 120°C/130°C. Thanks to its perovskite structure it has high dielectric and piezoelectric properties and it is interesting as piezoelectric bulk for several structural applications or as filler for piezocomposites for biomedical applications, being biocompatible [92,116-119]. Lead zirconate titanate (PZT) is an example of lead based polycrystalline ferroelectric ceramic and it seems to be the more promising choice for high temperature applications, in aeronautic and aerospace fields; it is characterized by high Curie temperature and high piezoelectric properties [91,92,120,121]. However, due to the presence of lead atoms, it is unsuitable for application in the biomedical area. Other lead-free perovskites worth mentioning are BNT (ternary compositions $BaO-TiO_2-Nd_2O_3$), potassium niobate ($KNbO_3$) and Sodium tantalate ($NaTaO_3$). All the perovskites are suitable for actuator and high-power applications [116]. Other ceramics with non-perovskite structure that can be used as bulks or to design

piezocomposite are: lead meta niobate (PbNb_2O_6), with tungsten bronze structure and Curie temperature of 570°C ; layer bismuth oxides such as bismuth titanate $\text{Bi}_4\text{Ti}_3\text{O}_{12}$ with higher Curie temperature of 675°C , which are particularly suitable for resonator applications and filters; Finally corundum structure-based ceramic such as LiNbO_3 with T_c of 1150°C [90-92,116]. When discussing ferroelectric materials, a necessary step to activate the piezoelectricity is the poling (or polarization), which means applying an electric field to orient the internal dipoles. This procedure is discussed in the next subsection.

1.4 Ferroelectric polarization

As previously explained, ferroelectric materials have a net polarization due to their unique polar axis. They do, however, contain numerous crystalline domains, *i.e.*, net polarization zones, which have differing polarization directions and annihilate each other, resulting in a zero net dipole [90,91]. Multiple crystallographic domains are usually separated by domain walls and in polycrystalline materials different domains may exist in the same single crystal. To exhibit piezoelectric behavior, all domains must be oriented in the same direction, and that may be accomplished by applying an external electric field across the material, technique named *poling*. During such a procedure all the dipoles orient parallel to the electric field lines and when the electric field is withdrawn, they exhibit a residual polarization [90,92,122]. Then, once a mechanical stress is applied on a poled material a shift of the residual polarization occurs, resulting in the piezoelectric phenomenon. There are no changes in the crystalline structure during the poling orientation for ferroelectrics. In some way, the poling treatment imparts artificial anisotropy to the material, allowing the ferroelectric component to exhibit piezoelectric behavior. The piezoelectricity is then maintained as long as the material is not de-poled: de-poling occurs when the ferroelectric material is exposed to temperatures higher than T_c , or when high electric fields are applied in the opposite direction to the previous poling direction. **Figure 19-a** shows the typical bipolar polarization curve, where the Polarization P (C m^{-2}) is displayed against the Electric field E (V m^{-1})[122,123]. The initial polarization of an unpoled ferroelectric material is zero. When an electric field is supplied across the ferroelectric, all of its dipoles align parallel to it. The polarization increases nonlinearly and eventually reaches a maximum, P_s , which is the saturation polarization corresponding to the maximum dipole alignment. When the electric field is released, the material retains a residual polarization, P_r , known as the net remnant polarization. E_c is the coercive electric field, or the electric field necessary to de-pole the material. **Figure 19-b** depicts the dipole orientation in a multiple domain system before, during, and after poling [124]. The electric field required for polarization saturation, E_s , is an intrinsic property of each ferroelectric.

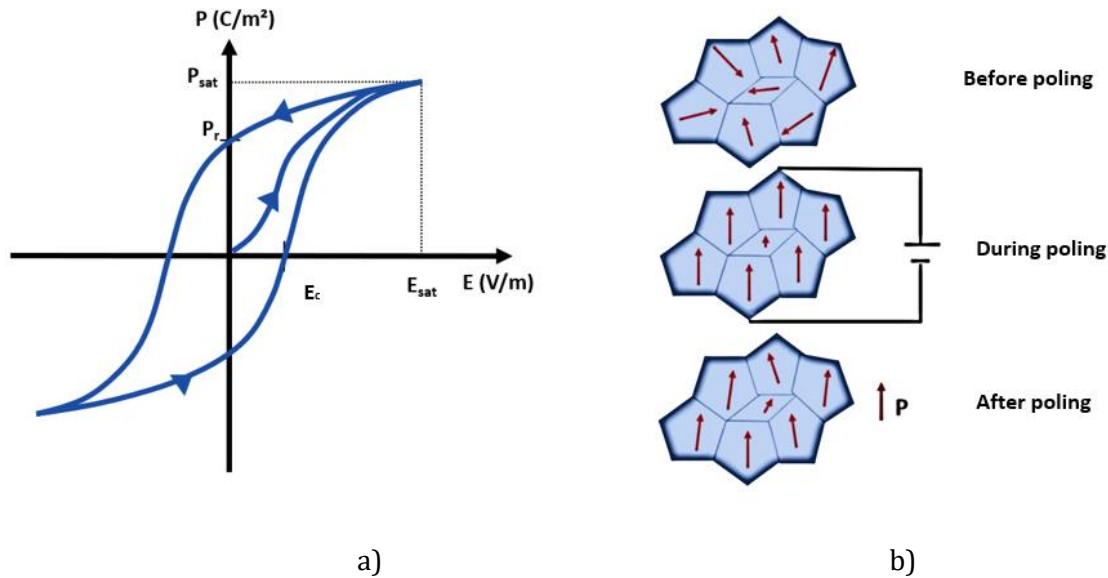


Figure 19 a) Typical bipolar polarization curve; b) dipole orientation in a multiple domain system before, during, and after poling.

1.5 Antiferroelectric ceramic materials

According to Kittel, antiferroelectric materials (AFE) have spontaneously ordered dipole moments that are antiparallel and cancel out at zero field on a unit-cell basis, *i.e.*, the net dipole is equal to zero [125]. The AFE phase is typically the consequence of a structural phase transition from a higher temperature paraelectric phase (PE) and occurs at Curie's critical temperature. PE to AFE phase transition occurs via displacive soft mode, *i.e.*, caused by atom or ion displacements via a mechanism involving a phonon frequency that falls to zero at the transition temperature, or by order – disorder process, where previously disordered dipoles become organized [126]. One of the most significant features of AFE is that the application of an adequate electric field may orient all the dipoles in the same direction, resulting in a shift from antiferroelectric to ferroelectric phase. An electric field might trigger a transition from AFE to FE since the free energy of AFE is equivalent to that of the polar phase. Double polarization hysteresis loops are used to represent this effect macroscopically (**Figure 20**) [127,128]. The critical field is temperature dependent; for example, $PbZrO_3$, a well-known AFE, cannot be reversed to FE at room temperature because its electric field threshold (E_f) to reach AFE to FE transition is greater than the material's electric breakdown; however, at high temperatures E_f decreases linearly, and the phase transition can occur at temperatures near the material's antiferroelectric T_c [127].

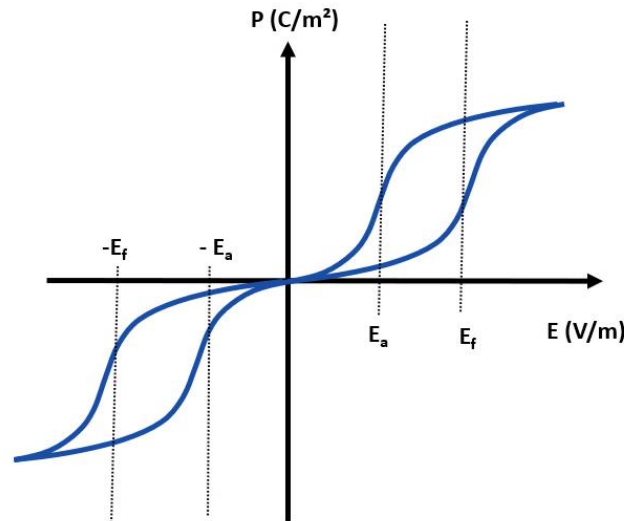


Figure 20 Typical antiferroelectric material's double hysteresis.

The phase transition produced by an electric field might be reversible or irreversible, depending on the material and on the temperature. For those that are reversible, it is feasible to revert to an antiferroelectric condition by lowering the electric field until a certain value named E_a , *i.e.*, the electric field to antiferroelectric state [126,127]. However, some AFE materials, such as NaNbO_3 , are irreversible, thus the application of an electric field induces FE phase, and then, at the removal of the electric field, a residual polarization is left on the material, with no coming back to AFE phase. The polarization loop for such irreversible AFE is not double, but rather a single loop, as for ferroelectrics (**Figure 19-a**). By raising the temperature or changing the chemical composition of materials that are reversible at ambient temperature, the irreversible phase transition can be achieved. A particular case is the one of NaNbO_3 : at any temperature, no double polarization hysteresis loops have been found for it [128,129]. In light of the foregoing, antiferroelectric materials can be employed as transducers in the same way as ferroelectrics can, or likewise as energy harvesting materials, and for such a reason are selected as fillers for the composites produced in this research, for bio-sensors development.

1.6. Piezoelectric composites

The large range of applications that need piezoelectric transducers has driven the design and development of novel and increasingly high-performance piezo-materials. Among them, piezocomposites are gaining incredible attention. Piezoelectric composites are a class of electroactive material consisting of a passive polymer matrix and embedded electroactive FE or AFE ceramic fillers [83]. As for bulk ceramics, they require poling to display piezoelectric activity [130]. Their expanding popularity stems from their capacity to be customized to meet a variety of application needs, which may be achieved by combining an appropriate matrix and fillers. As a result, they cover a wide range of applications as sensors, transducers and energy harvesters from aerospace and aeronautics, where high sensitivity to external stimuli, chemical and high temperature resistance are required, to biomedical fields where

biocompatibility, non-toxicity, sensitivity, and stretchability are essential [83,88,112,120,130-132].

Non-destructive testing, structural health monitoring, energy harvesting, underwater acoustics, medical imaging and treatments, and wire bonding are just a few examples of the typical applications [88,107,120,133,134]. While the filler determines the piezoelectric properties, the matrix dictates the composite's mechanical behavior. The possibility to select the matrix makes them extremely adaptable to any application and easy to integrate to complicated geometries and convoluted courses. This is a considerable advantage over piezoceramic bulks, which, although having much higher piezoelectric d_{ij} coefficients (more than ten times higher), are rapidly being abandoned in favor of piezocomposites, due to their stiffness, brittleness, and difficulty in shaping and integrating in complex systems. In addition to that, piezocomposites have a lower dielectric constant than bulks and hence a higher piezoelectric voltage coefficient g_{ij} [83,91]. They are also preferred to electroactive polymers (PVDF, P(VDF-TrFE)) for a variety of applications which requires high temperature resistance as well as flexibility and stretchability. Despite being extremely piezoelectric with an exceptional piezoelectric voltage coefficient, organic electroactive polymers frequently have low temperature resistance with Curie temperatures around 100°C, are stiffer than composites with elastomeric matrix, and require extremely expensive production cycles and expert manpower, as well as large polarization fields (100-200 V μm^{-1}) [89,135-137]. Several figures of merit can be designed to account for important factors such as working temperature, polarization electric field, elastic modulus, and so on, so that piezo materials can be effectively compared by selecting the most relevant application-related aspects [83,112,120]. For instance, in our prior study, we developed a FoM, computed according to Eq.6, to compare piezo-materials based on three different aspects which were piezoelectric coefficient d_{33} , poling electric field, E_{pol} , and degree of crystallinity (φ_{Cr}), (i.e., amount of filler for piezocomposites). The unit of measure of the FoM was $\text{C m V}^{-1} \text{N}^{-1} * 10^{-18}$.

$$FOM = \frac{d_{33}}{E_{pol} \times \varphi_{Cr}} \quad (6)$$

The aspects considered are quite critical; first of all, d_{33} is a measure of a material's transducer behavior; the higher the value of d_{33} , the larger the charge that is generated in response to a mechanical input. From a production standpoint, the electric polarization field is crucial; the larger the field, the less feasible manufacturing is; the volume content of crystallinity reflects the filler content in piezocomposites, and the crystalline phase in electroactive polymers. It has a significant impact on the mechanical properties; for instance, the higher the percentage, the more brittle the material. From an economic perspective high crystallinity means high costs since it is related to the filler content, while high poling field is inconvenient because it raises energy costs as well as safety issues. In that analysis, several piezoelectric composites and electroactive polymers were selected as reported in **Figure 21** [120]. The best material among those under analysis, according to this FoM, is a piezocomposite based on PZT fillers in PDMS matrix, with a particular connectivity named *quasi* 1-3, which will be introduced later in this chapter. Nonetheless being non-biocompatible it would not suit the biomedical application of this work. However, considering the elements on which the FoM is built,

piezocomposites outperform organic electroactive materials. This is an example of the usefulness of FoMs, which may be tailored to meet the needs of a specific application.

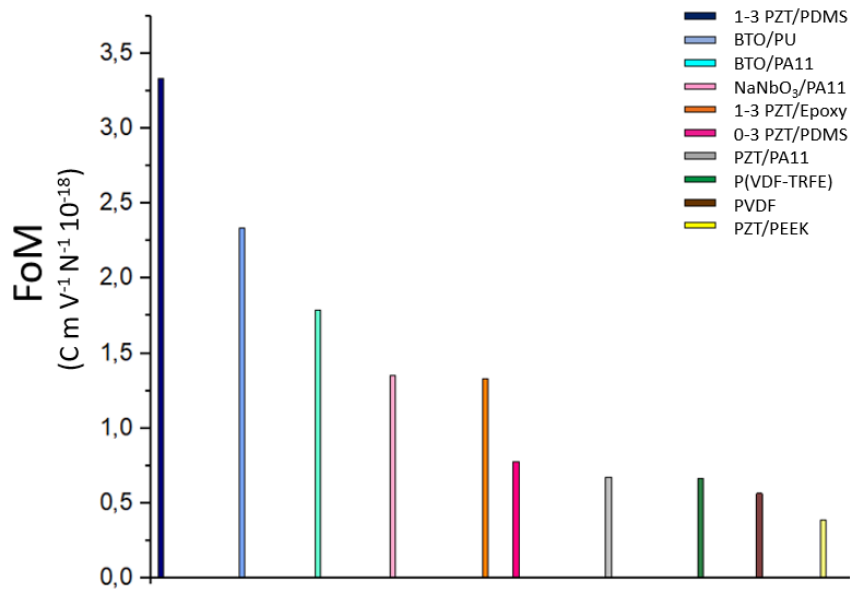


Figure 21 Comparisons between FoM of different piezoelectric composites and polymers described in the literatures [131,138-143].

The scientific interest on piezocomposites in the recent years is increasing (**Figure 22**) and much effort has recently been devoted into developing increasingly high-performance composites for a wide range of different applications (**Figure 23**).

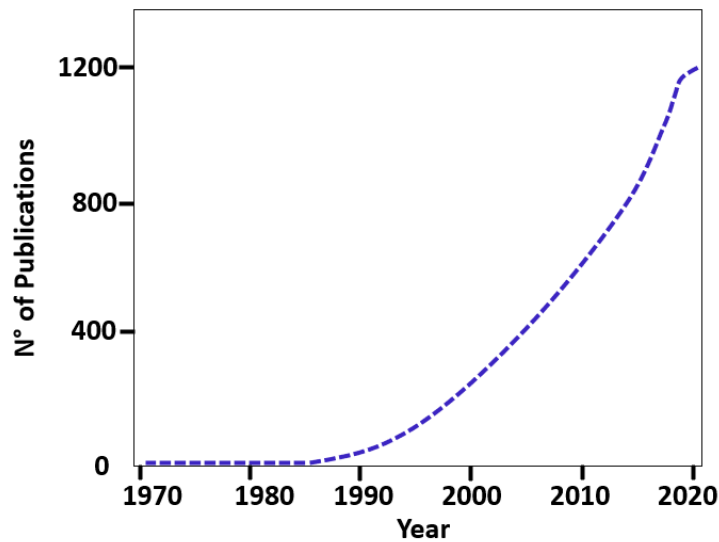


Figure 22 Number of publications on piezocomposites from 1970 to 2020.

Capsal *et al.* produced piezoelectric sensor coatings with a piezoelectric constant d_{33} of 5 pC N^{-1} based on BaTiO_3 in a Polyurethan matrix for real-time impact detection and localization on aircraft structures [138]. D'Ambrogio *et al.* designed PZT-based composites in PDMS matrix for aircraft ball bearings health condition monitoring, with d_{33} values of 16 pC N^{-1} [120]. Nguyen *et al.* recently fabricated composites for the same purpose, employing Barium titanate in Polyurethane acrylate, achieving a d_{33} of 1.5 pC N^{-1} [144]. Beside health condition monitoring, piezoelectric composites being flexible and reliable, are also implied for low vibration energy harvesters. Park *et al.* developed a flexible nanocomposite generator consisting of BaTiO_3 nanoparticles and graphitic carbons that can generate an open circuit voltage of 3.2 V and a short circuit current of $250\text{--}350 \text{ nA}$ when mechanically tapped on a regular basis[145]. Similarly, Xu *et al.* developed PMN-PT Nanowire/PDMS composites capable of producing 7.8 V and a short circuit current of 2.29 A when a $1 \text{ cm} \times 0.5 \text{ cm}$ sheet was mechanically tapped [146]. Piezocomposites have also been widely used in biomedical applications, most notably in medical imaging, as reported by Lee *et al.* [83]. Their strong coupling coefficients significantly enhance bandwidth and energy transmission, resulting in a significant rise in signal-to-noise ratio. Furthermore, their low acoustic impedance enables great energy transfer between transducers and propagating medium [83]. Recently, electroactive composites have been used for a novel set of application-related physical health monitoring for orthopedic implants. Grinberg *et al.* designed 3D printable BaTiO_3 /PU composites with d_{33} of 4 pC N^{-1} that could be included into smart orthopedic implants for *in vivo* monitoring and increased osteo-inductivity[147]. Tang *et al.* reported a similar results in their research on graphene/ BaTiO_3 /PMMA composites [148]. Finally, it is worth mentioning their use as tactile sensors, as described in the work of Kumar *et al.* who developed composites containing BaTiO_3 incorporated in a PDMS matrix[149].

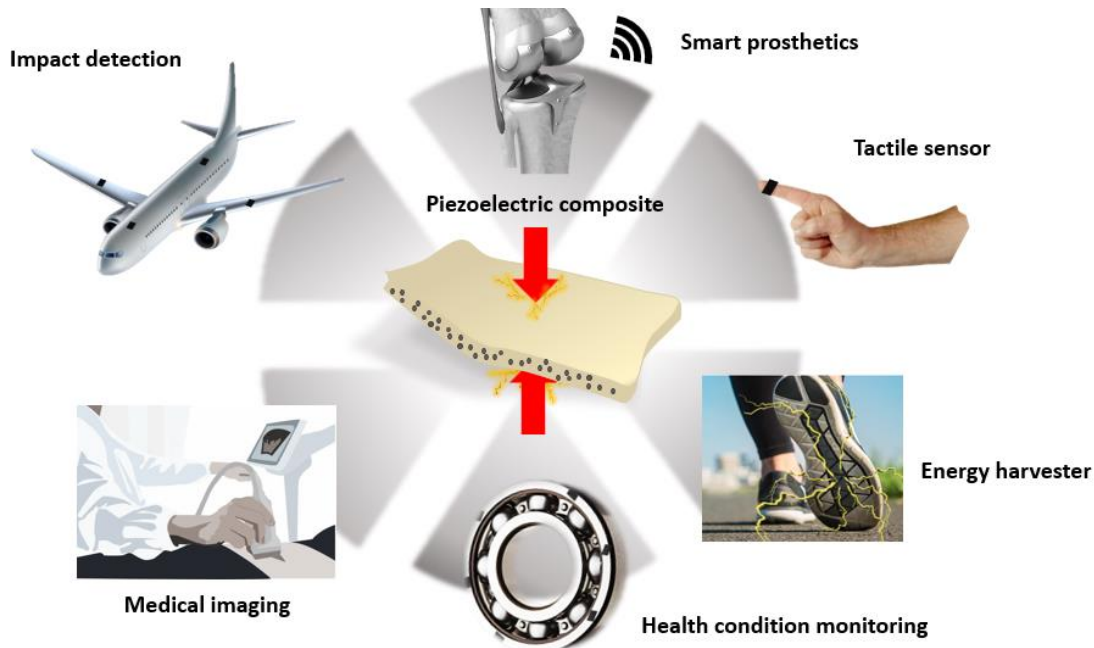


Figure 23 Example of the variety of applications that piezocomposites cover.

Several essential parameters must be considered when designing a piezocomposite, as displayed in **Figure 24**. The first step is to properly choose the phases, as their properties will determine the ultimate characteristic of the composite. Thus, dielectric, electric and piezoelectric properties of matrix and filler must be taken into consideration, together with mechanical and thermal properties [83,88,150]. Multiple filler types may be selected to develop ternary composites with additional conductive fillers, added to enhance the poling procedure [112,150]. The filler volume fraction, form factor and size are other factors that influence the final product together with the manufacturing process, extremely relevant in tuning the properties of the materials. One of the key criteria in the study of high-performance piezocomposites is the connectivity between the phases. As matter of fact, isotropy/anisotropy and ultimate performance of the composite are determined by how the filler is arranged in the matrix [83,108,150]. The next sections will address the selection of fillers and the matrix suitable for the application proposed. Finally, the role of connectivity will be explored.

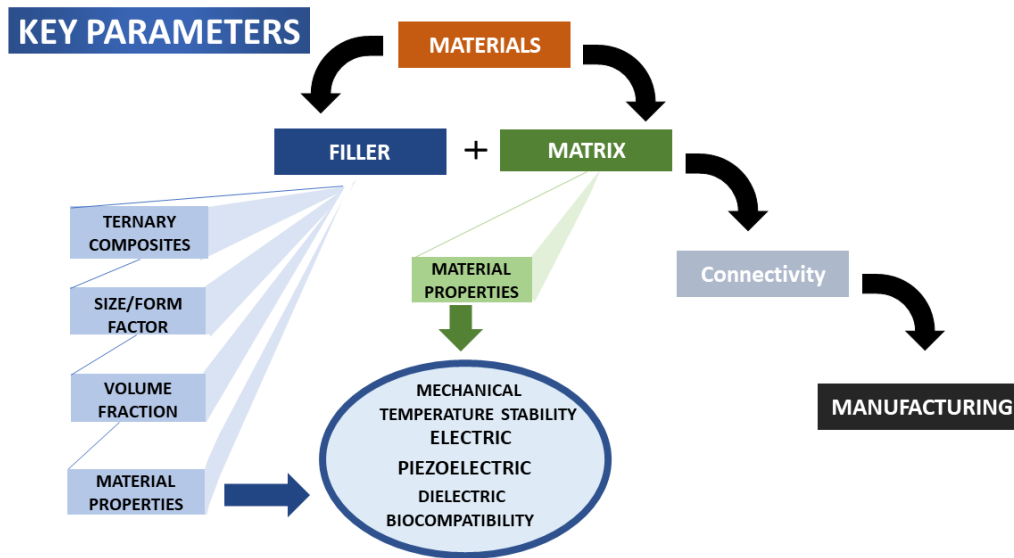


Figure 24 Fundamental parameters in designing piezocomposites.

1.7 Fillers: Biocompatible ferroelectric BaTiO₃ and antiferroelectric NaNbO₃

The ferroelectric filler determines the piezoelectric characteristics, but also greatly affects dielectric, electrical, mechanical, thermal, and biocompatibility properties [150]. Depending on the size of the ceramic particles, micro- or nanocomposites can be produced to develop piezoelectric composite materials with the suitable properties associated to the application and depending on the shape is possible to design particulate or fiber composites [88]. The biomedical application presented in this work requires biocompatible materials with high

electromechanical coupling: lead based fillers cannot be selected, being toxic for the human body, even if they present the best set of piezoelectric parameters. Biocompatible fillers that have been widely used are Zinc Oxide (ZnO), Barium Titanate (BaTiO₃), Sodium Niobate and Potassium Sodium Niobate (NaNbO₃, KNN) [83]. As matter of fact the moderate piezoelectric activity of ZnO, makes it unsuitable for the purposes mentioned in this work [151]. Lead-free ferroelectric BaTiO₃ and antiferroelectric NaNbO₃ fully match the application's requirements; their biocompatibility and remarkable piezoelectric activity are the distinguishing factors [118,152]. When properly embedded in a matrix, they can impart piezoelectricity to the composite. For instance, by carefully selecting the matrix, flexible piezoelectric biosensors can be easily integrated in FFR catheters that require substantial flexibility to enter tortuous venous conduits, or in smart vascular prosthetics, without compromising their mechanical features and operability.

1.8 The matrix

When designing a piezoelectric composite, the matrix must be carefully selected based on the application and the operating environment. The polymer phase's primary functions are to impose their mechanical properties while decreasing density and permittivity [83]. In terms of mechanical properties, elastomers are typically chosen as matrices for compliant and flexible composites because of their low Young's modulus and high Poisson ratio: these two qualities give less constraint to piezoelectric vibration, allowing for a great electromechanical coupling [8][29]. Epoxies, which are stiffer, are the best option if the material is intended to be used as a resonator, whereas thermoplastics, which are ductile, are appealing in terms of manufacturing because they can be easily shaped in various geometries, remolded, recycled, and combined with 3D printing processes [153,154]. When it comes to vascular devices, for instance smart catheters and prostheses, the flexibility of the matrix is critical, and an elastomer seems to be the ideal choice. Additionally, low dielectric permittivity is an essential parameter since it decreases the total composite's permittivity, resulting in a larger piezoelectric voltage coefficient, g_{33} , meaning better voltage sensitivity. There are several other parameters that must be taken into account, including temperature stability, biocompatibility, and electrical conductivity. For instance, the conductivity of a matrix is relevant for the poling process: a totally conductive matrix would induce a short circuit during the poling of the material; a modest conductivity, on the other hand, might intensify the poling effect [150,155]. Additionally, the polymer shouldn't have a low electric breakdown since it would make it difficult to apply an electric field to the sample. Temperature resistance is related to the environment of application, which is not a concern for implantable biosensors as the operating temperature is 37°C, *i.e.*, the human body temperature. One of the major constraints imposed by the application is biocompatibility. The material employed should be chemically inert and non-toxic in order to be harmless. The application's requirements motivated the use of an elastomeric passive silicone as the matrix (Poly-dimethyl siloxane) (Sylgard® 184 Dow Corning®) [156].

1.9 Connectivity

The filler/polymer design is critical in establishing the overall properties of the composite. The arrangement of the phases, named connectivity, can be tuned to gain the maximum

advantage from both the components and to improve the properties of the material [157]. There is a formal classification that defines all the current connectivities in a diphasic composite. According to Newnham's theory, for a composite with two phases, connectivity is defined by two numbers, of which the first represents the connectivity of the electromechanically active phase, whereas the second number characterizes the passive phase. Each number can range from 0 to 3, indicating the number of dimensions that are connected for the electroactive and for the passive phase [87,158]. For diphasic composites there are ten possible connectivity combinations: 0-0, 1-0, 2-0, 3-0, 1-1, 2-1, 3-1, 2-2, 3-2 and 3-3 (Figure 25) [158-160].

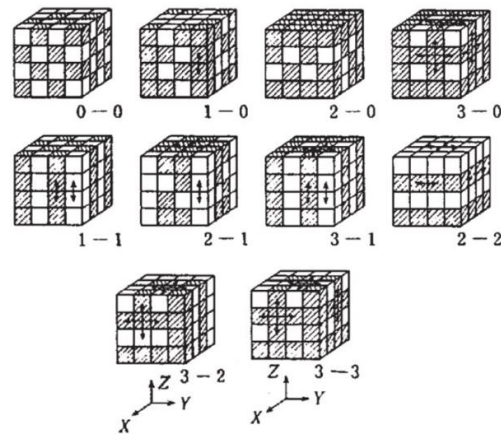


Figure 25 All the possible connectivity described by Newnham et al. for a diphasic composite [161].

Connectivity in piezoelectric composites influences electromechanical interaction between the phases and affects the distribution of the internal electric and mechanical fields. Additionally, it deeply affects the distribution of the electric field during the poling procedure. The most renowned structures for piezoelectric applications are “0-3”, where the particles are completely separated and surrounded by the polymer material, and “1-3”, where the active phase is in form of bars or columns aligned across a preferential direction. Since the connectivity dictates the composite properties, 0-3 and 1-3 structures exhibit different piezoelectric and mechanical behavior. The “1-3” connectivity outperforms the “0-3” one along the column axis. Another significant connectivity is the so-called “*quasi* 1-3”. In this design spherical or ellipsoidal fillers are aligned building columnar chain-like structures, but not in contact within the column, being separated by minor polymeric gaps. When compared to a 0-3 composite, *quasi* 1-3 connectivity shows higher dielectric and piezoelectric properties in the alignment direction; nonetheless, the composite is less performant than a fully 1-3 composite because the filler is not completely in contact within the columns. However, from a mechanical perspective, *quasi* 1-3 is more convenient; fully 1-3 may drastically enhance the stiffness of the material, whereas *quasi* 1-3 connectivity has a weaker effect over the mechanical properties of the composite. As a result, *quasi* 1-3 is a good compromise between improved piezoelectric properties and composite flexibility. The reason behind the improvement of dielectric and piezoelectric properties from 0-3 and to *quasi* 1-3 composites, is related to the displacement of the filler in pillars across the thickness: the particles are

tightly bunched along the thickness, and this induces an increase in the concentration of the filler along that direction (*i.e.*, higher density of dipoles), with consequent depletion of fillers in the others. The result is an anisotropic material with higher dielectric and piezoelectric properties along the alignment direction [160,162]. A schematic drawing of 0-3 and *quasi* 1-3 connectivity is reported in **Figure 26**.

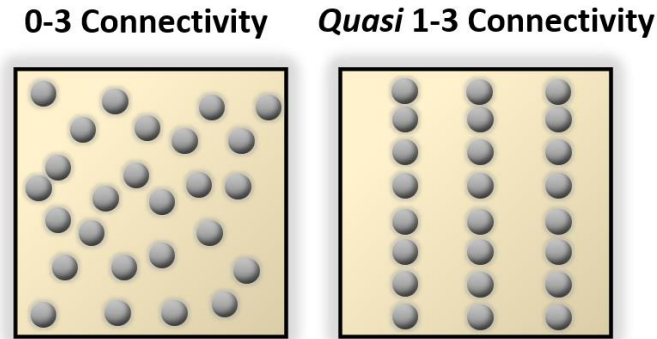


Figure 26 Schematic drawing of 0-3 and *quasi* 1-3 connectivity in 2D.

The enhancement in piezoelectric properties is also a consequence of the distribution of the electric field during the poling process, which is more efficient in *quasi* 1-3 composites rather than in 0-3 ones. Generally, for composites under poling field, the electric field distribution is non-homogenous in the two phases, due to the large difference in dielectric properties between the matrix and fillers, and it concentrates more effectively on the material with a lower dielectric constant, which is commonly the polymer. Clearly, the electric field distribution is not favorable in 0-3 connectivity, resulting in small electric field reaching the ceramic particles, due to the high matrix's shielding effect. After the removal of the electric field, the remnant polarization on the ceramic phase is lower than the one experienced by a bulk ferroelectric material poled in the same conditions, which leads to lower piezoelectric properties. To overcome the problem, high poling fields are required or alternatively high filler contents, which would result in increased filler connectivity [163]. However, firstly the electric field required could overcome the breakdown of the polymer, secondly a large concentration of filler would considerably worsen the mechanical properties [83]. On the other side, in *quasi* 1-3 connectivity, the filler is less masked by the matrix along the columnar direction, as less matrix surrounds it, resulting in a greater electric field inside the filler during the poling process than in 0-3 structures, thus, in better polarization and stronger piezoelectric activity. In other words, assuming that poling is parallel to the alignment direction, by applying the same poling field to the 0-3 and *quasi* 1-3 composites, the filler in the first configuration will receive a weaker electric field than the filler in the second configuration. Accordingly, to achieve similar piezoelectric performances, a lower electric field is required to polarize composite *quasi* 1-3 than composite 0-3, regardless of volume

content. To summarize, *quasi* 1-3 connectivity produces anisotropic composites with improved electrical impedance matching between particles and polymer matrix, resulting in exceptional piezoelectric and dielectric performance in the alignment direction, without compromising the composite's mechanical properties. Electrically conductive, thermally conductive, and magnetic composites may benefit from *quasi* 1-3 connectivity as well as piezoelectric characteristics do.

There are several physical models to describe the dielectric and piezoelectric activity of 0-3, 1-3 and *quasi* 1-3 connectivity. As for 0-3 connectivity, the simplest model for dielectric constants is the Maxwell-Garnett one, which considers the 0-3 composites as built with spheroidal particles in homogenous matrix (Eq.7). Bowen *et al.* experimentally proved the efficacy of this model [164]:

$$\varepsilon_{0-3 M-G} = 1 + \frac{3\varphi(\varepsilon_f - \varepsilon_m)/(2\varepsilon_m + \varepsilon_f)}{1 - \varphi \left(\frac{\varepsilon_f - \varepsilon_m}{2\varepsilon_m + \varepsilon_f} \right)} \quad (7)$$

Where φ is the particles volume fraction, ε_m is the dielectric constant of the polymer matrix in the poling direction, ε_f is the dielectric constant of the ceramic inclusions in the poling direction. Yamada *et al.* developed a more accurate model which describes ellipsoidal particles homogeneously dispersed in an isotropic matrix; the composite is considered to be mechanical and electrical loss free [165]; Van den Ende *et al.*, James *et al.* and Babu *et al.* studies confirmed the validity of the model [105,143,166]. Dielectric constant is modeled as follow:

$$\varepsilon_{0-3 Yamada} = \varepsilon_m \left\{ 1 + \frac{n\varphi(\varepsilon_f - \varepsilon_m)}{n\varepsilon_m + (\varepsilon_f - \varepsilon_m)(1 - \varphi)} \right\} \quad (8)$$

where n is the inverse of the depolarization factor, which is the electric field developed by a dielectric particle when subjected to an external field and changes in function of the ratio of the ellipsoidal axes of the particles; n should be 3 for perfect spherical particles. Like the dielectric coefficient, the piezoelectric charge coefficient may be physically predicted using models. Following the Yamada's model for d_{33} of the 0-3 composite with homogeneously dispersed ellipsoidal inclusions:

$$d_{33 Yamada} = \varphi \delta E_2 d_{33}^f \quad (9)$$

d_{33}^f is the piezoelectric charge coefficient for the ceramic inclusions, δ is the poling ratio of the ceramic inclusion and E_2 the local electric field coefficient in the poling direction acting on the particles:

$$E_2 = \frac{n * \varepsilon_{0-3 Yamada}}{n * \varepsilon_{0-3 Yamada} * (\varepsilon_f - \varepsilon_{0-3 Yamada})} \quad (10)$$

E_2 is function of the dielectric constant of the particles and the matrix. It is lower with respect to the applied electric field, and it is strongly dependent on the difference between the dielectric constants of the particles and the matrix. The piezoelectric voltage coefficient, g_{33} , is computed as [105]:

$$g_{33 \text{ Yamada}} = \frac{d_{33 \text{ Yamada}}}{\epsilon_{0-3 \text{ Yamada}} * \epsilon_0} \quad (11)$$

Where ϵ_0 is the vacuum permittivity, $8.85 * 10^{-12} \text{ C V}^{-1}\text{m}^{-1}$. There are several physical models that can be used to describe its dielectric and piezoelectric behavior of 1-3 connectivity composites. This connectivity is referred to structures as rods or bars inserted in a polymeric matrix. In these structures the piezoelectric phase is completely in contact within the direction of the column. The permittivity and the piezoelectric charge coefficient for those composites are usually described by the parallel mixing rule according to Eq.12 and Eq.13 [164,167]:

$$\epsilon_{1-3} = \epsilon_f \varphi + (1 - \varphi) \epsilon_m \quad (12)$$

$$d_{33 \text{ 1-3}} = \frac{(1-\varphi)d_{33}^m s_{33}^f + \varphi d_{33}^f s_{33}^m}{(1-\varphi)s_{33}^m + \varphi s_{33}^f} \quad (13)$$

Where s_{33}^m and s_{33}^f are the elastic compliances of polymer matrix and ceramic fillers for stresses normal to the electrodes. The dielectric and piezoelectric values reached by fully 1-3 composites are higher than those reachable by *quasi* 1-3 composites where particles are not in contact but among them there is a small portion of polymer matrix. The presence of the polymer particle interfaces disrupts the continuity of the filler phase causing a reduction of the permittivity of the composite. Bowen *et al.* developed a model to predict the dielectric behavior of *quasi* 1-3 structured composite. The particles within the columns are separated from each other by a small gap of the polymer. According to the model, the particles are squares and connected in series to the polymer within chains. Each chain is then connected in parallel within the outside neighboring polymeric area, which is depleted of filler (**Figure 27**) [105].

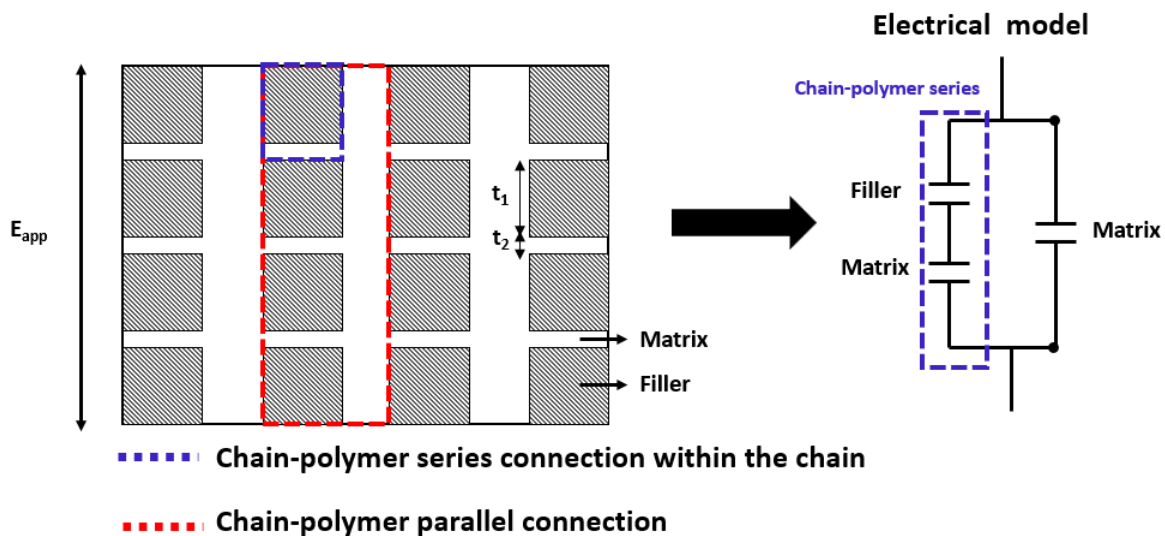


Figure 27 Figure displaying the electrical model proposed by Bowen *et al.* to describe the behavior of *quasi* 1-3 composites [164].

The dielectric properties of the overall composite can be computed using Eq.14

$$\varepsilon_{quasi\ 1-3} = \varphi \left(\frac{r \varepsilon_m \varepsilon_f}{\varepsilon_m + \varepsilon_f r} \right) + (1 - \varphi) \varepsilon_m \quad (14)$$

where r denotes the ratio between the average size of the particles (t_1 in **Figure 27**) and the interparticle distance (t_2 in **Figure 27**); interestingly, this ratio affects the fraction of electric field acting on the particle during the poling procedure. Following the model for permittivity, Van den Ende *et al.* modeled the piezoelectric properties of *quasi 1-3* composites considering electrical and mechanical behavior of the components. The particle-matrix within chains are equivalent to two capacitors in series (electrical domain) and two springs in series (mechanical domain) [105]. The piezoelectric charge coefficient of the structured composite is estimated as:

$$d_{33\ quasi\ 1-3}^f = \frac{(1+r)^2 * \varepsilon_f * \varphi * Y_{33}^f * d_{33}^f}{(\varepsilon_f + r \varepsilon_m) * [(1+r\varphi) * Y_{33}^f + (1-\varphi) * r Y_m]} \quad (15)$$

where d_{33}^f is the piezoelectric charge coefficient of the filler in 33 mode; Y_m and Y_{33}^f are the elastic moduli of the matrix and of the ceramic filler, respectively, in the chain direction. Clearly, *quasi 1-3* composites, due to the larger connectivity of the ceramic phase, feature improved piezoelectric properties in the direction of the alignment when compared to 0-3 ones [168]. In terms of manufacturing techniques, 0-3 composites are simple to develop, and both flexible and complex shapes can be easily obtained, as the procedure consists in mixing the uncured polymer with the filler until a homogeneous dispersion is obtained, casting, and then curing the blend. Fully 1-3 connectivity on the other hand requires specific and sophisticated procedures such as rod placement technique, dice-fill technique, ultrasonic cutting, injection molding, lost mold, laser machining, co-extrusion, tape lamination and fiber insertion methods to name a few [83]. Finally, *quasi 1-3* composites are produced via electric field assisted structuration. Such a technique, based on dielectrophoresis, consists of applying an external electric field before and during the polymerization, which will induce the structuration. However other techniques have been used to develop *quasi 1-3* connectivity, such as magnetic field structuring, as reported by Varga *et al.* and Farshad *et al.* [169,170]. The following paragraphs will be focused on explaining the process of dielectrophoresis and how is implemented to design *quasi 1-3* composites.

1.10 Dielectrophoresis (DEP) structuring

Dielectrophoresis is the most effective method for producing *quasi 1-3* structured piezoelectric composites. This technique is based on the dielectrophoretic effect: dielectric particles that are originally homogeneously dispersed in an uncured polymer are manipulated and redistributed using an AC electric field; upon electric field application they rearrange themselves into columnar structures. Because of the difference in dielectric permittivity between the medium and the particles, when an electric field is applied over the blend, it distributes non-homogeneously between the two phases. The electric field polarizes the particles, which then locally alter the electric field and interact with each other through

attractive and repulsive interactions based on their mutual location (dipole-dipole interaction), building a chain-like structure between the electrodes (**Figure 28**). Once the structure is assembled, the blend is cured under electric field, to secure the arrangement [105,160,162,171]. The main forces acting on the particles are the dipole-dipole interaction, the dielectrophoretic in inhomogeneous electric fields, the viscous drag force in the fluid, which resists particle motion, the gravitational force, which causes sedimentation of the polarized material and the Brownian force, which is related to the Brownian motion of particles suspended in a fluid. Frequency and amplitude of the electric field determine the quality of the structuration and must be investigated based on the filler/matrix combination. Additionally, the dimension and form factor of the fillers as well as dielectric permittivity of fillers and matrix will affect the dielectrophoretic process [172-174]. In the following paragraphs the analytical formulation of the procedure in a general condition will be illustrated.

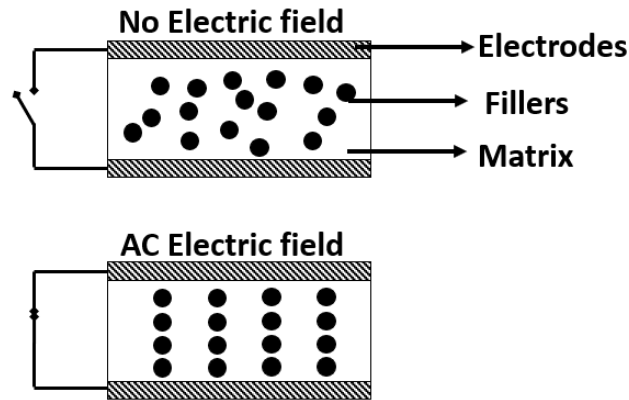


Figure 28 Schematic representation of the dielectrophoretic structuring. At zero applied field the particles are homogeneously dispersed. Under external AC electric field, dipole-dipole interactions occur, causing the orientation in columns[172].

1.11 Polarization of particles under non-homogeneous electric fields

To understand the dielectrophoretic structuring process, it is first necessary to explain what happens when an AC electric field is applied across an inhomogeneous system, that is, a system containing components with varying conducting and dielectric properties. Two cases must be distinguished: case 1) when the particles are less conductive than the nearby matrix, *i.e.*, their dielectric permittivity is higher, the electric field's lines will concentrate in the matrix; case 2) when the particles are more conductive than the surrounding polymer, the flux line will be deflected into them and avoid the matrix near to the particles. In this analysis we will consider dielectric particles and matrix in AC sinusoidal steady-state conditions. The matrix of piezoelectric composites usually exhibits lower dielectric permittivity (case 1). As a result, the field that surrounds the particles will cause charge separation on their surface. The charges are distributed as equal numbers of positive and negative on the opposite sides of the particle to form a dipole moment. The dipole moment is defined as [175]:

$$\mathbf{p}^* = 4\pi\epsilon'_m R^3 (CM) \mathbf{E}_0 \quad (16)$$

where R denotes the radius of the particle. The dipole (\mathbf{p}^*) is a function of the real dielectric permittivity of the matrix, ϵ'_m , and the sinusoidal applied electric field (\mathbf{E}_0). CM is the Clausius Mossotti factor and is defined according to Eq.17:

$$CM = \frac{\epsilon_f^* - \epsilon_m^*}{\epsilon_f^* + 2\epsilon_m^*} \quad (17)$$

ϵ_f^* and ϵ_m^* denote the complex dielectric permittivity of fillers and matrix computed as [176]:

$$\epsilon_f^* = \epsilon'_f - \epsilon''_f - i \frac{\sigma_f}{\omega} \quad (18)$$

$$\epsilon_m^* = \epsilon'_m - \epsilon''_m - i \frac{\sigma_m}{\omega} \quad (19)$$

With i imaginary vector ($i = \sqrt{-1}$), ω is the angular frequency of the applied electric field, ϵ'_f and ϵ'_m are real part of the dielectric permittivity of filler and matrix, ϵ''_f and ϵ''_m are the imaginary part of dielectric permittivity of filler and matrix, while σ_f and σ_m are the conductivity of the particles and the matrix, respectively. These equations are the most general complex dielectric permittivity expressions. Considering the definition of dipole moment as:

$$p = Qd \quad (20)$$

the charge Q on one side of a sphere of diameter d can be easily computed as:

$$Q = p/d \quad (21)$$

Ferroelectric particles in polymer uncured matrix under inhomogeneous electric field follow the model presented, and as results they are polarized under external electric field [173].

1.12 Dielectrophoresis model

Polarized particles in a medium under AC electric field are subjected to a rotational force and to a translational force. The rotational action, expressed by the dielectrophoretic torque, T_{DEP} , aligns the dipoles parallel to the electric field lines, and is present both in homogeneous and inhomogeneous electric fields. The translational dielectrophoretic force, F_{DEP} , is zero for homogeneous electric fields, and there is a net F_{DEP} only in inhomogeneous fields [160,172,173,177,178]. Considering the particle's dipole moment oriented at an angle θ with respect to the electric field, the particle experiences a time averaged torque expressed as follow [175]:

$$\langle T_{DEP}(t) \rangle = -4\pi\epsilon'_m R^3 \text{Im}(CM) |\mathbf{E}_0|^2 \quad (22)$$

Where ϵ'_m is the real part of the dielectric permittivity of the matrix, R is the radius, $\text{Im}(CM)$ is the imaginary part of the Clausius Mossotti factor (expressed in Eq.17) and $|\mathbf{E}_0|$ is the magnitude of applied electric field. The translational force averaged on time, F_{DEP} is computed as follow [172,173,175]:

$$\langle F_{DEP}(t) \rangle = 2\pi\epsilon'_m R^3 \text{Re}(CM) \nabla E_{0\text{RMS}}^2 \quad (23)$$

where $\text{Re}(CM)$ is the real part of the Clausius Mossotti factor and $E_{0\text{RMS}}$ is the root mean square magnitude of applied electric field. These formulae were reported by Sauer and Schlogl, taking into account the losses of the components. The dielectrophoretic force is function of the frequency of the applied electric field, which is contained in the CM factor. If the particles are more polarizable than the surrounding matrix, CM is positive, *i.e.*, the particles permittivity is greater than the one of the surrounding matrix, positive dielectrophoresis occurs, in which dielectrophoretic force is directed up a field gradient toward the electrodes. In the opposite case, CM is negative, the dielectrophoresis is negative, and the particles are directed down the field gradient, away from the electrodes [172,173];

In our case however the driving force related to the motion of the fillers is due to a dipole-dipole interaction of the polarized fillers. Indeed, when structuring a composite, the system subjected to an electric field has a high concentration of polarized particles. In a system with multiple particles embedded in a liquid matrix ($\epsilon_f > \epsilon_m$) and exposed to an electric field, polarized particles locally alter the electric field, inducing dipole-dipole interactions [177]. All the dipoles produced by the electric field distort the electric field that surrounds them and consequently exert a force to the adjacent particles. It is possible to describe this dipole-dipole interaction by using the following interaction potential model [160,177-180]:

$$U(s,\theta) = -\frac{\mu}{s^3} (3 \cos^2 \theta - 1), \quad s \geq 2R \quad (24)$$

$$\mu = \frac{(p)^2}{\epsilon'_m} \quad (25)$$

$U(s,\theta)$ is the internal potential related to particles interactions, s is the distance between two particles, θ is the orientation angle of the particles defined as the angle between the line connecting the centers of two particles in suspension and the applied electric field lines (defined in **Figure 30**) and p is the induced dipole moment. The potential is function of the applied electric field and of the Clausius Mossotti factor, thus of the difference between the dielectric properties of the particles and of the surrounding medium, and it is related to the interaction between particles caused by their polarization once an electric field is applied. Dielectrophoresis is always defined by the complex Clausius-Mossotti factor CM , which includes the conductivity σ , and the angular frequency ω , in circumstances when the particles or the surrounding medium is not a perfect dielectric, and being under AC electric field [171]. Increasing the applied electric field or using a filler material with high permittivity increases the attractive potential [173,177]. **Figure 29-a** shows the interaction potential vs. particles distance at different electric fields. Increasing electric field induces an increase in the critical distance below which the attraction occurs. Particles at larger separation feel the attraction. The reason why particles form chains along the electric field direction is related to the orientation angle. When θ goes from 0 to 55° the interaction is attractive and at 55° the interaction becomes repulsive. As displayed in **Figure 29-b** from θ greater than 55° an infinite barrier to agglomeration occurs [177].

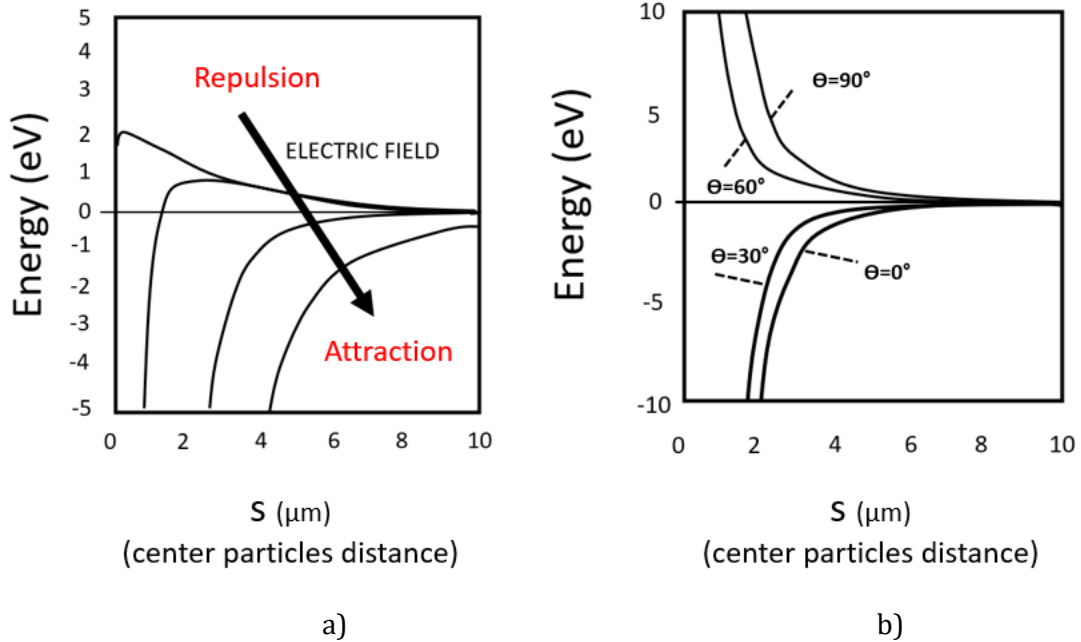


Figure 29 a) Effect of the electric field on the interaction potential vs. s , the center particles distance; b) effect of θ on the interaction potential [173,177].

Figure 30 is a schematic drawing of the interaction between two particles under inhomogeneous electric field, depending on their reciprocal position.

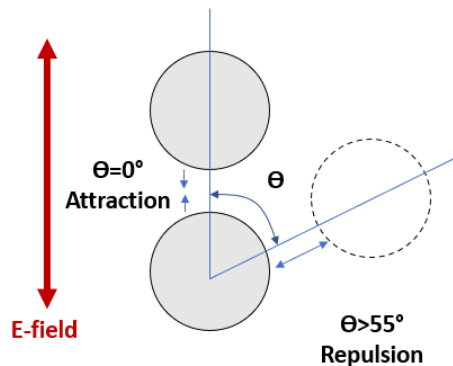


Figure 30 Interaction between two particles in function of θ [177].

Nevertheless, it is necessary to consider the sedimentation forces acting on the particles, caused by the gravitational force as well as the viscosity of the matrix and the randomizing Brownian force. According to Pethig *et al.* the Brownian force neglectable [173]. The viscosity force, on the other side, can affect the structuration; it is called drag force and is computed as following:

$$F_{drag} = 6\pi\eta Rv \quad (26)$$

Where η is the viscosity of the medium, R is the radius of the particle, v is the speed of the particle. An increase of viscosity causes a decrease of the speed of the particles and a delay in the alignment [105].

1.13 Parameters affecting the dielectrophoresis structuring

Different parameters affect dielectrophoresis structuring, among them it is possible to distinguish parameters related to the properties of the matrix and the particles and parameters related to the applied electric field [181]. For what concerns the medium and the fillers, as explained, their dielectric permittivity plays a determinant role; in order to have positive dielectrophoresis the matrix must have lower permittivity with respect to the filler; Moreover, to have a strong interaction between the fillers, the difference between permittivity of matrix and filler should be enhanced, as the CM strongly depends on the difference between them. A critical factor is the matrix's viscosity. The larger is the viscosity, stronger will be the opposition to the motion of the particles [105,160]. The matrix should also be insulating or slightly conductive and have a high break down strength to avoid electrical discharger during the application of the electric field, which would damage the polymer and the system [160]. These characteristics would cause polarization of the filler phase, allowing the dielectrophoretic chaining process to proceed [182]. As for the fillers, their size greatly affect structuration: bigger is their size, major are the interaction particles - electric field and particle-particle interactions [173,181]. This is in accordance with the Eq.24 where $U(\mathbf{s},\theta)$ strongly depend on R^3 . Also, the filler density should be taken in consideration, considering the sedimentation phenomenon that tends to occur during the process. The volume fraction and the form factor as well affect the structuration. At lower volume contents, particles would have more mobility in the medium, which means they can easily form columns; nevertheless, they would be wider apart, resulting in less interactions between them; With increasing volume content, there would be an appropriate percentage of filler that would enable good freedom of movement as well as interactions between the particles, however, if the filler volume content is too high, the structuring would be hampered owing to a lack of space. A larger form factor enhances the efficacy of structuration: fibers or ellipsoidal fillers are more favorable since they provide stronger connection along the structuring direction with reduced volume content.

The process parameters related to the electric field are its amplitude and frequency. Considering the interaction between the particles, a stronger electric field in terms of amplitude implies stronger interaction between the particles, as appears also from Eq.24. This has been confirmed by several studies [160,164,181]; The frequency has a great impact on the micro-structuring as well. An alternating electric field is applied instead of a direct electric field in order to avoid migration of the particles versus the electrodes: according to Randall *et al.* direct electric field applied to the suspension will induce both electrophoresis and dielectrophoresis [160,182]. Electrophoresis results in a migration of the filler to one of the electrodes. In order to nullify this effect, alternating fields can be used. Additionally, the

migration of ions towards the electrode would create a barrier reducing the electric field within the blend. Bowen *et al.* studied the dependence on the frequency using a modified Brookfield viscometer [164]. The attraction forces between the particles in function of the electric have been measured indirectly with this method: the stronger are the forces, the harder is to rotate the viscosimeter on the medium-particles system for different polymers. According to Bowen *et al.*, the optimal frequency for thermosettings, such as Polydimethylsiloxane, is in the range 1-10 Hz [164,174]. However, this value greatly depends on the dielectric properties of the matrix, as it is related to its losses. At low frequency the polymer matrix presents to high losses and mainly an ohmic behavior. Only approaching the unit of Hz, it is possible to reduce the losses and switch to a more capacitive behavior. For epoxies, on the other side, the optimal frequency values are much higher than for elastomers (~650Hz), due to their larger conductivity. At too high frequencies, on the other hand, the dipoles in the matrix may not be able to follow the electric field, thus affecting the DEP force [174,182].

2. Material and methods

In this section all the experimental procedures related to BT/PDMS and NN/PDMS composites 'production and characterization will be presented.

2.1 Materials

The polymer used is Sylgard® 184 silicone elastomer (PDMS) supplied by Dow Corning® made of two components: part A (monomers and oligomers) and part B (catalyst of the polymerization) at a ratio of 10:1. Its density is 1.03 g/cm³. The barium titanate nano-powder (BaTiO₃) used in this research is purchased from US Research Nanomaterials, Inc. The density of the powder is $\rho = 6.020$ g/cm³ with an average size of 569 nm computed with ImageJ® software on 40 particles (**Figure 31 a-b**). As visible in the SEM picture in **Figure 31-a**, the particles exhibit an average aspect ratio close to 1.

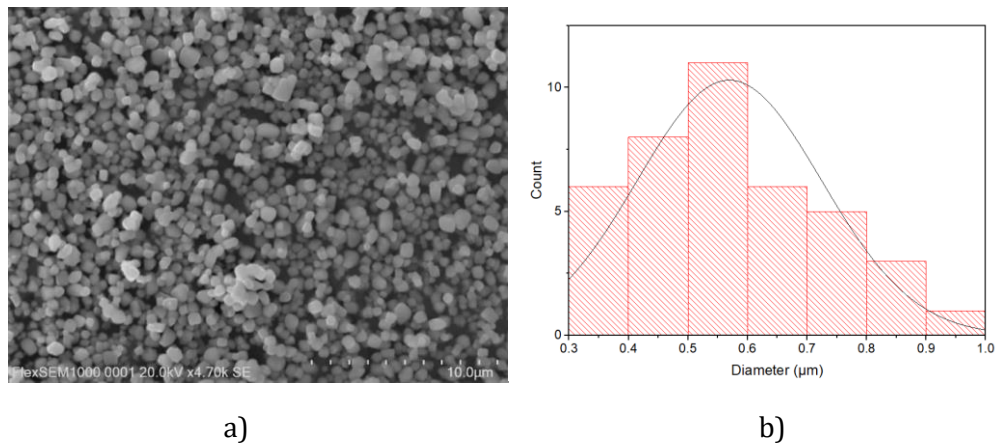


Figure 31 a) Scanning electron microscopy of the Barium Titanate filler used in this research; b) histogram of the distribution of the BaTiO₃ diameter, with an average size of 569 nm.

Sodium Niobate (NaNbO_3) micro-fibers and micro-particles were produced via hydrothermal synthesis using Sodium Hydroxide (NaOH) pellets, powder of Niobium(V) oxide (Nb_2O_5) and demineralized water. All the products were purchased from Sigma Aldrich®.

2.1.1 Polydimethylsiloxane (PDMS)

The application's requirements motivated the use of an elastomeric passive silicone as matrix (Poly-dimethyl siloxane) (Sylgard® 184 Dow Corning®). It is an excellent choice for human body insertable technology given to its high flexibility, chemical inertness, biocompatibility, and being already widely used in the biomedical field [156,183]. Every material introduced into the human body induces an inflammatory reaction as the immune system responds to an external synthetic surface; PDMS is considered one of the most biocompatible materials, causing just a brief inflammatory process in the organism, expanding its utility for biomedical long-term devices [184-187]. It also features structural biocompatibility, which means good and compatible mechanical interaction between the device and the surrounding tissue, due to its stretchability and low Young's modulus [156]. Additional advantages are its ease of manufacture and low cost [156]. In terms of chemical composition, PDMS is a silicone-based elastomer with a repeating unit ($-\text{O}-\text{Si}(\text{CH}_3)_2-$) (**Figure 32**) [188]. Johnston *et al.* studied the mechanical properties of Sylgard® 184 [183]. According to his work, this elastomer presents a low Young's modulus between 2.5 and 3 MPa, which may vary depending on the curing temperature, and a compression modulus of ~ 135 MPa [183]. The tensile Young's modulus linearly increases with the curing temperature, while the compressive modulus linearly decreases with it [183]. The poisson's ratio of the Sylgard® 184 is not available in literature but several studies suggest to consider its value from 0.45 to 5 [183]. The permittivity of the material at 100 kHz is 2.68, while the thermal conductivity is 0.27 W/m °K, the volume resistivity $2.9 \cdot 10^{14} \Omega \text{ cm}$ [189].

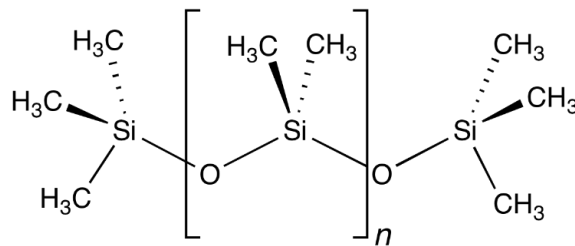


Figure 32 Silicone repeating unit.

2.1.2 Barium titanate

Barium titanate is a perovskite piezoelectric ceramic with a typical ABO_3 cell structure, studied extensively since the middle of the 20th century as promising material due to its excellent dielectric, ferroelectric and piezoelectric properties [90]. It is characterized by the following phase transitions: paraelectric cubic above the Curie temperature (120°C), ferroelectric tetragonal between 5°C and 120°C , orthorhombic between -90°C and 5°C and finally rhombohedral below -90°C (**Figure 33**) [90,91]. The more relevant phase transformation occurs below 120°C and leads to a ferroelectric phase: the replacement of the centrosymmetric cubic structure by a polar non-centrosymmetric one occurs when the cubic

cell elongates along an edge and becomes tetragonal. In this symmetry the titanium ions are displaced from the center, giving a net dipole moment. The elongated axis is called c axis, while the other two are equally named a axes. Lowering the temperature there are other two ferroelectric transitions [190]. The intrinsic polarization changes orientation at each transition, following the direction of elongation of the unit cell: from tetragonal to orthorhombic the cubic unit cell elongates along a face diagonal, while from orthorhombic to rhombohedral the cell gets elongated along a body diagonal (**Figure 33**) [191]. Piezoelectric, elastic and dielectric coefficients of poled BaTiO_3 are strongly temperature dependent. The most interesting values for this work are at ambient temperature, where the characteristic dielectric permittivity is 2000 and the piezoelectric charge coefficient in 33 direction is 180 pC N^{-1} ; the g_{33} is around 10 mV m N^{-1} [92]. An issue is the presence of multiple domains: when barium titanate cools down through the Curie point the cubic material becomes tetragonal elongating along one of the six possible axes, which in turn will become the polar tetragonal axis in the crystal. Consequently, different domains develop in the material during the cooling down, each one with a different polarization direction, depending along which axis the structure elongated. The direction in each domain depends on the stresses created at the Curie point, physical defects, and uncompensated surface charges. Consequently, the total dipole of a bulk BaTiO_3 is zero because all the domains annihilate each other [192]. By poling, all the dipoles in the domains will be aligned parallel to the electric field lines, conferring piezoelectric activity. Before the poling process, the ceramic is essentially isotropic and not piezoelectric. After the poling process, it becomes strongly piezoelectric, with an apparent anisotropy related to the axis of polarization [90-92,193]. Barium titanate, as explained in section, is lead-free, thus it is suitable for sensors for medical applications.

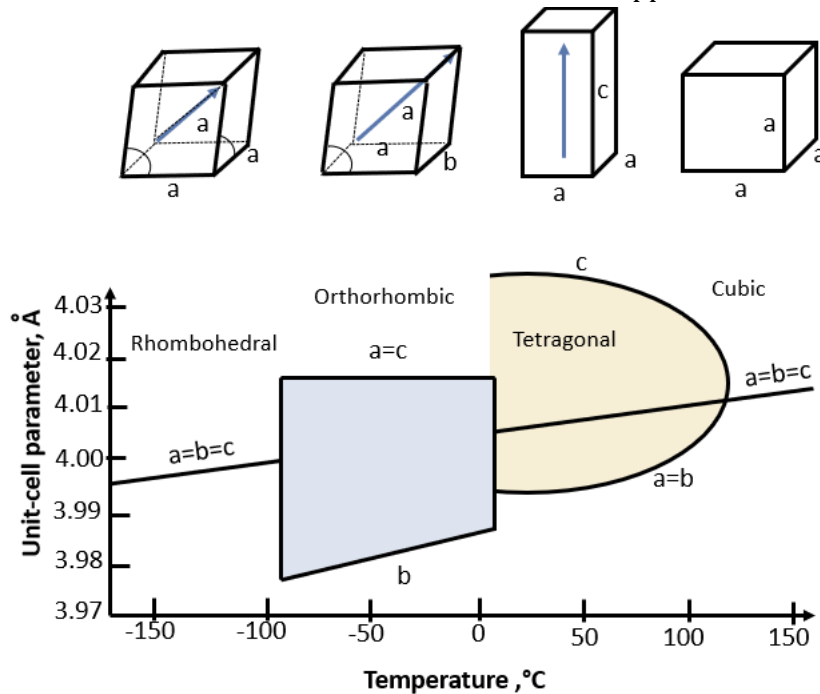


Figure 33 Crystalline unit cells at different temperature for BaTiO_3 and variation of the cube root of the volume of the cell with temperature for various phases of BaTiO_3 [191].

2.1.3 Sodium niobate

Sodium niobate, NaNbO_3 , is an antiferroelectric ceramic at ambient temperature with an orthorhombic $Pbcm$ crystalline structure, that can be tuned into metastable ferroelectric phase when suitably polarized. **Figure 34-a** represents the cell crystalline structure visualized using the software VESTA®. It has gained a considerable attention as electroactive material because of its piezoelectric and dielectric characteristics together with non-toxicity, which make it more interesting with respect to the lead based FE and AFE [129,194]. It experiences a great number of crystallographic transformations related to temperature variation. **Figure 34-b** depicts all the crystalline phase transitions it undergoes from -100°C to 640°C . The transition that occurs at 360°C and leads to a transition from paraelectric to orthorhombic antiferroelectric with space group $Pbcm$ is of particular interest [129]. This structure being antiferroelectric does not present net dipole [128]. However, by properly poling is possible to induce a further transition from AFE $Pbcm$ space group P phase, to $P2_1$ ma space group Q FE phase. This transition is irreversible and associated to a single hysteresis loop, and no double hysteresis loops have ever been reported for NaNbO_3 poling at any temperature [128,129]. The electric field causes FE domains to develop, which quickly align in parallel with the electric field lines. As a result, a non-centrosymmetric structure with piezoelectricity emerges. The poling field found suitable to induce AFE to FE phase transition is reported around $12 \text{ V } \mu\text{m}^{-1}$ [128]. According to the literature, the relative permittivity before poling (in AFE) is 200, while after poling it decreases to 132. Furthermore, the material develops a piezoelectric activity with a d_{33} of 30 to 35 pC N^{-1} [128,131,139,195]. The g_{33} of the poled material is $\sim 30 \text{ mV m N}^{-1}$.

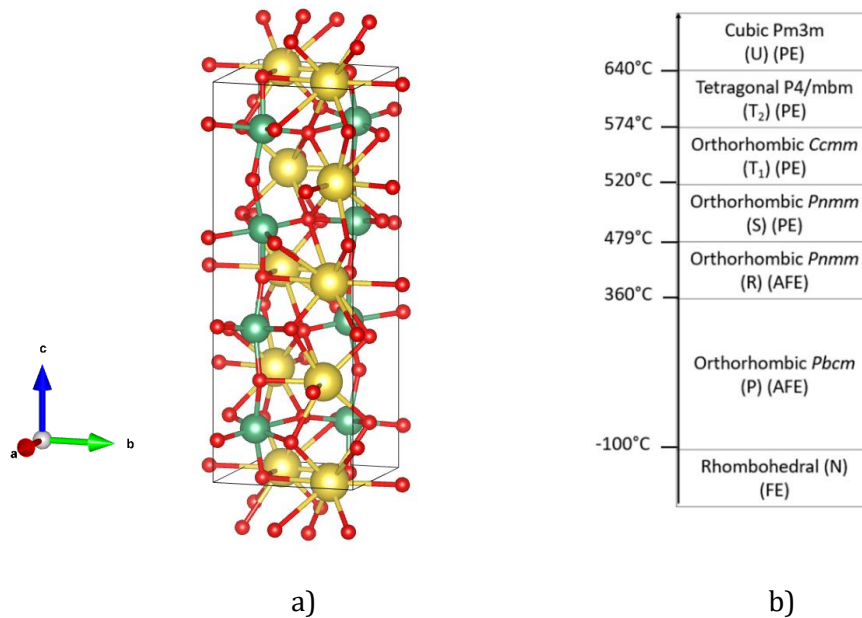
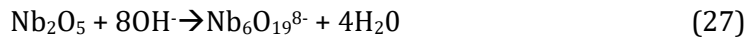


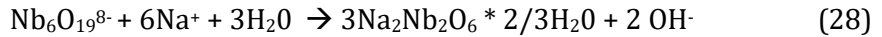
Figure 34 a) Orthorhombic $Pbcm$ NaNbO_3 visualized with Vesta®. b) Crystallographic phases of NaNbO_3 depending on the Temperature ($^\circ\text{C}$).

2.1.4 Hydrothermal synthesis of NaNbO_3

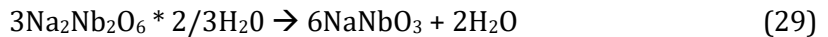
Both MF and MP fillers were hydrothermally synthesized starting from pellet of NaOH, powder of Nb_2O_5 and demineralized water using an autoclave Parr® with a total volume of 160mL, equipped with temperature and pressure control. This method was selected as it allows for a rapid and low-impact production of fillers in various morphologies. The approach is based on the work of Zhu *et al.*, but it has been improved to optimize time and temperature using an internal temperature control of the reaction [196]. Following are all the chemical and morphological transformations that occur during the reaction. The synthesis reaction mainly concerns Nb_2O_5 and OH^- . The highly concentrated NaOH solution causes corner-sharing rupture of the niobium-oxygen polyhedron (decahedra and octahedra) in the Nb_2O_5 reagent, producing intermediates with edge-sharing octahedra and shortening the distance between Nb and O. The crystallinity of these intermediates is reduced and they are considered highly metastable with low crystallinity. Following the reaction that describes this first step:



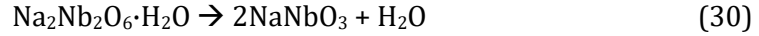
The compounds are $\text{Nb}_6\text{O}_{19}^{8-}$, or similar species with edge-sharing NbO_6 octahedra. From the poor crystalline compounds crystallized fibers of $\text{Na}_2\text{Nb}_2\text{O}_6$ grows as they are thermodynamically more stable:



If the reaction is prolonged, fibers transform in highly stable NaNbO_3 cubes:



All the crystalline and phase changes were well described by Zhu *et al.* [196]. To produce 2 g of fibers, 31.9 g of NaOH were added to 64.9 g of demineralized water (concentration of 10M). After 5 minutes of mechanical mixing, 2 g of Nb_2O_5 were added into the solution. The whole mixture was transferred to the autoclave where a PTFE (100 mL) container was previously inserted to protect the device. Once the autoclave was closed, the magnetic stirring was launched during the heating ramp where the temperature increased from 55°C (temperature of the exothermic reaction occurring between NaOH and water) up to 160°C in 35 minutes. As soon as the temperature reached 160°C, the stirring was ceased, and the solution was kept at 160°C for 45 minutes. The autoclave was then immersed in cold water to induce a fast cooling. The precipitate obtained from the reaction was the intermediate fiber shaped compound mentioned above which needed to be diluted in a 2L demineralized water to remove residual sodium hydroxide and to neutralize the pH. The final solution was filtered through a vacuum system to isolate the fibers from the liquid. All the steps are displayed in **Figure 35 a-i**. The fibers were then placed in an alumina crucible and annealed at 600°C for 4 hours to develop NaNbO_3 micro-fibers (MF), with orthorhombic crystalline structure and *Pbcm* space group with a perovskite-like structure [197,198]:



The same procedure was applied to fabricate NaNbO_3 micro-particles (MP), however, after the heating ramp, the solution was left at 160°C for 15 hours. Once the solution was cooled, vacuum washing and filtration were performed. Finally, the fillers were annealed for 4 hours at 600°C in an alumina crucible to obtain NaNbO_3 perovskite MP.

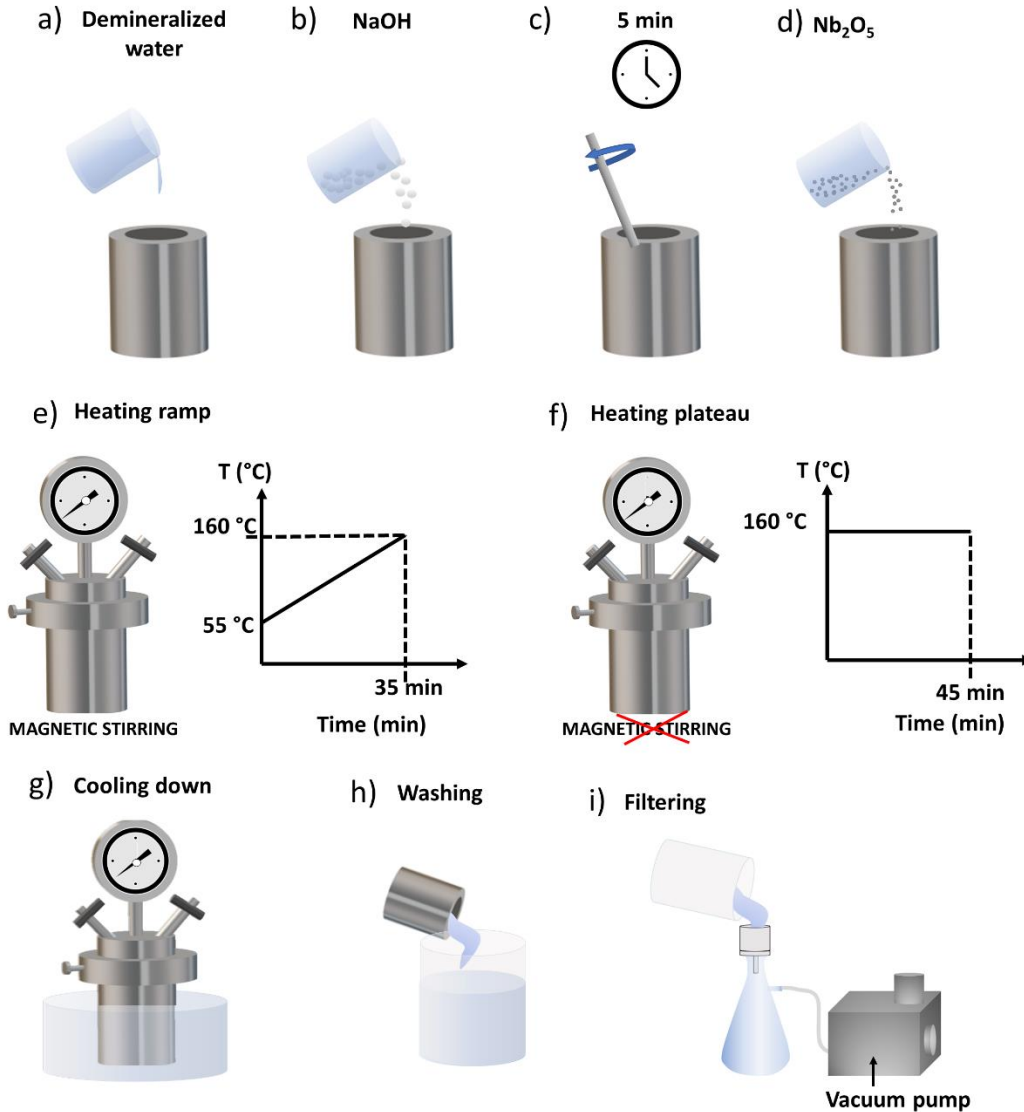


Figure 35 a)-i) All the steps for hydrothermal synthesis of fibers of Sodium Niobate.

2.2 Fabrication procedure

2.2.1 BT/PDMS piezocomposites

The BaTiO_3 powder was poured into the PDMS base (Part A) and dispersed by ultrasonic stirring (Hielscher Ultrasound Technology, UP400S) for 10 min in a ventilated table (class II ADS air laminar sterile dust collector PPS). Then, the cross-linker (Part B) was added into the

blend, which was then mechanically mixed to form a homogenous mixture. The slurry was subjected to vacuum at 25°C for 30 min in a Memmert Vacuum oven. The mix was poured in a die consisting of a Mylar sheet (300 μm thickness) with a $4 \times 4 \text{ cm}^2$ surface cut-out positioned on a metallic plate (**Figure 36**). Subsequently, a second evacuation was carried out for 10 minutes (**Figure 37 a-f**), following a metallic mass was positioned above the blend with a weight load (4kg), added to ensure the thickness. To prepare the 0-3 samples, the composite was cured for 3 h at 100°C (**Figure 37-g**).

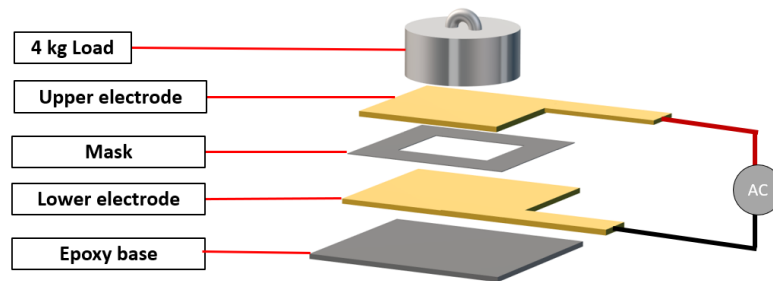


Figure 36 Setup designed to fabricate the composites.

The 1-3 chain-like structure was built by applying a high voltage across the blend before and during the curing process. For this, the upper metallic mass and the bottom metallic plate were connected to a voltage amplifier (Ampli HT TREK Tech 20/20) coupled to a sinusoidal wave generator (Agilent 33220A), which delivered an AC electric field with adjustable amplitude and frequency. Electric field amplitude and frequency were $3 \text{ V } \mu\text{m}^{-1}$ and 1 Hz, respectively, selected after performing in-situ microscopy of the process. The mold was placed in an oven (VOTSCH VT 7004) at room temperature (25°C) for 15 min; then the temperature was increased to 100°C for 3 h (**Figure 37-h**).

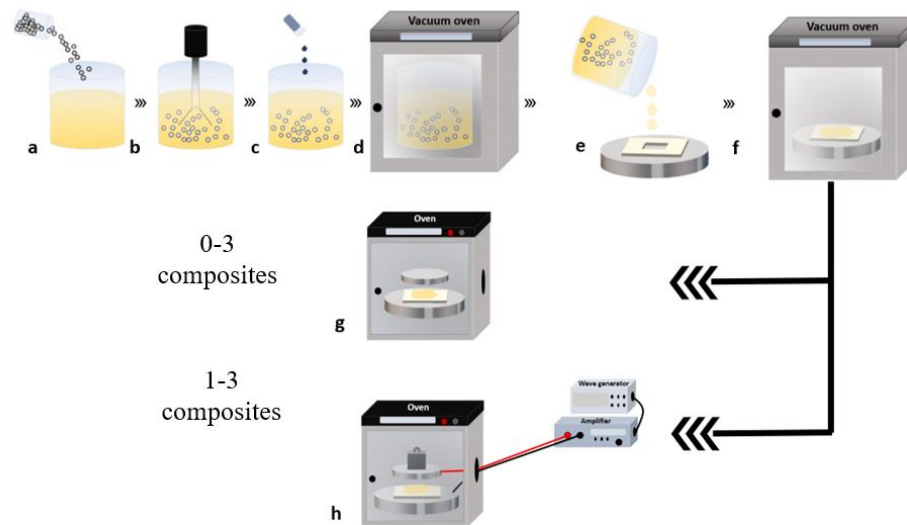


Figure 37 a)-h) Step by step procedure followed to produce 0-3 and quasi 1-3 composites.

The metallic plates operated as electrodes conveying the electric field through the sample, which directed the filler in pillars along its lines. For both 0-3 and *quasi* 1-3 configurations, samples were elaborated with different volume contents comprising 2.4%v, 12%v, and 24%v. For each sample type (volume content and connectivity), 5 samples were manufactured.

2.2.2 NN/PDMS composites fabrication

MF composites (NN_MF/PDMS) were elaborated with different filler volume fractions of 1%v, 3%v and 5%v while MP composites (NN_MP/PDMS) with a filler volume content of 5%v for comparative purposes. The samples were produced under a hood by the following process: PDMS base was mixed with the filler, both mechanically and by ultrasound stirring for 10 minutes. Then, the curing agent was added at a ratio of 1:10 to the PDMS base and mixed vigorously. The blend was vacuumed for 30 minutes to remove any air bubbles that may have got trapped after mixing. Subsequently, it was poured into the same mold designed for BT/PDMS composites (**Figure 36**). A further 10 minutes of evacuation were carried out and then a 4 kg metal load, acting as the upper electrode, was placed on the top of the blend to ensure homogenous thickness. To develop composites with *quasi* 1-3 connectivity, the mold was placed in an oven, initially at 25°C. The two electrodes were connected to a voltage amplifier coupled to a wave generator, which transmitted an alternating (AC) sinusoidal voltage to the system. The NN_MF/PDMS composites were structured by AC electric fields with a 1Hz frequency and 4 or 6 V μm^{-1} amplitude for 15 minutes at room temperature. Subsequently, the electric field was reduced to 2 V μm^{-1} and the temperature was increased to 140°C and maintained for 2 hours. As the electric field selected in the preparation of these composites is higher than the one used to produce BT/PDMS there was the need to reduce it when heating, to reduce the risk of arcs and breakdown, however this reduction did not affect the properties of the composites as it was enough to keep the columns built before heating. The same procedure was followed for 1-3 NN_MP/PDMS which was structured with AC electric field of 1 Hz and 6 V μm^{-1} . To produce the 0-3 composites, the blend was poured in the same mold described above and the whole was transferred to an oven where the mixture would cure at 140°C for 2 hours without any applied electric field.

2.3 Method of Characterization

In these sections, we will discuss the methodologies used to characterize the piezocomposites.

2.3.1 DEP process analysis

Before the fabrication of the BT/PDMS samples (presented in subsection 2.2.1), dielectrophoresis process was investigated, with the aim of identifying the best parameters to optimize the performance of the structured composites. This study was performed only for BaTiO₃-based composites. It is focused on the influence of electric field frequency and amplitude on the structuring. A slurry with low filler volume content (1.2%v) was studied using the set up shown in **Figure 38 a-b**. The composite was placed on a glass plate between two parallel conductive tape stripes, which acted as electrodes, being connected to an amplifier coupled to a sinusoidal wave generator (**Figure 38-b**). A light was positioned below the glass, above which was placed a USB camera digital microscope. First different amplitudes

were analyzed (1, 2 and 3 V μm^{-1}) at 1 Hz, and then, once selected the best one, different frequencies were tested (1, 100, 1000 Hz). The camera recorded 10 min of the process for each combination of frequency and amplitude. At the end of the recording time, a frame was taken to be able to qualitatively compare the processes. The test were performed at room temperature.

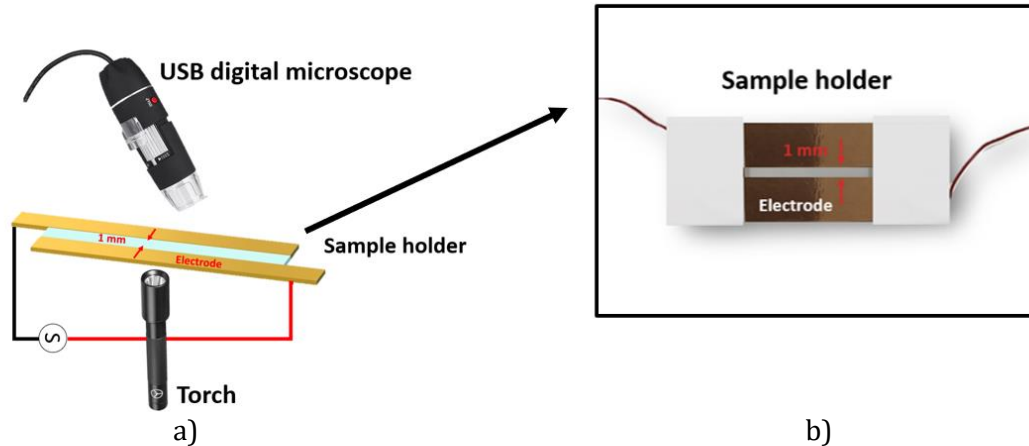


Figure 38 a) Set up developed to perform in-process microscopy; b) detail of the sample holder where the blend was placed during the observation.

2.3.2 Optical Microscopy

1-3 BT/PDMS composite with 2,4%v was examined in transmission optical microscopy (Olympus BH). Optical microscopy analysis of 0-3 BT/PDMS composite with 2,4% is not reported since the phase distribution was not observable in transmission mode.

2.3.3 Scanning Electron microscopy (SEM) characterization

The shape of the fillers (BaTiO_3 and NaNbO_3 fibers and particles) as well as the internal structure of composites (BT/PDMS, NN_MF/PDMS and NN_MP/PDMS) were examined via scanning electron microscopy (SEM). SEM imaging is a non-destructive characterization test that enables visualization of the topography of materials' surface, as well as chemical composition. This method is based on the interaction of a focused beam of high-energy electrons with the surface of a sample, which results in the generation of a signal from the material. The sample signal can be attributed to the secondary electrons (SE), which enable to visualize the topography of the surface, or the back scattered electron (BSE), whereas the chemical composition and distribution of phases can be visualized. First, the fillers used in the process were visualized via SEM (FlexSEM 1000II) in SE mode. The fillers were mixed with ethanol and a drop of the solution was placed on a carbon black tape previously stuck on the microscopy sample holder. Then, the cross section of the samples was imaged to assess the effect of DEP structuration in BSE mode. The cross section of the samples was cut with a precision cutter and glued on the carbon black tape. For BT/PDMS, the study was carried out on 0-3 and *quasi* 1-3 connectivity at content of 2.4%v. At such a low volume content the difference in disposition of the phases is easy to observe. For NN_MF and NN_MP/PDMS in 0-3 and 1-3 connectivity all the volume contents prepared were imaged. All the images were taken with a voltage of 15 and 20 kV in back scattered electron setting. Prior to SEM

observation all the samples (powder and composites) were sputtered with gold (30s 20mA) to avoid charge accumulation during the measurement. The pressure during the measurement was either in low vacuum mode (30 Pa) or high vacuum mode.

2.3.4 Dielectric spectroscopy

Broadband dielectric spectroscopy (BDS) was used to characterize the dielectric properties of the 0-3 and 1-3 composites (BT/PDMS, NN_MF/PDMS and NN_MP/PDMS) at all the volume fractions produced, as well as for pure PDMS. The tests were performed at room temperature with a AC voltage of 0.1V. The goal was to determine the effect of structuration on the dielectric properties of the material. BDS is usually used to determine the real and imaginary components of a material's complex relative dielectric permittivity when exposed to an alternating current electric field across a large frequency range. The primary focus was on the real component of relative permittivity, which is connected to material polarization in reaction to an electric field, and the loss tangent, ratio of the imaginary part over the real part, indicating the losses in the material in terms of ion conductivity and interfacial space charge relaxation. The test was carried out with a Solartron spectrometer (1296A Dielectric Interface System) before the poling procedure. The poling influences the dielectric properties of the material, as the orientation of all the dipoles is the same, generating a sort of anisotropy related to the direction of poling. The measurement was performed over a range of frequency from 0.1 to 10^6 Hz. Then, the real part of the relative permittivity at 1 kHz was reported in function of volume fraction and connectivity. The results were compared with the theoretical model presented in subsection 1.9.

2.3.5 Poling procedure and piezoelectric characterization

Gold electrodes were sputtered on all the samples using Crossington sputter coater (model 208 HR). The samples were then poled to orient the internal dipoles of the fillers. To trigger the piezoelectric behavior, all 0-3 and *quasi* 1-3 BT/PDMS composites were poled at 80°C for 30 min under a DC electric field of $25 \text{ V } \mu\text{m}^{-1}$ amplitude. Next, the samples were cooled under an electric field to ensure the remnant polarization. The procedure was executed in a silicone oil bath to prevent voltage breakdown and to optimize the isotherm quality (**Figure 39**) [162,199]. The initial high temperature was required to permit movement of the domain wall within the piezoelectric phase [139,162,199,200]. Finally, the samples were short circuited, before measuring their d_{33} . For NaNbO_3 -based composites, the poling was carried out at 110°C for 30 minutes under a DC electric field of 10, 20 and $30 \text{ V } \mu\text{m}^{-1}$ in silicone oil bath. This is the maximum value that could be reached in order to prevent any electrical breakdown inside the polymer matrix. Once again, the samples were cooled under an electric field to ensure the remnant polarization. Higher temperature was maintained during the poling as the Curie temperature of NaNbO_3 is much higher than the one of BaTiO_3 . If the poling is conducted at temperatures too close to T_c , the sample may turn to its paraelectric phase. After poling, all the samples were short circuited to eliminate the surface charges accumulated during the process.

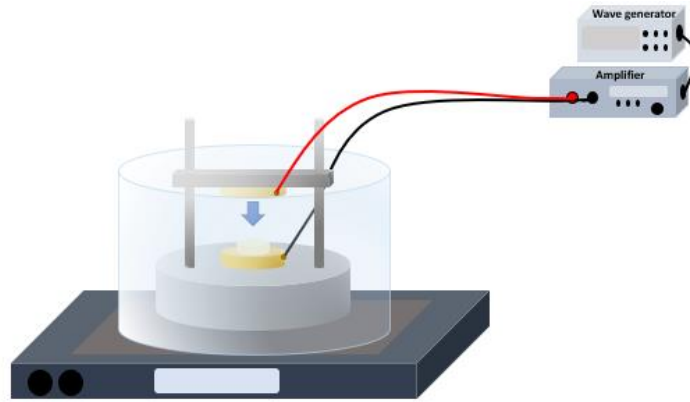


Figure 39 Set up used to pole the composites.

After poling and annealing, the piezoelectric charge coefficient was measured using an APC YE2730 d_{33} meter. This technique is based on the *Berlincourt* method which is a way to assess the direct piezoelectric coefficient in the 33 directions, *i.e.*, the piezoelectric charge coefficient, d_{33} . Such a characterization is based on the measurement of the charge developed per unit of area, per unit of applied stress. Usually, the measured area corresponds to the solicited one, meaning d_{33} is computed as the charge developed divided by the applied force. The force applied by the measurement device is 0.25N at 110Hz. d_{33} was then plotted as function of the volume content and connectivity for all the composites developed. To reduce uncertainty, ten measurements were carried out for each sample. The values for BT/PDMS were then compared to those estimated from the theoretical model (Eq.9 and Eq.15). All the results were compared with the FE estimations made via COMSOL® modelling.

2.3.6 Thermal stability of the piezoelectric response

To confirm the piezoelectric stability in temperature of the BT/PDMS samples, a study on the temperature effect over the d_{33} was conducted. Only 0-3 and *quasi* 1-3 composites with a volume content of 24%_v were tested. The samples were polarized according to the procedure explained in subsection 2.3.5, and annealed for 10 min in a short circuit at various temperatures of 25, 50, 100, 150, and 200°C. After each annealing step, the samples were cooled down at T_{room} , and their d_{33} coefficient was measured by an APC YE2730 d_{33} meter.

2.3.7 X-ray diffraction

Morphological analysis of the BT/PDMS composites at different temperatures of 25, 100, 130, and 150°C, via X-Ray diffraction (XRD) performed using Philips X'Pert MRP diffractometer. The XRD measurements were taken in continuous mode, over a range of 20–90° angles, with carbon filtered CuK α (1.5406 Å) source. To calibrate the temperature of the diffractometer (T°), the following equation was used [201]:

$$T^\circ = 1.0582 T_{REAL} + 1.3086 \quad (31)$$

where T_{REAL} is the desired temperature that was set in the XRD program.

As for NaNbO₃-based composites, after annealing, fibers and particles were characterized using the same diffractometer at ambient temperature to assess the crystalline structure.

Once again, the measurements were carried out in continuous mode, over a range of 20–90° angles.

2.3.8 Dynamic mechanical Analysis (DMA)

Dynamic mechanical analysis in tensile mode was performed at ambient temperature using Q800 DMA (T.A. instruments). All the structured and non-structured composites at all the filler contents and pure PDMS were tested to assess the effect of fillers' type, content, and connectivity over the stretchability. For *quasi* 1-3 composites the strain was transversal with respect to the structuring direction (**Figure 40**). This measurement allowed to study the storage and dissipation moduli from which the Young's modulus could be evaluated. The test was performed in tensile mode, at ambient temperature over a range of frequencies (1, 25 and 50 Hz). The applied strain was 0.5%. The samples' dimension was 7x1 mm² with a thickness of 300µm ± 50 µm. For each sample type at least 5 different measurements were repeated. Then, Young's modulus (*Y*) at 1 Hz was computed. Pure PDMS was also tested, but only at 1 and 25 Hz since the equipment could not read the mechanical behavior of the polymer at 50 Hz.

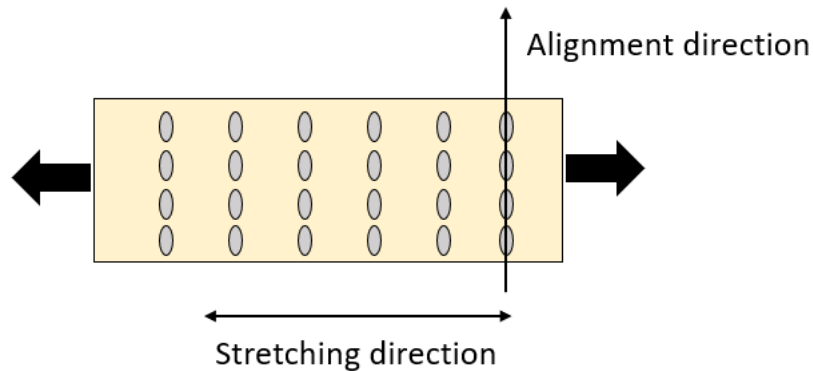


Figure 40 Schematic drawing representing the direction of stretching during the DMA test with respect to the alignment direction for 1-3 composites.

2.3.9 Differential Scanning Calorimetry (DSC)

Differential Scanning Calorimetry (SETERAM DSC131 evo) was used to investigate the influence of filler concentration and connectivity on the polymer chain configuration. The test was carried out on all the samples prepared of BT/PDMS, on 5%v NN_MF/PDMS and NN_MP/PDMS and on pure PDMS over a temperature range of -150°C to 15°C with a heating rate of 10°C/min. The samples were placed in a 100 mL aluminum crucible, in turn inserted in the test chamber under N₂ atmosphere. An outer chamber was placed around it and filled with liquid nitrogen to reach low temperature. First a cooling down from 25°C to -150°C at a rate of -3°C/min was promoted. A low rate was necessary to allow the sample time to reach -150°C. Then, following a plateau of 20 minutes at -150°C to stabilize the temperature of the sample, the heating ramp was started from -150°C to 15°C at 10 °C/min. Only the second (heating) ramp is relevant to the DSC results that are reported. The cycle can be summarized in **Figure 41**. The test was carried out on all BT/PDMS samples as well as NN_MF/PDMS at 5%v and NN_MP/PDMS. All the data were normalized over the mass of the polymer, computed knowing the mass of the sample and the mass fraction.

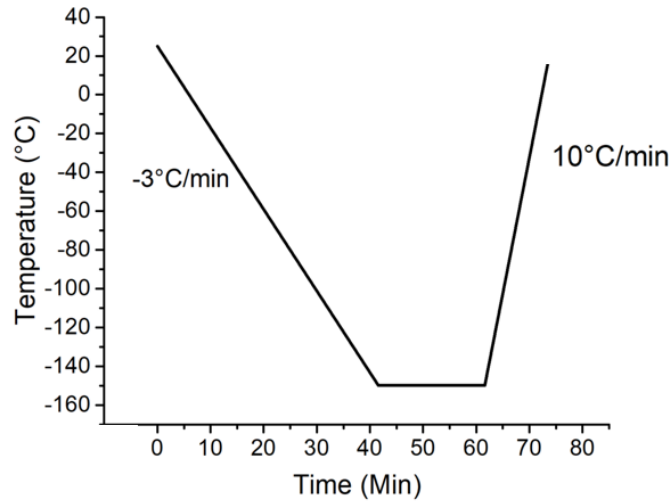


Figure 41 Thermal cycle for DSC measurements of PDMS, BaTiO₃-based and NaNbO₃-based composites.

2.3.10 Broadband dielectric spectroscopy in temperature

Broadband Dielectric spectroscopy in temperature was performed between -140°C and 0°C, from 100 mHz to 1MHz. The sample under test were pure PDMS , 0-3 BT/PDMS with 24%v and 1-3 BT/PDMS with 24%v. The test was performed using the Broadband dielectric/impedance spectrometer Novocontrol® Alpha-A high performance frequency analyzer equipped with a temperature control (Quatro) and Vacuum system. The data were collected using the data acquisition software DETACHEM®. Liquid Nitrogen was used to cool down the samples. A broadband spectroscopy in the frequency range reported above was measured each 3°C starting from -140°C until 0°C. The samples were sputtered with gold (circular surface diameter 8mm) prior to start the test. This analysis allowed us to understand the mobility of the polymer chains in absence of filler and when 24%v of filler is added in 0-3 and 1-3 connectivity. The results (Tanδ vs. Temperature at different frequencies) allowed to assess the relaxation occurring in the polymer related to glass transition (α and α') and to confirm the results obtained via DSC. Real permittivity vs. Temperature analyzed in the frequency range reported allowed to assess the glass transition temperature range, and its effect of the permittivity.

RESEARCH ARTICLE

Structuring BaTiO₃ /PDMS Nanocomposite via Dielectrophoresis for Fractional Flow Reserve Measurement

Giulia D'Ambrogio, Omar Zahhaf, Marine Bordet, Minh Quyen Le, Nellie Della Schiava, Richard Liang, Pierre-Jean Cottinet,* and Jean-Fabien Capsal

This work focuses on the development of piezoelectric sensors for the fractional flow reserve (FFR) technique, a procedure based on the measurement of blood pressure within a vessel to evaluate the severity of coronary stenosis. Considering the medical application, biocompatibility is a mandatory requirement that justifies the selection of fillers and matrix. Two composites made of lead-free barium titanate nanoparticles (BaTiO₃) incorporated in polydimethylsiloxane (PDMS) elastomer are developed: the first composite with particles randomly dispersed and the second one with particles aligned along one direction, via an innovative technique known as dielectrophoresis. The experimental characterization indicates that the electroactive and dielectric properties are coherent with the models' prediction, confirming that the alignment of the filler gives rise to considerably enhanced dielectric and piezoelectric properties relative to the random dispersion. Thermal stability together with X-ray diffraction is conducted, demonstrating superior piezoelectric response of the structured sample under high-temperature conditions. FFR application is then simulated by applying an arterial pulse-shape stimulus on the developed sensor, which is finally integrated into a catheter and directly inserted in a simulation arm.

1. Introduction


Cardiovascular disease is a major cause of death. Among them, coronary stenosis (the narrowing of the artery due to atherosclerosis) is particularly frequent.^[1] In the event of worsening, such

G. D'Ambrogio, O. Zahhaf, M. Bordet, M. Q. Le, N. Della Schiava, P.-J. Cottinet, J.-F. Capsal
 INSA-Lyon

LGEF
 University of Lyon
 EA682, F-69621 Villeurbanne, France
 E-mail: pierre-jean.cottinet@insa-lyon.fr

M. Bordet, N. Della Schiava
 Department of vascular and endovascular surgery
 Grouperment Hospitalier Edouard Herriot
 69003 Lyon, France

R. Liang
 High-Performance Materials Institute (HPMI)
 Florida State University
 Tallahassee, FL 32310, USA

 The ORCID identification number(s) for the author(s) of this article can be found under <https://doi.org/10.1002/adem.202100341>.

DOI: 10.1002/adem.202100341

Adv. Eng. Mater. 2021, 23, 2100341

2100341 (1 of 13)

© 2021 Wiley-VCH GmbH

constriction can lead to complete occlusion of the artery and thus to a heart attack. The clinical relevance of coronary stenoses of mild intensity can be difficult to evaluate.^[2] Fractional flow reserve (FFR) is a new technique developed to evaluate the significance of artery narrowing. It is based on the measurement of the FFR index, which is defined as the maximum myocardial blood flow in the presence of stenosis divided by the theoretical maximum flow in the absence of the stenosis (Equation (1)). The blood flow is evaluated by a pressure drop. Thus, a pressure sensor integrated into the catheter can be used to calculate the ratio between the coronary pressure in the presence of the stenosis and the normal coronary pressure (Figure 1).^[3–5]

$$FFR = \frac{P_d}{P_a} \quad (1)$$

where P_d is the distal coronary pressure and P_a the proximal coronary pressure.^[2]

The existing pressure sensor used in FFR measurements is of three different types: optical, capacitive, and piezoresistive.^[6] All of these show some limitations. An optical sensor is advantageous due to its small size and ability to withstand environmental effects and is extremely sensitive to the bending of the fibers. Indeed, imposing stiffness to the catheter provokes limitation in the case of tortuous vessels.^[4,5] Capacitive sensors, characterized by easy and cheap processability, high sensibility, and lower power consumption, require complex readout circuitry.^[6] Finally, piezoresistive sensors offer mechanical stability, but at the same time, they show critical drawbacks, like high power requirement, large temperature dependence offset, nonlinearity, long-term instability in dynamic field conditions, and impart undesirable stiffness to catheters.^[6]

Piezoelectric thin-film transducers are great solutions as implantable and biocompatible pressure sensors and thus more easily implemented on a catheter for FFR pressure measurement. In the biomedical field, various organic piezoelectric materials are used. Several studies have focused on polyvinylidene fluoride (PVDF) and its composites as a sensing element in endovascular catheters.^[4,8] This class of organic ferroelectric polymer is attractive, thanks to its piezoelectric activity ($d_{33} \approx -20 \text{ pC N}^{-1}$), flexibility, stretchability, and biocompatibility. Sharma et al. used

3. Improving piezoelectric particle-composites via DEP: BaTiO₃/PDMS

3.1 Introduction

This section investigates DEP structuring of composites containing nanometric spherical fillers. Piezoelectric composites based on barium titanate nano-particles (BaTiO₃) embedded in Polydimethylsiloxane matrix (PDMS) with 0-3 and *quasi* 1-3 connectivity are designed to study the empowerment gained by DEP structuring. The goal is to combine the electroactive activity of the filler with the mechanical behavior of the matrix in such a way that the piezoelectric properties of the material are maximized, resulting in a flexible material with a low poling electric field, good transducing performance, and biocompatibility [24,25]. Thanks to its processability, the material developed could be easily integrated into cardiovascular devices for blood pressure measurements [13,21,26].

0-3 and *quasi* 1-3 composites are first simulated via Finite element analysis to investigate the electric field distribution in the two different connectivities, to determine the voltage developed as response to an external stress and to predict dielectric and piezoelectric coefficients. A study of the dielectrophoresis process is carried out using in-process microscopic imaging to discover the best combination of electric field's frequency and amplitude. Following that, the composites are manufactured in two distinct configurations, 0-3 and *quasi* 1-3, at different volume contents (2.4%v, 12%v and 24%v) labelled 0-3 BT/PDMS and 1-3 BT/PDMS. The composites' dielectric and piezoelectric properties are then examined to determine the improvement achieved by DEP structuration. Furthermore, a study of thermal stability of electroactive properties from 25°C to 200°C together with X-Ray diffraction from 25°C to 150°C are performed to understand the temperature range of use. The stretchability of the samples is assessed using dynamic mechanical analysis (DMA) to further understand the impact of DEP on mechanical properties. In conclusion, DSC (-140 – 15°C) and BDS in temperature (-140 – 0°C) are used to analyze how connectivity and filler content impact the glass transition temperature (T_g).

3.2 Finite Element Analysis (FE) of BT/PDMS

FE analysis (COMSOL®) is used to simulate the electric field distribution in BT/PDMS composites, with 0-3 and *quasi* 1-3 connectivity. All the samples in the simulation, designed with 5%v volume fraction of fillers, are subjected to an electric field polarization of 30 V μm^{-1} across their thickness (z direction). In the 0-3 nano-particle composite, fillers are randomly dispersed within the polymer matrix, while being aligned along the z -axis at inter-particle distance of 10 nm in the *quasi* 1-3 composite. The particles diameter is 500 nm. The permittivity of matrix and filler are 2.9 and 2000, respectively, and the piezoelectric charge coefficient of the filler in the 33 direction is set as 180 pC N⁻¹. As displayed in **Figure 42 a-b**, the average electric field in the particles computed along the poling direction, E_z , is almost three-fold higher when the particles are arranged in columns (0.41V μm^{-1} for 1-3 and 0.14 V μm^{-1} for 0-3). *Quasi* 1-3 connectivity allows for optimized distribution of the electric field, as the polymer shielding effect is lower along the poling direction. These preliminary findings are significant since they reveal how the material will behave when subjected to poling.

Polarization will be more effective in *quasi* 1-3 composite because a larger fraction of the electric field will reach the filler. The shielding effect is caused by permittivity inhomogeneity between the matrix and the particles. The electric field is more intense in the lower permittivity phase, whereas the higher permittivity phase (*i.e.*, fillers) experiences only a part of it. However, along a column, the polymer thickness around the filler is reduced, minimizing the shielding, and allowing for improved electric field distribution. It is also worth noting that the electric field on each particle in the *quasi* 1-3 configuration varies from $0.4 \text{ V } \mu\text{m}^{-1}$ (in the center of the fillers) to $1.8 \text{ V } \mu\text{m}^{-1}$ (in the extremity of the fillers), as highlighted in **Figure 42-b**. The electric field in 0-3 connectivity, on the other hand, depends on the random location of the fillers; for instance, the filler at the bottom of the configuration undergoes to a less homogenous E_z , reaching on the bottom $0.23 \text{ V } \mu\text{m}^{-1}$. Then, FE simulation of poling applied transversely to the column, hence along the y -axis ($E_y=30 \text{ V } \mu\text{m}^{-1}$) is reported (**Figure 42 c-d**). In this scenario, the *quasi* 1-3 connectivity exhibits a stronger shielding effect of the matrix, resulting in a lower average electric field in the filler, *i.e.*, E_y of $0.09 \text{ V } \mu\text{m}^{-1}$, with a range that goes from 0.06 to $0.11 \text{ V } \mu\text{m}^{-1}$; whereas the 0-3 structure exhibits a range of 0.09 to $0.15 \text{ V } \mu\text{m}^{-1}$, with an average value of $0.13 \text{ V } \mu\text{m}^{-1}$. This is a first proof of structured composite's anisotropy, characterized by one direction (the alignment one) that outperforms the others.

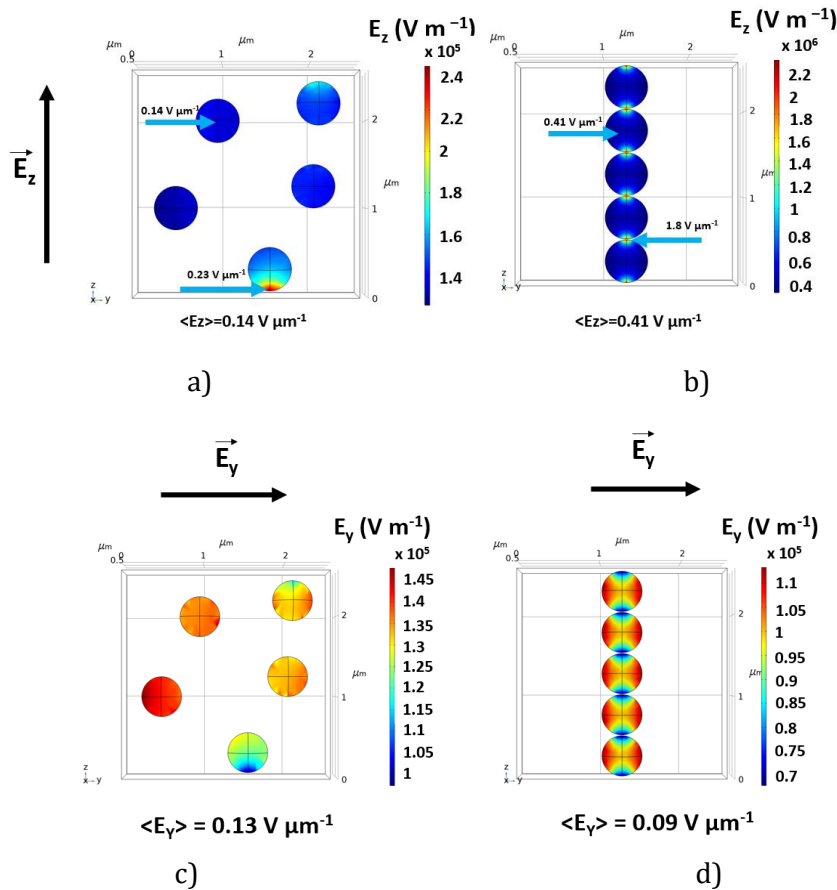


Figure 42 a) and b) FE simulation of fillers' electric field distribution in 0-3 and quasi 1-3 connectivity respectively under external electric field of $E_z=30 \text{ V } \mu\text{m}^{-1}$. c) and d) FE simulation of electric field

distribution in 0-3 and quasi 1-3 connectivity composites, respectively, under an external electric field $E_y = 30 \text{ V } \mu\text{m}^{-1}$.

After, the piezoelectric effect is examined: the upper surface of the composites is subjected to a compressive stress of 10 kPa in the z direction. The piezoelectric reacts to the applied stress by producing a surface charge, which is related to a potential difference across the sample. Given that the top surface is grounded, it is possible to evaluate the voltage developed by the composite in the two different configurations. The voltage created by the *quasi* 1-3 composite (0.73 mV) is 10 times greater than the 0-3 one (0.07 mV), as displayed in the **Figure 43 a-b**, implying a superior electromechanical coupling of structured composites. The g_{33} coefficient (V m N^{-1}) is then computed from the value of the voltage, as the electric field across the sample per unit of stress applied (Eq. 32).

$$g_{33} = \frac{E_z}{\sigma} \quad (32)$$

E_z is the electric field across the sample, computed as the Voltage, V , divided by the thickness, t , which is $2.55 \text{ } \mu\text{m}$

$$E = \frac{V}{t} \quad (33)$$

The piezoelectric voltage coefficient for the non-structured composite is 2.90 mV m N^{-1} , while the structured one presents a g_{33} of $28.74 \text{ mV m N}^{-1}$.

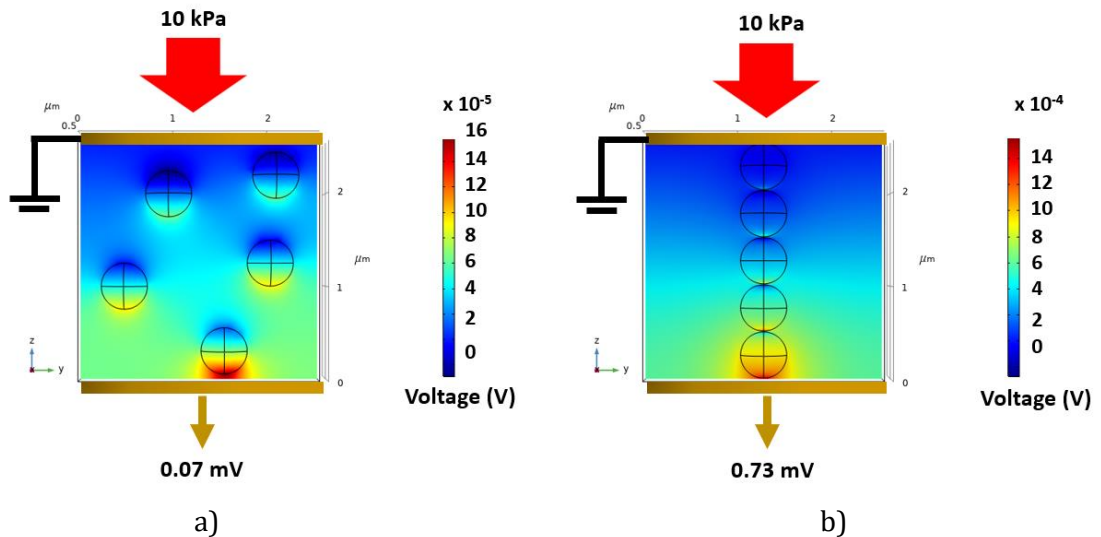


Figure 43 FE simulation of a) 0-3 connectivity composites and b) quasi 1-3 connectivity composites under compressive stress of 10 kPa applied in the z direction. The color map indicates the voltage developed across the sample.

Subsequently, the permittivity of the two composites is evaluated by applying an external electric field through the thickness of the composite and measuring the total dielectric displacement (D), measured in C m^{-2} . The electric field applied is $1 \text{ V } \mu\text{m}^{-1}$ and the resulting dielectric displacement is $30.58 \text{ } \mu\text{C m}^{-2}$ for 0-3 connectivity, while $38.66 \text{ } \mu\text{C m}^{-2}$ for *quasi* 1-3 connectivity. Following Eq. 34, the dielectric constant is computed for the two systems.

$$\varepsilon_r = \frac{D}{\varepsilon_0 * E_z} \quad (34)$$

The values of ε_r for 0-3 and *quasi* 1-3 are 3.45 and 4.36, respectively. Following Eq. 35, the d_{33} of the two composites is evaluated:

$$d_{33} = g_{33} * \varepsilon_0 * \varepsilon_r \quad (35)$$

The piezoelectric charge coefficient for *quasi* 1-3 composite is almost 14 times higher than the 0-3 one. All the results, summarized in **Table 1**, allow to predict the improvement in term of dielectric and piezoelectric activity gained through dielectrophoresis alignment.

Table 1 Voltage, g_{33} D, ε'_r and d_{33} for 0-3 and 1-3 BT/PDMS 5%v simulated using COMSOL®.

Sample	Voltage (mV)	g_{33} (mV m N ⁻¹)	D (μC m ⁻²)	ε'_r	d_{33} (pC N ⁻¹)
0-3 BT/PDMS 5%v	0.07	2.90	30.58	3.45	0.08
1-3 BT/PDMS 5%v	0.73	28.74	38.66	4.36	1.10

3.3 Experimental results and discussion

3.3.1 Dielectrophoresis optimization

Figure 44 a-f displays the 10-min frames of each examined video taken via in-process microscopy described in subsection 2.3.1. First, the influence of electric field amplitude (1 V μm⁻¹, 2 V μm⁻¹ and 3 V μm⁻¹) at a fixed frequency (1 Hz) was evaluated. The pictures qualitatively show that the highest field strength of 3 V μm⁻¹ leads to superior columnar assembly compared to the other tested (**Figure 44 a-c**). At 3 V μm⁻¹ the columns are well defined, at 1 V μm⁻¹ the alignment is almost not present, while it is slightly visible at 2 V μm⁻¹. As matter of fact, stronger electric field amplitude favors interaction between the particles, leading to coarser and more defined columns. This is in accordance with Eq.24 in subsection 1.12. This result has been confirmed by several studies and is in agreement with the physical theory behind dielectrophoretic structuring [105,160,164,181]. In this investigation, amplitudes greater than 3 V μm⁻¹ are not reported as excessively high amplitude triggered electrical breakdown of the blend, due to high difference in permittivity between matrix and fillers that strongly enhances the electric field in the matrix. After selecting the optimal amplitude, the study focused on the role of the frequency. As illustrated in **Figure 44 d-f**, three different frequencies were analyzed, including 1, 100, and 1,000 Hz at the same amplitude of 3 V μm⁻¹. The results are qualitative, but clearly indicate that 1 Hz induces a superior structuring with respect to the other tested frequencies. In previous studies, 1-5 Hz were reported as the best values for blends of PZT in PDMS matrix, in accordance with our results [202]; at these frequencies there is a lossy capacitive behavior of the blend, where both the capacitive part and the resistive part contribute to the enhancement of F_{DEP} and dipole-dipole interactions[174]. From one side, the fillers' dipoles have enough time to follow the variation of electric field, meaning greater polarization, and on the other side the slight conductivity

may contribute to the interaction potential between the particles, as ionic species may locally enhance the electric field around the filler leading to greater structuring forces. It has been revealed in this study that higher frequencies, for instance 100 Hz and 1,000 Hz, are less effective; this may be because at higher frequency the drag force, related to the viscosity of the matrix, negatively impacts the structuration, hindering the movement of the particles. Furthermore, at too high a frequency the polymer exhibits less polarization and a lower permittivity, which may have an impact on the electric field experienced by the particles. Frequency values lower than 1 Hz, on the other hand, were not even considered as they would lead to inefficient structuration. As reported by Bowen *et al.*, this is first related to the dielectric behavior of the matrix: the ionic conductivity of the matrix at frequencies < 1 Hz induces too high losses in the polymer. The real permittivity and the loss tangent of PDMS increase fast below 1 Hz, which means also lower difference in the permittivity between the matrix and the filler inducing a decrease of polarizing force [174]. The migration of ions that occurs at low frequency may also create a layer at the electrode, decreasing the electric field in the blend. In conclusion the effect of the frequency is more intricate than the amplitude, as the optimal frequency depends on several factors, such as losses and conductivity of the matrix and dielectric mismatch between the phases, however our results are in well agreement with those reported in previous studies, indicating that the best frequency for PDMS based composites is in the range of the unit of Hz. In this analysis blends with 1.2%v of fillers were observed. Clearly increasing the amount of filler would lead to some changes in the structuration: more fillers would enhance the drag force, but at the same time this would be counterbalanced by fillers proximity: being closer to each other particles would have stronger interactions, following Eq.24, where the interaction potential is inversely proportional to the cube of the interparticle distance. Nonetheless, this preliminary experiment provides a useful insight of the optimal match between electric field amplitude and frequency, which in theory should be consistent even when the filler content is increased. In conclusion, following this investigation, it was possible to set the optimal parameters that were then used for processing all the structured BT/PDMS. Subsequently, the 0-3 and *quasi* 1-3 composites were produced according to the modalities explained in subsection 2.2.1.

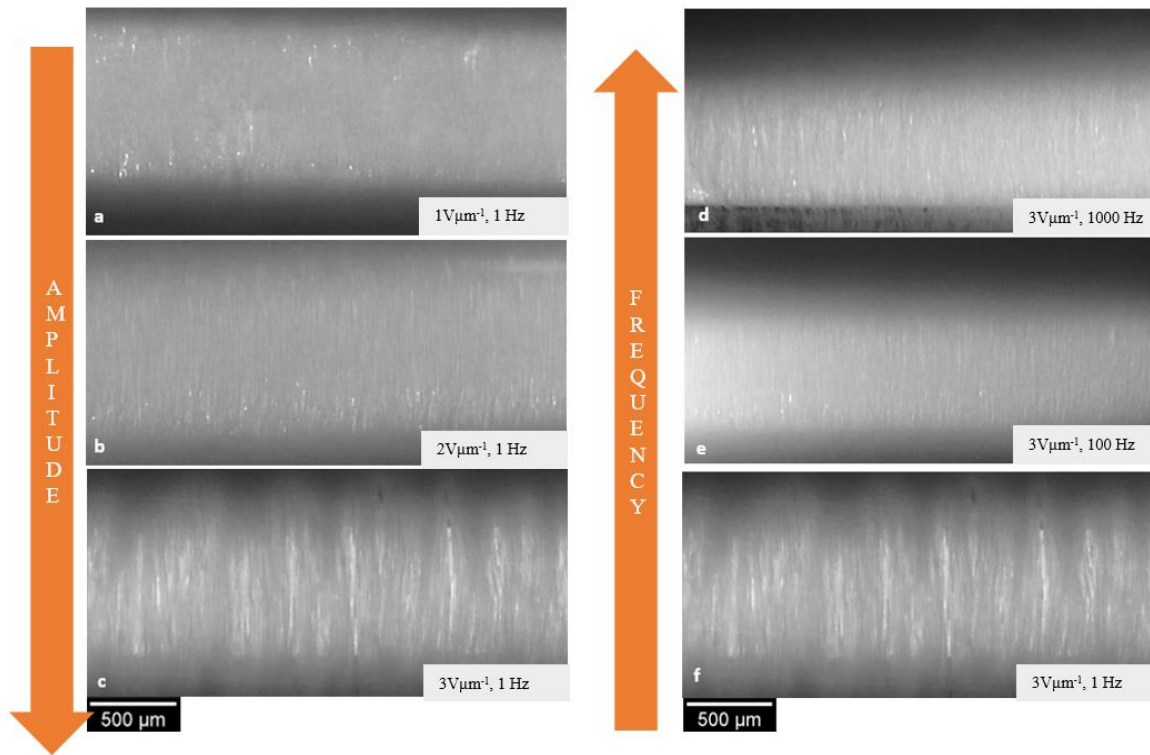


Figure 44 In process microscopy results: left pictures represent the results from the study of electric field amplitude: three frames from the in-situ microscopy analysis taken 10 minutes after structuration at a) $1 \text{ V } \mu\text{m}^{-1}$ and 1 Hz, b) $2 \text{ V } \mu\text{m}^{-1}$ and 1 Hz and c) $3 \text{ V } \mu\text{m}^{-1}$ and 1 Hz. Right pictures represent the study of frequency effect on dielectrophoresis: three frames from the in-situ microscopy analysis taken 10 minutes after structuration at d) $3 \text{ V } \mu\text{m}^{-1}$ and 1000 Hz, e) $3 \text{ V } \mu\text{m}^{-1}$ and 100 Hz and f) $3 \text{ V } \mu\text{m}^{-1}$ and 1 Hz. All the tests were performed at room temperature.

3.3.2 Optical microscopy and Scanning electron microscopy

Figure 45 shows the cross-section of BT/PDMS composites at 2.4%v with *quasi* 1-3 connectivity, observed via optical microscope. The columnar distribution of the particles in the matrix is an immediate and clear proof of the dielectrophoresis effect on the internal arrangement of the phases. Structured and unstructured samples of BT/PDMS with 2.4%v were then analyzed via SEM in back scattered electron (BSE) mode. **Figure 46 a-b** shows the cross-section composites with 0-3 and *quasi* 1-3 connectivity, respectively. In 0-3 BT/PDMS the particles are randomly and homogeneously dispersed, while in 1-3 BT/PDMS they are aligned in unidirectional pillars; the 1-3 columnar structure may appear less prominent than in optical microscope investigation: actually, optical microscopy in transmission mode allows to observe the structure on several z planes, providing the appearance of denser columns, but SEM in BSE mode only studies the layers closest to the surface.

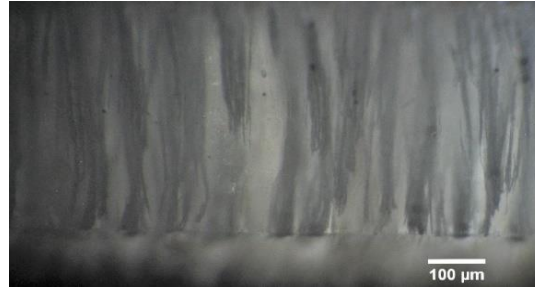


Figure 45 Optical microscopy in transmission mode of the cross section of 1-3 BT/PDMS 2.4%v.

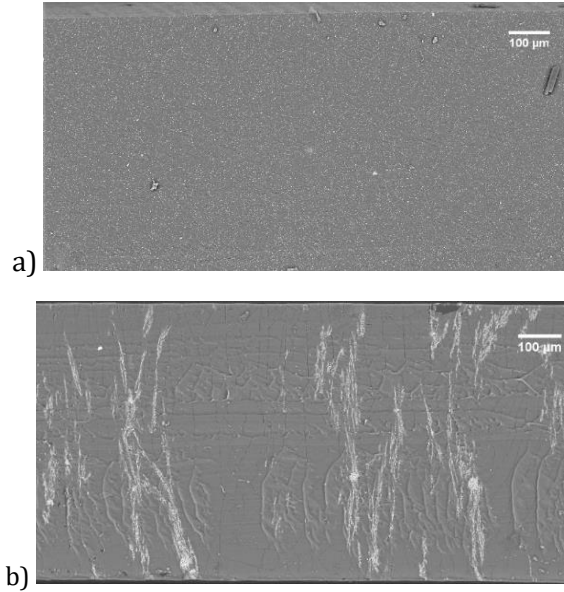


Figure 46 SEM pictures in BSE mode of a) 0-3 BT/PDMS 2.4%v and b) 1-3 BT/PDMS 2.4%v.

3.3.3 Dielectric spectroscopy

BDS allowed to understand the effect of structuration on the dielectric properties of the composites. **Figure 47 a-b** report the real part of the relative permittivity (ϵ'_r) vs. frequency for 0-3 and *quasi* 1-3 composites respectively, at 2.4%v 12%v and 24%v, from 10^{-1} to 10^6 Hz measured at room temperature. Depending on the range of frequency analyzed, different phenomena occur in the composite. Low frequency measurements are associated with interfacial polarization and electrode polarization (space charge) (usually for frequencies equals and lower than 1 Hz), followed by dipolar polarization ($1-10^6$ Hz). At higher frequencies there is the so-called resonance regime with atomic (10^6-10^{12} Hz) and electronic relaxation ($>10^{12}$ Hz), which are not investigated in this study. For each sample examined, the plots of the ϵ'_r follow the same trend: starting from 10^6 Hz and decreasing the frequency there is a slight increase in the real part of the relative permittivity, as the dipoles become more capable of following the fluctuation of the applied field, resulting in increased polarization. This rise becomes more pronounced below 1 Hz, when interfacial and electrode polarization contribute. From the plots it emerges that as the filler content grows, so does ϵ'_r throughout the full frequency range studied, for both non-structured and structured composites. Additionally, no matter the frequency, passing from 0-3 to *quasi* 1-3 connectivity comes with

an increase of ε'_r , as the density of fillers' dipoles rises along the electric field direction. The loss tangent, $Tan\delta$, which is computed as the ratio between the imaginary and real part of the relative permittivity, represents the ratio of dissipated over the stored energy, *i.e.*, the power loss, in a dielectric material under applied electric field (Eq.36). It is independent on the capacitor geometry and allows for a direct comparison between different materials. For all the composites the losses are quite low and present a slight increase at low frequency possibly due to interfacial polarization and space charge, as previously explained, as well as conductivity contribution, which could be suppressed by means of Kramers-Kronig equations [203]. The conductivity term may be related to the humidity absorbed on the surface of the fillers [203]. For 0-3 composites, increasing the filler content causes a modest, but noticeable, increase in losses. The same holds true for structured composites, although the increase in losses is larger. This may be related to Maxwell-Wagner-Sillars interfacial polarization, as increasing the fillers content there is an increase of interfaces along the poling direction. Interfacial polarization is indeed enhanced in electrically heterogeneous systems with two or more phases [204]. This phenomenon has been already reported in several studies: the difference in conductivity and permittivity between matrix and filler at the interface leads to an accumulation of charges which locally redistribute the electric field [205,206]. In summary, values of loss tangent rise as the filler content increases, in particular at low frequency, as the composites become more heterogeneous, charges collect at the interfaces and hence interfacial polarization rises. This seems to be more prominent in structured the composites, where the losses are enhanced with respect to non-structured composites. The cause might be connected to the filler's closer proximity, which could establish routes for the charges. Additionally, the presence of fillers and their proximity to one another may interfere with crosslinking, resulting in constrained amorphous phase as well as hindering the polymerization. In any case, the composites losses remain low; maintaining a low dielectric loss is critical for capacitors since loss contributes considerably to Joule heating effect [207].

$$Tan\delta = \varepsilon''_r / \varepsilon'_r \quad (36)$$

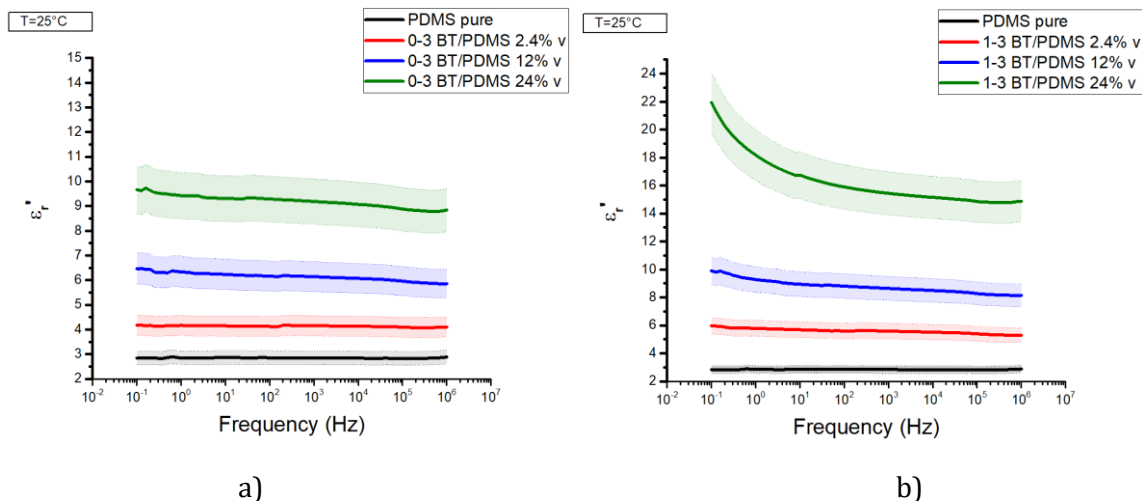


Figure 47 Relative permittivity real at room temperature for a) PDMS and 0-3 BT/PDMS with 2.4%v, 12%v and 24%v and b) PDMS and 1-3 BT/PDMS with 2.4%v, 12%v and 24%v.

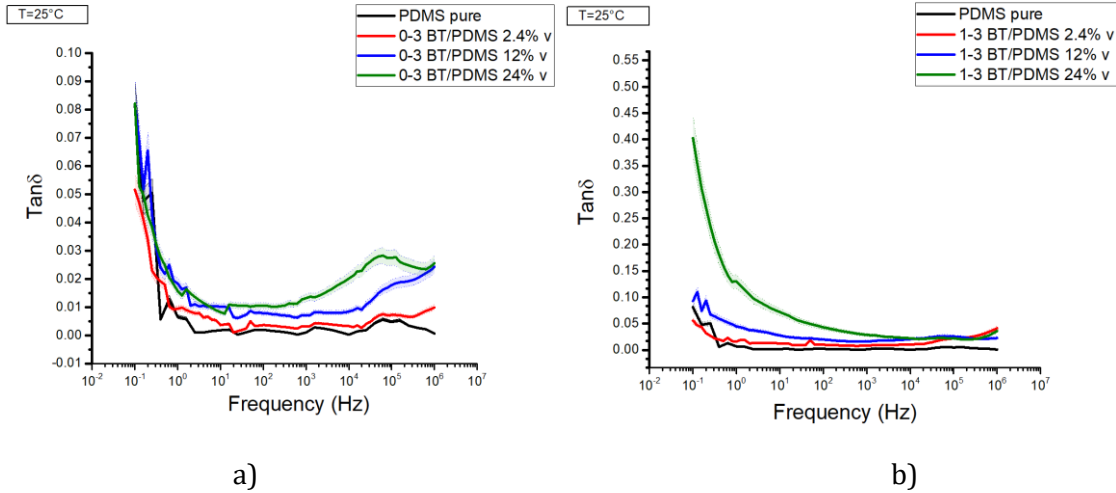


Figure 48 Loss tangent at room temperature for a) PDMS and 0-3 BT/PDMS with 2.4%v, 12%v and 24%v and b) PDMS and 1-3 BT/PDMS with 2.4%v, 12%v and 24%v.

In order to visualize the effect of structuration over the dielectric permittivity, the values of relative permittivity at 1kHz are plotted in function of the volume fraction (%v) for 0-3 and *quasi* 1-3 composites, and the results are fitted with the models presented in subsection 1.9 (**Figure 49**). Each result, reported in **Table 2**, presents a relative error of around 10%. Dielectric analysis successfully verifies the effect of dielectrophoresis on composites. As predicted, DEP structured composites present increased permittivity along the columnar direction [105,164,208]. The models' predictions (Yamada for 0-3 and Bowen for *quasi* 1-3 reported in subsection 1.9) are in good agreement with the experimental results. The fillers in *quasi* 1-3 composites are densely arranged along the alignment direction, which results in an apparent increase in volume content; consequently, the fillers' dipole density on the structuring axis is much higher leading to unidirectional enhancement of permittivity. Additionally, the smaller gaps of polymer between the fillers within a column shield less the electric field rather than on 0-3 connectivity. Meanwhile, the relative permittivity will presumably be lower in the other directions. Regarding the 0-3 composites, on the other hand, their permittivity is lower and expected to be the same in any direction, *i.e.*, relating to isotropic behavior. These findings are consistent with the FE modeling presented in subsection 3.2 where we predicted that a more efficient electric field distribution would develop in structured composites. A direct comparison of the results with FE simulation is not feasible since the volume fraction simulated was 5%v and was not replicated experimentally, although the trend between 0-3 and 1-3 remained the same.

Table 2 Relative dielectric permittivity (real part) for 0-3 and 1-3 BT/PDMS at 2.4%v, 12%v and 24%v, compared to pure PDMS.

Volume fraction (%vol)	ϵ'_r 0-3	ϵ'_r 1-3
0%	2.9 ± 0.3	2.9 ± 0.3
2,4%	4.2 ± 0.4	$5,6 \pm 0.5$
12%	6.1 ± 0.6	$8,6 \pm 0.8$
24%	9.1 ± 0.9	15.5 ± 1.5

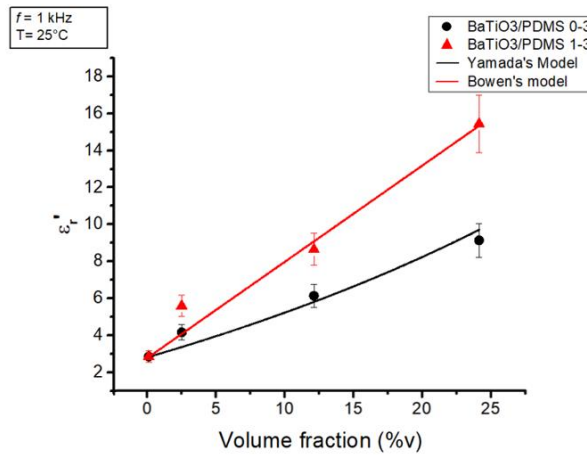


Figure 49 Relative dielectric permittivity real vs. filler volume content for 0-3 and 1-3 BT/PDMS at 1 kHz and measured at room temperature, fitted with the models presented in subsection 1.9.

3.3.4 Piezoelectric characterization

To assess the piezoelectric performances of the 0-3 and *quasi* 1-3 composites, evaluation of piezoelectric charge and voltage coefficients, d_{33} and g_{33} , at different BaTiO₃ concentrations was carried out. The piezoelectric charge coefficient, d_{33} (pC N⁻¹), indicates the electrical charge developed on the materials surfaces, consequence of the internal electric displacement produced in response to applied stress, and it is a direct measurement of the piezoelectricity. The experimental results are reported in **Table 3** and plotted in **Figure 50-a**. From the plot we can deduce that:

- Increasing the filler volume fraction there is an increase of d_{33} , regardless the connectivity.
- At any fillers content, structured composites exhibit superior piezoelectric response than the 0-3 isotropic counterparts.

As explained in subsection 1.9, in *quasi* 1-3 connectivity, the piezoelectric filler is arranged almost compactly along a preferred direction, leading to substantial improvement of piezoelectric properties along that direction, where density of dipoles is higher. However, since small portions of polymer are present between the fillers, it is not a fully 1-3 composite, so the values of d_{33} are limited to the tens of pC N⁻¹, far from the hundreds achieved by ceramic

bulk. Excellent coherence between experimental and theoretical results are achieved, reflecting the high reliability of the analytical model proposed in subsection 1.9, (Yamada' model for 0-3 and Van den Ende for 1-3). The increase in piezoelectric behavior may also be related to the distribution and intensity of the electric field during the poling. The chain alignment of the fillers favors the intensification of the electric field, as the shielding of the matrix is reduced, which in turn optimizes the polarization. Therefore, under the same electric field, a structured composite can reach higher levels of polarization than a randomly dispersed one. It is noticeable that such a piezoelectric behavior is triggered at lower electric field ($25 \text{ V } \mu\text{m}^{-1}$) with respect to PVDF based polymers, which require at least $60 \text{ V } \mu\text{m}^{-1}$. Furthermore, the ferroelectric content of the composite with optimized properties is 24%v, while the crystalline ferroelectric content of PVDF and its composites is around the 50%v, which indicates that the composites require less ferroelectric phase to have good piezoelectric activity [120].

Table 3 d_{33} and g_{33} for 0-3 and 1-3 BT/PDMS at 2.4%v, 12%v and 24%v, compared to pure PDMS.

Volume fraction [%v]	d_{33} 0-3 [pC N ⁻¹]	d_{33} 1-3 [pC N ⁻¹]	g_{33} 0-3 [mV m N ⁻¹]	g_{33} 1-3 [mV m N ⁻¹]
0%	0	0	0	0
2.4%	0.06 ± 0.02	2.15 ± 0.10	1.64 ± 0.49	43.35 ± 4.38
12%	0.7 ± 0.10	6.5 ± 0.20	12.83 ± 1.42	83.37 ± 8.36
24%	2.4 ± 0.20	8.5 ± 0.50	29.19 ± 3.00	60.40 ± 6.09

The piezoelectric voltage coefficient, g_{33} (mV m N⁻¹), is a widely used parameter to compare the properties of piezoelectric sensors, as it incorporates both the d_{33} and the dielectric properties of the material, quantifying the electric field generated by a piezoelectric material per unit of mechanical stress applied. It is calculated following Eq.37.

$$g_{33} = \frac{d_{33}}{\epsilon'_{33}} = \frac{d_{33}}{\epsilon_0 \epsilon'_r} \quad (37)$$

For this computation, the value of ϵ'_r was taken at 100 Hz, as the piezometer perform measurements at $\sim 100\text{Hz}$. The results are reported **Table 3** in and displayed in **Figure 50-b**. Furthermore, the theoretical plot of g_{33} was traced for both 0-3 and 1-3 connectivity, using the permittivity models developed by Yamada and Bowen and the d_{33} models developed by Yamada and Van den Ende. The comparison of theoretical and experimental curves revealed good agreement. In 0–3 composites, the piezoelectric voltage coefficient (g_{33}) rises with the particle concentration, while in quasi 1-3 composites it exhibits a maximum value at 12%v of BaTiO₃ content. Indeed, in quasi 1-3 composites, increasing the volume fractions from 12%v to 24%v induces a rise in d_{33} of the $\sim 30\%$, but the dielectric permittivity experiences a far greater improvement (*i.e.*, $\sim 80\%$ increase), therefore, g_{33} falls from 83 to 60 mV m N⁻¹. We can draw the conclusion that, regardless of the BaTiO₃ volume content, dielectrophoresis structured composites exhibit greater piezoelectric response with superior voltage and charge coefficients, with respect to 0-3 ones.

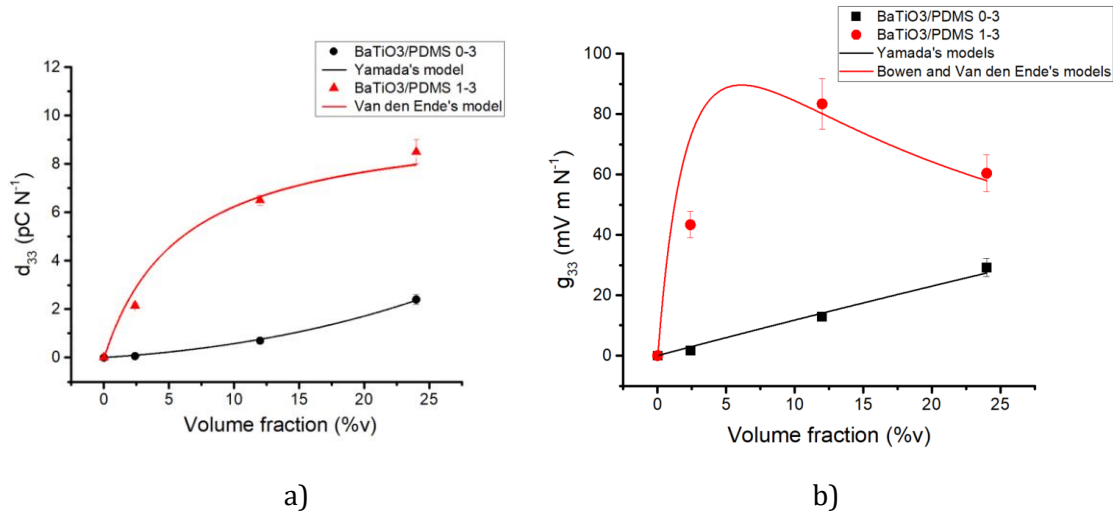


Figure 50 a) d_{33} vs. filler volume content and b) g_{33} vs. filler volume content for 0-3 and 1-3 BT/PDMS. All the data are fitted with the models presented in subsection 1.9.

Although we cannot directly compare the experimental results to the FE analysis, the increase from 0-3 to quasi 1-3 connectivity is consistent for d_{33} and g_{33} , confirming that DEP structure improves the piezoelectric sensitivity of piezocomposites.

3.3.5 Thermal stability and XRD analysis

The thermal stability of non-structured and structured BT/PDMS was evaluated by observing the evolution of piezoelectric response after annealing at various temperatures. **Figure 51** shows the evolution of the normalized charge coefficient ($d_{33}/d_{33}^{25^\circ\text{C}}$, where $d_{33}^{25^\circ\text{C}}$, corresponds to the value measured at room temperature before the thermal study) under a large temperature range (25–200°C). For the sake of simplicity, only composites with 24%v of fillers were tested. The result highlights that the piezoelectric properties of the two samples are fully stable until 50°C. There is a slight advantage in temperature stability for the *quasi* 1-3 composite at a higher temperature of 100°C, where the normalized d_{33} only slightly decreases and attains a value of almost ~80%, while it attains a value of 70% for the 0-3 samples. Increased temperatures allow greater mobility of dipoles, which therefore tend to partially lose their orientation, reducing the d_{33} to some extent. However, this phenomenon seems somewhat minimized in structured composites, which might be attributable to a variety of variables. First, dipole orientation is larger in *quasi* 1-3 structures, as proved both by FE analysis and empirically. As a result of the higher density of oriented dipoles, the influence of temperature weighs less on a *quasi* 1-3 composite than on a 0-3 composite with a lower density of oriented dipoles. Furthermore, the fillers along the columns in *quasi* 1-3 composites are extremely close together, presumably only a few nanometers apart, thus, the possibility of dipole-dipole interaction between the closed particles cannot be discounted. In theory, this might mitigate the temperature-induced dipole randomization effect.

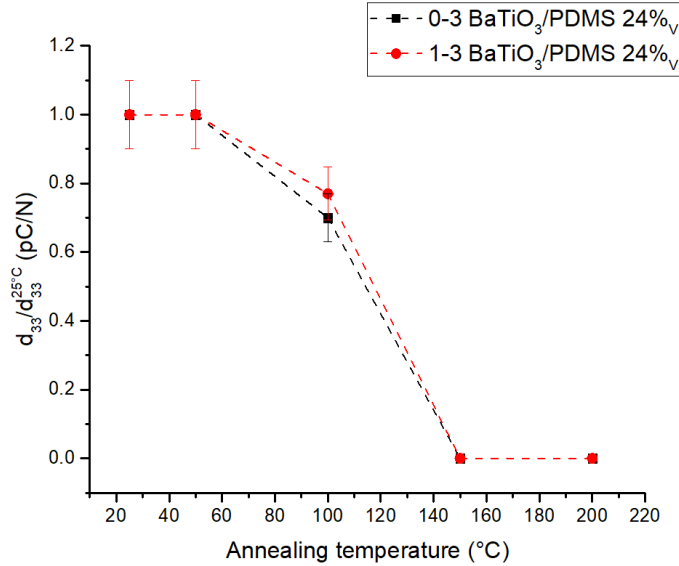


Figure 51 Normalised d_{33} vs. annealing temperature for 0-3 and 1-3 BT/PDMS at 24%v.

Nonetheless, once reached the Curie temperature, a transition from tetragonal to cubic occurs, the piezoelectric activity is lost, and this is reflected in the values at 150°C. As expected, 0-3 and *quasi* 1-3 samples totally lose their piezoelectric behavior at 150°C respectively, as the Curie temperature (T_c) of barium titanate ($\sim 120\text{--}130^\circ\text{C}$) is exceeded. Indeed, a structural change of crystalline cells occurs with the temperature increasing above the Curie value, as the cell structure transits from tetragonal (*i.e.*, ferroelectric behavior) to a cubic structure (*i.e.*, paraelectric behavior). Then, XRD analysis was carried out on the 0-3 and *quasi* 1-3 samples at the following specified temperatures (**Figure 52**): 25°C (*i.e.*, room temperature), 100°C (*i.e.*, below T_c), 130°C (*i.e.*, considered as T_c), and 150°C (*i.e.*, above T_c). As explained, in this range there are two possible crystalline structures of BaTiO₃, tetragonal at a temperature below T_c , and cubic at a temperature above T_c . The significant peaks for the crystalline structures are located within a 2θ range of 43- 46°. From 25°C to 100°C, the prevalent symmetry is the tetragonal one (*i.e.*, characterized by the double peak near $2\theta = 45^\circ$). For 0-3 samples, at 130°C the double peak is completely disappeared replaced by a single peak at $2\theta = 45^\circ$ related to cubic crystalline phase. On the other hand, for the aligned sample, at 130°C the transition from tetragonal to cubic is not complete as we can still see a remnant of the double peak, indicating that there still is a reduced portion of fillers in tetragonal configuration. Beyond 150°C, no morphology differences are detected between the structured and non-structured composites. The reason behind this difference is still under investigation, however it may be related to a difference in the heat transfer through the sample.

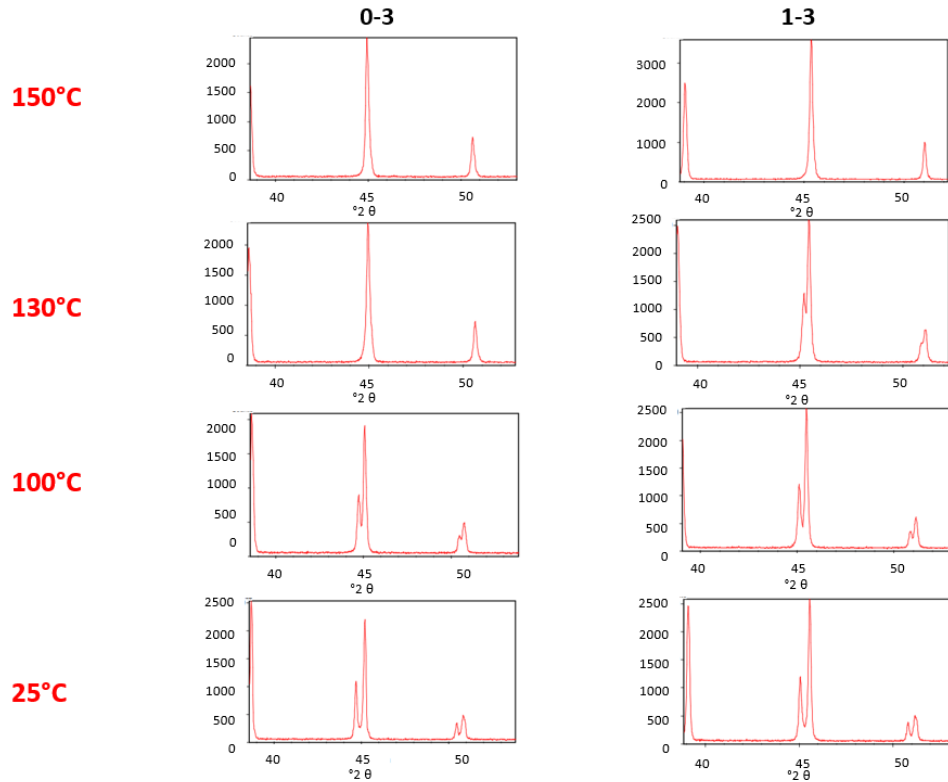


Figure 52 X-ray diffraction of 0-3 BT/PDMS (left side) and 1-3 BT/PDMS (right side) at 25, 100, 130 and 150°C.

3.3.6 Dynamic mechanical analysis (DMA)

The impact of DEP alignment on the mechanical behavior of the composites was examined using DMA. This assessment is necessary to ensure that no high stiffness is produced, since it could interfere with the biomedical application. Through DMA, Y' and Y'' , storage and loss moduli respectively, were analyzed at different frequencies (1, 25 and 50 Hz) for 0-3 and 1-3 BT/PDMS and for pure PDMS. The test was performed at 25°C. The results are reported in **Figure 53 a-b** and **Figure 54 a-b**. As mentioned in subsection 2.3.8, pure PDMS is only evaluated at 1 Hz and 25 Hz since at 50 Hz the resolution of the analysis device was insufficient to capture the measurement. Starting from 1 Hz, the value of Y' and Y'' increases with the frequency for each volumetric content and connectivity. This happens because as the frequency raises, there is more energy on the polymer chains, which also have less time to deform, increasing the storage component; yet, since the polymer's chains have less time to move at higher frequencies, the loss modulus increases [209]. This is valid for both 0-3 and 1-3 BT/PDMS. Furthermore, both Y' and Y'' increase with the filler content, regardless the connectivity; as matter of fact, the filler has high Young's modulus with respect to the matrix ($Y_{\text{filler}} \sim 60$ GPa, $Y_{\text{matrix}} \sim 3$ MPa), and its addition inevitably induces an increase in the stiffness. Moreover, it inhibits chains' movement, and therefore there is a further increase in stiffness and in losses as well [183,210]. Many investigations have found that the polymer chains polymerize differently around the filler, resulting in stiffer chains than those far from the particles [211]. Due to the tighter spacing between the fillers and the increased number of interfaces, the interaction zone may thus play a role in the stiffening that occurs at greater

volume fractions. Nonetheless the glass phase is present only below -115°C , and at ambient temperature the phase is amorphous, hence the effect of constrained amorphous phase is clearly reduced, as there may be just a difference in degree of freedom related to the constrained chains. Regarding the rise in losses with the volume fraction, it is generally acknowledged that increasing the volume fraction, or the interfacial contact between the polymer matrix and the filler particles, raises the loss modulus of polymer composites by increasing the damping force for molecular motion [212-214].

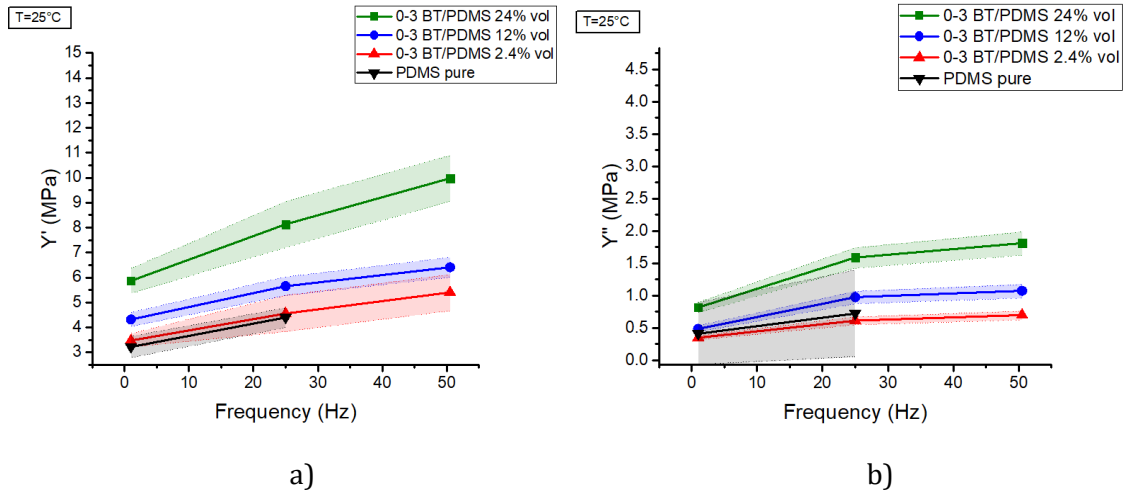


Figure 53 a) Storage modulus and b) Loss modulus for 0-3 BT/PDMS at all the volume contents produced examined at 25°C .

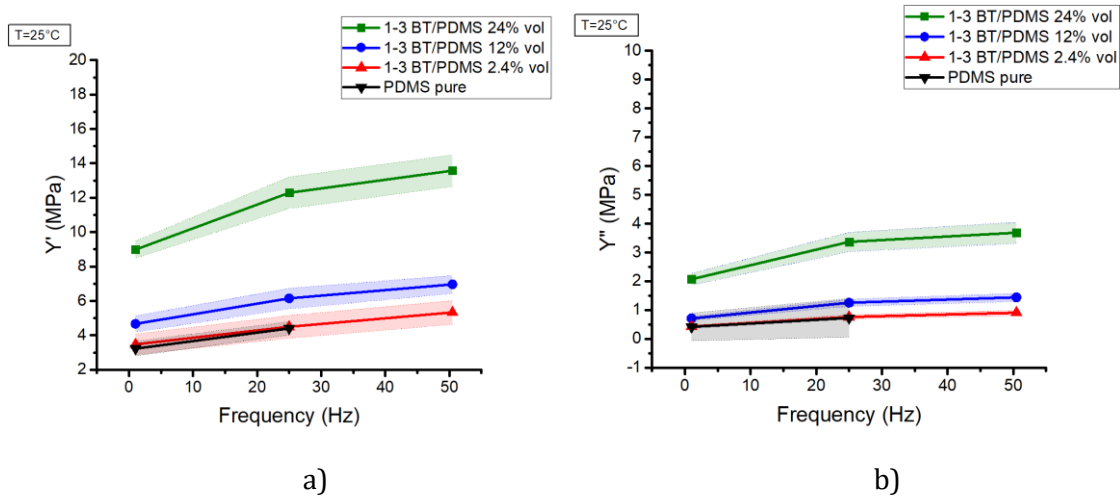


Figure 54 a) Storage modulus and b) Loss modulus for 1-3 BT/PDMS at all the volume contents produced examined at 25°C .

Y was computed according to Eq. 38.

$$Y = \sqrt{Y'^2 + Y''^2} \quad (38)$$

The values were evaluated at 1 Hz, as the materials are in linear regime, and it is the most interesting for the application presented in this work. The results are reported in **Table 4** and

displayed in **Figure 55**. In this investigation, we insist on the differences between 0-3 and 1-3 composites. Y of 0-3 composites exhibits a linear dependence with the filler content. This is not verified in 1-3 structured BT/PDMS. At low volumetric filler content, 1-3 alignment does not provide significant differences in elastic modulus with respect to 0-3 structures. However, at higher volume content the connectivity seems to influence more the mechanical behavior, as fillers alignment produces a substantial rise in elastic modulus. This was already reported in other works: Farshad *et al.* for instance, reports on the influence of magnetic field alignment and demonstrates a rise in Young's modulus in the perpendicular direction of the columns for small deformation. Among the reason behind this enhancement, it could be the presence of the occluded elastomer in the chains which are sort of agglomerates of particles: the fillers are tightly packed closed together in a columns and it shields the elastomer from the mechanical strain; according to the occluded elastomer theory this occluded elastomer increases the effective filler content, hence the mechanical modulus. A further element affecting the mechanical properties may be the existence of agglomerates. In conclusion, the filler structuring generates a rise in Young's modulus, but still not enough to induce stiffness in the composite, which, by remaining within the range of few MPa, is suitable for the applications outlined in Chapter I.

Table 4 Values of the Young's Modulus evaluated at 1 Hz at room temperature for all the composites of BT/PDMS with 0-3 and 1-3 connectivity and pure PDMS.

Volume fraction (%v)	Y 0-3 (MPa)	Y 1-3 (MPa)
0	3.2 ± 0.3	3.2 ± 0.3
2.4	3.4 ± 0.3	3.5 ± 0.3
12	4.3 ± 0.4	4.7 ± 0.4
24	5.9 ± 0.5	9.2 ± 0.9

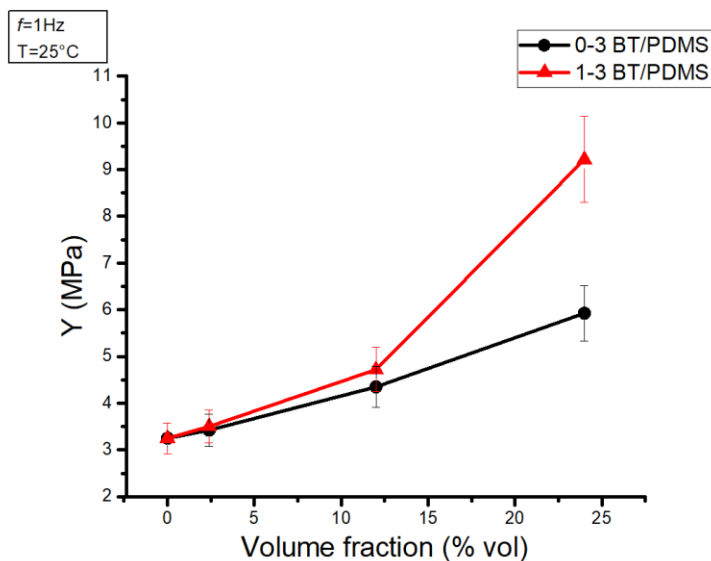


Figure 55 Y vs. volume fraction for 0-3 and 1-3 BT/PDMS.

3.3.7 Differential Scanning Calorimetry

The previous results raised question about the effect of the filler on the chain polymerization. DSC was studied from -150°C to 15°C to better understand the influence of filler content and alignment on the properties of the composites. The purpose was to determine the glass transition temperature (T_g) of the polymer (which is typically in the range -115°C and -120°C) as a function of volume content of filler. This may give important information about the amorphous phase as it is highly reliant on the chain's organization, and identify any change related to the interaction with the particles' surface. **Figure 56-a** reports the results of BT/PDMS 0-3 while **Figure 56-b** is related to BT/PDMS 1-3, where heat flow vs. sample temperature is reported. These data allow for the extraction of several remarkable insights. As for 0-3 composites, the glass transition occurs at about -117°C while for pure PDMS is -116.5°C . The transition inflexion point, which is present in all composites and connected to the polymer's amorphous phase, marks a change from a glassy to a somewhat viscous state. In **Figure 56-a**, a red arrow points to the point of inflexion. Secondly, the composite with the largest filler percentage (24%v) exhibits a melting peak at about -48°C . This peak corresponds to a melting crystalline phase, suggesting that the presence of the filler induces a crystalline phase and possibly partially hinder chemical crosslinking. The large number of interfaces may be the reason. This phenomenon was already observed in other studies where they underlined that is quite common to observe lower degrees of crosslinking due to the effect of filler content and also that crystallization may occur at the interface of the fillers, which act as heterogeneity for heterogeneous nucleation [215-220]. **Figure 56-b**, which shows structured composites 1-3, reveals several noteworthy findings: all samples exhibit a glass transition, but interestingly, the sample with 24%v has a larger transition temperature shift (ΔT_g) which seems to be related to a second glass transition (a second inflection point may be distinguished just after the first one). This suggests that the amorphous phase is very heterogeneous, leading to the presence of two distinct transitions. This heterogeneity may be due to the formation of a constrained amorphous phase in the nanometric gaps between particles along a column. The two transitions are denoted by black arrows in **Figure 56-b**. The existence of a melting peak at both 12%v, where it is less pronounced, and 24%v, where it is quite prominent, is another interesting discovery. This suggests once more that the closeness of the fillers, which is amplified by the dielectrophoresis effect, induces in some way crystallization. These three phases, amorphous, constrained amorphous, and crystalline, provide a lot of interfaces, which may be the cause of the rise in dielectric losses shown for 1-3 BT/PDMS 24% mentioned in section 3.3.2.

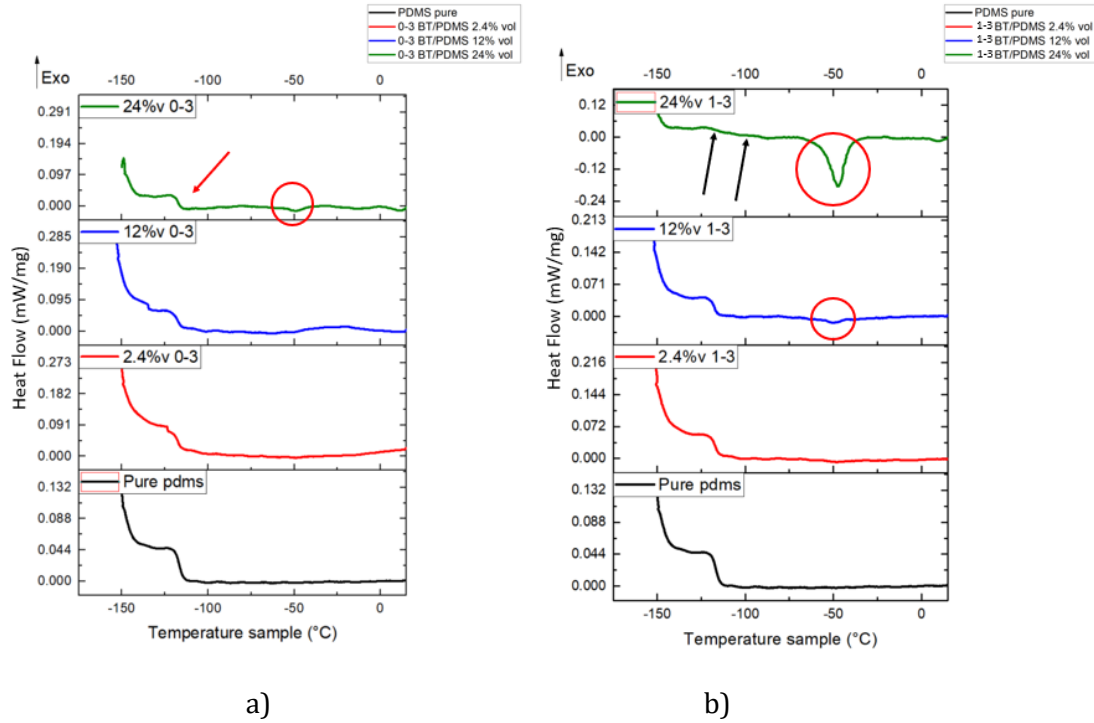
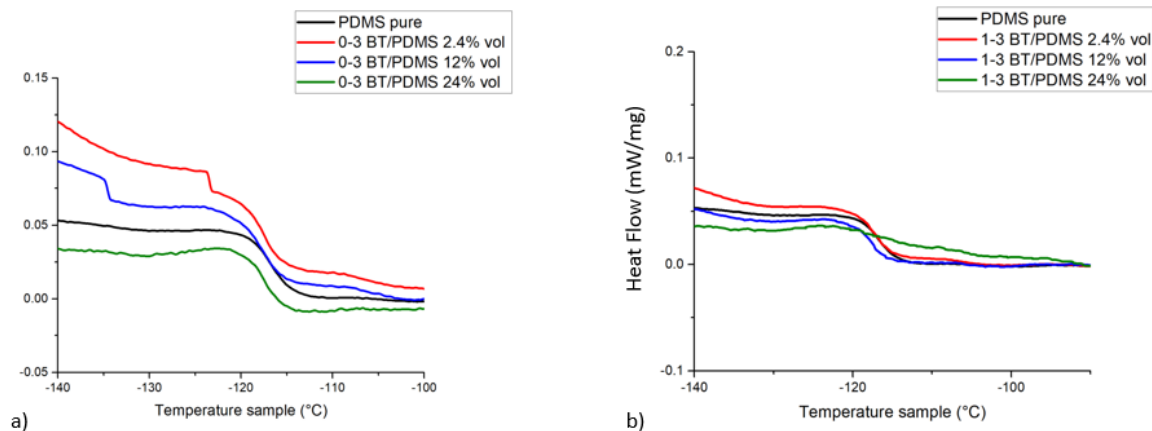


Figure 56 Heat flow (mW/mg) from [-150°C to 15°C] measured with DSC for a) 0-3 BT/PDMS from 0%v to 24%v and b) 1-3 BT/PDMS from 0%v to 24%v. The red arrow indicates the inflection point of the glass transition, while the red circle is surrounding the melting peak at ~-48°C. The black arrows are indicating the glass transitions that appears in 1-3 24%v BT/PDMS.

Figure 57 a-b compare the inflection points related to the glass transition for composites with 0-3 and 1-3 connectivity, respectively. **Figure 57-c** depicts the overall variations of the glass transition temperature as a function of filler content and connectivity, which were evaluated using *Calisto*[®] processing software. T_g is consistent across all samples. Yet not all transition occurs within the same temperature range, which is due to the amorphous phase's heterogeneity. **Figure 57-d** demonstrates that ΔT_g for the 0-3 composites is almost constant. The abrupt increase in ΔT_g for the 24%v BT/PDMS with 1-3 connectivity, is a marker of substantial amorphous phase heterogeneity.



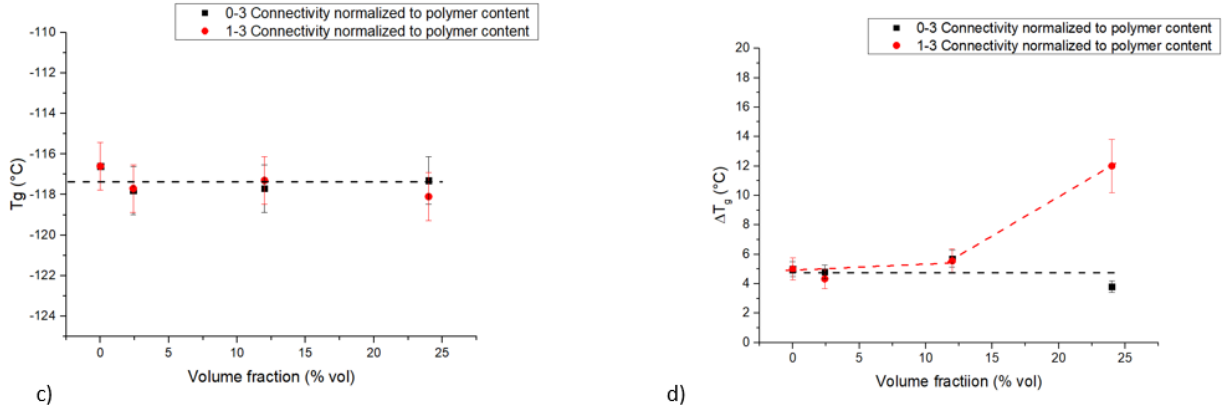


Figure 57 a) Zoom over the glass transition for 0-3 BT/PDMS from 0%v to 24%v of filler and b) zoom over the glass transition for 1-3 BT/PDMS from 0%v to 24%v of filler. c) T_g (°C) variation with filler content for 0-3 (black dots) and 1-3 (red dots) BT/PDMS composites. D) Variation of the ΔT_g (°C) for 0-3 and 1-3 BT/PDMS in function of the volume content.

The specific heat (C_p) is the amount of heat that must be added to one gram of the substance in order to raise its temperature by one Kelvin. The glass transition is associated with a ΔC_p that somewhat indicates the amount of amorphous phase. The values are reported in **Figure 58-a**. The ΔC_p of the 0-3 composites is almost constant, but that of the 1-3 composites drops at 24%v of BaTiO₃. This is related to the fact that some polymer crystallizes due to the effect of the filler, hence it is crystalline at -117°C, as was mentioned before. Because there is less polymer in the amorphous phase, the glass transition is associated with reduced specific heat. Finally, **Figure 58-b** shows the melting enthalpy of the composites BT/PDMS 0-3 with 24%v and BT/PDMS 1-3 with 12%v and 24%v. It is noteworthy that the crystalline phase is related to both connectivity and content of filler material, suggesting that it may be caused by the filler's proximity. To fully comprehend the nature of this heterogeneous system, atomic force microscopy, DMA in temperature and DSC in temperature might be helpful tools.

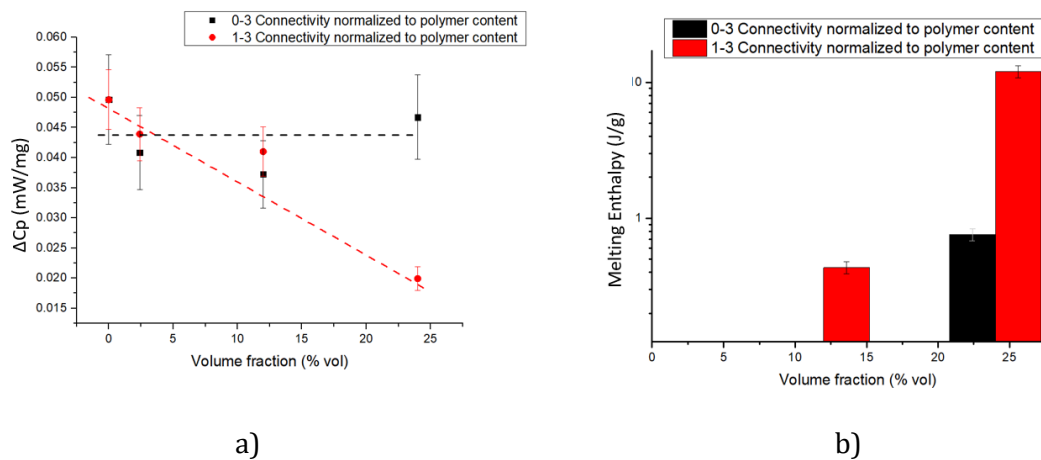


Figure 58 a) Variation of ΔC_p with volume content and connectivity; b) melting enthalpy for 0-3 BT/PDMS 24%v and 1-3 BT/PDMS with 12%v and 24% v of filler.

Figure 59 provides a comparison between pure PDMS and 24%v BT/PDMS 0-3 and 1-3. This DSC plot highlights the variations brought on by filler proximity and amount. The main conclusions of the analysis are summarized as follows:

- Filler addition affects polydimethylsiloxane polymerization. A crystalline phase that melts at -48°C emerges for a filler quantity of 24%v in 0-3 connectivity. The enthalpy of its melting is 0.75 J/g.
- Structuration further increases the effect above mentioned, lowering the threshold at which a crystalline phase will be present in the composite. Already at 12%v, a tiny melting peak with an enthalpy of 0.43 J/g can be noticed. At 24% of filler volume, the enthalpy of the melting peak significantly rose to 12 J/g, indicating a substantially larger proportion of the crystalline phase.
- High filler content in 1-3 connectivity (1-3 24%v BT/PDMS) also induces a very heterogenous amorphous phase characterized by a wide glass transition that seems containing two different glass transitions. The first one is located at almost the same temperature than pure PDMS, while the second one is at higher temperatures, meaning that a second phase with less mobility is present. Indeed, lower mobility amorphous phases require higher temperature to transit from glass to viscous. It may be associated with a constrained amorphous phase that formed due to the close proximity of the fillers induced by DEP structuring.

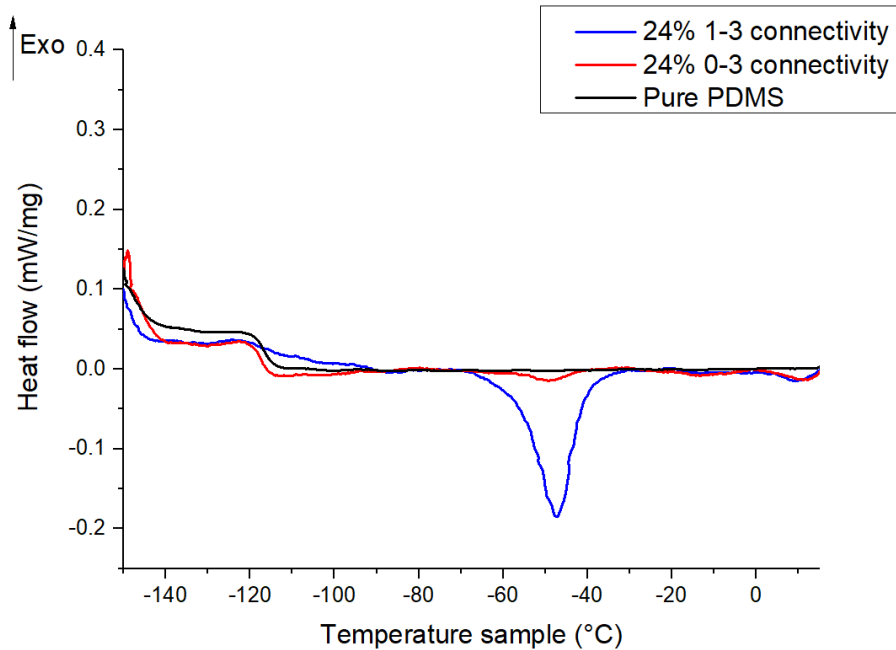


Figure 59 Heat flow vs. Temperature for pure PDMS, 0-3 and 1-3 BT/PDMS 24%v.

3.3.8 Broadband dielectric spectroscopy

The analysis of the dielectric spectrum between -140°C and 0°C allowed us to further verify relevant observation regarding the mobility of the polymer chains in relation to the volume content and connectivity of the fillers. This analysis enabled confirmation of the observations made by DSC, which indicated, the presence of a heterogeneous amorphous phase within the polymer phase in the 24%v-structured BT/PDMS composite, as well as the presence of a crystalline phase in both the 24% structured and the 0-3. **Figure 60 a-c** shows the loss tangent ($\tan\delta$) vs. temperature from 100 mHz to 1MHz for (a)PDMS, (b)PDMS loaded with 24%v BaTiO₃ in 0-3 connectivity and finally (c) 1-3 BT/PDMS 24%v. From the losses it is possible to identify the resonance of α relaxation associated with the glass transition occurring in the amorphous phase of the polymer. The peak for each sample moves to higher temperatures with an increase of frequency. This is a rather common result since at higher frequencies, the mobilization of smaller chain components is observed, which are associated with higher resonance temperatures as well. We may already infer some information from the comparison of these three graphs. If just one resonance peak, *i.e.*, α relaxation, is present for pure PDMS, then for 1-3 structured composites we can observe the appearance of a second peak at higher temperatures (about 100°C), which is connected to the relaxation of a second amorphous phase with reduced mobility. This peak, that is especially discernible at low frequencies (*e.g.*, black curve 100 mHz) associated with the mobility of significant sections of chains, is probably due to the α' relaxation of the constrained amorphous phase. At higher frequencies α' is less detectable since amorphous and constrained amorphous have similar mobility at such frequencies, which resonate with smaller parts of chains, and thus the two relaxation modes tend to merge. However, a second shoulder can be observed at 1 MHz, associated with α' . This observation was related to 1-3 BT/PDMS 24%v. A second relaxation can also be glimpsed in the 0-3 BT/PDMS composite; indeed, a second relaxation (α') is partially discernible at both 100 mHz and 1 MHz, related to a presence of a constrained amorphous phase, however lower in amount with respect to 1-3 composite. This is very low and neglectable. A second important observation is related to a melting isotherm marker about -50°C that can be seen in composite 1-3 (**Figure 60-c**). Up until 1kHz, it persists at the same temperature before disappearing. Furthermore, for the curves at low frequencies, it can be observed that after melting there is an increase in losses associated with the polarization of the melted crystalline phase, which is not visible at high frequencies. After melting, there is a considerable contribution of MWS as reported by Klonos *et al.*[221]. In **Figure 61** we compare the $\tan\delta$ vs. temperature of all three materials under analysis at three different frequencies, 100 mHz, 1 kHz and 1 MHz. The first noteworthy observation is that the structured composite has lower losses than the 0-3 composite and pure PDMS, which is obviously connected with the fact that it has less amorphous phase after increasing the crystalline phase. It is also worth noting that the red peak of the structured composite occurs at a slightly lower temperature than the other two, showing that the amorphous phase relative to α relaxation slightly differs because of the interaction with the structured filler. In addition, the red curve (BT/PDMS 1-3) is broader than the others. This is an indication of high heterogeneity of the amorphous phase. The 0-3 shows a greater broadness than the pure PDMS, although less than the 1-3 composite, at 1 MHz, again associated with heterogeneity and the partial appearance of a constrained amorphous phase induced by both the crystalline phase and the proximity of fillers. Indeed, the constrained amorphous phase develops at the interfaces between different phases.

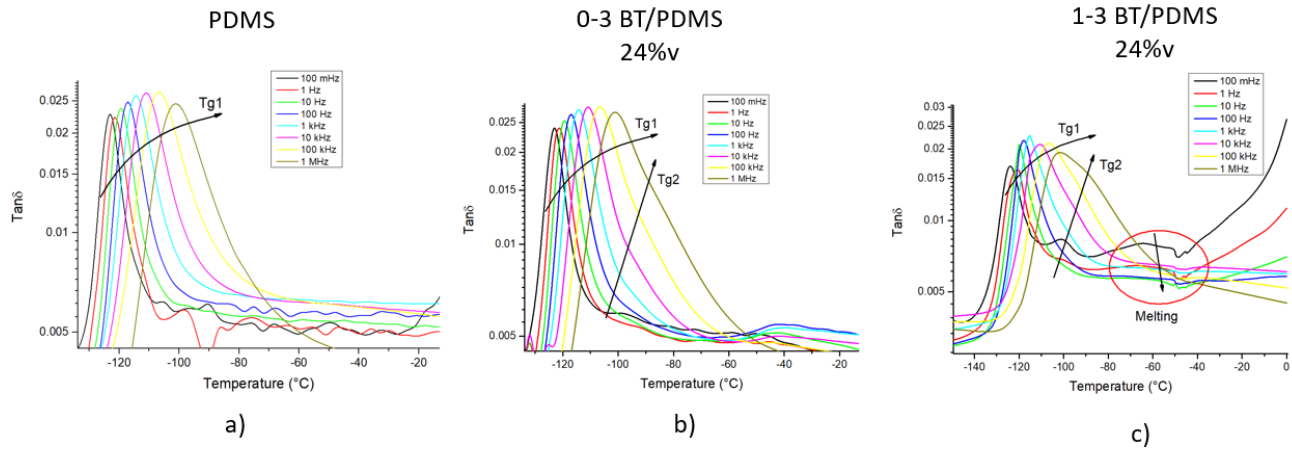


Figure 60 $Tan\delta$ vs. Temperature from 100 mHz to 1 MHz for a) pure PDMS, b) 0-3 BT/PDMS 24%v and c) 1-3 BT/PDMS 24%v

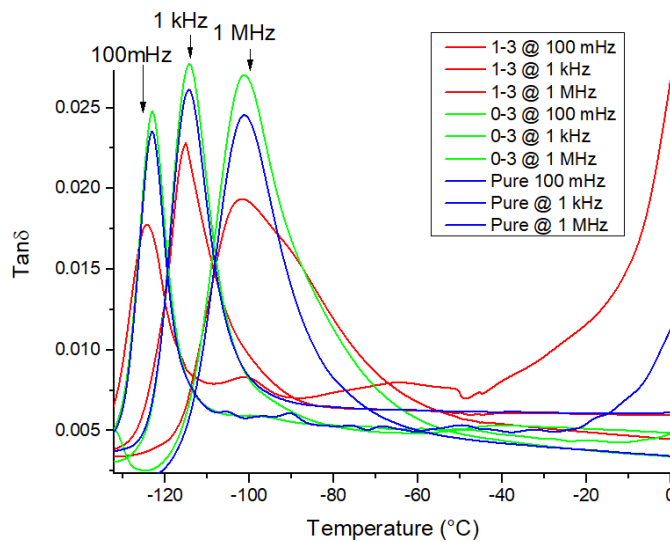


Figure 61 $Tan\delta$ vs. temperature for 1-3 BT/PDMS 24%v (red lines), 0-3 BT/PDMS (green lines) and pure PDMS (blue lines) for 100 mHz, 1kHz and 1MHz as indicated in the graphs.

Finally, **Figure 62** shows a comparison of the real permittivity vs. temperature for all three materials under study at 100 mHz, 1 kHz and 1MHz. The glass transition induces greater mobility of chains associated with an increase in permittivity, which is observed in all composites. This transition occurs over a wide temperature range. The presented results corroborate what was found using DSC. The combination of DSC and DBS at temperature helped us to understand more about the mobility of PDMS chains when a substantial amount of filler is introduced, and when the filler is structured. Studies on relaxation times and activation energy are planned to improve knowledge of the materials produced.

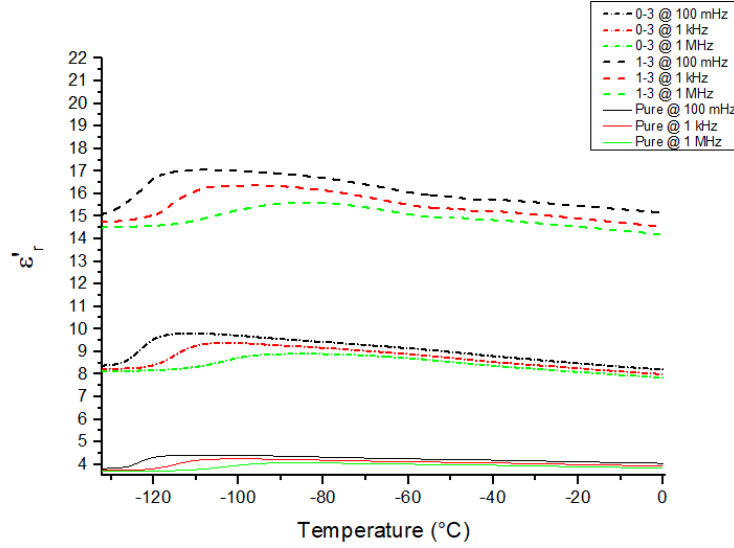


Figure 62 ϵ' vs. Temperature at 100 mHz (black curves), 1kHz (red curves) and 1MHz (green curves), for pure PDMS (continuous line), 0-3 BT/PDMS 24%v (dash and dot lines) and 1-3 BT/PDMS 24%v (dash lines).

Figure 63 reports the Arrhenius plot (τ vs. $1000/T$) for the three samples under analysis. The relaxation times were extrapolated from Havriliak-Negami fitting of the BDS plot of ϵ'' , using the WinFIT® software. The so obtained values were then used in the Arrhenius plot. The data were fitted with the Vogel-Tammann-Fulcher model (VTF), which describes the thermic dependence of the relaxation time for the glass transition temperature (Eq. 39). Indeed, the glass transition does not follow the typical Arrhenius model, (Eq. 41), hence it is not linear. The VTF theory is strongly related to the concept free volume in a polymer. The VTF equation is reported as follows:

$$\tau(T) = \tau_{0a} \exp\left(\frac{1}{(T-T_{\infty})\alpha_f}\right) \quad (39)$$

τ_{0a} is the preexponential factor, T_{∞} is a homogeneous constant at a certain temperature and α_f is the dilatation coefficient of the free volume, inverse of the temperature. α_f can be associated to the fragility parameter D , as proposed by the theory of Adam and Gibbs, following Eq. 40:

$$\alpha_f = 1/(DT_0) \quad (40)$$

Higher is D higher is the strength of the interactions. Also following Adam and Gibbs theory $T_{\infty}=T_0$. T_0 is usually $\sim T_g-30^\circ\text{K}$ and is selected by iterative procedure.

$$\tau(T) = \tau_0 \exp\left(\frac{E_a}{RT}\right) \quad (41)$$

The equation above reported is the Arrhenius equation, which describes the law temperature-relaxations associated with the relaxing entities of small dimension. E_a is the activation energy ($\text{kJ}\cdot\text{mol}^{-1}$), R is the constant of the perfect gas and τ_0 is the preexponential factor. Our data do not follow the Arrhenius law. In our results it is interesting to notice that for pure PDMS and unstructured BT/PDMS 24%v only one curve appears, which is associated

with the α transition, while 1-3 BT/PDMS 24%v presents two transitions, α and α' . Interestingly, the two relaxations for the 1-3 composite meet at higher frequencies and higher temperatures (notice that the x axis is inverted so that greater temperatures are on the right side and lower temperatures are on the left); this stands to reason since greater frequency and temperature activate the mobility of the smaller components of the chains, making it very difficult to discriminate between amorphous and restricted amorphous phases, which are distinguishable with activation of a larger portion of the polymer chains.

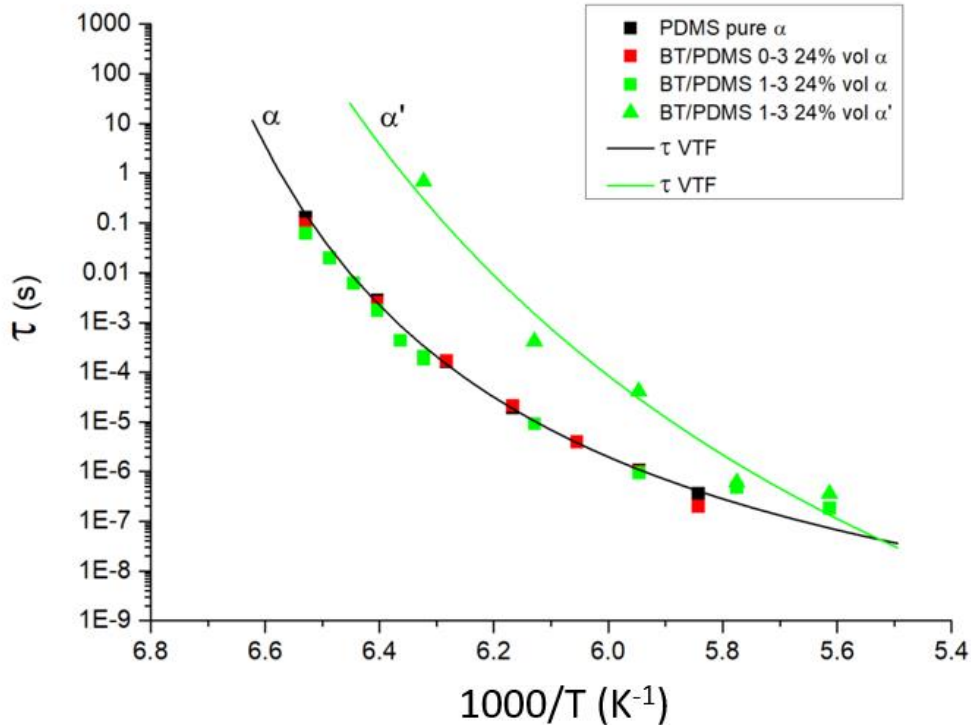


Figure 63 Arrhenius plot reporting the relaxation time τ (s) vs $1000/T$ (K^{-1}) for pure PDMS, 0-3 and 1-3 BT/PDMS 24%v. The x axis is reversed so that the high temperature is on the right side and the lower one on the left. The data are fitted with the VTF law, showing two relaxations associated with glass transition.

3.4 Conclusions

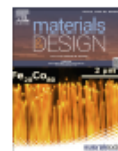
In this section we studied the effect DEP alignment of BaTiO₃ particles embedded in PDMS matrix. First, a FE analysis improved comprehension of the electric field distribution in 0-3 and quasi 1-3 connectivity, and as well as piezoelectric and dielectric characteristics, suggesting that *quasi* 1-3 composites are more performant. Subsequently a study on the DEP parameters allowed us to select the most performing in terms of frequency (1 Hz) and amplitude ($3 \text{ V } \mu\text{m}^{-1}$) of the applied electric field. Composites with different volume content (2.4%v, 12%v and 24%v) were prepared with both 0-3 and *quasi* 1-3 connectivity and compared. The results successfully confirmed an enhancement in ϵ'_r , d_{33} and g_{33} imparted by the DEP structuring. Compared to the unstructured composite (24%v), the piezoelectric charge coefficient (d_{33}) of the *quasi* 1-3 composite was enhanced by more than 3-times,

together with an increase of 2-times for the piezoelectric voltage coefficient (g_{33}). The study on piezoelectric thermal stability highlighted that the *quasi* 1-3 composite maintained good piezoelectric properties at a large temperature range. XRD analysis conducted at different temperatures (25–150°C) also confirmed the structural stability of both materials' configurations, which start to lose their piezoelectric phase at around 130°C. DMA analysis proved that DEP structuring slightly affects the mechanical properties of the composite enhancing the stiffness in the perpendicular direction of the alignment. DSC analysis allowed to understand the effect of the filler content and connectivity over the glass transition temperature, indicating that structuring 24%v of filler affects the chains polymerization, induces a second glass transition related to constrained amorphous phase and the appearance of a melting peak at -48°C, related to crystalline PDMS. Finally, DBS in temperature enabled us to verify the observation made via DSC, confirming the coexistence of an amorphous phase (α relaxation) with a constrained amorphous phase (α' relaxation) and a crystalline phase in 1-3 BT/PDMS 24%v. In conclusion 1-3 BT/PDMS designed in this work shows a good combination of mechanical and piezoelectric properties, together with low poling electric field and low ferroelectric filler volume content. Besides, the ease of production and the low cost of the materials make it extremely advantageous with respect to other organic and inorganic biocompatible piezoelectric materials, such as PVDF-based polymers. In Chapter III the structured sample developed at 24%v will be tested as biosensor for blood pressure monitoring, integrated on a FFR catheter.



Contents lists available at ScienceDirect

Materials & Design

journal homepage: www.elsevier.com/locate/matdes

Piezoelectric biosensor for smart cardiovascular grafts based on NaNbO_3 fibers/PDMS structured composite



Giulia D'Ambrogio^a, Omar Zahhaf^a, Minh-Quyen Le^a, Marine Bordet^{a,b}, Patrick Lermusiaux^b, Nellie Della Schiava^{a,b}, Richard Liang^c, Pierre-Jean Cottinet^a, Jean-Fabien Capsal^{a,*}

^a Univ. Lyon, INSA-Lyon, LGEF, EA682, F-69621 Villeurbanne, France

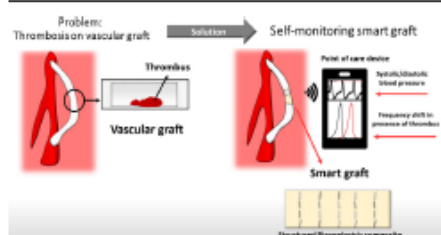
^b Groupement Hospitalier Edouard Herriot, 69003 Lyon, France

^c High-Performance Materials Institute (HPMI), Florida State University, Tallahassee, FL 32310, United States

HIGHLIGHTS

- Impact of dielectrophoresis (DEP) on fiber-based piezoelectric composites is investigated.
- The combination of fiber filler with DEP results in the greatest piezoelectric coefficient to volume content ratio yet developed.
- The structured piezoelectric composite is employed as biosensor for self-monitoring vascular grafts able to detect clot development.
- The biosensor connected to an inductive coil and implemented into a vascular simulator proves its ability to detect clots.

GRAPHICAL ABSTRACT



ARTICLE INFO

Article history:
Received 18 July 2022
Revised 15 September 2022
Accepted 22 September 2022
Available online 23 September 2022

Keywords:
Smart graft
Vascular prosthesis
Piezoelectric biosensor
Structured composite
Dielectrophoresis
Hydrothermal synthesis

ABSTRACT

An artificial graft inserted in the vascular system can cause thrombosis, which may lead to catastrophic consequences. New intelligent vascular prosthetics that can recognize the presence of clots are urgently needed. For this purpose, a novel biocompatible piezocomposite is designed for self-monitoring smart vascular grafts. The new insight of this work involves the fabrication of a composite with low filler content (5 $\text{Vol}\%$) and high piezoelectric sensitivity ($g_{31} \sim 130 \text{ mV m N}^{-1}$) suitable for biosensors. The composite is produced by structuring fibers (NaNbO_3 fibers) in elastomeric matrix via dielectrophoresis. The matrix with low elastic modulus offers great stretchability to prevent graft performance deterioration. Numerical simulation together with experimental characterizations confirm the improvements in terms of electric field distribution, dielectric and piezoelectric properties. The new composite, integrated on a graft and placed into a motorized cardiovascular simulator performs successfully online monitoring of the blood pressure, identifying anomalies related to a thrombus. The composite coupled with an inductive coil forms a resonant sensor, whose resonance frequency shifts when an occlusion develops. In the future, this system could be implemented using radio frequency identification tags (RFID-tag) to wirelessly supervise the condition of the graft, paving the way to a next generation of self-monitoring grafts. © 2022 The Authors. Published by Elsevier Ltd. This is an open access article under the CC BY-NC-ND license (<http://creativecommons.org/licenses/by-nc-nd/4.0/>).

* Corresponding author.
E-mail address: jean-fabien.capsal@insa-lyon.fr (J.-F. Capsal).

<https://doi.org/10.1016/j.matdes.2022.111195>
0264-1275/© 2022 The Authors. Published by Elsevier Ltd.
This is an open access article under the CC BY-NC-ND license (<http://creativecommons.org/licenses/by-nc-nd/4.0/>).

4. The effect of the aspect ratio: connectivity improvement via DEP structuring of fiber composites

4.1 Introduction

The conclusion of the previous chapter reveals that the connectivity of the electroactive fillers is crucial in determining the electromechanical coupling of a composite. DEP structuring apports great benefit to the performances, allowing for a substantial increase in connectivity along a selected direction; nevertheless, the use of spherical particles with low aspect ratios limits the maximal improvement due to the restricted maximum particle dimension/inter-particle distance ratio, r , that can be achieved. DEP structured composites are indeed labeled “*quasi* 1-3” as the fillers are relatively close but not in contact along the alignment axis, which we have referred to as the z -axis, and they differ from fully 1-3 composites, which have full contact of the electroactive phase along z . As matter of fact, fully 1-3 composites provide substantial benefits over ceramic bulks as well as over 0-3 and *quasi* 1-3 particle composites, including the ability to achieve higher coupling coefficients and voltage sensitivity; however the production procedures are quite complex and costly, especially to replicate on a large industrial scale [105]. Thus, the challenge is to design high connectivity composites, as close as possible to full-contact 1-3 connectivity, without introducing unduly complicated procedures. The goal is to increase the particle size/inter-particle distance ratio within the chains. In the previous sections, we demonstrated that one strategy to improve r is to properly select the amplitude and frequency of the structuring electric field, since they have a significant impact on the structure; nevertheless, the improvement is restricted because an excessively high electric field cannot be achieved due to polymer breakdown [179,202,222]. In this regard, the use of high aspect ratio fillers, such as fibers, in the manufacturing of *quasi* 1-3 composites via DEP appears to be a promising solution. Indeed, by using fibers, the r ratio along the columns may considerably increase, resulting in a minimal quantity of polymer gaps along the length of a column. This would be advantageous as the mismatch in permittivity between filler and polymer is a significant hindrance in electromechanical coupling. Fiber-alignment would result in higher dielectric and piezoelectric constants with respect to *quasi* 1-3 particles-based composites. However, the use of high permittivity fillers may lead to an excessive rise in the composites’ dielectric constant, with a consequent decrease in g_{33} , and hence in the electric field generated per unit of applied stress. To address this issue, it is crucial to select piezoelectric fillers with moderate dielectric constant.

In this section we target the role of filler aspect ratio developing biocompatible piezoelectric composites with lead-free Sodium Niobate (NaNbO_3 , or NN for a shorter name) micro-fibers (MF) and microparticles (MP) embedded in PDMS matrix. First FE analysis is used to understand the electric field distribution, and to predict the piezoelectric and the dielectric behavior in particles and fibers composites with 0-3 and *quasi* 1-3 connectivity. Then, after production of NaNbO_3 fillers via hydrothermal synthesis in micro-fiber (MF) shape, 0-3 and *quasi* 1-3 composites are elaborated with different volume fractions (1%v, 3%v and 5%v) in PDMS (samples named as NN_MF/PDMS). To better highlight the shape effect of the fillers, random and aligned composites are also made with 5%v of NaNbO_3 micro-particles, equally

produced via hydrothermal synthesis (samples named as NN_MP/PDMS). The crystalline structure of the fillers is assessed via X-ray diffraction. Scanning electron microscopy is carried out to observe the fillers and the cross section of all the composites. Dielectric broadband spectroscopy is then performed with the aim of highlighting the effect of connectivity and form factor over dielectric permittivity and losses for the fabricated samples. All the samples are poled, and the piezoelectric charge coefficients (d_{33} and g_{33}) are evaluated. Finally, DMA is used to examine the influence of structuring fibers on mechanical behavior, while DSC is employed to highlight the effect of structuring on the glass transition temperature and on chains polymerization.

4.2 DEP on high aspect ratio filler: a model description

This section describes the action of an external electric field applied on a rod immersed in fluid matrix, following the formulation expressed by Tao *et al.* [223]. The rod is modelled as an ellipsoidal particle of axes a , b and c . When an electric field is applied, two actions occur: rotational and translational. The time averaged DEP force, responsible of the translation of the fiber, is expressed as follow:

$$\langle \mathbf{F}_{DEP} \rangle = \frac{v}{4} \text{Re}[\alpha] \nabla |\mathbf{E}_0|^2 \quad (42)$$

\mathbf{E}_0 is the external applied electric field, “ v ” is the volume of the wire and α is the polarizability which is frequency dependent and relates to the parameters of medium and fiber, as well as orientation of the filler with respect to the electric field. For a homogeneous ellipsoidal particle, the polarizability along an axis j ($j = a, b, \text{ or } c$) is $\alpha_j = 3 \varepsilon_m K_j^*$, where ε_m is the permittivity of the surrounding medium and K_j^* is the frequency dependent factor, also known as complex polarizability factor expressed as follow [224]:

$$K_j^* = \frac{\varepsilon_f^* - \varepsilon_m^*}{3[\varepsilon_m^* + (\varepsilon_f^* - \varepsilon_m^*)M_j]} \quad (43)$$

ε_f^* and ε_m^* are the complex permittivity of fillers and matrix respectively. M_j is the depolarization factor along the axis j , and it reflects the ratio of the internal electric field created by charges on the surface of a dielectric when an external field is applied to the dielectric; for $a > b = c$ it is computed as follows:

$$M_a = \frac{b^2}{2a^2e^3} (\ln \frac{1+e}{1-e} - 2e) \quad (44)$$

$$M_{b,c} = \frac{1}{2}(1 - M_a) \quad (45)$$

e is the eccentricity of the ellipsoid computed as follow:

$$e = \sqrt{1 - \frac{b^2}{a^2}} \quad (46)$$

For a wire with $a \gg b = c$, it is possible to describe the effect of an external electric field over the fiber in the x-y plane. First, we start describing it considering \mathbf{E} either parallel or perpendicular to the major axis a :

$$M_{//} = M_a = 0 \quad (47)$$

$$M_{\perp} = M_{b,c} = \frac{1}{2} \quad (48)$$

Thus, it is possible to compute the time averaged F_{DEP} when a fiber is parallel or perpendicular to the electric field's lines:

$$\langle \mathbf{F}_{DEP//} \rangle = \frac{\pi R^2 L}{2} \varepsilon'_m \operatorname{Re}[K_{//}^*] |\nabla |\mathbf{E}_0|^2| \quad (49)$$

$$\langle \mathbf{F}_{DEP\perp} \rangle = \frac{\pi R^2 L}{2} \varepsilon'_m \operatorname{Re}[K_{\perp}^*] |\nabla |\mathbf{E}_0|^2| \quad (50)$$

Where R and L are the radius and the length of the fiber, and $K_{//}^*$ and K_{\perp}^* are the parallel and perpendicular complex polarizability factors, respectively. The electric field applied also generates an alignment of the ellipsoid; the orientation axis is the one with lowest depolarization factor. The torque acting on the dipole \mathbf{p} in a uniform applied electric field is

$$\mathbf{T}_{DEP} = \mathbf{p} \times \mathbf{E}_0 \quad (51)$$

Considering a rotation in the x-y plane, the DEP induced torque becomes:

$$\langle \mathbf{T}_{DEP} \rangle = \frac{\pi R^2 L}{3} \varepsilon'_m \operatorname{Re}(M_{\perp} - M_{//}) E_{//} E_{\perp} \operatorname{Re}[K_{//}^* K_{\perp}^*] \quad (52)$$

$E_{//}$ and E_{\perp} are the parallel and perpendicular components of the local electric field on the fiber. In this first description we considered only two possible cases, *i.e.*, fibers parallel or perpendicular to \mathbf{E}_0 . However, the fibers could have any orientation. To take that into consideration we assume ϱ the angle of the fiber with respect to the electric field. The electric field can thus be decomposed in parallel and perpendicular components. DEP force produced by the parallel and perpendicular components, depending on the angle orientation, can be written as follow:

$$\langle \mathbf{F}_{DEP//} \rangle = \frac{\pi R^2 L}{2} \varepsilon'_m \cos^2 \varrho \operatorname{Re}[K_{//}^*] |\nabla |\mathbf{E}_0|^2| \quad (53)$$

$$\langle \mathbf{F}_{DEP\perp} \rangle = \frac{\pi R^2 L}{2} \varepsilon'_m \sin^2 \varrho \operatorname{Re}[K_{\perp}^*] |\nabla |\mathbf{E}_0|^2| \quad (54)$$

The composition of these two components gives the total time averaged F_{DEP}

$$\langle \mathbf{F}_{DEP} \rangle = \frac{\pi R^2 L}{2} \varepsilon'_m (\cos^2 \varrho \operatorname{Re}[K_{//}^*] + \sin^2 \varrho \operatorname{Re}[K_{\perp}^*]) |\nabla |\mathbf{E}_0|^2| \quad (55)$$

In this calculus we are assuming that the dimensions of the fiber are smaller than the non-uniformity of the electric field. This is not fully correct and to address this problem it is possible to use a similar approach to the finite element method by dividing the fiber into small components where the electric field is uniform. Following this approach, we can apply the Eq.55 and the torque equation to each smaller component of the fiber, and the sum of all of them will yield the overall F_{DEP} and T_{DEP} averaged over time. It is important to note that each DEP force on each component creates an extra torque with respect to the fiber's center, which adds to the DEP torque and contributes to fiber rotation. This description is valid for a single fiber in the fluid in inhomogeneous electric field. In the situation of multiple fibers, the polarization of each fiber will cause deformation of the electric field in a fluid. A single filler will experience a net force due to distortions caused by others in its proximity. The size of the distortions is proportional to the distance between the fillers [224].

Finally, other forces, such as the Drag force and Drag torque, associated with viscosity, impede the motion and the rotation of the fiber. The Drag force contribution can be calculated as follow

$$\mathbf{F}_{Drag} = \frac{2\pi\eta L}{\ln\left(\frac{L}{R}\right)-0.5} \boldsymbol{v}_{//} - \frac{4\pi\eta L}{\ln\left(\frac{L}{R}\right)+0.5} \boldsymbol{v}_{\perp} \quad (56)$$

where η is the viscosity of the fluid, and $\boldsymbol{v}_{//}$ and \boldsymbol{v}_{\perp} are the parallel and perpendicular velocity of the fiber. In order to compute the Drag torque, the fiber is evenly divided in N segments of little cylinders. When the fiber rotates with an angular velocity ψ , each segments receive $F_{Drag i}$ related to its velocity \boldsymbol{v}_i . The Drag force on each cylinder generates a torque with respect to the center of the fiber and by summing up all the torques we can estimate the total torque reported as follow:

$$T_{Drag} = -2 \sum_{i=1}^{\frac{N}{2}} \frac{\frac{4\pi\eta L}{N}}{\ln\left(\frac{L}{NR}\right)+0.5} \psi \left[\left(i - \frac{1}{2} \right) \frac{L}{N} \right]^2 = -\frac{(N^3-N)\pi\eta L^3 \psi}{3N^3 \left[\ln\left(\frac{L}{NR}\right)+0.5 \right]} \quad (57)$$

4.3 Simulation based on finite element (FE) analysis

FE analysis (COMSOL®) is used to simulate the electric field distribution in the fiber-composites (NN_MF/PDMS) and particle-composites (NN_MP/PDMS), with 0-3 and *quasi* 1-3 connectivity. All the samples, designed with 5% volume fraction of NaNbO₃ fillers, are first subjected to a poling electric field of 30 V μm^{-1} across their thickness. Microparticles are 1 μm in diameter, whereas fibers are 1 μm in diameter and 17 μm in length. The permittivity of the matrix is set as 2.9. The filler's permittivity is set to 200 to measure the composite's permittivity, and adjusted to 130 to measure the piezoelectric coefficients, since NaNbO₃ changes its dielectric characteristics when polarized. The piezoelectric charge coefficient of the fillers is 30 pC N⁻¹ [138,195]. In the 0-3 micro-particle (MP) composite, fillers are randomly dispersed within the polymer matrix, while being aligned along the z-axis at inter-particle distance of 10 nm in the 1-3 MP composite. As displayed in **Figure 64**, the electric field in the particles is around three-fold higher when they are arranged in columns rather

than randomly dispersed. *Quasi* 1-3 connectivity allows for enhanced distribution of the electric field, as the polymer shielding effect is decreased. Similar findings have been made with micro-fiber (MF) composites: three different structures are presented (**Figure 65**): 0-3 with randomly dispersed fibers (**Figure 65-a**); *quasi* 1-3 with perfectly aligned fibers spaced 500nm apart along the z-axis (ideal case) (**Figure 65-b**) ; *quasi* 1-3 with slightly tilted fibers (real case) (**Figure 65-c**). According to the results, the best structure is the one presented in **Figure 65-b**, with fibers completely aligned and experiencing an electric field that is about 2.5 times stronger than in structure 0-3. This system, however, is ideal and challenging to replicate empirically. **Figure 65-c** depicts a more realistic case, in which the columns tend to align due to their interaction with the electric field and with each other, but without attaining perfect alignment. This structure is less effective than perfect alignment, but it clearly outperforms the random dispersion as the fibers receive twice as much electric field. As a comparison between the MF and MP composites, the electric field experienced by the MFs fillers is higher than in MP fillers both in 0-3 and *quasi* 1-3 structures (more than 4 times for the 0-3 and 3.5 for the 1-3). In addition, the distribution of the electric field in fibers is more beneficial: as shown in **Figure 65 b-c**, the field is greatest in the middle of the fibers, gradually diminishes on both sides, and reaches its minimum at the two extremities. Based on the scale color, it can be stated that a high field level is located on most of the MF surfaces. In contrast, the MP have just two maximal peaks of electric field at the two extrema, and the bulk of particles are stimulated by lower electric field values (**Figure 64-b**). To some extent, the combination of high form factor fillers and the DEP procedure appears to be the most effective. The length of the fibers is aligned parallel to the electric field lines, making it easier to properly drive and enhance the electric field. The electrical behavior undoubtedly affects the dielectric and piezoelectric characteristics of composites, which are expected to be improved using DEP.

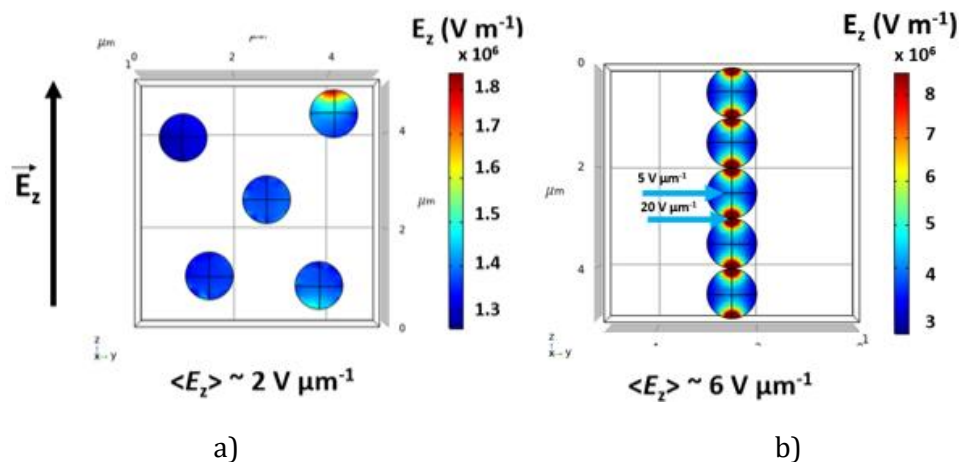


Figure 64 COMSOL® FE simulation of spherical filler composites with a) 0-3 and b) *quasi* 1-3 connectivity. For each configuration, the electric field inside the fillers is displayed, when an external field of $30 \text{ V } \mu\text{m}^{-1}$ is applied to the entire system in the z direction.

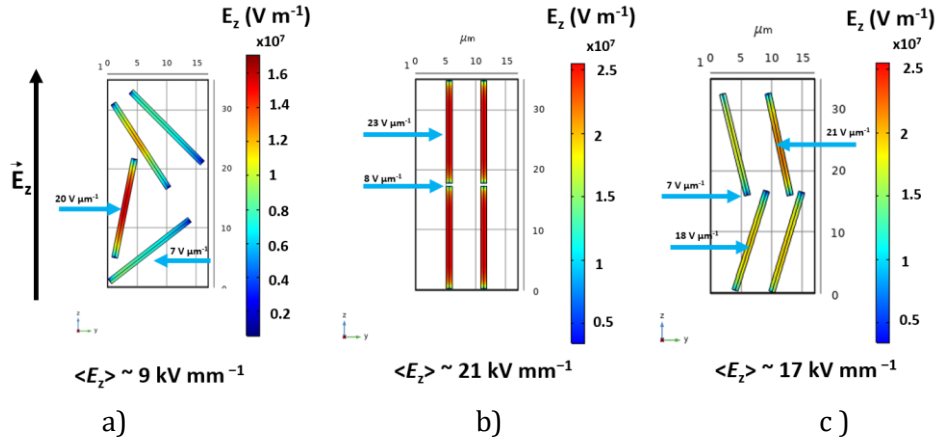


Figure 65 COMSOL® FE simulation of fibers composites with a) 0-3 connectivity, b) perfectly aligned fibers and c) slightly tilted fibers. For each configuration, the electric field inside the fillers is displayed, when an external field of $30 \text{ V } \mu\text{m}^{-1}$ is applied to the entire system in the z direction.

To further investigate the effect of structuring high aspect ratio fillers, additional FE simulation is done. Similarly to the study performed on BT/PDMS, all the systems presented are subjected to a compressive stress of 10 kPa, applied on the upper surface, which is grounded. The voltage developed across the thickness is evaluated on the bottom surface. The results reported in **Figure 66** and **Figure 67** follow what observed in the electric field analysis. For MP composites, the structured one develops a voltage 10 time higher than the non-structured one (3 mV and 0.3 mV, respectively), indicating a greater electromechanical coupling. These results are in accordance with what observed for BT/PDMS. As for MF composites, the perfectly aligned system exhibits the maximum voltage of 87.9 mV, the imperfectly aligned system produces 60.4 mV, and the random alignment almost 5.7 mV. This further proves that structuring fibers clearly enhances the piezoelectric activity of a composite, with an improvement of 15 times leading to highly performant sensors. These values are greater than for BT/PDMS due to the lower permittivity of NaNbO_3 .

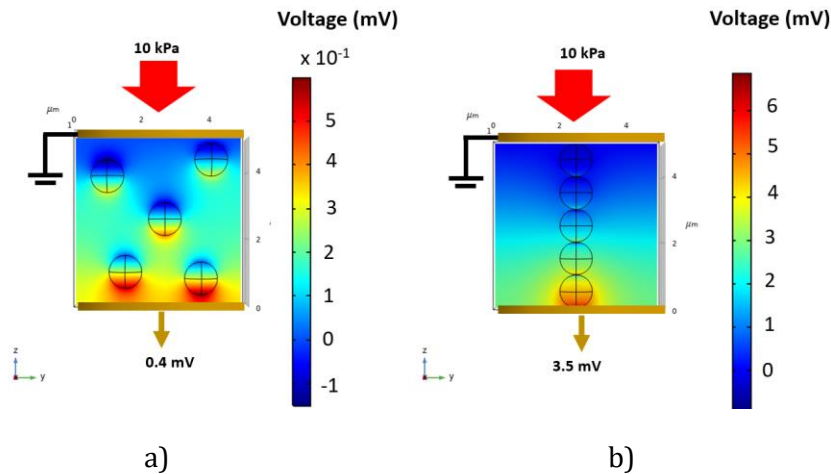


Figure 66 Voltage distribution in response to an external compressive stress of 10 kPa simulated using COMSOL® for a) 0-3 particle based composite and b) quasi 1-3 particle based composite.

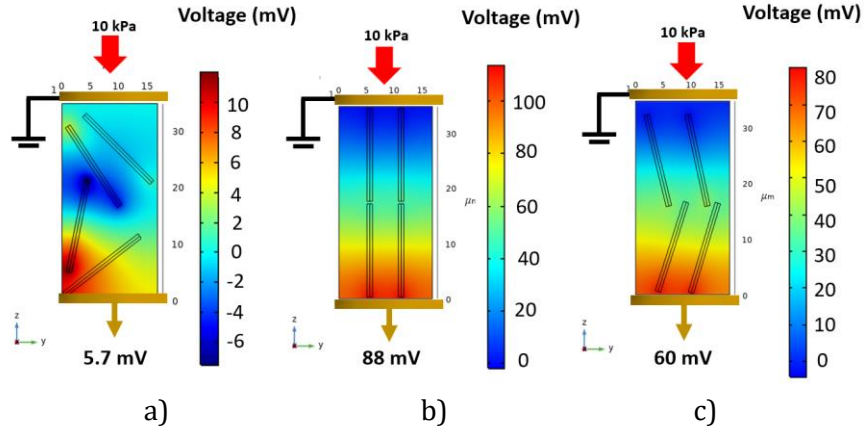


Figure 67. Voltage distribution in response to an external compressive stress of 10 kPa simulated using COMSOL® for a) 0-3 fiber composite, b) composite with perfectly aligned fibers and c) composite with slightly tilted fibers.

Following the simulation performed for BT/PDMS, permittivity, g_{33} and d_{33} of all the systems are evaluated and reported in **Table 5**. ϵ'_r was initially assessed by setting the fillers' permittivity at 200 in order to measure the composites' permittivity before to poling, while being 130 when measuring the Voltage, g_{33} and d_{33} . The results clearly support the initial assumption:

- *quasi* 1-3 connectivity improves dielectric permittivity as well as piezoelectric charge and voltage coefficients along a preferred direction, inducing anisotropy;
- additional improvement can be reached by using high form factor fillers, such as fibers, which lead to higher connectivity along the fibrils, hence better electromechanical coupling.

Finally, FE simulation is an excellent tool to explain why a higher form factor of the fillers is further advantageous over an isotropic spherical shape.

Table 5 Voltage, g_{33} D, ϵ'_r pre-poling and after poling, and d_{33} for 0-3 and 1-3 NN_MF/PDMS and NN_MP/PDMS with 5%v, simulated using COMSOL®.

Sample	Voltage [mV]	g_{33} [mV m N ⁻¹]	D [$\mu\text{C m}^{-2}$]	ϵ'_r (Permittivity NaNbO ₃ =130)	ϵ'_r (Permittivity NaNbO ₃ =200)	d_{33} [pC N ⁻¹]
0-3 NN MP/PDMS 5%v	0.3	7.5	30.0	3.4	3.4	0.2
1-3 NN MP/PDMS 5%v	3.0	60.0	37.4	4.2	4.3	2.2
0-3 NN MF/PDMS 5%v	5.7	16.3	47.0	5.3	5.8	0.8
Perfect 1-3 NN MF/PDMS 5%v	87.9	251.1	67.4	7.6	9.3	19.6
Tilted 1-3 NN MF/PDMS 5%v	60.4	172.6	59.8	6.7	7.6	10.3

4.4 Experimental results and discussion

4.4.1 X-ray Diffraction

X-ray diffraction was performed at ambient temperature to assess the crystalline structure of the fillers produced via hydrothermal synthesis. **Figure 68** reports the XRD pattern of NaNbO_3 that is identical for particles and fiber-shaped fillers. At room temperature, Sodium Niobate presents orthorhombic (R) crystalline structure (space group $Pbcm$), which is non-polar antiferroelectric, tunable to ferroelectric by applying an external electric field under high temperature conditions. The intensities and positions of the peaks, underlined by the small triangles in **Figure 68**, are consistent with the values of the orthorhombic $Pbcm$ reported in the literature[131,196,197,225].

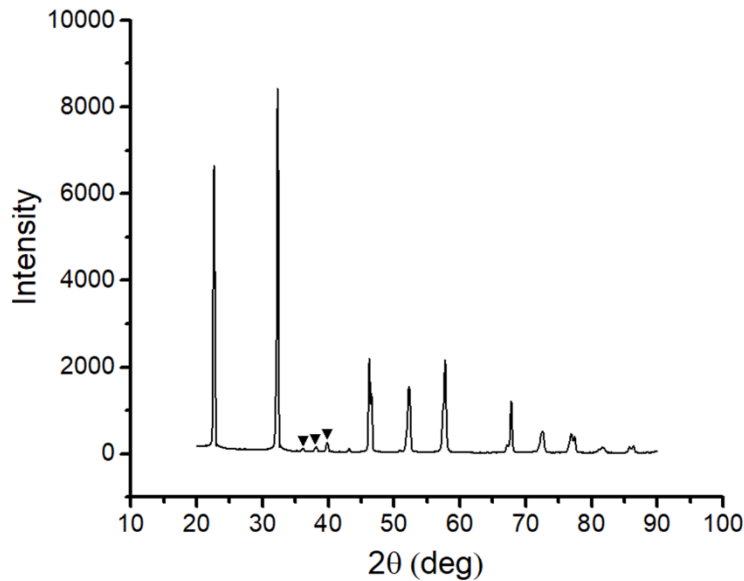
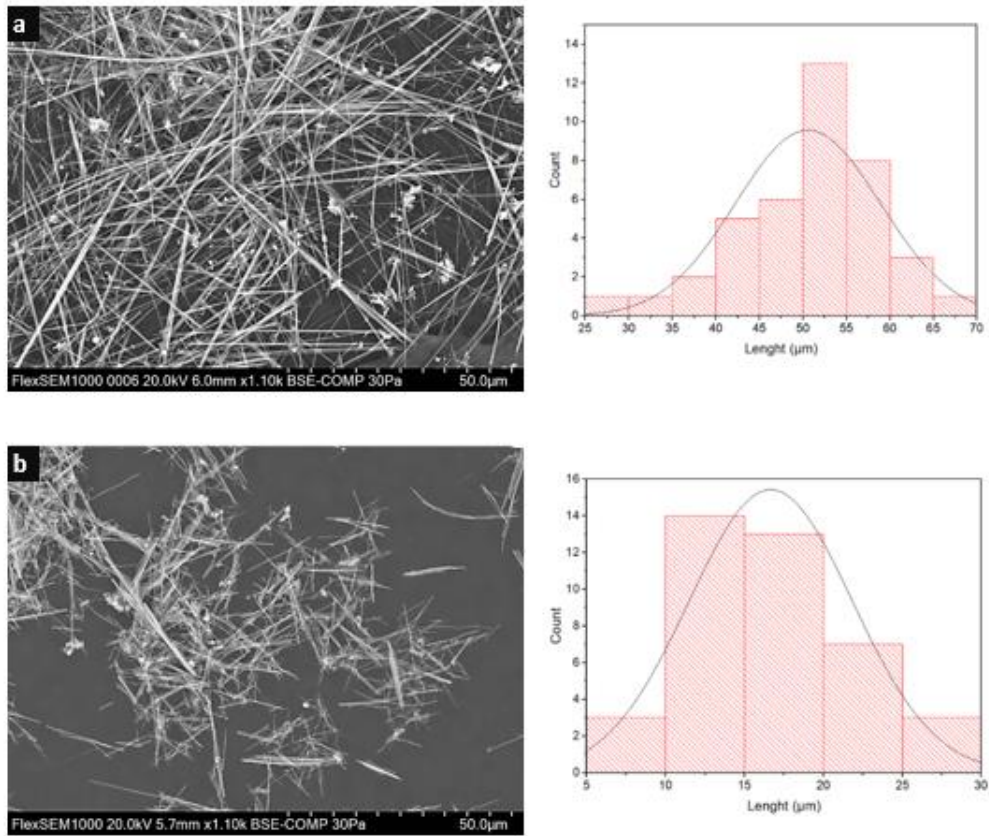


Figure 68 X-ray diffraction at 25°C of NaNbO_3 fibers and particles after 4h annealing at 600°C

4.4.2 Scanning electron microscopy (SEM)

The fillers were observed through SEM microscopy to assess their shape and size. **Figure 69 a-b** depict the fibers before and after annealing, respectively. Near to each SEM picture the distribution in length computed via ImageJ® is reported. The average length of the fibers pre- and after annealing decreased from $\sim 50 \mu\text{m}$ to $\sim 17 \mu\text{m}$. The annealing step led to a $\sim 60\%$ reduction in filler. **Figure 69-c** represents the particulate fillers with average diameter of $\sim 1.1 \mu\text{m}$, after the annealing step. The filler is clearly not spherical, but rather has an irregular polyhedral shape. Cross sectional images of the sample with 0-3 and quasi 1-3 connectivity provided insight into the phases' arrangement. **Figure 70 a-f** illustrate 0-3 and 1-3 NN_MF/PDMS with 1%v, 3%v and 5%v of fibers, respectively, while **Figure 70 g-h** represent the NN_MP/PDMS ones (5%v). All of the pictures on the left side are in 0-3 connectivity (**Figure 70 a, c, e and g**), whereas the 1-3 structured counterparts are shown on the right in **Figure 70 b, d, f and h**. When it comes to fiber-based composites with low volumetric content, the difference between 0-3 and 1-3 is obvious: while the fibers in **Figure 70-a** are homogeneously distributed and have a random inclination, the fibers in **Figure 70-b** are organized to create columns along the z-axis, *i.e.*, the structuring axis. It's interesting to note

that not all the fibers in **Figure 70-a** are completely visible; some only emerge partially from the surface because their length is not parallel to the observed surface. This is true for all of the given composites, but in the 0-3 ones it is more pronounced. The cross section cut may not be parallel to the fiber's length. When the fiber content is raised to 3% and 5%, a distinction between 0-3 and 1-3 may still be visible: in contrast to 0-3 composites, where fibers maintain their random distribution, in 1-3 ones fibers clearly exhibit an overall orientation parallel to the field direction (z axis) [226]. Regarding the composites containing 5%v particles, the influence of electric-field structuration is visible in their cross sections reported in **Figure 70 g-h**. As opposed to **Figure 70-g**, where the particles are spread throughout the volume, **Figure 70-h** shows the particles reorganized into thick columns. SEM enabled us to analyze and compare the structural differences of composites with various types of fillers, volumetric contents, and connectivity, hence validating the achievement and degree of structuration.



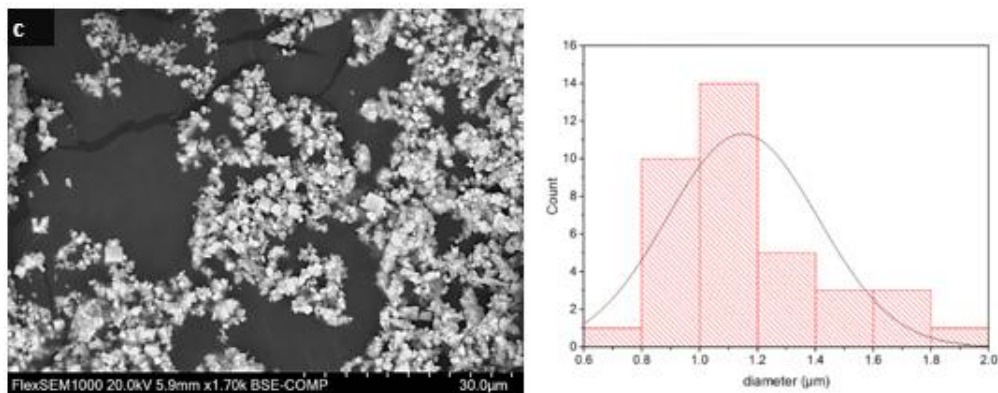
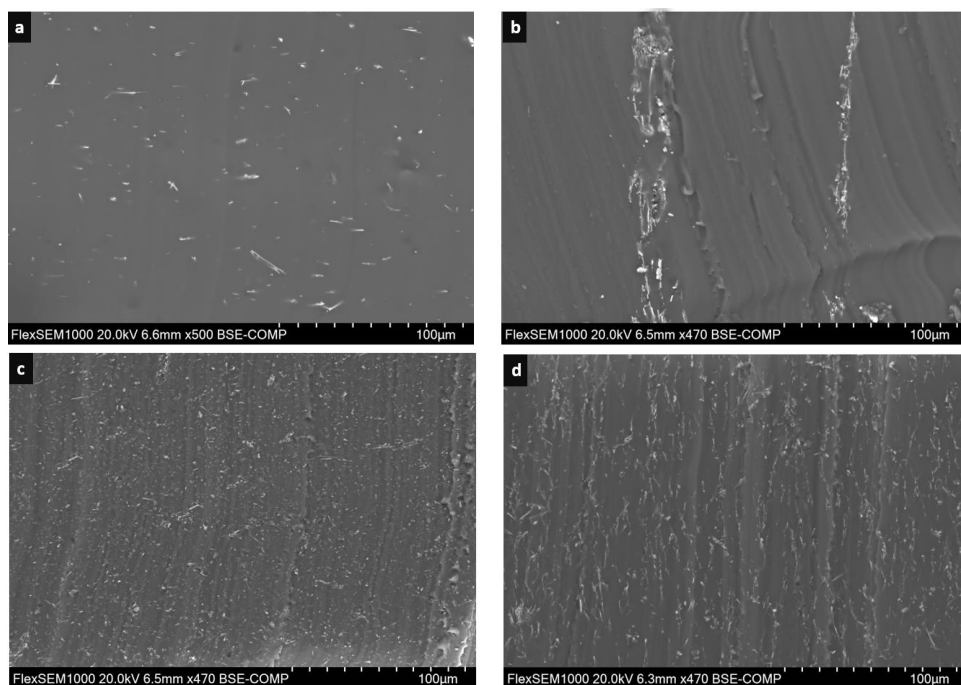


Figure 69 SEM images depicting a) $\text{Na}_2\text{Nb}_2\text{O}_6$ fibers produced via hydrothermal synthesis prior to annealing, b) NaNbO_3 fibers annealed for 4 hours at 600°C , c) NaNbO_3 particles produced via hydrothermal synthesis and annealed for 4 hours at 600°C . Near to each picture the distribution in length (for fibers) or diameter (for particles), computed via ImageJ[®], is reported.



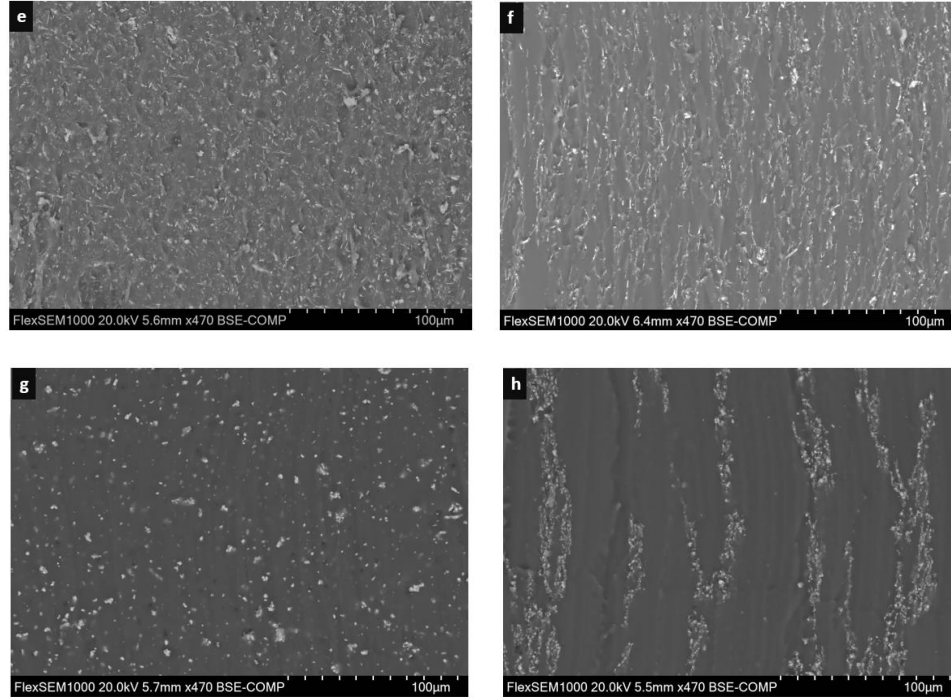


Figure 70 Images acquired by SEM of a) 1%v NN_MF/PDMS with 0-3 connectivity, b) 1%v NN_MF/PDMS with quasi 1-3 connectivity, c) unstructured NN_MF/PDMS 3%v, d) structured NN_MF/PDMS 3%v, e) unstructured NN_MF/PDMS 5%v, f) structured NN_MF/PDMS 5%v, g) 0-3 NN_MP/PDMS 5%v, h) 1-3 NN_MP/PDMS 5%v.

4.4.3 Dielectric spectroscopy

BDS was performed on both random and structured micro-fiber composites (NN_MF/PDMS) elaborated with different volume fractions, between 10^{-1} to 10^6 Hz, at room temperature. All samples were characterized across their thickness to assess the effect of structuration along the alignment direction. Furthermore, to highlight the influence of the connectivity as well as of the filler's form factor on the dielectric properties, fiber-based composites were compared to 0-3 and *quasi* 1-3 particle-based composites (NN_MP/PDMS) doped with the same filler concentration (5%v). **Figure 71 a-b** report the real part of the relative permittivity (ϵ'_r) vs. frequency for 0-3 and *quasi* 1-3 fiber composites respectively, at 1%v, 3%v and 5%v compared with pure PDMS. 1-3 NN_MF/PDMS structured with $4 \text{ V } \mu\text{m}^{-1}$ are not reported in BDS analysis, but their permittivity at 1 kHz will be explored later in this section. As previously discussed for BT/PDMS composites (subsection 3.3.3), we can discern several frequency ranges linked to various phenomena in the BDS analysis. Interfacial polarization and electrode polarization (both less than 1 Hz) and dipolar polarization (1- 10^6 Hz) are observed within the range analyzed in our characterization. For each sample under investigation, the plots of the real relative permittivity are similar in shape. Starting at 10^6 Hz and decreasing the frequency, there is a slight increase in the real part of the relative permittivity as the dipoles can follow more efficiently the fluctuation of the applied field, leading to increased polarization. This rise becomes more pronounced in the presence of interfacial and electrode polarization (below 1 Hz). Additionally, we can observe that:

- The addition of fillers to the matrix induces a rise in ϵ'_r over the whole frequency range. This increase is the result of the filler's permittivity, which is around 70 times higher than the matrix's one.
- Regardless of the frequency, switching from 0-3 to *quasi* 1-3 connectivity always causes a rise in ϵ'_r , because the density of the dipoles increases in the direction of the applied electric field.

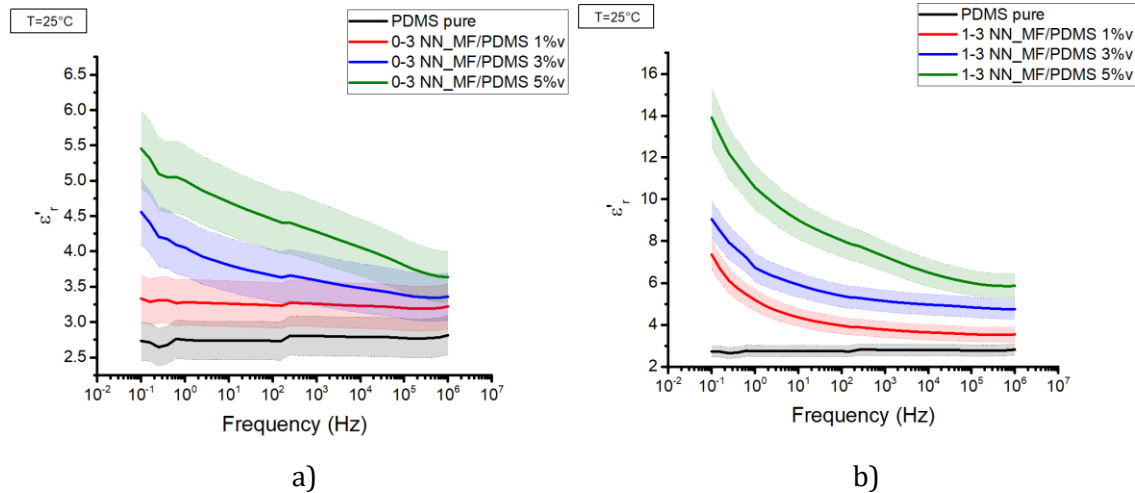


Figure 71 Relative permittivity real for a) PDMS and 0-3 NN_MF/PDMS with 1, 3 and 5%v and b) PDMS and 1-3 NN_MF/PDMS with 1, 3 and 5%v.

As reported in **Figure 72 a-b**, all composites have relatively low losses that only slightly rise at low frequencies due to interfacial polarization and space charge, as well as conductivity of ionic species present in the material. For 0–3 composites, increasing the filler content also results in a slight but discernible increase in losses. The same applies to structured composite, however this rise is greater. In general, it has been shown that adding filler to a polymeric matrix causes losses to rise, and the more the filler added, the greater the losses. This has to do with an increased number of interfaces, which might be related to the Maxwell-Wagner-Sillars interfacial polarization. The conductivity and permittivity differences between the matrix and filler at the interface cause a buildup of charges that locally redistribute the electric field, as has already been observed in various investigations [203]. Another reason behind the low frequencies rise in losses might be the role of conductivity. According to Kremer *et al.*, in heterogeneous systems composed of fillers embedded in polymeric matrix, a water conductive layer exists between the filler and the matrix itself. This is brought on by the filler's propensity to surface-adsorb water from the surrounding environment [203]. As a result, conductive related losses develop. Presence of ionic species due to the synthesis of the filler, residual salts for instance, may also play a role in the conductivity. This tendency seems to be more pronounced in 1-3 composites. It's conceivable that fillers arranged in columns may provide routes for the charges to follow, strengthening this effect. Other works reported similar findings [227]; Regardless, the composite losses are less than 30%.

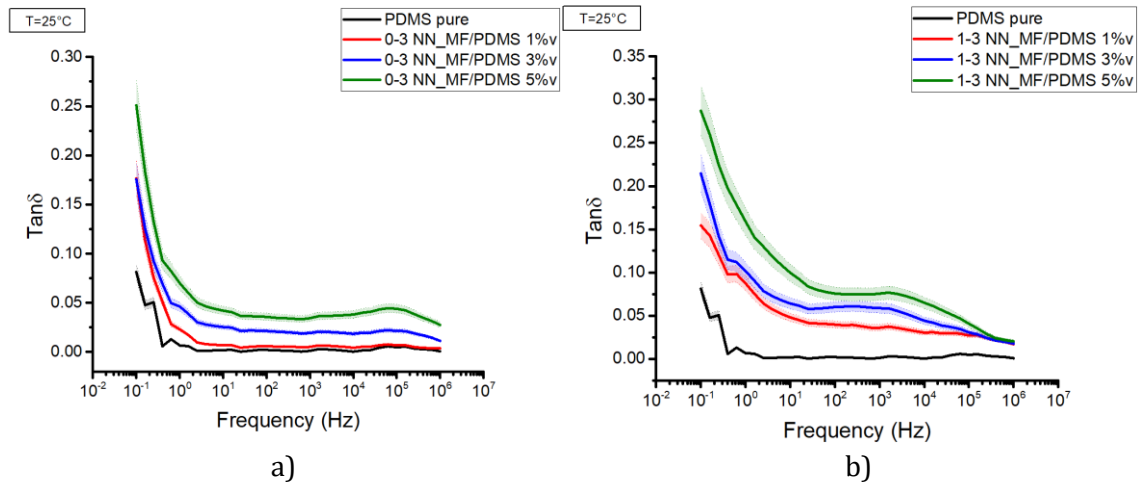


Figure 72 Loss tangent for a) PDMS and 0-3 NN_MF/PDMS with 1%v, 3%v and 5%v and b) PDMS and 1-3 NN_MF/PDMS with with 1%v, 3%v and 5%v.

Similar results to those reported for fiber-based composites were discovered for 0-3 and 1-3 NN_MP/PDMS composites (**Figure 73 a-b**). Only a volumetric concentration of 5%v is examined in this instance. In terms of permittivity, the pure PDMS (black curve) has a lower value than the 0-3 composite (red curve). The permittivity is raised by the addition of filler. Structuring the filler provides a further increase in permittivity (blue curve). With the addition of filler, dielectric losses rise as well, especially in the interfacial polarization region. DEP structuring, just like for fiber-based composites, causes an additional rise in losses at low frequencies, probably due to ionic species and salts from the hydrothermal synthesis.

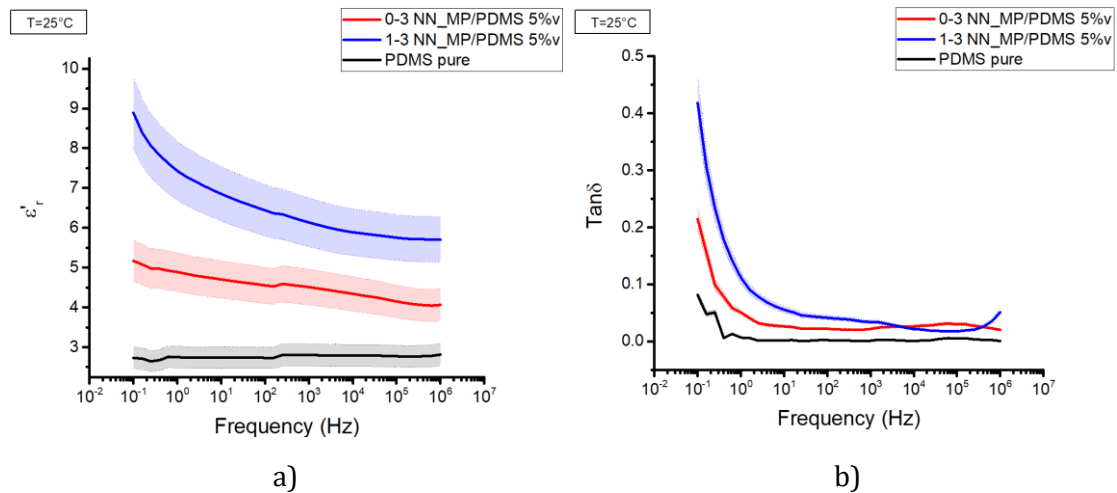


Figure 73 a) Relative permittivity real part and b) dielectric loss tangent for PDMS and NN_MP/PDMS 5%v with 0-3 and 1-3 connectivity.

Figure 74-a reports the ϵ_r' at 1 kHz at room temperature as function of the filler content for both 0-3 and 1-3 NN_MF/PDMS composites structured with $6 \text{ V } \mu\text{m}^{-1}$. This plot allows to better visualize the dependence of ϵ_r' over volume content and connectivity. As observed in the BDS analysis, whatever the connectivity, higher filler concentration gives rise to an increase in the permittivity, as the filler has a much higher ϵ_r' than the polymer. No higher

volume contents than 5%v were reported as the viscosity of the blend would be too high and there would not be enough freedom of movement for the fibers to properly orient and move to build columns as reported in other studies of DEP-fiber composites [227]. Overall, *quasi* 1-3 composites achieve greater ϵ'_r than the 0-3 one regardless of filler content. As previously explained, structuring provides anisotropy in the dielectric properties, which are clearly improved along the columnar direction as fillers are closely packed and less shielded by the matrix. Concerning the other directions, however, ϵ'_r is supposed to be lower in the *quasi* 1-3 composite, in contrast to the 0-3 composites, whose behavior may be the same or enhanced as the fibers tends to be flat, due to the lowest energy configuration [179,222]. To assess the effect of the electric field amplitude on the quality of the structure, composites with fillers content of 1%v, 3%v and 5 %v were also structured with $4 \text{ V } \mu\text{m}^{-1}$ and their permittivity was compared to those structured with $6 \text{ V } \mu\text{m}^{-1}$. Examining the results reported in **Figure 74-b**, *quasi* 1-3 composites structured with $4 \text{ V } \mu\text{m}^{-1}$ exhibit superior dielectric properties than the non-structured (reported in **Figure 74-a**), nonetheless inferior to those structured with $6 \text{ V } \mu\text{m}^{-1}$. These results confirm that increasing the amplitude of the electric field brought the fibers closer together and improved their alignment. While this is consistent with what has been observed for BT/PDMS, we were able to significantly increase the amplitude of structuration for NN based composites. Indeed, the difference in permittivity between matrix and NN fillers is ten times smaller, implying a lower likelihood of polymer breakdown due to a local enhancement in the electric field. Nonetheless, using electric fields greater than $6 \text{ V } \mu\text{m}^{-1}$ would have resulted in break down during the structuring.

Table 6 Real part of dielectric permittivity at 1 kHz, for all the composite of NN_MF/PDMS and NN_MP/PDMS.

Volume fraction (%v)	ϵ'_r	ϵ'_r	ϵ'_r	ϵ'_r	ϵ'_r
	NN_MF/PDMS 0-3	NN_MF/PDMS 1-3 ($4 \text{ V } \mu\text{m}^{-1}$)	NN_MF/PDMS 1-3 ($6 \text{ V } \mu\text{m}^{-1}$)	NN_MP/PDMS 0-3	NN_MP/PDMS 1-3
0%	2.85±0.3	2.85±0.3	2.85±0.3	2.85±0.3	2.85±0.3
1%	3.2±0.3	3.5±0.3	3.6±0.3	/	/
3%	3.5±0.3	4.6±0.4	5.1±0.5	/	/
5%	4.2±0.4	6.7±0.7	7.2±0.7	4.2±0.4	6.2±0.6

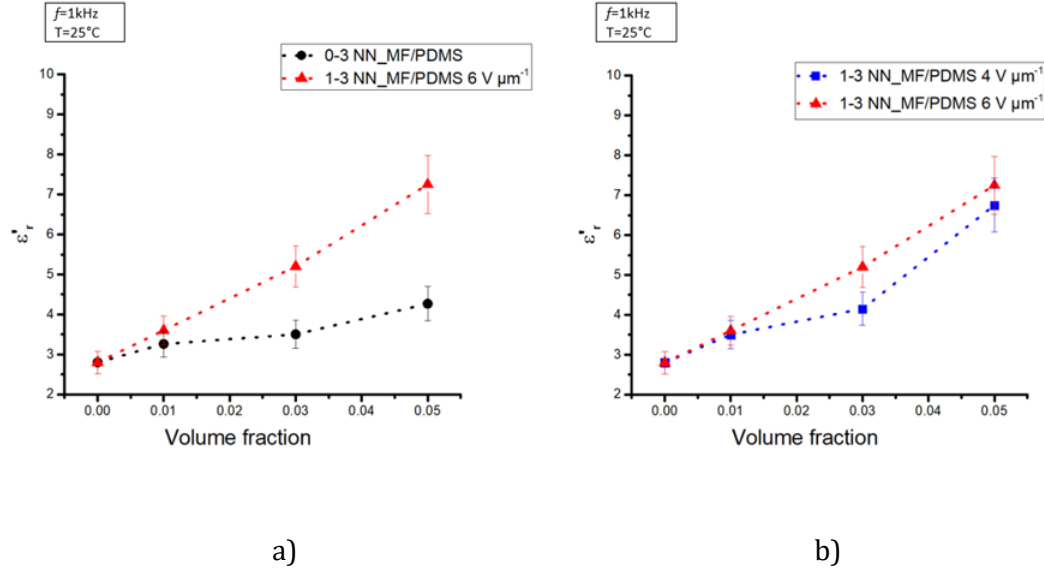


Figure 74 Real part of dielectric constant (ϵ'_r) versus fiber volume content for a) 0-3 and 1-3 NN_MF/PDMS structured with $6 \text{ V } \mu\text{m}^{-1}$ b) 1-3 NN_MF/PDMS structured with $4 \text{ V } \mu\text{m}^{-1}$ and $6 \text{ V } \mu\text{m}^{-1}$.

Table 7 reports a comparison between the experimental results and the COMSOL® simulations. It is interesting to notice that the results follow the trends reported by FE simulation, with however some discrepancies. The major difference is found for 0-3 fiber-based composites where distribution of the fibers is difficult to predict and model. In our simulation the fibers were randomly oriented, and this led to a higher permittivity with respect to the one observed empirically, nonetheless in reality fibers may tend to be flat, (*i.e.*, low angle of inclination), as it is the equilibrium position in 0-3 fibers composites. On the other hand, 1-3 fiber-based composites are matching the simulation results relative to 1-3 composites with tilted fibers. Another relevant element that could justify the differences is related to the fillers size distribution which is not homogeneous. Next, we compared particle and fiber-based composites with 0-3 and *quasi* 1-3 connectivity and with a volume fraction of 5%v to examine the impact of high aspect ratio on ϵ'_r .

Table 7 Comparison between experimental permittivity and FE permittivity at 5%v for fiber and particle-based composites with 0-3 and *quasi* 1-3 connectivity.

Sample	ϵ'_r <i>experimental</i>	ϵ'_r FE simulation
0-3 NN_MF/PDMS 5%v	4.2 ± 0.4	5.8
1-3 NN_MF/PDMS 5%v ($6 \text{ V } \mu\text{m}^{-1}$)	7.2 ± 0.7	7.6 (tilted) 9.2 (perfect)
0-3 NN_MP/PDMS 5%v	4.0 ± 0.4	3.4
1-3 NN_MP/PDMS 5%v	6.2 ± 0.6	4.3

The data are reported in **Table 6** and displayed in **Figure 75**. A 50% improvement in ϵ'_r is found in DEP-structured MP composites with respect to 0-3 ones. Nonetheless, regardless of the connectivity, composites with particles exhibit always lower ϵ'_r than those with fiber-shaped fillers. Additionally, the percentage of improvement for fiber-based composite is higher (~70%). As predicted by COMSOL® simulation (section 4.3), the form factor strongly affects the electric field distribution in the fillers, playing a fundamental role in the composite dielectric properties. This is true for 1-3 connectivity, however in 0-3 connectivity, there isn't a significant difference in the use of fibers or particles. Indeed, the connectivity of structured NN_MP/PDMS defined as *quasi* 1-3 where the particles within a column are more spaced and shielded by the polymer, leads to lower ϵ'_r than an ideal fully 1-3 connectivity. On the other hand, in NN_MF/PDMS, greater connectivity is achieved along the alignment axis due to the form factor of the fibers, *i.e.*, closer to a fully 1-3 connectivity. In other words, in fiber-based composites there should be a higher ratio r (filler dimension/inter-fillers distance). The empirical values that we reported for particles composites are somewhat higher with respect to those found via FE simulation: for 0-3 particle composites on one side the value that we found was 3.4, while experimentally we found 4 ± 0.4 , thus we can consider the results quite in good agreement; the main difference may be related to the ideality of the FE model, which does not take into account the particle size distribution, as well as the aggregation; indeed, the distribution of fillers in the volume is recreated in an ideal or near-ideal way. The comparison between experimental and FE simulations data is reported in **Table 7**. Additionally, and more importantly the NN particles were modeled with spherical morphology, while it is quite clear from the SEM investigation that the shape is polyhedral and irregular. For what concern the results reported for *quasi* 1-3 particle composites the value that we computed via FE modeling was 4.3 while the value that we empirically measured is 6.2 ± 0.6 . This discrepancy might be also related to the spacing between the particles, which, in reality, is less than 10 nm, as we modeled with COMSOL®, and again to the ideality of spherical particles, clearly not perfectly representative of NN microparticles.

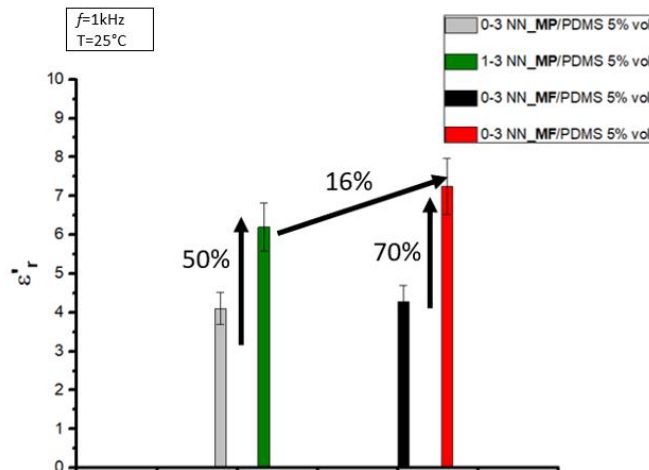
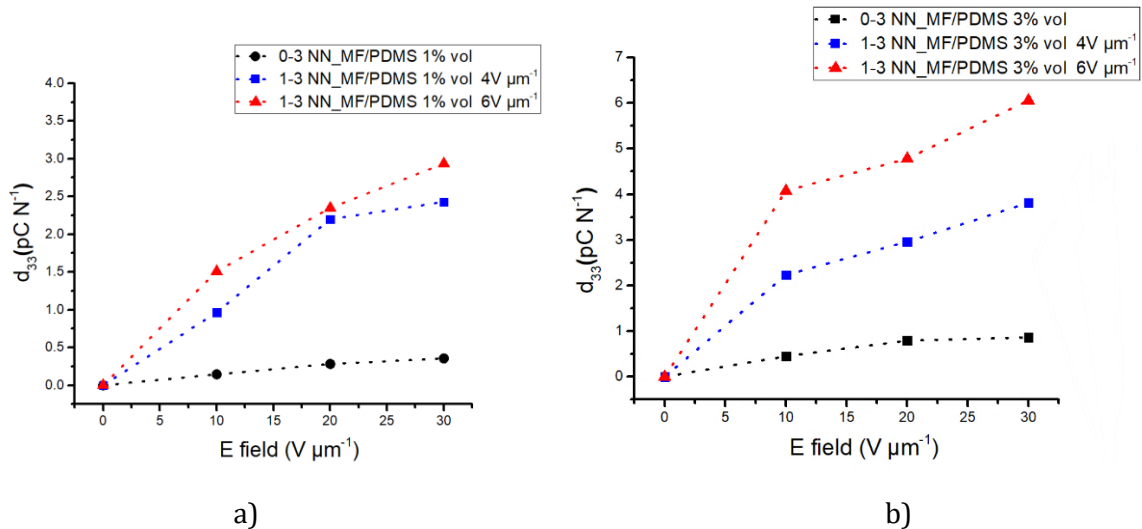


Figure 75 ϵ'_r for 5%v NN_MP/PDMS and NN_MF/PDMS composites in both 0-3 and quasi 1-3 connectivity. The arrows indicate the increasing rate of ϵ'_r achieved by DEP structuration, and the increase of ϵ'_r related to the shape of the filler in quasi 1-3 composites.

4.4.4 Piezoelectric analysis

In ferro/antiferroelectric composites, an optimal electric field distribution is required in order to reach full polarization of the fillers (*i.e.*, close to saturation of the charge displacement) and thus maximize d_{33} . In this regard, the shape and connectivity of the fillers are the key factors. As described in subsection 2.3.5, all samples were poled up to $30 \text{ V } \mu\text{m}^{-1}$, and their piezoelectric charge coefficient (d_{33}) was tested by *Berlincourt* method. First the saturation of polarization was evaluated by poling all the composite at 10, 20 and $30 \text{ V } \mu\text{m}^{-1}$. Electric fields higher than $30 \text{ V } \mu\text{m}^{-1}$ pose a substantial likelihood of breakdown and thus are not reported. From the results, reported in **Figure 76 a-d** we can state that:

- None of the composites fully reaches saturation of polarization, as the values of d_{33} do not reach a plateau;
- *quasi* 1-3 composites reach higher values of d_{33} rather than the 0-3 counterparts, no matter the filler content and poling field;
- fiber-composites structured at $6 \text{ V } \text{mm}^{-1}$ are always more piezoelectric than those structured at $4 \text{ V } \text{mm}^{-1}$, suggesting a better distribution of the electric field during the poling.
- Composites with 5%v of particles appear to be further from saturation than their fiber-based counterparts (**Figure 75 b-c**) in agreement with the FE results reported in subsection 4.2.



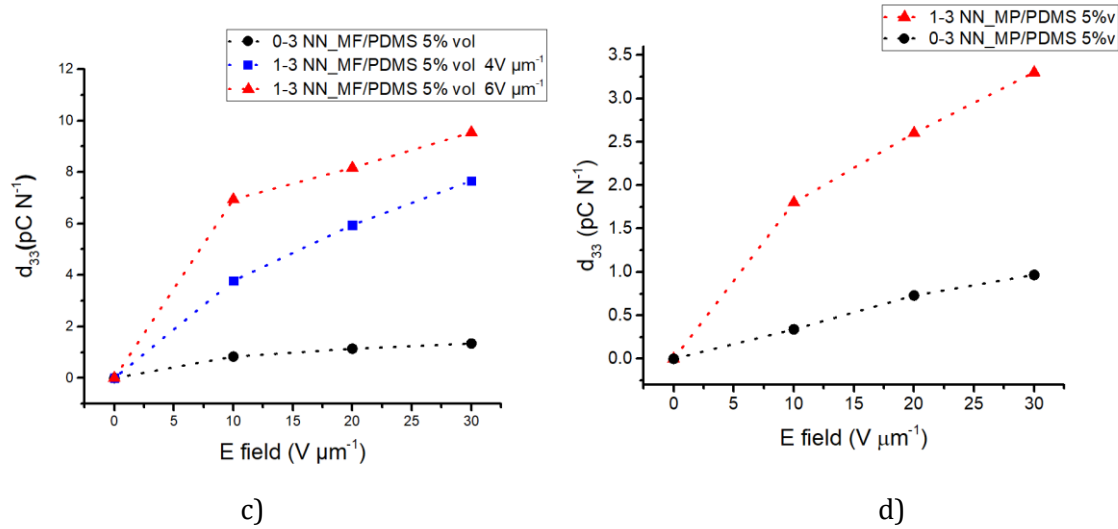


Figure 76 Saturation of poling field for non-structured and structured composites (4 and $6\text{V } \mu\text{m}^{-1}$) with a) 1%v of NN fibers, b) 3%v of NN fibers, c) 5%v of NN fibers and d) 5%v of NN particles.

The variation of d_{33} over the volumetric content for 0-3 and 1-3 NN_MF/PDMS samples is reported in **Table 8** and plotted in **Figure 77 a-b**. Quasi 1-3 composites ($6\text{V } \mu\text{m}^{-1}$) exhibits higher d_{33} with respect to the 0-3 ones, at any filler percentage (**Figure 77 a**). For instance, at 5%v, d_{33} of NN_MF/PDMS structured with $6\text{V } \mu\text{m}^{-1}$ is over 7 times higher than its 0-3 counterpart. **Figure 77 b** represents d_{33} vs. volume fraction of fibers for composites structured with 4 and $6\text{V } \mu\text{m}^{-1}$. When structuring at $6\text{V } \mu\text{m}^{-1}$, the piezoelectric constant is larger, which supports our previous statement: as the strength of the structuring electric field grows, the degree of fiber structuring increases. **Table 10** provides a comparison between the experimental results with the simulation of section 4.3. The experimental values are slightly higher compared to those from the FE simulation, but they still fall within the same range of values. According to our results, the FE structure in **Figure 43 c** (fibers almost aligned but tilted presented in section 4.3) accurately reflects the structured composite containing 5%v fibers.

Table 8 d_{33} for 0-3 and 1-3 NN_MF/PDMS and NN_MP/PDMS composites developed in this work.

Volume fraction (%v)	d_{33} (pC N^{-1}) NN_MF/PDMS 0-3	d_{33} (pC N^{-1}) NN_MF/PDMS 1-3 ($4\text{V } \mu\text{m}^{-1}$)	d_{33} (pC N^{-1}) NN_MF/PDMS 1-3 ($6\text{V } \mu\text{m}^{-1}$)	d_{33} (pC N^{-1}) NN_MP/PDMS 0-3	d_{33} (pC N^{-1}) NN_MP/PDMS 1-3
1%	0.35 ± 0.04	2.20 ± 0.22	2.90 ± 0.30	/	/
3%	0.86 ± 0.09	3.81 ± 0.38	6.00 ± 0.60	/	/
5%	1.34 ± 0.13	7.60 ± 0.76	9.54 ± 0.95	0.90 ± 0.09	3.30 ± 0.3

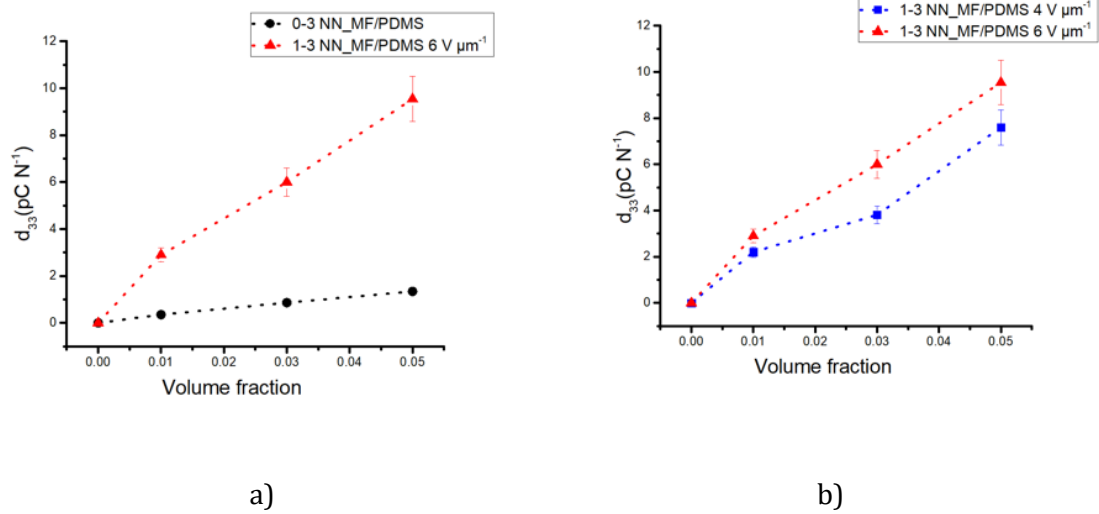


Figure 77 a) Piezoelectric charge coefficient (d_{33}) plotted as function of fibers volume content for unstructured and structured ($6 \text{ V } \mu\text{m}^{-1}$) NN_MF/PDMS composites. b) d_{33} vs. filler content for NN_MF/PDMS composites structured with 4 and $6 \text{ V } \mu\text{m}^{-1}$.

Figure 78 compares 0-3 and *quasi* 1-3 NN_MP/PDMS and NN_MF/PDMS, each with 5%v of fillers. In contrast to the 7-times improvement for fiber-based composites, structuring of particle-based composites only increases piezoelectricity by 3.5 times. Combining DEP together with fiber-shaped fibers significantly improves the sensitivity of the composite, explaining why the 1-3 NN_MF/PDMS leads to a threefold rise in d_{33} compared to the equivalent structured particle composite. These results agree with the dielectric analysis and the FE summarized in **Table 10**. Structured fiber-composites achieve a condition much closer to full-contact 1-3 connectivity rather than particles-based composites. In such a configuration, there is a redistribution of the filler that induces anisotropy, resulting in considerably enhanced piezoelectric activity along the alignment axis. Besides, the filler experiences stronger polarization in *quasi* 1-3 fiber-composites than in 0-3 ones, resulting in a larger piezoelectric constant [222]. All the results for d_{33} analysis are summarized in **Table 8**.

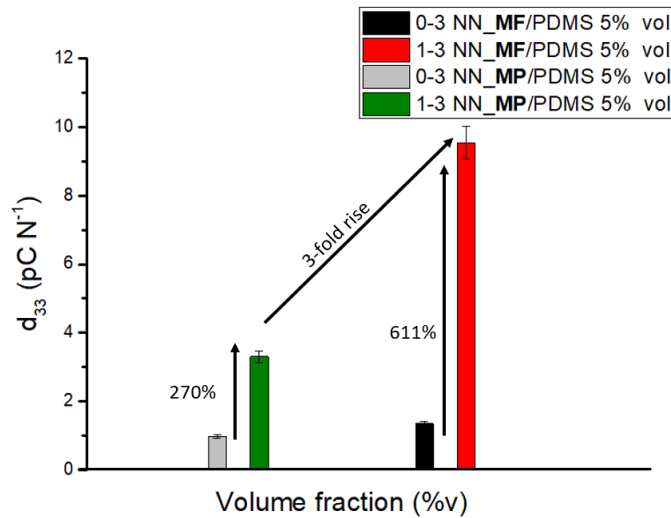


Figure 78 d_{33} of 5%v NN_MP/PDMS and NN_MF/PDMS in 0-3 and quasi 1-3 connectivity ($6 \text{ V } \mu\text{m}^{-1}$). The arrows indicate the increasing rate in d_{33} achieved by structuring for both particle and fiber composites, and the rise in d_{33} from structured NN_MP/PDMS to structured NN_MF/PDMS.

Finally, the piezoelectric voltage coefficient, g_{33} , was computed according to Eq.37 and reported in **Figure 79 a-b** and **Table 9**. The results confirmed that fiber-structured composites develop higher electric field per unit of external stress, meaning higher g_{33} , than 0-3 NN_MF/PDMS, at each volume content. Again, an electric field amplitude of $6 \text{ V } \mu\text{m}^{-1}$ enhances more the properties rather than $4 \text{ V } \mu\text{m}^{-1}$. Additionally, structured composites made of fibers achieve g_{33} that are more than twice as high then a structured particle-based composites (**Figure 79-b**).

Table 9 g_{33} for 0-3 and 1-3 NN_MF/PDMS and NN_MP/PDMS developed in this work.

Volume fraction (%v)	g_{33} (mV m N ⁻¹) NN_MF/PDMS 0-3	g_{33} (mV m N ⁻¹) NN_MF/PDMS 1-3 ($4 \text{ V } \mu\text{m}^{-1}$)	g_{33} (mV m N ⁻¹) NN_MF/PDMS 1-3 ($6 \text{ V } \mu\text{m}^{-1}$)	g_{33} (mV m N ⁻¹) NN_MP/PDMS 0-3	g_{33} (mV m N ⁻¹) NN_MP/PDMS 1-3
	1%	12 ± 0.3	71 ± 0.5	91 ± 0.6	/
3%	27 ± 0.4	107 ± 0.8	130 ± 1.1	/	/
5%	35 ± 0.5	123 ± 1.5	148 ± 1.5	24.2 ± 0.5	60 ± 1

The empirical values fall within the same range of values as those reported in the FE analysis and exhibit the same trend. The minor discrepancies between modeling and experimental results are most likely due to the causes mentioned in subsection 4.4.3. Despite this, the values' trend is fairly congruent with the FE simulation, and the tendency of improvement acquired through structuring and fiber-use is respected. The results that are most in conflict are those for composites 0-3, suggesting that conglomerates and sedimentation are likely to have a substantial impact on the measurements obtained. A comparison is summarized in **Table 10**.

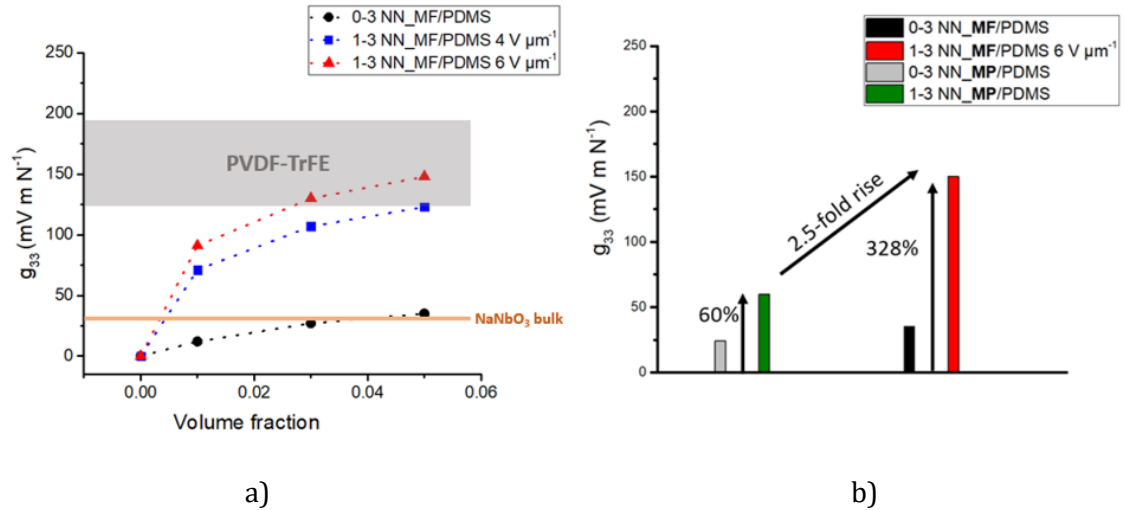


Figure 79 a) g_{33} in function of fibers volume content for 0-3 non-structured composites and quasi 1-3 composites structured with 4 and 6 $\text{V } \mu\text{m}^{-1}$; b) g_{33} of 5%v NN_MP/PDMS and NN_MF/PDMS in 0-3 and quasi 1-3 connectivity ($6 \text{ V } \mu\text{m}^{-1}$). The arrows indicate the increasing rate in g_{33} achieved by structuring for both particle and fiber composites, and the rise in d_{33} from structured NN_MP/PDMS to structured NN_MF/PDMS.

Table 10 Comparison between the experimental results and the FE analysis for particle and fiber-based composites at 5%v of filler (0-3 and 1-3 connectivity).

Sample	d_{33} (pC N^{-1})	d_{33} (pC N^{-1})	g_{33} (pC N^{-1})	g_{33} (pC N^{-1})
	experimental	FE simulation	experimental	FE simulation
0-3 NN_MF/PDMS 5%v	1.34 ± 0.13	0.8	35 ± 0.5	16.3
1-3 NN_MF/PDMS 5%v ($6 \text{ V } \mu\text{m}^{-1}$)	9.54 ± 0.95	10.3 (tilted) 19.6 (perfect)	148 ± 1.5	172.6 (tilted) 251.1 (perfect)
0-3 NN_MP/PDMS 5%v	0.9 ± 0.09	0.2	24.2 ± 0.5	7.5
1-3 NN_MP/PDMS 5%v	3.3 ± 0.3	2.2	60 ± 1	60

4.4.5 Dynamic Mechanical Analysis (DMA)

DMA was performed to assess the effect of structuring over the elasticity of the composites. The storage (Y') and loss moduli (Y'') are reported in function of the frequency (1, 25 and 50 Hz), for 0-3 fiber composites (**Figure 80 a-b**), and quasi 1-3 fiber composites for all the filler volume fractions produced (**Figure 81 a-b**). As the frequency increases both Y' and Y'' increase, no matter the volume content or the connectivity. This is consistent with the observation made for BT/PDMS; rising the frequency leads to increased energy on the chains as well as increase of losses as the chains are unable to follow the mechanical cycles, thus more energy is dissipated. Filler volume fraction directly influences both storage and dissipation moduli as the fillers impart their high stiffness as well as obstacle chains

movement. Similar frequency behavior is followed by NN_MP/PDMS 0-3 and *quasi* 1-3 with 5%v particles (**Figure 83 a-b**).

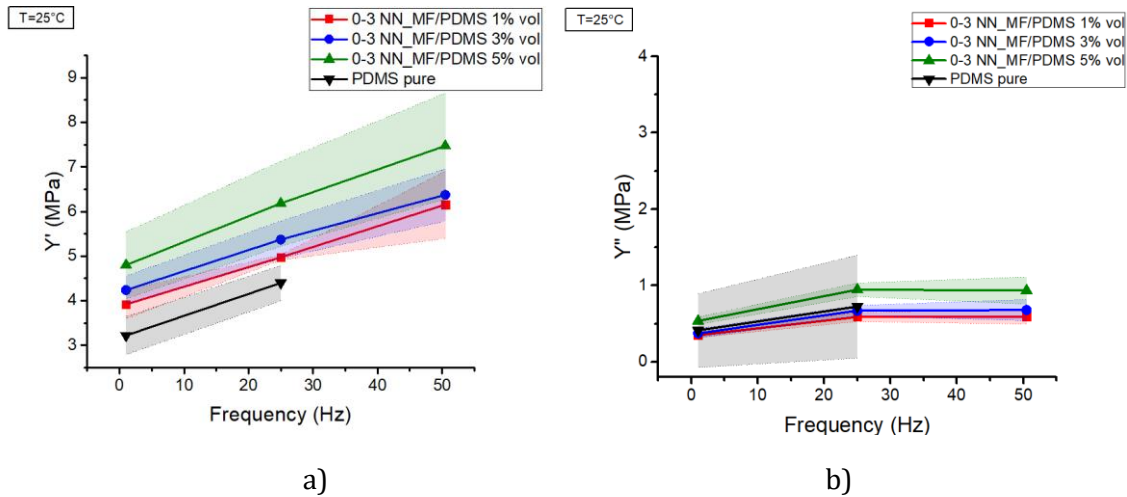


Figure 80 a) Storage modulus and b) Loss modulus for 0-3 NN_MF/PDMS at all the volume contents produced and pure PDMS.

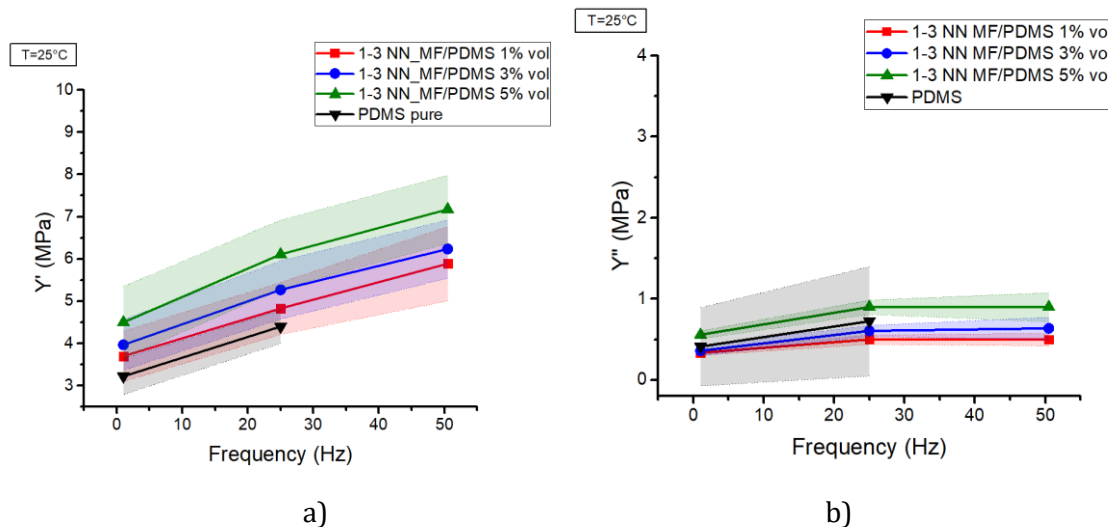


Figure 81 a) Storage modulus and b) Loss modulus for 1-3 NN_MF/PDMS at all the volume contents produced and pure PDMS.

From Y' and Y'' at 1 Hz we computed the Young's modulus (Y) for all the composites according to Eq.38. The results are reported in **Table 11** and illustrated in **Figure 82-a** for composites made with fibers. Interestingly, structured fiber composites exhibit a slightly lower Y than their 0-3 counterparts at each volume fraction: it is well known that the orientation angle of the fibers affects the mechanical properties of both long and short fiber composites. Short fiber composites represent mostly the situation investigated in this work. Their mechanical

properties have been modeled according to the semi-empirical Halpin-Tsai model which allows to evaluate the Young's modulus in function of the angle of fibers with respect to the applied stress (Eq.58) [228].

$$Y(\theta) = \left(\frac{\cos^4\theta}{Y_L} + \frac{\sin^4\theta}{Y_T} + \frac{1}{4} \left(\frac{1}{G_{LT}} - \frac{2\nu_{LT}}{Y_L} \right) \sin^2 2\theta \right)^{-1} \quad (58)$$

Where Y_L , Y_T , G_{LT} are longitudinal, transversal and shear modulus of the composite respectively and ν_{LT} Poisson ratio of the composites. θ is the angle of inclination of the fibers with respect to the x axe. According to Halpin-Tsai those quantities are calculated as follow:

$$Y_L = Y_m \frac{1 + \frac{L}{r} \eta_L \varphi}{1 - \eta_L \varphi} \quad (59)$$

$$\text{with } \eta_L = \frac{\frac{Y_f}{Y_m} - 1}{\frac{Y_f}{Y_m} + \frac{L}{R}} \quad (60)$$

With Y_m and Y_f the Young's moduli of matrix and fillers respectively, L length of the fibers, R radius of the fibers, and φ filler volume content

$$Y_T = Y_m \frac{1 + 2\eta_T \varphi}{1 - \eta_T \varphi} \quad (61)$$

$$\text{with } \eta_T = \frac{\frac{Y_f}{Y_m} - 1}{\frac{Y_f}{Y_m} + 2} \quad (62)$$

$$G_{LT} = \frac{Y_L}{2\frac{Y_L}{Y_T} + \nu_{LT}} \quad (63)$$

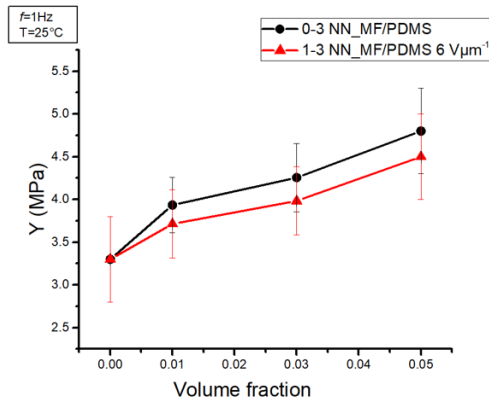
$$\nu_{LT} = \nu_m(1 - \varphi) + \nu_f \varphi \quad (64)$$

Where ν_m and ν_f are the Poisson ratio of matrix and filler, respectively. In accordance to the model, Y_L is the Young's modulus for composites with fibers aligned parallel to the applied stress and Y_T is the Young' modulus for composites with fibers aligned perpendicular to the stress; Y_L (0°) presents the highest possible value, it rapidly decreases until 45° and then a minor decrease towards 90° occurs, at which Y_T is measured [228]. The equation is plotted on **Figure 82-b**, for 1%v, 3%v and 5%v of NN fibers. Square and circles in the plot are the experimental values for 1-3 and 0-3 respectively. Halpin-Tsai slightly underestimates the transversal Young's Modulus of our *quasi* 1-3 composites, as it does not consider several factors, for instance the distribution of fibers sizes, agglomeration and imperfect alignment, inter-fibers distance and fillers/polymer interface. For instance, the value for Y_T according to the model for a 5%v composite with fibers aligned at 90° is 3.8 MPa, *i.e.*, 15% smaller than the experimental one (4.5 MPa). Decreasing the volume content, more agreement is found between the model and the empirical data; it is possible that when the filler increases in volume content, there is less free space for the fibers to align, which leads to lower angles of alignment, and this could justify the higher mismatch between model and experiments found for 5%v. Furthermore, no matter the percentage of filler, *quasi* 1-3 composites exhibit a slight decrease of Y with respect to the random composites, which indicates a dissimilar orientation;

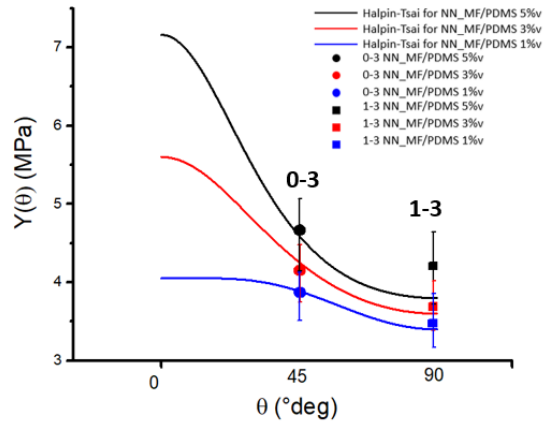
in principle, in 0-3 composites, fibers should exhibit an average angle is around 45° , being randomly dispersed. As visible in **Figure 83-b**, the experimental values (squares) are in good agreement with the model for each volume content.

Table 11 Y for 0-3 and 1-3 NN_MF/PDMS and NN_MP/PDMS developed in this work.

Volume fraction (%v)	Y (MPa)	Y (MPa)	Y (MPa)	Y (MPa)
	NN_MF/PDMS 0-3	NN_MF/PDMS 1-3 ($6 \text{ V } \mu\text{m}^{-1}$)	NN_MP/PDMS 0-3	NN_MP/PDMS 1-3
0%	3.3 ± 0.5	3.3 ± 0.5	3.3 ± 0.5	3.3 ± 0.5
1%	3.9 ± 0.4	3.7 ± 0.4	/	/
3%	4.2 ± 0.4	3.9 ± 0.4	/	/
5%	4.7 ± 0.5	4.4 ± 0.6	4.9 ± 0.5	4.53 ± 0.5



a)



b)

Figure 82 a) Y vs. volume fraction for 0-3 and 1-3 NN_MF/PDMS. b) Comparison of the experimental results with the Halpin-Tsai model, which evaluate the Young's modulus as function of the angle θ ($^\circ\text{deg}$), which is the inclination of the fiber with respect to the applied stress. Dots and squares are the experimental values for 0-3 and 1-3 NN_MF/PDMS composites.

Finally, Y was computed for 0-3 and 1-3 NN_MP/PDMS composites and the results are displayed in **Figure 84**. There is no substantial difference between *quasi* 1-3 and 0-3, as the filler content is too low for the connectivity to have a significant influence on mechanical properties. The same results were found in BT/PDMS for low fillers content.

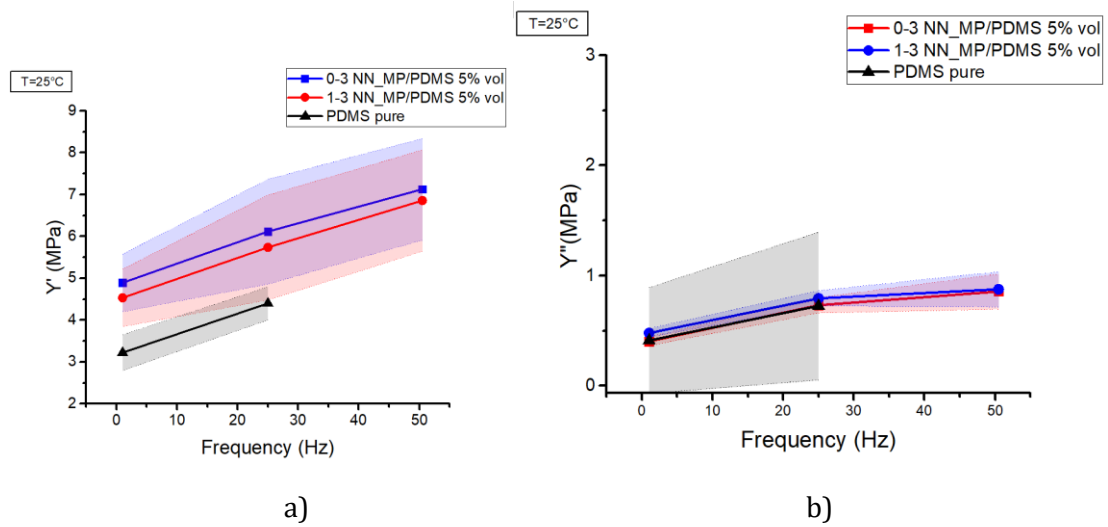


Figure 83 a) Storage modulus and b) Loss modulus for 0-3 and 1-3 NN_MP/PDMS at 5%v.

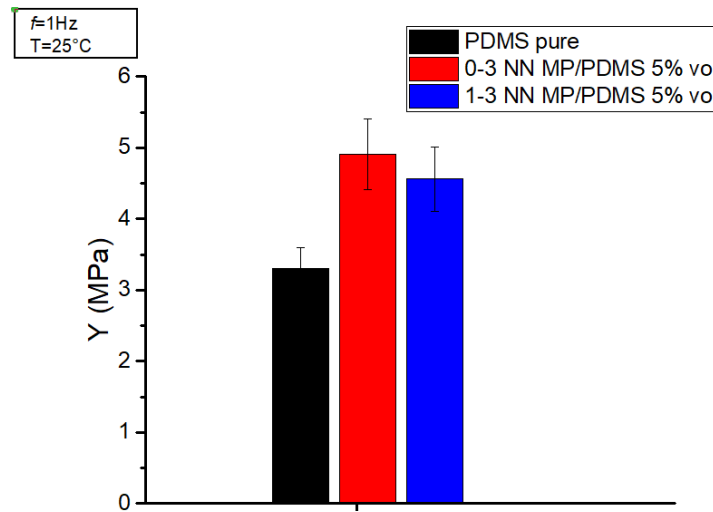


Figure 84 Y for pure PDMS, 0-3 and 1-3 NN_MP/PDMS.

4.4.6 DSC

In order to assess how fillers and DEP structuring impacted the properties of the composites, DSC was performed between -150°C and 15°C . Evaluation of the polymer-based composite's glass transition temperature was the objective. The heat flow vs. temperature variation for 0-3 NN MF/PDMS, 1-3 NN MF/PDMS, 0-3 NN MP/PDMS, and 1-3 NN MP/PDMS, all with 5%v filler, are presented in **Figure 85-a**. The inflection point connected to the glass transition can be identified in all graphs. T_g , ΔC_p , and ΔT_g relative to the glass transition were extrapolated from the results of heat flow. The glass transition occurs for all of the composites at about -117°C , as shown in **Figure 85-b**, with no discernible variations from the pure PDMS, whose DSC was reported in subsection 3.3.7. The T_g for the particle-based composite is

slightly lower, which indicates more mobility of the polymer chains. All four composites had comparable ΔC_p values, as indicated in **Table 12**, and these values were equivalent to the value recorded for pure PDMS (0.04 mW/mg). Finally, the temperature range where the transition occurred (ΔT_g) was between 3.5 and 5 °C, fairly homogeneous for all the composites and comparable to the pure PDMS (~5°C). We can conclude that neither the addition of NaNbO_3 fillers nor the DEP-structuration significantly change the polymer's chain polymerization and amorphous phase characteristics. Because the filler amount is kept to 5%v, there is no constrained amorphous phase or crystalline phase with T_m at -50°C, unlike composites containing high content of BaTiO_3 fillers.

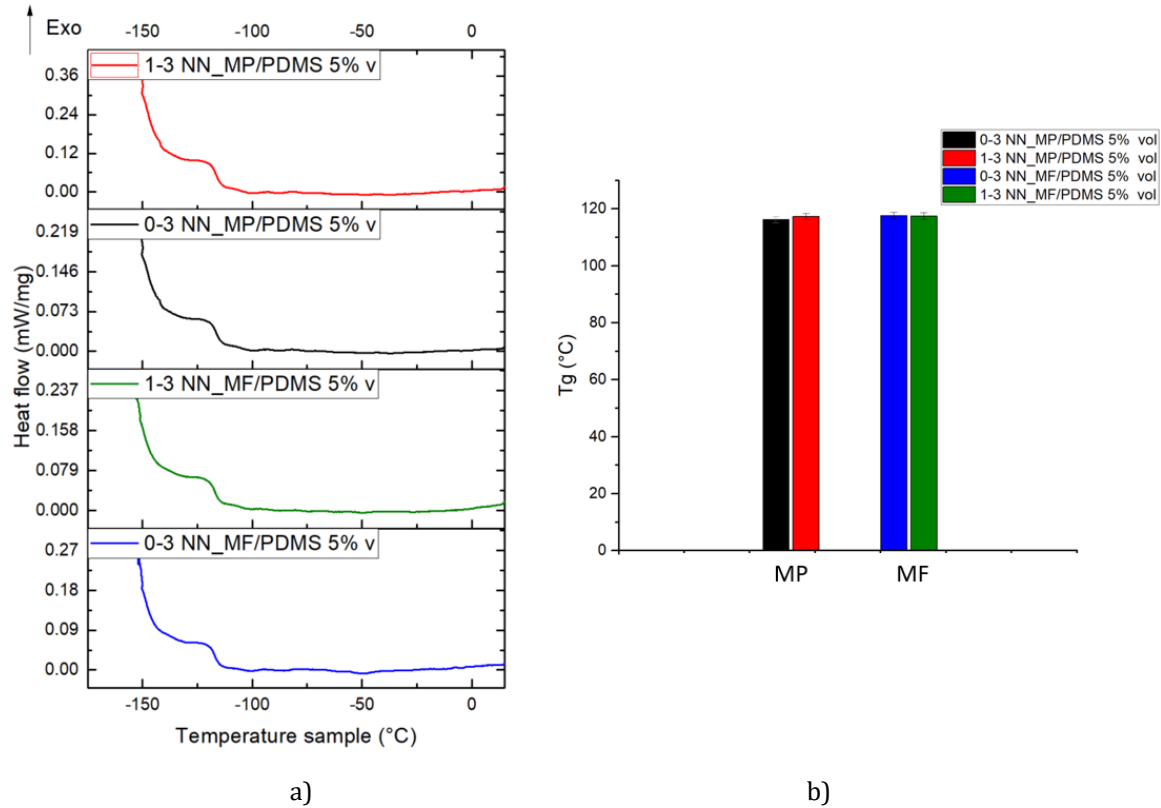


Figure 85 a) Heat flow (mW/mg) vs. Temperature measured via Differential Scanning Calorimetry for particles and fibers-based composite at 5%v of filler with 0-3 and 1-3 connectivity; b) Glass transition temperature for the four composites NaNbO_3 -based under investigation.

Table 12 ΔC_p and ΔT_g associated with the glass transition for 0-3 and 1-3 NN_MP/PDMS and 0-3 and 1-3 NN_MF/PDMS 5%v.

Sample	ΔC_p (mW/mg)	ΔT_g (°C)
0-3 NN_MP/PDMS 5%v	0.034 ± 0.003	3.5 ± 0.3
1-3 NN_MP/PDMS 5%v	0.046 ± 0.004	3.8 ± 0.3
0-3 NN_MF/PDMS 5%v	0.046 ± 0.004	3.7 ± 0.3
1-3 NN_MF/PDMS 5%v	0.048 ± 0.005	5.0 ± 0.5

4.5 Comparing piezoelectric materials

Structured composites containing 5%v fibers appear to be the best performers among those developed in this study. In terms of piezoelectric and mechanical behavior, it is interesting to compare them to other piezoelectric materials described in the literature (*e.g.*, electroactive fluoropolymers, piezocomposites, and bulk ceramics) [138,151,202,222,229-231]. The comparison is based on the piezoelectric voltage coefficient g_{33} (involving the d_{33} and ϵ'_r parameters as expressed in Eq.37) together with the material's stretchability (determined as the reciprocal of the Young's modulus Y , so denoted as $1/Y$). As matter of fact, to develop a sensor suitable to vascular prosthetics, the major criteria are the high voltage generated as a response to a stimulus, as well as softness and stretchability, so that the graft's activity is not compromised. **Figure 86** depicts an Ashby plot of g_{33} versus $1/Y$ for a variety of typical piezoelectric materials reported in literature. As shown, the bulk piezoceramics exhibit a combination of high Young's modulus, *i.e.*, low stretchability, and low g_{33} , making them unsuitable for the target application. On the other hand, although electroactive polymers such as PVDF and its copolymers have great piezoelectric activity, they are still quite stiff (\sim GPa). Finally, piezoelectric composites include the best mechanical properties in terms of stretchability, together with a good range of g_{33} values. Furthermore, the structured fiber composite presented in this study outperforms all previously reported particle composites, such as BT/PDMS 0-3 and 1-3, or NN_MP/PDMS 0-3 and 1-3, with a g_{33} of 148 mV m N⁻¹, confirming to be the most suitable choice for smart biomedical sensors [138,151,202,222,229-231]. These benefits stem from the combination of a low dielectric constant and a somewhat high d_{33} , which ultimately leads to increased g_{33} .

Another strength is the markedly lower filler content as compared to other composites described in earlier studies, 5% vs. 24% v, meaning lower elastic moduli, lower costs, and a simpler processing. It is worth noting that the developed sensor performs somewhat lower g_{33} value (1.2 times) with respect to the P(VDF-TrFE), but it requires much lower poling field, *i.e.*, 30 V μm^{-1} against 100–200 V μm^{-1} (3 to 7 times), which implies lower energy costs as well as lower risk of material breakdown. Taking all of these parameters into consideration, it is clear that our sensor provides the optimal trade-off between electromechanical coupling and energy cost. This is such an outstanding achievement, also considering that the material can be designed for many other applications, from biomedical to aerospace, or even energy harvesting, by simply adapting the matrix to the mechanical constraints given for specific use.

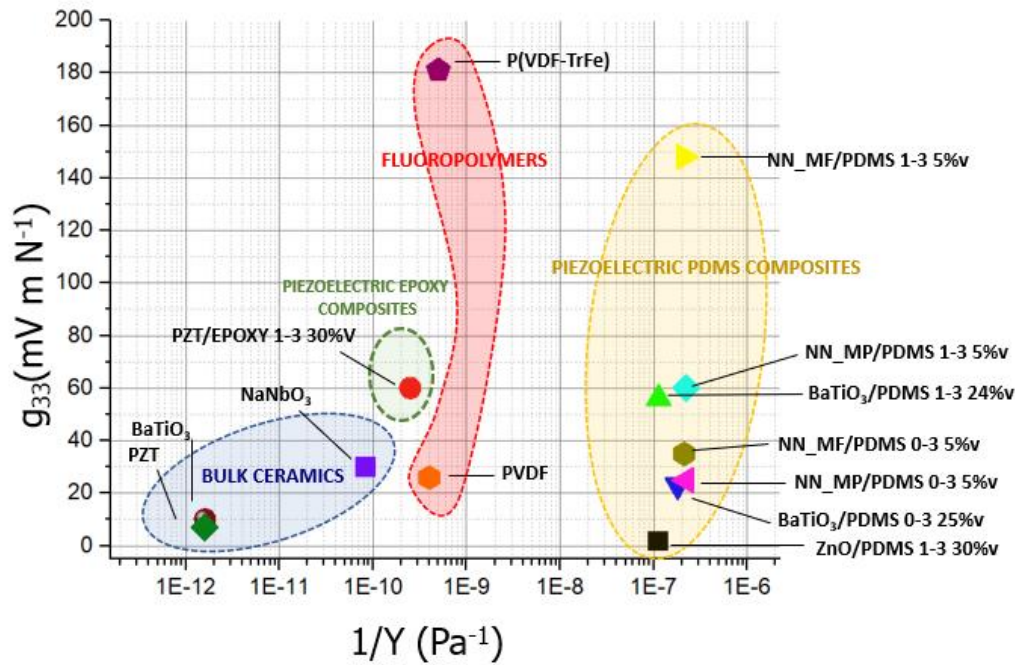


Figure 86 Piezoelectric charge coefficient (g_{33}) versus the reciprocal of the Young's modulus ($1/Y$) for the composite developed in this research compared to other piezoelectric materials reported in the literatures [138,151,202,222,229-231].

4.6 Conclusions

In this chapter, we investigate the impact of DEP structuring on composites with high aspect ratio fillers based on NaNbO_3 in PDMS matrix; NN fillers are successfully produced in fiber and particle shape via hydrothermal synthesis. SEM reveals the good morphology and XRD confirms the good crystal structure of the fillers. The primary objective is to demonstrate the improvement that may be achieved by DEP structuring on fibers rather than particles in polymeric matrix. According to our results, *quasi* 1-3 fiber composites outperform *quasi* 1-3 particle ones as well as any 0-3 particle or fiber composite. This is first predicted via FE simulation (COMSOL[®]) used to estimate the structuring impact on both particle and fiber composites. These findings are subsequently corroborated by dielectric and piezoelectric characterization; In *quasi* 1-3 fiber composites, ϵ'_r is 70% greater than in 0-3 counterparts and 16% higher than in 1-3 particle composites, whereas g_{33} is almost 4.5 times larger than that of a 0-3 fiber composite and 2.5 times than that of a *quasi* 1-3 particle composite for the same volumetric content. DMA testing in tensile mode reveals that fiber structuring causes a modest drop in Y modulus transversely to the columns, while no remarkable changes are identified between 0-3 and *quasi* 1-3 particle-based composites. This may be beneficial to our application. The results show good agreement when compared to the semi-empirical Halpin-Tsai model intended for composites made of short fibers. DSC reveals no relevant changes in the chain polymerization, thanks to the low volume content of filler inserted in the matrix. Finally, an Ashby plot based on g_{33} vs. $1/Y$ is provided to compare the materials developed in this project with existing piezoelectric materials for sensor applications; the results clearly

show that NN_MF/PDMS with a 5%v of filler exhibits the optimal trade between piezoelectric properties and stretchability, prompting us to select it for application target of this project. In this regard the sample will be implemented in a smart graft and tested to perform blood pressure monitoring.

Chapter III

Piezoelectric sensors for blood pressure monitoring

Summary

In this chapter we demonstrate that the sensors developed in Chapter II are suitable for blood pressure monitoring and for identifying anomalies connected to blood thrombosis, intimal hyperplasia, or atherosclerosis. First the 24%v BT/PDMS composite with 1-3 connectivity is integrated into a vascular catheter and placed in a cardiovascular simulator to reproduce the Fractional Flow Reserve (FFR) surgical procedure. The sensor is able to detect systole/diastole fluctuations caused by the action of the pumping engine proving to be an excellent solution for blood pressure sensors. Following that, 5%v NN_MF/PDMS with 1-3 connectivity is integrated into a vascular graft that is placed into a cardiovascular simulator. Again, a pump boosts the fluid flow by replicating systolic and diastolic pressures. The presence of blockages in the system, mimicking a clot, causes the pressure to locally decrease or rise. The piezocomposite allows the graft to sense pressure changes and outwardly broadcast these irregularities, paving the way for a new generation of vascular prostheses able to perform in vivo coagulation monitoring.

1. Developing Fractional Flow Reserve Catheters: a proof of concept

The aim of this section is to provide evidence that the piezoelectric sensors developed in this project are suitable for blood pressure monitoring. We have focused on two main blood pressure detection techniques, the first more invasive, based on the measurement of fractional flow reserve (FFR) via vascular catheters, and the second less invasive and highly innovative based on the development of smart grafts. First, we employed an experimental setup that allowed us to recreate the FFR measurement and evaluate the BT/PDMS-based sensor in circumstances that were comparable to those of the actual FFR procedure. The goal was to monitor fluctuations in blood pressure in real time. In this case, BT/PDMS 24%v with 1-3 connectivity was incorporated on an electrode-equipped vascular catheter and put into an arm-simulator with vessels. Water was pumped by an engine mimicking the heart. The sensor's surface charge allowed to follow the systolic and diastolic blood pressure with reasonable accuracy and sensitivity. The following paragraphs provides an overview of the FFR technique, its role in preoperative bypass grafting as well as the current state of FFR sensors; subsequently the proof of concept carried out is detailed, providing evidence that the materials developed in this work are perfectly suitable for of blood pressure monitoring.

2. Fractional flow reserve: state of art

Fractional flow reserve (FFR) is a technique developed to evaluate the significance of artery narrowing. It is mostly employed as preoperative procedure for coronary artery bypass

grafting, but it has been recently employed for peripheral artery bypass grafting preoperative checks (pFFR) showing good correlations with standard morphologic and indirect functional parameters [232,233]. It is based on the measurement of the FFR index, which is defined as the maximum myocardial blood flow in presence of stenosis divided by the theoretical maximum flow in absence of stenosis (Eq.65)[234]. It gives an accurate assessment of the degree of ischemia in downstream cardiac areas by comparing the maximum flow in a stenosed coronary artery to the theoretical maximum flow in the same artery without any stenosis [235]. Usually, a pressure sensor or an optical sensor integrated into the catheter can evaluate the pressure (**Figure 87**) [234,236,237].

$$FFR = P_d / P_a \quad (65)$$

P_d is the pressure after a stenosis (distal) and P_a the pressure before (proximal) [236].

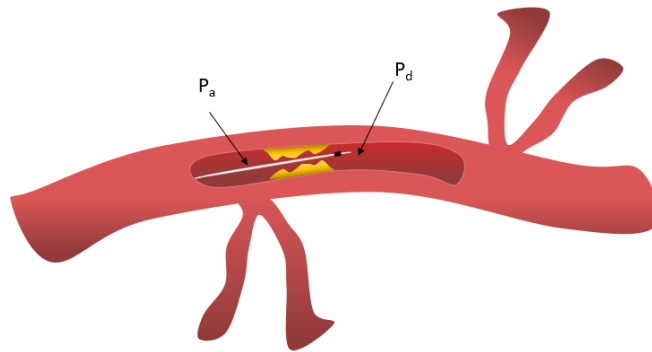


Figure 87 Representation of FFR sensor implemented inside the vessel. P_a is the proximal coronary pressure while P_d is the distal coronary pressure.

Patients with intermediate coronary artery lesions were found to benefit greatly from the use of FFR in making revascularization decisions. Usually values equals or below 0.75 are considered critical and require intervention, as they indicate that a plaque or a stenosis significantly hinder the blood flow, which is reduced of more than 25% [235]. FFR-guided coronary artery bypass grafting has revealed to be a good replacement to angiography-guided one; indeed, angiography is considered a qualitative test and often unreliable as it does not clearly identify mild ischemic lesions. FFR-guided revascularization, according to Fearon *et al.*, improves outcomes while decreasing the costs to the healthcare system [238,239]. As reported by Toth *et al.*, FFR-guided CABG decreases the number of graft anastomoses when compared to CABGs that are solely angiographically guided. Moreover, FFR-guided bypass has a greater 3-year patency rate [240]. Although the use of FFR in peripheral artery disease (pFFR) is far less widespread than in coronary FFR, it has lately gained interest [232]. For instance, Albayati *et al.* proved that FFR is a useful index to address the severity of peripheral artery stenoses and for predicting successful interventions [241]. The sensor employed in FFR measurements can be of three different types: capacitive, piezoresistive and optical [242]. Because it operates with high pressure sensitivity and low temperature, the capacitive pressure sensor is one of the most developed and often used pressure sensors for FFR measurements. The basis of a capacitive sensor is a parallel plate capacitor; when a mechanical stress induces a geometrical deformation of the capacitor, the capacitance

changes, detecting a variation in the pressure [243-245]. The advantages of capacitive sensors are their high sensibility and low power consumption. Moreover, they are easy and cheap to process. Nonetheless they may require complex readout circuitry and they subjected to mechanical drifts [242]. In piezoresistive sensors a deformation causes a change in electrical resistance of a material, and this enables to measure the blood pressure. This class of sensors offers mechanical stability, however they show critical drawbacks, like high power requirement, large temperature dependence offset, non-linearity, long-term instability in dynamic field conditions, and impart undesirable stiffness to catheters. At last, there are optical sensors composed of an optical membrane and two beams in phase focused on it. When the membrane deflects in response to an external pressure the beams are no longer in phase and this allows to measure the blood pressure [246]. An optical sensor is advantageous due to its small size and ability to withstand environmental effects; however, it is extremely sensitive to the bending of the fibers. Indeed, imposing stiffness to the catheter provokes limitation in the case of tortuous vessels [242,247].



Figure 88 a) Optical FFR catheter COMET™ II produced by Boston Scientific [248]. b) St. Jude Medical's New FFR Measuring Pressure Wire [249].

In this instance, we propose BT/PDMS-based piezo-composite as pressure sensor that after being inserted into the catheter can quickly detect blood pressure measurements. The advantages include its piezoelectric sensitivity, stretchability that does not restrict catheter motions when put into convoluted artery paths, thermal stability, low power consumption, and simple circuitry. This method is appropriate for finding stenosis connected to the presence of clots and atherosclerosis inside a blood vessel, nevertheless it could be used to perform post-transplant monitoring. Post-transplant monitoring is usually performed by ultrasound, computed tomography and angiography protocols, which are performed periodically. In this regard, current techniques present procedural morbidity, possible exposure to nephrotoxic contrast material, and are time-consuming and expensive. Pellicano *et al.* propose the use of the fractional flow reserve (FFR) technique as it could allow for postoperative monitoring of graft status, being able to indicate the degree of occlusion of the conduct [20].

3. Experimental section

3.1 Dynamic mechanical excitation

To test whether the BT/PDMS piezoelectric sample properly performs as a pressure blood sensor, the 24%v 1-3 composite is subjected to an arterial pulse shape, and its electrical response is recorded. The sensor, sputtered with gold and inserted among two electrodes, is placed between a floating column and a preload screw, as illustrated in **Figure 89**. Dynamic mechanical excitation is driven by a piezoelectric stack actuator (PI 246-50) with tunable amplitude and frequency, controlled by a waveform generator (Agilent, 33500B) coupled with a voltage amplifier (Trek, Model 20/20C). The mechanical pulse has an arterial pulse shape with a frequency of ~ 66 bpm (beats per minute) and an amplitude of 0.6 N (which is the minimum value achievable with the set up used in this work), corresponding to the pressure values of ~ 11 kPa applied to a 4-mm radius circular surface. The sample's electrodes are connected to a high-sensitivity charge meter (KISTLER, Type 5015). During the movement, the force is quantified via a load sensor (HBM) located between the top electrode and the screw. Both charge and force signals are simultaneously recorded in real-time through a DEWE® card (Sirius 8XSGT).

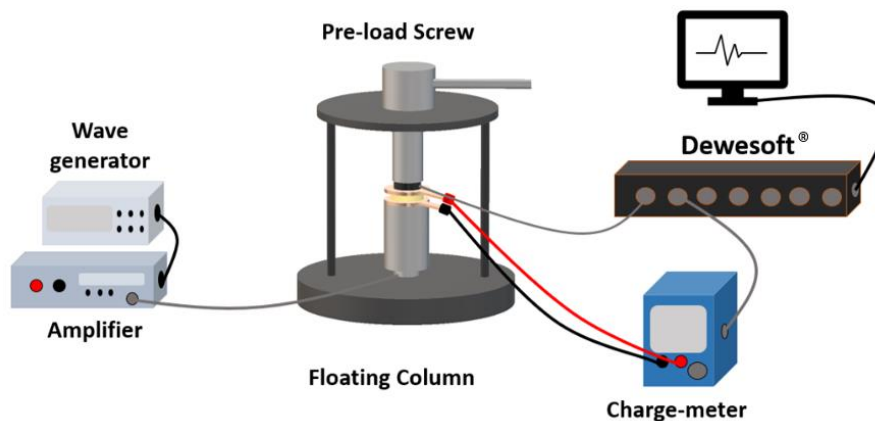


Figure 89 Schematic drawing of the set up used to study the piezoelectric behavior of the film under dynamic mechanical excitation simulating an arterial pulse shape stress.

3.2 FFR simulation

To further assess the piezoelectric response of BT/PDMS in FFR conditions, a second experimental test is carried out. As depicted in **Figure 90 a-b** the fabricated sensor implemented on a catheter is inserted into a cardiac simulation arm where water is circulating driven by an engine. The vascular catheter is equipped with electrodes which enables us to connect the sensor to a charge meter. The selected heart rate is chosen equal to ~ 60 bpm. The charge meter is connected to the piezoelectric sensor through the electrodes on the catheter and the emitted signal is monitored by the Dewesoft® card. Post-data treatments are performed with the Origin® software.

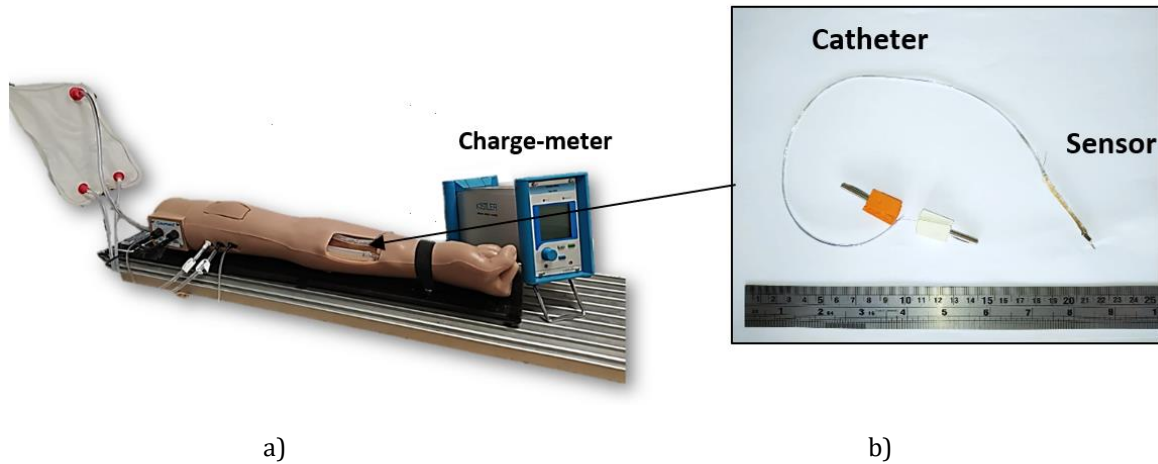


Figure 90 a) Picture representing the cardiac simulator arm. b) Detail of piezoelectric sensor applied on the catheter to perform the simulation.

4. Results and discussions

4.1 FFR simulation

Figure 91 depicts a typical architecture of FFR guidewire implemented with piezoelectric composite, which is located at the proximal end of a flexible wire tip. The piezoelectric sensor enables the measurement of dynamic and/or quasi-static pressure of blood vessels, ensuring that an applied pressure specifically loads the elements in one direction. Deformation of the crystals in the material generates an electrical charge, which is transmitted along with a thin sensor inside the guidewire.

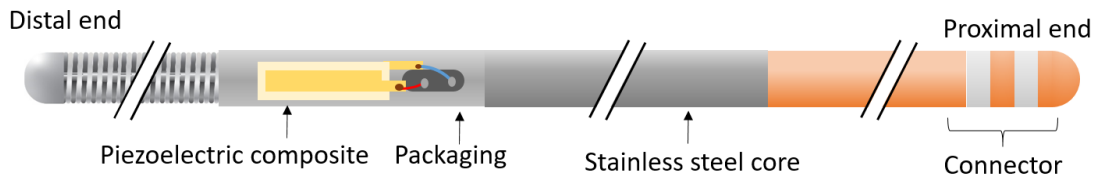


Figure 91 Typical architecture of FFR sensor made of piezoelectric composite.

In this study, a structured composite with 24%v of BaTiO_3 particles was selected as the best candidate for FFR application. The composite acts as a pressure sensor as it develops charge in response to the external stress. Therefore, d_{33} is more significant than g_{33} , and that justifies the choice of 24%v composite over the 12%v one (**Figure 92**). The arterial pulse-shape stress applied on the material is shown on **Figure 93-a**. Under a mechanical solicitation, the piezoelectric sensor emits sufficient charge variation to be detected via a charge meter (~ 5 pC) (**Figure 93-b**).

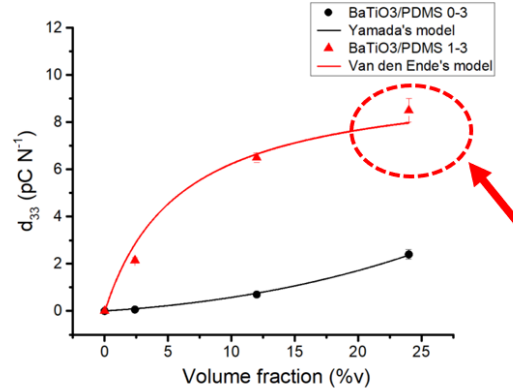


Figure 92 d_{33} at different volume contents for BT/PDMS 0-3 and quasi 1-3; For pressure sensors the most performing is 1-3 at 24%v, indicated by the red arrow.

Using the charge response and the charge meter's conversion factor, the open-circuit voltage is then calculated (**Figure 93-c**). A similar trend between the force, the charge, and the voltage signals confirms the good sensitivity of the developed sensor. The sensitivity is around $\sim 0.8 \text{ mV kPa}^{-1}$, which corresponds to $100 \mu\text{V mmHg}^{-1}$. This value is comparable to common pressure sensors available in the market and reported in several researches ($30\text{--}100 \mu\text{V mmHg}^{-1}$), with the advantage of the flexibility provided by the elastomeric matrix [242,250-252].

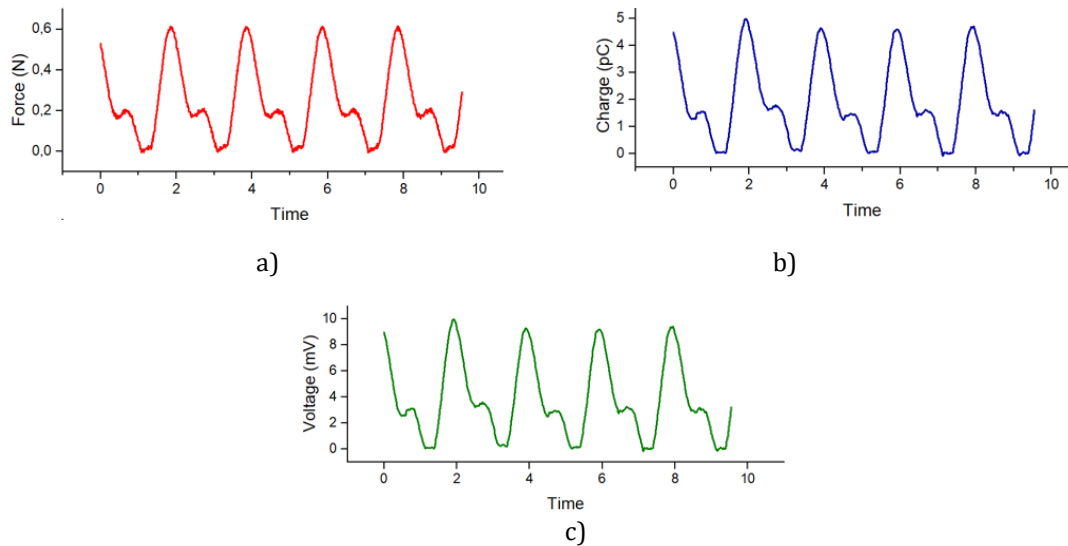


Figure 93 Performance of the developed piezoelectric sensor: a) Force input applied on the sensor with the set-up represented in Figure 89 a to simulate FFR measurement; b) charge output response of the sensor; and c) computed voltage output response.

To further simulate the FFR procedure, the 1-3 piezoelectric film with a filler content of 24%v is integrated into a catheter that is inserted into the cardiac simulation arm. A commercial catheter pressure sensor usually has core wire architecture, and the sensor is located at the proximal end of the radiopaque flexible wire tip (**Figure 91**). Thus, in this experiment, the

sensor is placed on the proximal end of a special catheter provided with electrical connections through which it is possible to collect the charge emitted by the film. The catheter is inserted into a tube through which a stream of water pumped by a motor at 66 bpm heart rate is passing, simulating a typical systolic/diastolic pressure variation. The charge evolution, displayed in **Figure 94-a**, is compared with a medical FFR measurement performed with an FFR sensor available in the market (**Figure 94-b**)[253]. Clearly the sensor is able to detect the blood pressure variation, and in principle it could measure changes in amplitude associated to an occlusion and evaluate the FFR value.

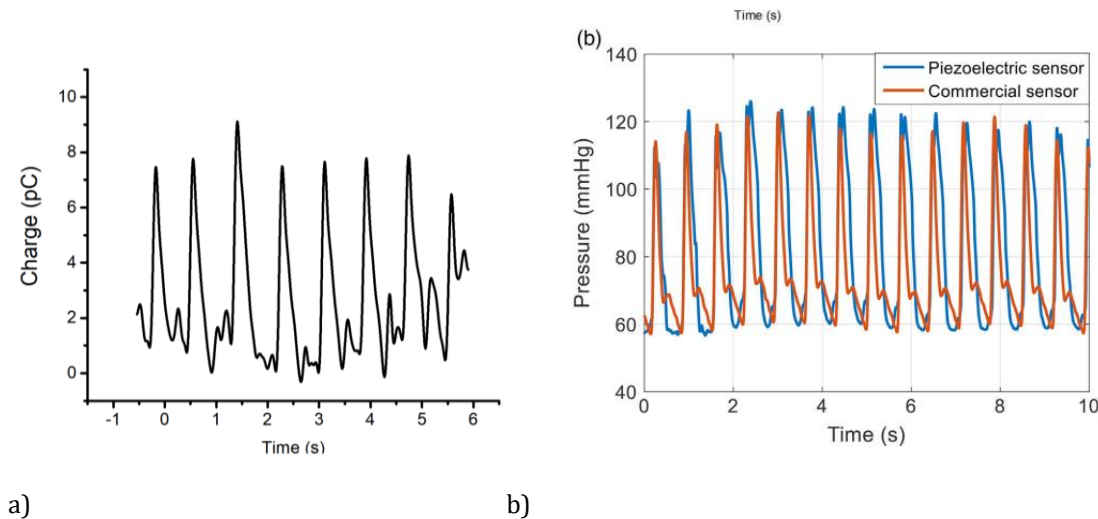


Figure 94 a) Charge response of sensor developed in this study integrated in a catheter during the simulation setup shown in Figure 90-b, compared with b) FFR measurement carried out with a pressure wire available in the market [253].

The pilot tests described in these sections show the material's strong potential for use in pressure sensor technology, which might be included into the FFR tools. In two different proofs of concept the BT-based piezocomposite proves to be able to detect systolic/diastolic pressure variations with a sensitivity of $100 \mu\text{V mmHg}^{-1}$. The efficient transducing activity combined with the flexibility and ease of integration make it a viable substitute for conventional FFR devices, which are typically constrained by their stiffness and intricate circuitry. Nevertheless, biocompatibility and hemocompatibility need more investigation and further *in vitro* and *in vivo* tests are under consideration for future research. Additionally, compatible electrodes that can withstand several cycles without deteriorating should be designed. Finally, future efforts will focus on scaling up the material.

5. Smart Vascular Grafts for Thrombosis detection: a proof of concept

5.1 Introduction

In this section the piezocomposite NN_MF/PDMS 5%v with connectivity 1-3 is integrated into an ePTFE graft and tested as sensor for blood pressure monitoring. The purpose is to demonstrate that the sensor can measure cardiac pressure (systole/diastole) and

simultaneously identify pressure amplitude variations related to the presence of an obstruction in the flow. The use of synthetic prosthesis has significant drawbacks, many of which connected to the development of thrombi in the conduit, which restrict blood flow and endanger the patient's life. We have discussed this extensively in Chapter I. Because of this, it's critical to develop new prostheses that can track blood pressure fluctuations in order to, if required, identify changes due to a stenosis. To this end, two proofs of concept are developed: the composite abovementioned is integrated into the ePTFE graft which in turn is inserted in an endovascular simulator; upon passage of a liquid, the sensor generates a surface charge that can be tracked by a charge meter. Occlusions are performed to simulate the presence of thrombi, inducing a local change in the pressure and consequently a change in the charge developed by the sensor. Changes in charge can be consequently correlate to the presence of clots. The second proof of concept is performed using the same set up, however in this case the sample is coupled with an inductive coil; the composite and the coil together build an LC resonant filter where the coil playing a role of L_f , *the inductance*, and the capacitor-like composite playing the role of C_f , *the capacitance*. Such a system acts as resonant sensor capable of wireless controlling based on existing RFID protocols. A shift in the resonance frequency of the filter induced by a change of pressure can be detected by an analyzer, enabling early identification of thrombi. The material selected appears to be a suitable match for the application because it is flexible, non-toxic, soft, and does not hinder the graft's functioning. Indeed, PDMS is selected as a polymer matrix because of its low Young's modulus, easy process, and extensive use in biomedical devices, as reported by Johnston *et al.*, Victor *et al.* and Ionescu *et al.* [156,183,254]. The choice of the lead-free NaNbO_3 as a filler, to some extent, stems from its biocompatibility, high piezoelectric activity and low dielectric constant, allowing for significant electromechanical conversion [255,256]. Furthermore, its manufacture (via hydrothermal synthesis) is cost-effective and with minimal environmental impact. In the next paragraphs the proofs of concept developed will be detailed.

6. Experimental section

6.1 Smart graft demonstrator

A system made of silicone tubes (internal diameter of 6 mm) coupled with a motorized pump is used to reproduce the cardiovascular system, as illustrated in **Figure 95-a**. A picture of the real set up is displayed in **Figure 96**. The engine is pumping a liquid, similar in viscosity to blood, composed by 30%v glycerin in water, at 1 Hz frequency to mimic human's heart rate (60 bpm) in a normal condition, with a pressure average of 9.5 kPa, *i.e.*, 71 mmHg. A part of the tubing is connected to an ePTFE graft to simulate the bypass grafting. A structured 300 μm -thick NN_MF/PDMS composite with 5%v fibers, metallized via gold sputtering, is stuck with a thin layer of PDMS glue (Dowsil™ 3145) around the graft and connected to a charge meter (**Figure 97**).

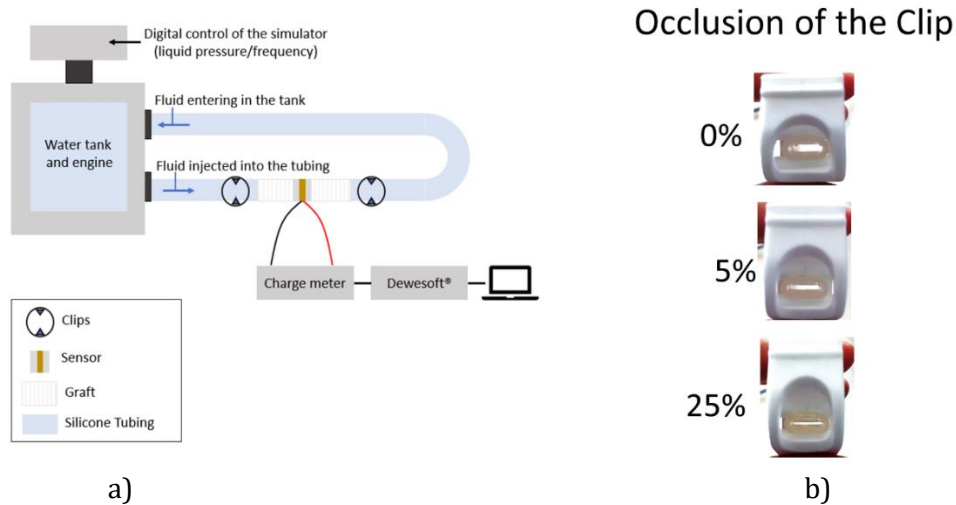


Figure 95 a) Illustrative sketch of the setup simulating the cardiovascular system, where is inserted an artificial graft together with the developed piezoelectric sensor. b) Cross section of the tube when the clip is inserted and is open (0%), is clicked once (5%) and is clicked twice (25%).

The fibers are radially oriented around the tube. The total metallized surface is $1 \times 3.2 \text{ cm}^2$. The glue layer allows to insulate the gold electrodes from eventual liquid leakage from the graft. The graft internal diameter is 9 mm. ePTFE Young's modulus is $\sim 0.5 \text{ GPa}$ [257]. The piezoelectric sensor stressed by the pressure of the liquid generates electric charges on its surface, which are detected by the charge meter (KISTLER, Type 5015) and visualized through Dewesoft® software. Two clips are placed before and after the graft to simulate a thrombus and therefore the obstruction of the flow. The presence of each clip induces an occlusion of 65%, in open condition. This initial value is normalized as a reference of 0%, for a sake of simplicity. Hence, closing a clip at occlusion of 70% and 90% correspondingly leads to an increase of 5% and 25% with respect to the set reference. The occlusion of the clip can be understood from **Figure 95-b**, where cross section of the tube when the clip is inserted and is open (0%), is clicked once (5%) and is clicked twice (25%) are reported. These values are chosen to perform typical obstructions of the circulation caused by the formation of thrombi in the blood vessels. The easiest technique to mimic a stenosis would be to introduce an obstruction in the vessel that reduces the circulation diameter inside the tube. However, in practice, this is more challenging to implement, whereas simulating an occlusion using clips is an easier technique to replicate the development of a thrombus. Such devices may mimic a stenosis, which would limit the circulation zone and cause hemodynamic changes where the sensor is positioned.

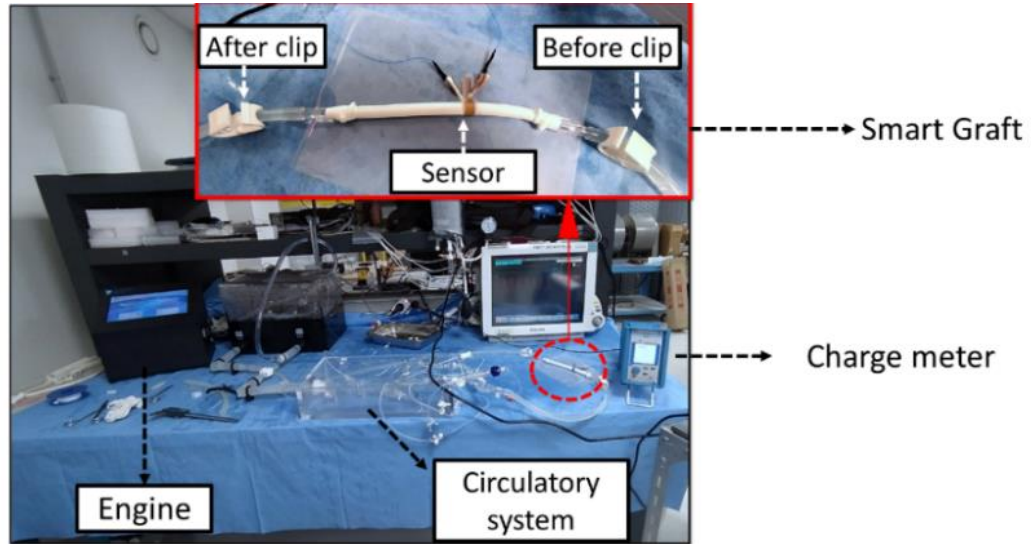


Figure 96 Picture of the setup simulating the cardiovascular system used to perform the proofs of concept.

First, the “before-graft” clip is closed and a change in the charge amplitude is recorded. Then, the same measurement is repeated by gradually closing the “after-graft” clip. As second proof of concept, the sensor is connected in parallel with an inductive coil (purchased from RS® operating at a carrier frequency of 125 kHz) in order to build a resonant sensor. Indeed, the capacitive behavior of the composite together with the inductive property of the coil naturally creates a LC filter whose resonance characteristics strongly depends on the capacitance change of the sensor (denoted C_f). Hence, the filter connected to an analyzer (E4990A Impedance Analyzer) allows for a detection of the system resonance frequency (denoted f_r). As matter of fact, a pressure variation caused by the occlusion of the clips generates a change in C_f (while the inductance L_f of the coil is assumed to be constant), and thus a shift in the resonance frequency (see Eq.66). Accordingly, the coil could be a RFID coil, able to wireless detect variations in f_r and reveal the presence of an obstruction due to a clot by delivering the information to an external reader.

$$f_r = 1 / (2\pi\sqrt{L_f C_f}) \quad (66)$$

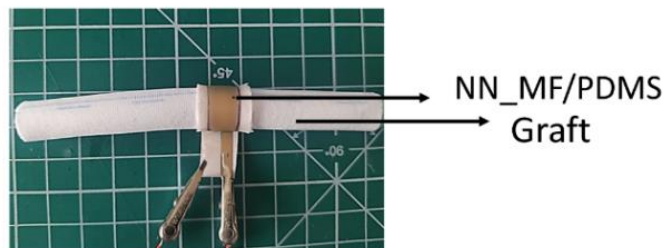
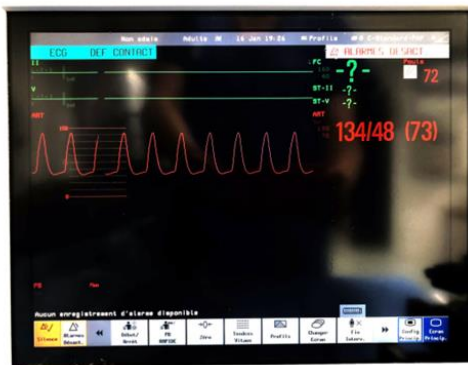


Figure 97 Detail of the ePTFE graft incorporated with the smart sensor made of piezoelectric composite.

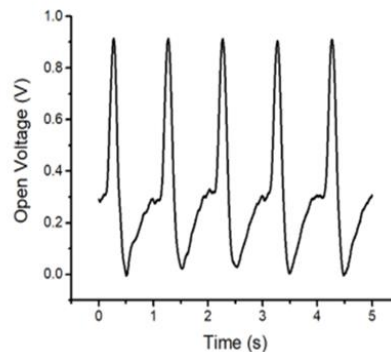
7. Results and discussion

7.1 Smart graft pressure sensor

The first proof of concept involves measuring the charge developed by the composite 1-3 NN_MF/PDMS 5%v, in response to blood pressure. The sensor encloses the graft, which in turn is inserted into the cardiovascular simulator, as described in subsection 7.1. When a liquid is pumped through the system, an output voltage signal is generated by the piezoelectric sensor matching the pressure evolution during systole and diastole visualized on the blood pressure monitor, as displayed in **Figure 98 a-b** (data are reported in an equivalent open-circuit voltage) [258]. Diastole occurs when the heart muscle relaxes and its chambers fill with blood, leading to decrease pressure (so-called diastolic pressure). Systole, on the other hand, occurs when the heart contracts and pushes blood out of the chambers, making the pressure drops (so-called systolic pressure).



a)



b)

Figure 98 a) Picture of the evolution of the blood pressure measured by the blood pressure monitor of the cardiovascular simulator. b) Evolution of the open-circuit voltage generated by the smart graft which follows the systolic-diastolic pressure variation when the clips are open.

To simulate a vascular stenosis caused by a thrombus, two clips are integrated on the tubes, one before and one after the sensor (**Figure 99**). The insertion of each open clip leads to a tube occlusion of 65%, being considered as the reference so that can be normalized by 0%. The two clips can be gradually closed at occlusion variation of 5% and 25% with respect to the set reference. When the “before-clip” is closed, the pressure of the liquid in the graft decreases, as less fluid is able to pass through it, due to the narrowing of the section. Consequently, the higher the degree of occlusion of the “before-clip”, the smaller the liquid pressure. On the other side, a gradually closure of the “after-clip” induces a gradually increase of pressure experienced by the graft.

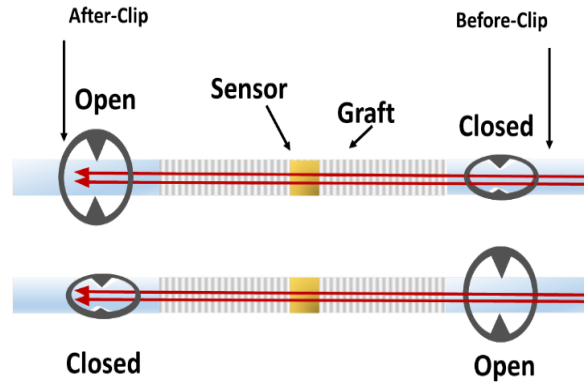


Figure 99 Schematic drawing of the smart graft integrated sensor, where two clips are applied prior and after the graft and individually closed to simulate the presence of a clot occlusion.

As illustrated **Figure 100 a-b** the sensor is able to detect the pressure changes based on the normalized dimensionless data: the results reveal that the more clenched is the “before clip”, the less charge develops on the sensor and therefore the amplitude of the recorded signal is reduced. Alternatively, as the occlusion of the stenosis positioned after the sensor increases, there is a substantial increase in the output signal amplitude.

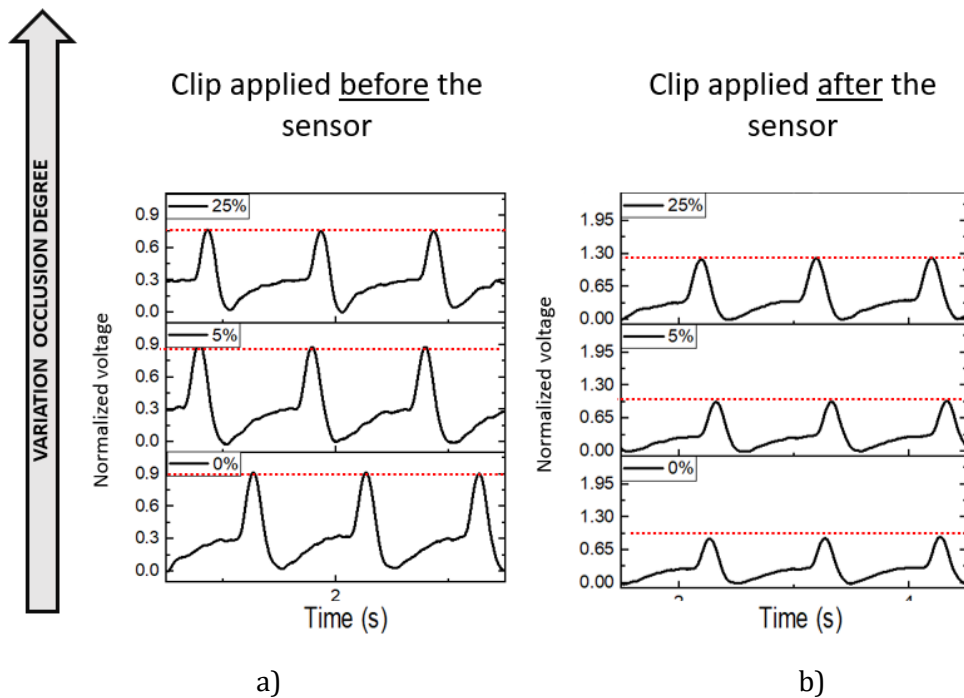


Figure 100 Evolution of the piezoelectric response on the graft sensor following the systolic-diastolic pressure for: a) occlusion applied before the sensor, where the amplitude of the signal decreases with an increasing % of occlusion (from 0% to 25%); b) an occlusion applied after the sensor, where the increasing the % of occlusion induces an increase in the pressure sensed in the graft, leading to an increase of the output signal from the sensor. All the values are reported as normalized voltage, meaning that the voltage measured was normalized over the maximum voltage developed at 0%.

Figure 101 displays the real physical value of the output voltage in response to the clip configuration, reflecting a quasi-linear trend of the electromechanical coupling. Such a behavior is consistent with the well-known linear model of a typical piezoelectric material operating in the elastic regime. Extrapolation based on the linear fitting of **Figure 101** allows to deduce the output voltage generated at 100% occlusion of the before-clip, corresponding to the extreme configuration where the pressure is revealed to be minimum. The resulting voltage in that case is equal to 0.27 V, which is much higher than the lower limit (~ 10 mV) that could be detected by the measuring devices. In practice, the minimum occlusion variation degree detectable is of 0.5%. Regarding the sensitivity of the composite developed in this study the minimum detectable pressure is estimated as 20 Pa (*i.e.*, 0.15 mmHg), which is far lower than the normal systolic/diastolic pressures ($\sim 100/60$ mmHg) in a normal condition of the patient.

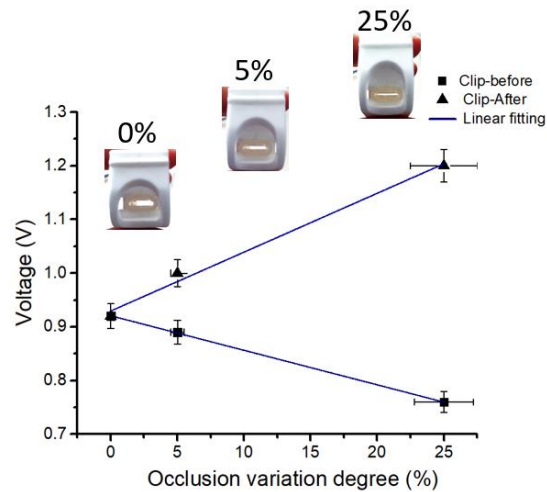


Figure 101 Linear variation of the voltage amplitude vs. the % of occlusion variation for the before-clip and after-clip, respectively; in the graph are also reported pictures of the cross section of the tube for ground state, *i.e.*, 0%, 5% and 25%.

These preliminary results demonstrate the high potential of the developed composite as integrated sensor into a smart graft, which therefore fully succeeds in detecting the presence of a thrombosis by measuring the blood pressure. However, the sensing measurement should be implemented without the need of a charge meter, which would be challenging to integrate into a human prosthesis. The objective is to perform wireless measures that can communicate with devices placed outside the human body. As mentioned, one solution is the use of RFID-tags, or inductive coils, capable of making wireless measurements. In this work, as early proof of concept, we use a coil connected to an impedance-meter that could be easily replaced with a RFID wireless coil to perform wireless measurements. Hence, instead of connection with the charge meter, the capacitive-like sensor is coupled in parallel to an inductive coil to develop a resonant sensor. The charge developed on the composite surface leads to an apparent capacitance change, resulting in a resonant frequency (f_r) shift. Consequently, it is possible to detect the pressure variation related to an occlusion by monitoring the filter losses (denoted D_f), whose peak value is at the resonance of the LC circuit. To this end, monitoring D_f with an impedance analyzer enables for the identification of the resonance frequency, which in our test is found around 233.6 kHz with open clips. This value, relatively low in the

radio-frequency range, is intentionally chosen to achieve the best performance of RFID-tags employed in the human body. As reported on several studies, under such frequency range and short distance between receiver and transmitter (a few tens centimeter), there is no significant attenuation of the signal caused by biological tissues [259-261]. The resonance frequency may be customized based on the demands of the target application. For instance, higher frequency range can improve the tag-reader distance while lower frequency is less sensitive to noise and attenuation. More research might be pursued to thoroughly understand the mechanism of tissue absorption in order to find out appropriate tag-reader distances. **Figure 102 a-b** illustrates the normalized losses (computed as $D_f/D_{f,max}$) confirming that both “after and before clips” generate a shift in the resonance frequency. In case of decrease of pressure caused by a stenosis applied before the sensor, the resonance shifts at higher frequencies (**Figure 102-a**): the lower the pressure, the lower the output charge, leading to a decrease in the capacitance, which in turn increases f_r (see Eq.66). If the stenosis is applied after, the resonance shifts at lower frequency because of an increase in the pressure that gives rise to higher output charge (**Figure 102-b**).

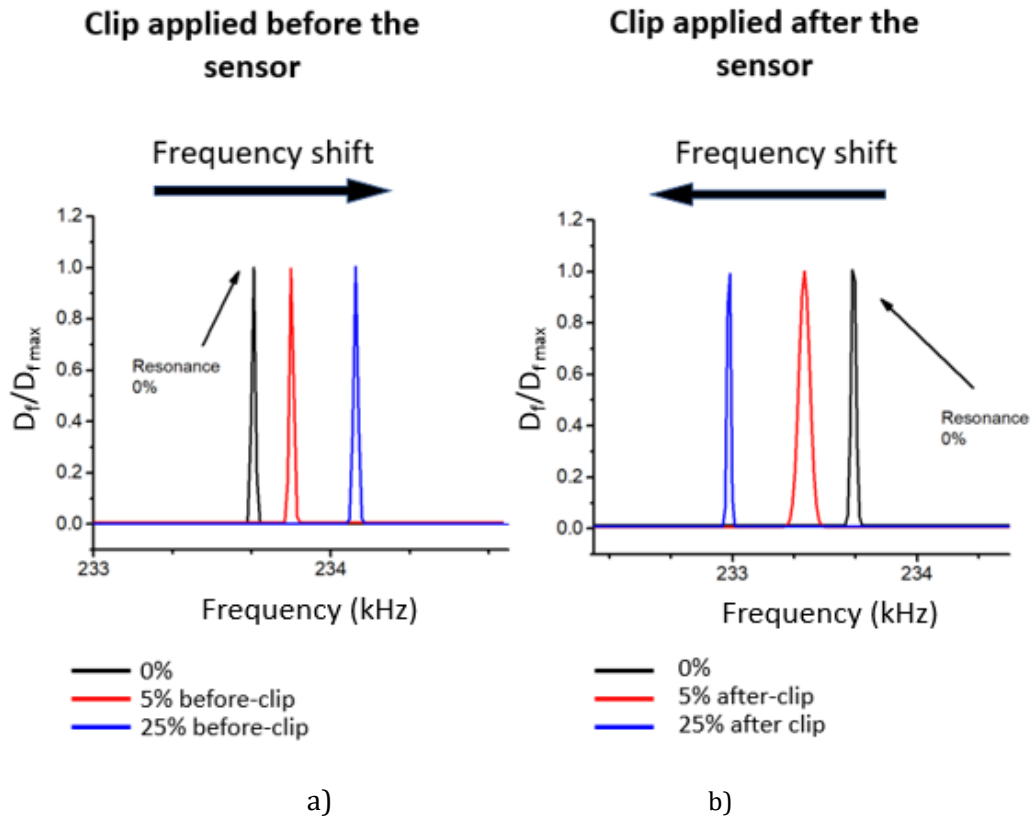


Figure 102 Normalized losses versus frequency for the LC system with the liquid passing through it: the shift of the resonance frequency due to the partial closure of the clip applied before a) and after b) the sensor (from 0% to 5% to 25%).

The magnitude of the shift can be associated to the occlusion variation degree as reported in **Figure 103**. In conclusion, we have successfully proved that the LC filter, consisting of an inductive coil and the piezocomposite NN_MF/PDMS, can detect the presence of a thrombus

in an artificial graft, simply by measuring the resonant frequency. This discovery opens the door to the use of RFID technology to carry out the same measurement but through wireless connection. As a matter of fact, a RFID-tag can work as antennas which, once coupled to the composite and integrated into the prosthesis, would be able to wirelessly report the state of the vascular graft.

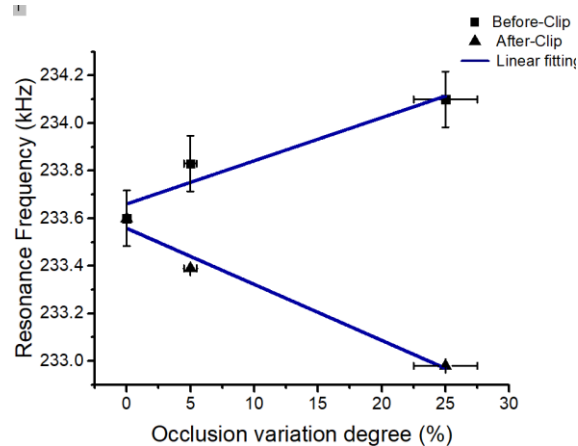


Figure 103 Resonance frequency of the filter vs. the occlusion's degree for before clip and after clip, respectively.

8. Conclusions

In this chapter, we present two different vascular devices that incorporate the composites developed in Chapter II as blood pressure biosensors. First, BT/PDMS 24%v 1-3 embedded with a vascular catheter is employed as a Fractional Flow Reserve sensor in an endovascular simulator. It shows to be appropriate for measuring blood pressure to determine the FFR coefficient. This approach is very important for bypass grafting preoperative inspections, but it also shows promise for postoperative checks. Second, NN MF/PDMS 5%v 1-3 is included in a graft and tested as pressure sensor in a vascular simulator. The composite performs flawlessly as a blood sensing element, demonstrating great accuracy in the measurement of systolic and diastolic pressure, as well as the ability to identify the presence of obstructions in the flow that, in real-life scenarios, may be produced by thrombi. In this experiment, the sensor was connected to an inductive coil to create an LC resonant filter. When there was an obstruction, the resonance frequency of the filter changed, signaling the development of a clot on the prosthesis. The developed system could be implemented into the human body to provide real-time information about the graft's status. In the future, the coil will be substitute with a RFID tag capable of wireless communication. Additionally, the composite's size will be optimized to be incorporated into a smart graft, and wireless tests will be performed in a real clinical environment. Biocompatibility as well as *in vivo* preliminary studies will be planned to validate the sensor reliability. To achieve this stage, one of critical issues is related to the sterilizability of the sensing system. Further considerations should be investigated to confirm whether or not sterilization process would affect the material properties. The new insight of this research might be useful to pave the way for a next generation of smart grafts that can

easily monitor and communicate their actual condition to the treating physician, allowing for early intervention in the event of a thrombus.

Article

Investigation of Blood Coagulation Using Impedance Spectroscopy: Toward Innovative Biomarkers to Assess Fibrinogenesis and Clot Retraction

Giulia D'Ambrogio ¹, Omar Zahhaf ¹, Minh-Quyen Le ¹ , Yves Gouriou ² , Laurie Josset ³, Vincent Pialoux ³, Patrick Lermusiaux ⁴, Jean-Fabien Capsal ¹ , Pierre-Jean Cottinet ^{1,*} and Nellie Della Schiava ^{1,4}

¹ University Lyon, INSA-Lyon, LGEF, EA682, 69621 Villeurbanne, France; giulia.dambrogio@insa-lyon.fr (G.D.); omar.zahhaf@insa-lyon.fr (O.Z.); minh-quyen.le@insa-lyon.fr (M.-Q.L.);

jean-fabien.capsal@insa-lyon.fr (J.-F.C.); nellie.della-schiava@chu-lyon.fr (N.D.S.)

² CarMeN Laboratory, University Lyon, INSERM, INRA, INSA Lyon, Université Claude Bernard Lyon 1, 69500 Bron, France; yves.gouriou@univ-lyon1.fr

³ Laboratoire Interuniversitaire de la Biologie et de la Motricité (LIBM), Université Claude Bernard Lyon 1, EA 7424, 69266 Villeurbanne, France; laurie.josset@univ-st-etienne.fr (L.J.); vincent.pialoux@univ-lyon1.fr (V.P.)

⁴ Groupement Hospitalier Edouard Herriot, 69003 Lyon, France; patrick.lermusiaux@chu-lyon.fr

* Correspondence: pierre-jean.cottinet@insa-lyon.fr



Citation: D'Ambrogio, G.; Zahhaf, O.; Le, M.-Q.; Gouriou, Y.; Josset, L.; Pialoux, V.; Lermusiaux, P.; Capsal, J.-F.; Cottinet, P.-J.; Schiava, N.D. Investigation of Blood Coagulation Using Impedance Spectroscopy: Toward Innovative Biomarkers to Assess Fibrinogenesis and Clot Retraction. *Biomedicines* **2022**, *10*, 1833. <https://doi.org/10.3390/biomedicines10081833>

Academic Editor: Luca G. Della Carbonare

Received: 26 June 2022

Accepted: 27 July 2022

Published: 29 July 2022

Publisher's Note: MDPI stays neutral with regard to jurisdictional claims in published maps and institutional affiliations.



Copyright © 2022 by the authors. Licensee MDPI, Basel, Switzerland. This article is an open access article distributed under the terms and conditions of the Creative Commons Attribution (CC BY) license (<https://creativecommons.org/licenses/by/4.0/>).

Abstract: This study focused on a coagulation assessment based on the novel technique of blood-impedance-magnitude measurement. With the impedance characterization of recalcified human blood, it was possible to identify two significant biomarkers (i.e., measurable indicators) related to fibrin formation (1st marker) and clot retraction (2nd marker). The confocal microscopy of clotting blood provided a complete visual analysis of all the events occurring during coagulation, validating the significance of the impedance biomarkers. By analyzing the impedance phase angle (ϕ) of blood during coagulation, as well as those of the clot and serum expelled after retraction, it was possible to further clarify the origin of the 2nd marker. Finally, an impedance-magnitude analysis and a rotational thromboelastometry test (ROTEM[®]) were simultaneously performed on blood sampled from the same donor; the results pointed out that the 1st marker was related to clotting time. The developed technique gives rise to a comprehensive and evolutive insight into coagulation, making it possible to progressively follow the whole process in real time. Moreover, this approach allows coagulation to be tested on any materials' surface, laying the ground for new studies related to contact coagulation, meaning, thrombosis occurring on artificial implants. In a near future, impedance spectroscopy could be employed in the material characterization of cardiovascular prostheses whose properties could be monitored in situ and/or online using effective biomarkers.

Keywords: blood coagulation; impedance spectroscopy; electrical biomarker; thrombosis; clotting time; clot retraction; confocal microscopy; fibrinogenesis

1. Introduction

When a vascular injury occurs in the human body, the coagulation process is activated. The mechanism of coagulation involves the activation, adhesion and aggregation of platelets, as well as the activation of a fibrin network. The activation of clotting factors follows the so-called coagulation cascade, which can be triggered by contact with tissue factor (TF) in the sub-endothelium (extrinsic pathway) and/or the activation of factor XII (*fXII*) due to subendothelial-collagen exposure (intrinsic pathway) [1,2]. Both pathways end with the formation of a fibrin network around platelets and red cells [1,3,4]. Once the clot has formed, it contracts (clot retraction) to become more stable; clot retraction is a consequence of the action of platelets that impose contractile forces on the fibrin network, which, over time, increases its density and expels serum (plasma deprived by clotting

Chapter IV

In vitro thrombosis monitoring via impedance characterization

Summary

This study focuses on coagulation assessment based on a novel technique of blood impedance magnitude measurement. Through impedance characterization of recalcified human blood, it is possible to identify two significant biomarkers (i.e., measurable indicators) related to fibrin formation (1st marker) and clot retraction (2nd marker). Confocal microscopy of clotting blood providing a complete visual analysis of all the events occurring during coagulation, validates the significance of the impedance biomarkers. By analyzing the impedance phase angle (Φ) of blood during coagulation, as well as of clot and serum expelled after retraction, it is possible to further clarify the origin of the 2nd marker. Finally, impedance magnitude analysis and rotational thromboelastometry test (Rotem®) are performed simultaneously on blood sampled from the same donor; the results confirm that the 1st marker is related to clotting time. The developed technique gives rise to a comprehensive and evolutive insight of coagulation, making it possible to progressively follow the whole process in a real time. Moreover, this approach allows coagulation to be tested on any materials' surface, laying the ground to new studies related to contact coagulation, meaning thrombosis occurring on artificial implants. To this end, the test is used to examine coagulation in contact with surfaces that exhibit varying degrees of wettability. This enables to verify the different reaction of blood depending on how wettable the surface is. This novel technique is promising as it allows to study the hemocompatibility of synthetic materials, and it could be integrated into vascular and cardiac prosthetics, to monitor in vivo coagulation.

1. Introduction

When a vascular injury occurs in the human body, the coagulation process is activated. The mechanism of coagulation involves activation, adhesion and aggregation of platelets, as well as formation and maturation of a fibrin network. Once the clot has formed it contracts (clot retraction) to become more stable, and plugs the wound to minimize any blood loss [262–265]. Even pathological thrombosis, which occurs when haemostasis is activated in the absence of bleeding and vascular wall damage, can set off the clotting [266]. Additionally, the contact with extraneous synthetic surfaces, such as a vascular implant, can activate the coagulant factors, leading to thrombus development, also known as contact coagulation. Regardless of the trigger, a thrombus in autologous or artificial vessel can be fatal, obstructing the normal blood flow to the tissues, causing ischemia, infarct, or embolism [76,85,266,267]. *In vitro* studies are useful to assess blood coagulation as well as to detect disorders, including hypocoagulability (i.e., insufficient amount of clotting factors in blood), hypercoagulability (i.e., exaggerated coagulation) and clot-retraction disorders, which may be hindered in

pronounced thrombocytopenia (poor platelet count) [268–270]. Nowadays viscometry tests, which includes Rotational Thromboelastometry (Rotem®), Thromboelastography (TEG®) and Sonoclot®, are the most widely used *in vitro* analysis of clotting blood. These non-invasive tests use a low shear stress to assess the dynamic changes in the blood's viscosity during coagulation, evaluating the blood's capacity to form clots. Both Rotem®, TEG® and Sonoclot® enable a rapid and global approach to assess coagulation via a specially designed system called thromboelastograph [271,272]. Nonetheless, viscoelastic measurements are unable to characterize contact coagulation of blood in contact with a broad range of materials, which is crucial for investigating hemocompatibility of antithrombogenic prosthetics. This work proposes an alternative and simple solution to assess blood coagulation through impedance characterization, which has been generally used to characterize electrical properties of biological (tissues and cells) and non-biological materials (polymers and ceramics) [273,274]. During the measurement, the blood sample undergoes to an alternating sinusoidal voltage (amplitude V), and its current response (amplitude I) is recorded. Through the collected RMS data, the impedance magnitude ($|Z|$) is computed according to Eq.67 [275].

$$|Z| = \frac{V}{I} \quad (67)$$

Impedance characterization enables evaluation of the electrical behavior of blood throughout the coagulation, allowing identification of the main stages of the process, such as fibrin formation and clot retraction. Impedance markers related to the onset of coagulation (clotting time) and the start of clot retraction are identified and validated by comparison with confocal microscopy and Rotem® analysis. Additionally, by analyzing the phase variation of the impedance (*i.e.*, corresponding to the phase shift between the input voltage and the output current) it is possible to identify the resistive/capacitive behavior of the sample. This technique can also provide an easy way to test coagulation on different surfaces. During the measurement, blood is placed on the surface of an arbitrary material, where two electrodes, previously placed and connected to a voltage generator, drive the voltage through the sample. To this end, four distinct surfaces with varying wettability are evaluated in this research. Clotting varies based on the blood contact angle, demonstrating the test's potential for studying contact coagulation. The proposed approach provides a complete view of the clotting and a new insight on coagulation assessment, paving the way for future studies on antithrombogenic implants. In the next paragraphs the principles behind coagulation, as well as thromboelastography and bioimpedance spectroscopy will be presented.

2. The mechanism of coagulation

When a vascular wall is injured, blood encounters endothelial collagen and tissue factor (TF) produced by endothelial cells. As a result of this contact, platelets and a group of proteins in the blood, called clotting factors, are triggered, initiating the clotting process, whose purpose is to plug the damage in the vascular wall and interrupt the outflow of blood. First, the vessel narrows (vasoconstriction), and the activated platelets form a plug on the injury (1^{ry} haemostasis). At the same time, the clotting factors get activated through a chain reaction, known as coagulation cascade, which leads to the development of a fibrin network (2^{ry}

haemostasis) [74,76,262]. Finally, the clot contracts to strengthen. **Figure 104** reports the steps occurring during coagulation in a damaged vessel [276-278]. The so-formed clot of fibrin, red blood cells and platelets seals the vascular damage and limit any further blood loss [74,76,262]. Extrinsic and intrinsic pathways are the two potential blood clotting mechanisms involved in the coagulation cascade, as already briefly described in subsection 5.4 Chapter I, and in most cases both pathways are operating at the same time (**Figure 105**). The extrinsic pathway is triggered when blood comes into touch with TF, which is generated by endothelial cells outside the lumen when the artery is injured. TF activates factor *fVII* in to *fVIIa* which in turn activates factor *fX* into *fXa* after which the common pathway starts. On the other hand, the intrinsic pathway is triggered by the activation of the protein factor *XII* (*fXII*) following exposure to subendothelial collagen. From *fXIIa*, a chain reaction starts, during which several proteins get activated (*fXI* → *fXIa*, *fIX* → *fIXa*), until factor *fX* gets activated into *fXa*.

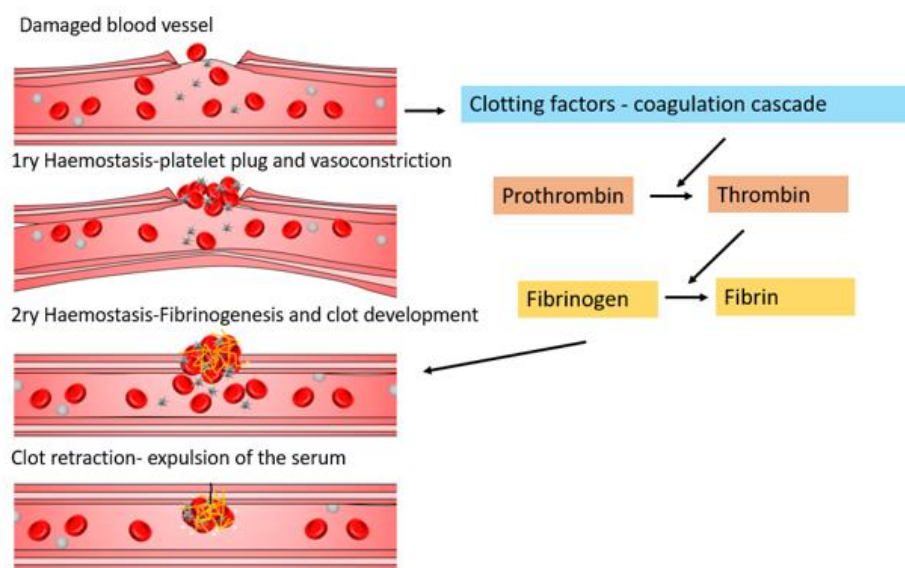


Figure 104 Drawing representing the primary and secondary haemostases occurring after vessel's damage.

Once again the activation of factor *fX* starts the common pathway, where prothrombin activates in thrombin to convert fibrinogen into fibrin, resulting in the creation of a network surrounding platelets and red blood cells (**Figure 105**) [76-78]. Subsequently, clot retraction occurs, which refers to the process whereby activated platelets impose contractile forces on the fibrin network of a thrombus, which over time increases its density and decreases its size, expelling serum (plasma deprived of clotting factors) (**Figure 104**). This process is considered important for promoting clot stability and maintaining blood vessel patency [276-278]. As mentioned in the introduction several pathologies can initiate the coagulation pathway within the lumen without any damage to the wall. Additionally, contact with artificial surfaces like vascular and cardiac prosthesis as well as in "*in vitro*" experiments might trigger the coagulation cascade. The contact coagulation largely depends on surface charge and wettability [80]. Hydrophobic surfaces encourage the adsorption of fibrinogen, fibronectin, or von Willebrand factor which promote platelet deposition, aggregation and activation.

Platelets provide a reactive phospholipid surface on which the coagulation cascade can develop. Thrombin, in turn, induces the release of platelet granule contents such as serotonin, adenosine diphosphate, and calcium, which promotes additional platelet activation and aggregation. On the other hand, negatively charged and hydrophilic surfaces induce binding of plasma *fXII* which consequently undergoes to conformational changes that activate it in *fXIIa*. The activated factor *fXIIa* catalyzes the activation of factor *fXI* and resulting in the synthesis of *fXIa*. Once again, prothrombin is transformed into thrombin by factor *fXIa*, which initiates the common path of cascade [74,79]. In each scenario, the process concludes with fibrin production and the development of a durable clot [79]. Studying novel antithrombogenic materials to create prostheses requires a thorough understanding of how surfaces and clotting blood interact [31,75,80].

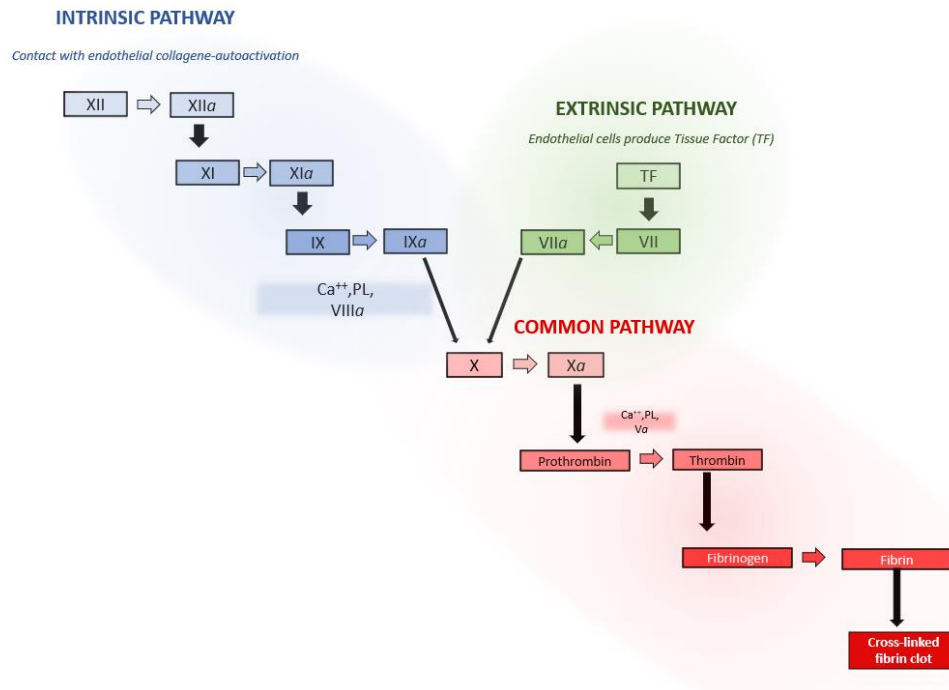


Figure 105 Scheme displaying the coagulation cascade. The blue path is the intrinsic pathway, the green one is the extrinsic pathway and the red one is the common pathway.

3. *In vitro* blood test

Currently, the clotting time of whole blood is measured using thromboelastographic assays, which quantify the viscosity of the blood during coagulation. Rotem®, TEG®, and Sonoclot® are the viscosity tests used to measure blood coagulation. They all offer an overview of the clotting process, from the onset (clotting time) until the clot dissolution.

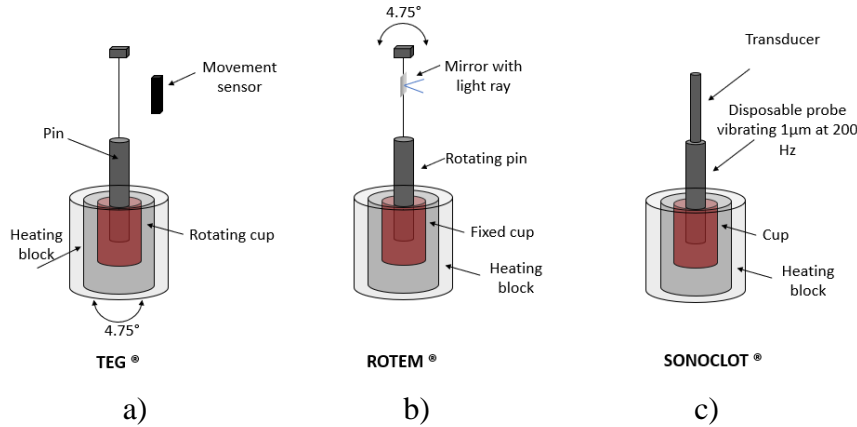
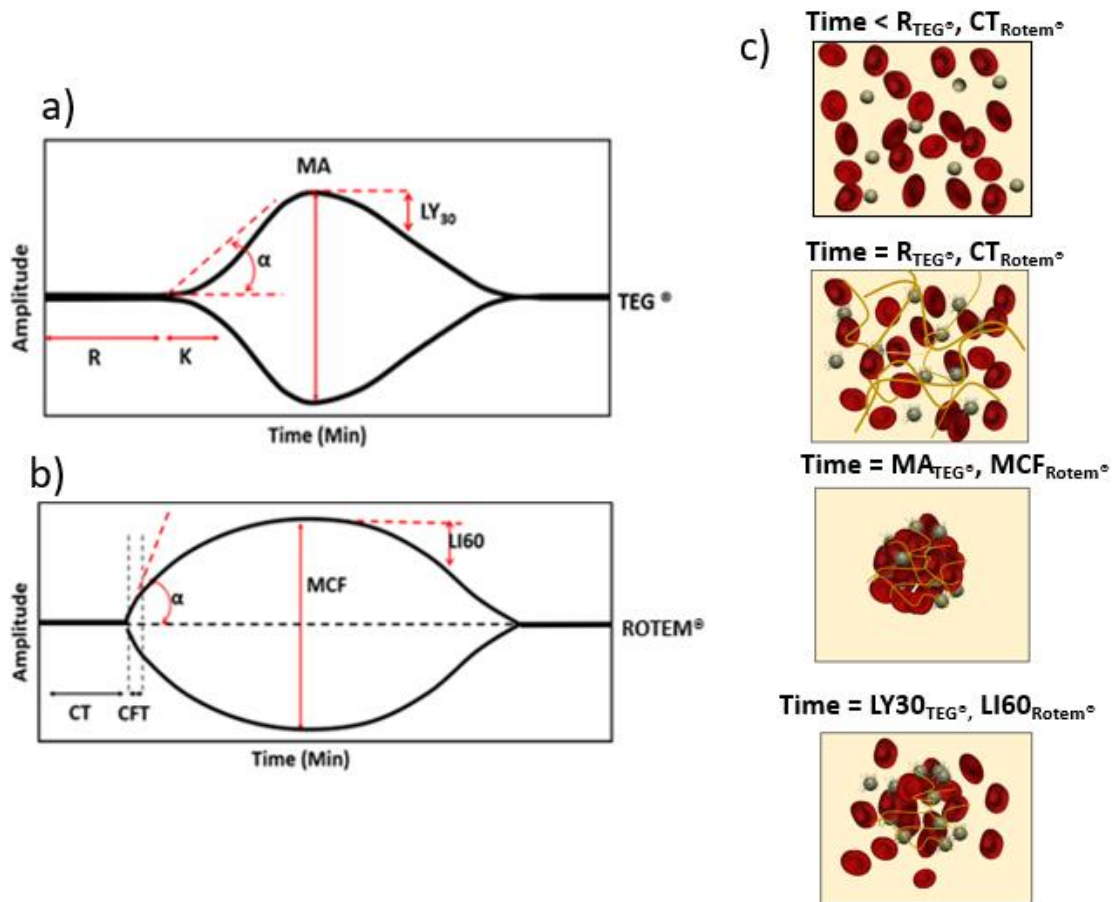


Figure 106 Schematic representation of a) TEG® technology; b) Rotem® technology; c) Sonoclot® technology.

TEG® was the first thromboelastography test developed: a suspended pin is submerged in blood confined in a tiny cup that gently spins, creating a 4.75° arc. When fibrinogenesis begins, fibrin strands develop between the cup and the pin, restricting rotation; the difference in viscosity allows the onset of coagulation to be identified. The clot goes through a series of viscosity changes that are related to its state and that are measured by the movement sensor (**Figure 106-a**) [271,272]. Rotem®, or rotation thromboelastography, works on a similar principle however the cup is stationary while the pin rotates. When fibrin develops between the cup and pin, impeding movement, the machine signals a coagulation start point (**Figure 106-b**) [268,279]. Rotem® and TEG® provide a signature plot indicating the main phenomena occurring in the blood under test. **Figure 107 a-b** represent the typical graphs provided by TEG® and Rotem®; in both there is a steady condition before clot starts, an increase in amplitude associated to fibrinogenesis, a peak related to the maximum strength of the clot and a decline of the amplitude associated to dissolution of the clot, hence fibrinolysis. More specifically the parameter given by TEG® and Rotem® are clotting time, *i.e.*, the starting of fibrin formation, which is the \mathcal{R} time for TEG® and CT for Rotem®; the time between the start of clot formation and the reaching of an amplitude of 20mm (kinetic time K for TEG® and clot formation time CFT for Rotem®); the alpha angle, which gives information about the clot kinetics (α for both the tests); the clot strength, which is reported as maximum amplitude (MA) by TEG® and maximum clot firmness (MCF) by Rotem®; Finally, the clot stability is assessed as LY30 by the TEG®, meaning lysis value 30 minutes after MA, and as lysis index LI60 by Rotem® as the residual clot firmness 60 minutes after the MCF [272]. The meaning of all these markers is represented in **Figure 107-c**. The blood viscosity is also at the basis of the coagulation measurement known as Sonoclot®. In this measurement there is a plastic probe placed onto a transducer, while the blood is contained in a cuvette where the probe is then immersed. The probe oscillates in the blood during the coagulation, and when the fibrin starts to impede the movement, its mechanical impedance is electronically measured as resistance to the movement of the probe (**Figure 106-c**) [268]. This gives useful information about the state of blood during the clotting. In Sonoclot® signature the main parameters are activated clotting time (ACT) which is related to initial fibrin formation; R1, which is the rate

of fibrin formation, also named clot rate CR; R2 which is the second slop related to the platelet action on the contraction of the clot, further fibrin formation and fibrin polymerization; time to peak (TP) which is the moment of maximal clot strength, and R3 associated with fibrinolysis. Between R2 and R3 clot retraction occurs (**Figure 107-d**) [268]. These three viscosity measurements are very useful to assess the primary clotting parameters, nonetheless they present many limitations; for instance, they preclude the possibility of characterizing clotting in contact to different materials, which would be useful in identifying the least thrombogenic for prostheses. Indeed, the sample-holders are of standard materials and difficult to exchange. In addition, viscoelastic measurements are often considered affectable by various external factors, such as the operator and the conditions of the machine in use that requires frequent calibrations [268,271,272]. A new test with good repeatability, precision and adaptable to different surfaces is demanded in order to analyze of blood interaction with several types of materials. Nevertheless, thromboelastography can be a helpful tool for providing gold standard measurements to evaluate the significance of innovative tests based on new technologies.



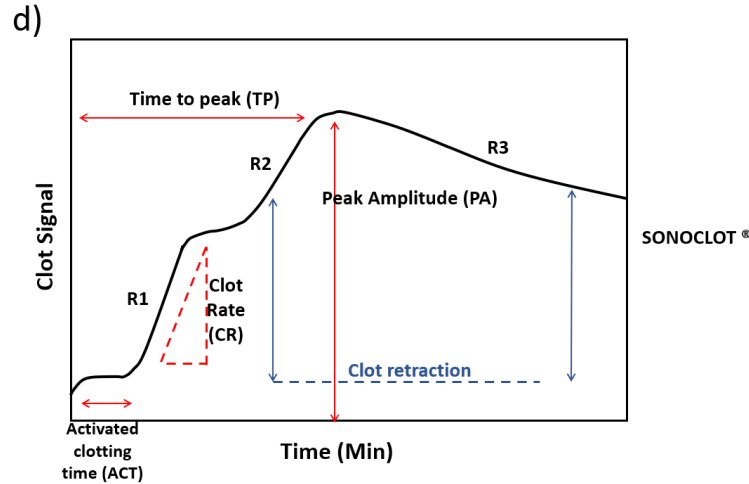


Figure 107 Typical signature of a) TEG®, b) Rotem®, c) Illustration of the phenomena related with the TEG® and Rotem® indicators; d) Sonoclot® signature.

4. Bioimpedance characterization of biological systems

Bioimpedance testing is a technique used to characterize the electrical response of biological systems to an applied alternate electric field. A sinusoidal voltage (or current) is applied across the material under study and the developed sinusoidal current response (or voltage potential) of the sample is measured. The impedance magnitude, Z , is computed as the ratio of the voltage applied over the current response. The impedance Z (Ω) is a complex quantity, defined by real and imaginary parts and phase angle Φ ($^{\circ}$ deg), indicating the phase difference between the voltage and the current. Depending on the frequency of the signal as well as the tissue composition, structure and health condition, the value of the impedance varies, giving relevant information about the material under study [280]. Because of its many benefits, including its low cost, simplicity of use, noninvasiveness, and capacity for online monitoring, bioimpedance spectroscopy has been used for decades to study the electrical characteristics of cells and tissues [281]. Human biological tissues are composed by cells suspended in extracellular fluids (ECF); the cells, in turn, are composed by intracellular fluids (ICF) and cell membranes (M). Each one of these three main components exhibits different electrical properties, meaning they exhibit a different response to an applied electric field. More specifically, ICF, the inner part of the cell, is composed by cytoplasm and nucleus, which in turn are solution of proteins, water, and salts. ICF acts like a resistor and provides resistive/conductive paths to the electrical current that passes through the tissue, hence it is characterized by a resistance R_{ICF} . The cell's membrane, on the other side, is composed by non-conducting lipids inserted between two conducting protein layers (P-L-P structure), thus it is more often modeled as a capacitor and characterized by a capacitance C_M (**Figure 108-a**). In case of alternate E_{fields} , the membrane produces a capacitive reactance X_M strongly dependent on the value of the applied frequency:

$$X_M = \frac{1}{\omega C_M} = \frac{1}{2\pi f C_M} \quad (68)$$

Finally, the extracellular fluids, ECF, are a complex network of macromolecules composed by proteins and polysaccharides, providing highly conductive paths and R_{ECF} is their resistance. The combination of these three components produces a complex bioelectrical impedance, whose value depends on the frequency of the AC field. **Figure 108-b** displays the electrical model describing a human cell in extracellular fluid [282].

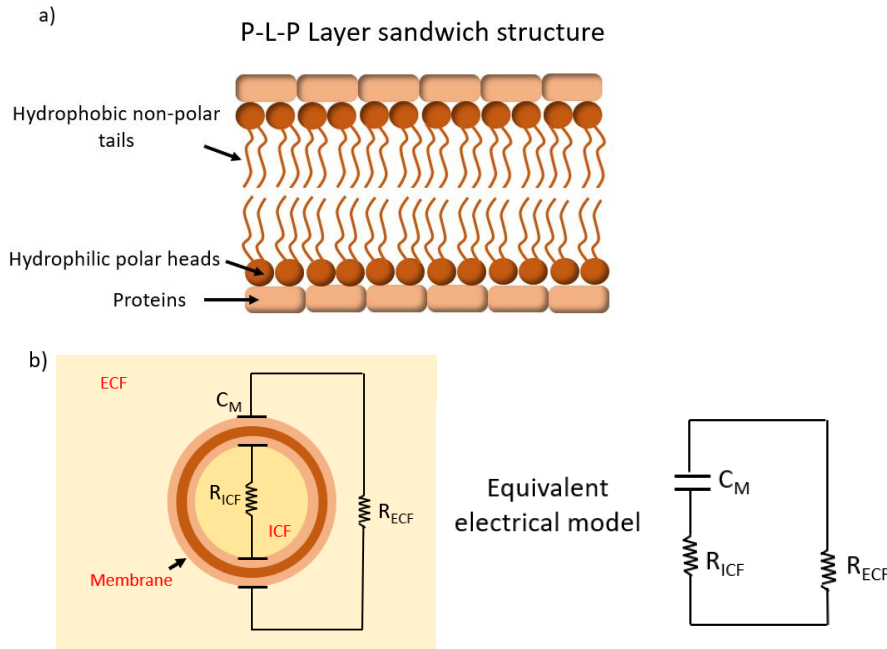


Figure 108 a) P-L-P structure of the membrane of the cells. b) Electrical model of the system made of ECF, ICF and membrane.

At low frequencies X_M is very large, meaning that currents are not allowed to pass through the membrane; The majority of the current will pass through the extracellular fluid, which is low resistive. On the other side, at high frequencies the capacitive reactance decreases, and the current penetrates the membrane reaching the core of the cell (**Figure 109**). It is possible to conclude that high frequencies are more suitable to study ICF, ECF and CM. Bera *et al.* estimated the impedance equation of a tissue, which is reported as follow (Eq.69) [282].

$$Z_{cell} = \frac{R_{ICF}R_{ECF}(R_{ICF}+R_{ECF})+(X_M)^2R_{ECF}}{(R_{ICF}+R_{ECF})^2+(X_M)^2} - j \frac{X_M(R_{ECF}(R_{ICF}+R_{ECF})-R_{ICF}R_{ECF})}{(R_{ICF}+R_{ECF})^2+(X_M)^2} \quad (69)$$

Both real and imaginary part of the impedance depend on the capacitive reactance, hence on the frequency [280].

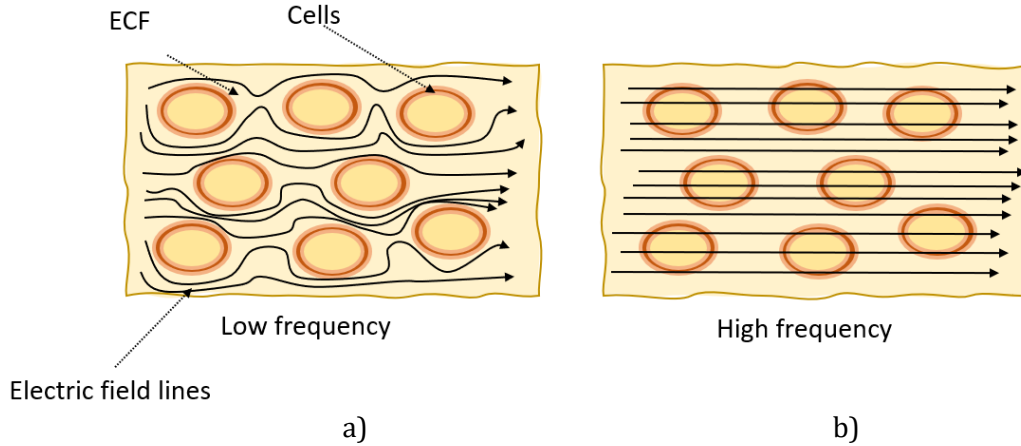


Figure 109 Electric field distribution for a) low frequency voltage, b) high frequency voltage.

In this study we propose a novel technique based on bioimpedance spectroscopy of blood to assess coagulation markers. Blood follows the electrical model previously presented; red blood cells (RBCs) are non-conducting ellipsoids containing a conductive ICF in a conductive medium, the plasma, full of proteins and ionic species. Platelets as well are non-conducting cells, nonetheless, being their shape and size different from RBCs, they have a different capacitance [283]. Bioimpedance can be a useful tool to assess several blood parameters, for instance the number of erythrocytes, and blood disfunctions. Many studies have employed bioimpedance spectroscopy to examine blood. For instance, Amaral *et al.* used bioimpedance technique to study the level of glucose in the blood [284]. This technique proved to be useful also for cholesterol detection as reported by Aghaei *et al.* [285]. Additionally, the electrical characterization of blood and its constituents is crucial for understanding several clinical applications, including the separation of cancer cells from healthy blood cells and the degradation of stored blood [286–288]. This approach can enable coagulation monitoring by identifying the activation of clotting factors which turn plasma into serum, the activation of platelets, a local accumulation and aggregation of red cells, and the polymerization of the fibrin. Similar to biological tissues, the voltage frequency plays a key role in the characterization of blood. Different electrical responses occur depending on the frequency range of investigation, and this may be easily observed when examining the broadband dielectric behavior of blood from few Hz to MHz (**Figure 110-a**) [289].

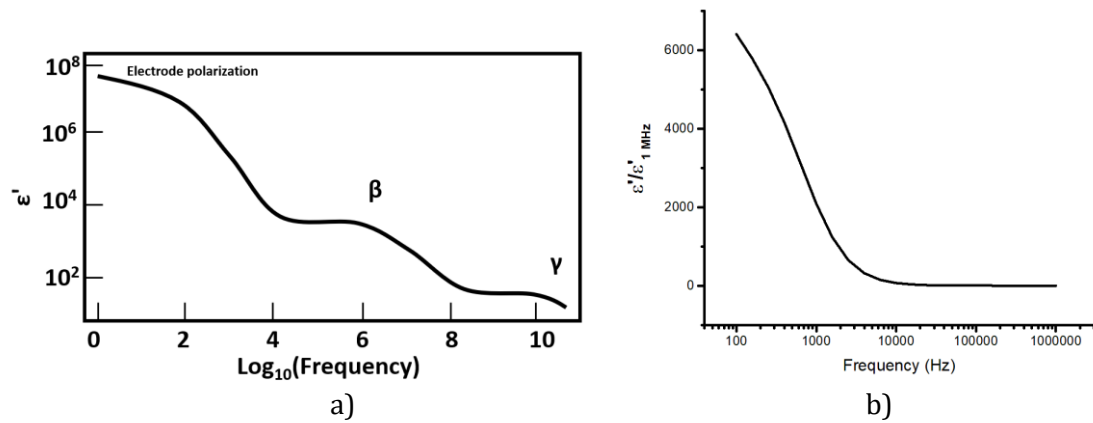


Figure 110 a) Broadband dielectric spectroscopy (relative permittivity real part) of whole blood [289]. b) Dielectric broadband spectroscopy (real permittivity) of whole blood normalized over the value at MHz, performed in this work at 37°C.

Blood exhibits electrode polarization and two dielectric relaxations named β , and γ . Between 10 Hz to 10 kHz there is the electrode polarization, related to ions diffusion; the β dispersion is of Maxwell-Wagner type and is in the range of 10 kHz to 200 MHz, as is the result of the dielectric and electric properties of cells' membrane, ICF and ECF. Finally, at extremely high frequencies, above the GHz, the γ dispersion takes place, and it is associated with water in the tissues [289,290]. **Figure 110-b** displays a broadband dielectric spectroscopy that we performed on whole blood. The test performed between 100-10⁶ Hz follows the one reported by Wolf *et al.* [289]. Blood is a heterogeneous system with a conductive medium and cells with an insulating zone (membrane of the cells) and a conductive core. The interface dominates capacitance and conductance at low frequency, and this is connected to high dielectric constant and lower conductivity. However, at higher frequencies, the capacitor burns out and the bulk characteristics of the cell are sensed. This causes an increase in conductance and a decrease in the real component of permittivity. The increased conductivity is due to the fact that bulk conductance is substantially greater than membrane conductance, which is shorted by the interface capacitor at high frequencies [289]. Electrodes to convey and gather the signal are required for bioimpedance spectroscopy. The measurement can be performed using different electrodes arrangements; the most used are two and four electrode configurations (**Figure 111 a-b**). In two-electrodes method, as the name suggests, only two electrode will be put in contact to the sample; these will inject the electric signal and collect the response; on the other side, in four-electrodes method two electrodes are in charge of delivering the signal (driving electrodes) and two others to collect the response from the tissue under examination (sensing electrodes)[282].

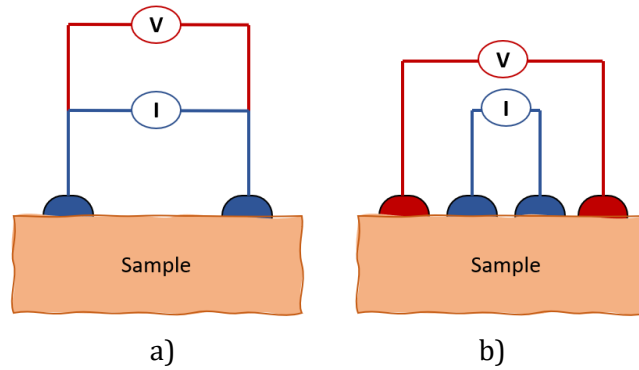


Figure 111 a) Two-electrodes and b) four-electrodes bioimpedance configuration.

5. Materials and methods

5.1. Materials

This study was approved by the local Ethics Committee. Human blood was provided by "Etablissement Français du Sang" in citrate tubes (vacutainers) from deidentified healthy volunteers. Calcium solution (CaCl_2 in HBS (Hepes Buffered Solution) (200mM)) and Tissue Factor (TF) solution (TF in HBS (1nM)) were provided by inter-university Laboratory of Human Movement Sciences (LIBM). Fibrinogen from Human plasma, Alexa Fluor™ 488 Conjugate, used to visualize fibrin via confocal microscopy, was purchased from Thermo Fisher Scientific®.

5.2 Blood clot preparation

Each blood sample was analyzed within 24-30 hours after collection and stored at 4°C until use. It was not possible to analyze the samples immediately after withdrawal since the blood was delivered (by French Blood Establishment) the day after collection. Several studies have revealed that a storage of blood samples under a temperature of 4°C within 24h did not lead to significant change on their coagulation parameters [291,292]. The whole citrated blood was incubated 5 minutes at 37°C before testing. In a first cycle of tests the blood was coagulated only by recalcification: 3.5 μL of calcium solution were added to 60 μL preheated blood. The final concentration of calcium in the blood was 11 mmol/L. Recalcification allowed the activation of the coagulation process. After recalcification the blood was tested immediately at 37°C via impedance magnitude spectroscopy. In a second cycle of experiments, following 5 minutes of incubation at 37°C, recalcification was performed, respecting the proportions written above with the further addition TF solution, according to the following ratio: 3.5 μL of TF solution per 60 μL of blood and 3.5 μL of calcium solution, which allowed a study of coagulation via extrinsic pathway. After the addition of the clotting agents, the blood was tested immediately at 37°C via impedance magnitude spectroscopy.

5.3. Impedance magnitude spectroscopy

Impedance of blood coagulation was carried out with two-electrodes configuration. 60 μL of recalcified blood, with or without TF, were placed on a PET substrate where two gold lines, acting as electrodes, were previously deposited via gold sputtering. The thickness of the two lines was $a = 0.5 \text{ mm}$ and the distance was $w = 5 \text{ mm}$ (**Figure 112-a**). According to Eq.70, the penetration depth (T) of the electric field lines was estimated equal to 1.65 mm [293].

$$T = \left(\frac{w}{2}\right) * \left[\left(\frac{(2*a)+w}{w}\right)^2 - 1\right]^{\frac{1}{2}} \quad (70)$$

The electrodes were connected to a wave generator (Agilent 33220A), providing a voltage input to the blood. The current output delivered from the sample was measured via a current amplifier (Stanford Research Systems SR70). The generator and the amplifier were coupled to Dewesoft®, a data acquisition software, allowing simultaneous monitoring and recording of the input voltage and the current response (**Figure 112-b**). Based on the expression of Eq.67, the changes in the impedance magnitude (denoted $|Z|$) of blood during coagulation could be estimated. RMS values of current and voltage were used to compute Z . The sinusoidal-waveform voltage was set at 0.05 V amplitude and initially different frequencies were tested (100 Hz, 1 kHz, 10 kHz, 100 kHz and 1 MHz); 10 kHz was selected as the optimal frequency to identify the markers of coagulation. In light of this, that parameter was used for all following measurements. The sampling rate was chosen equal to one value per second (1 Hz), adequate to detect the clotting variations which are of the minute order. The test was carried out in a small, closed chamber of a 0.5 cm^3 volume so as to prevent the blood from drying. The measurement was performed in incubation at 37 °C for 45 min (**Figure 112 a-b**). The recorded data were normalized over the first value (denoted $|Z|/|Z_{t=0}|$) and plotted as a function of time.

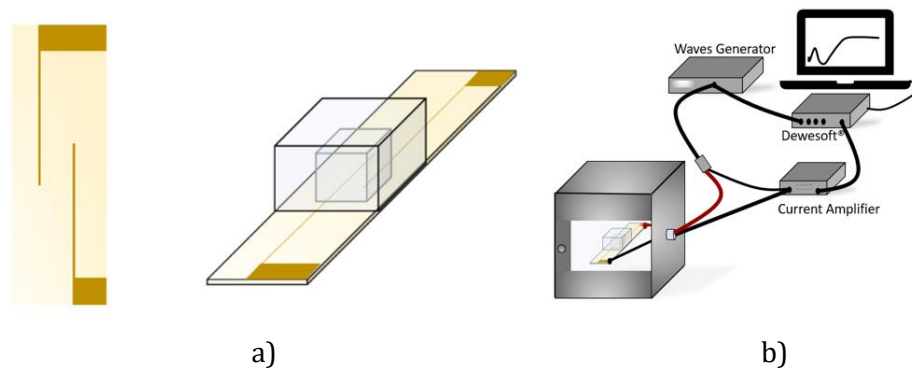


Figure 112 a) Sample-holder used for blood impedance magnitude spectroscopy. b) Complete set-up employed in $|Z|$ measurements.

5.4 Impedance phase angle

The changes of blood's impedance phase angle (Φ) during coagulation were recorded using Solartron spectrometer (1296A Dielectric interface System) at a 10 kHz frequency and a 0.05V amplitude. Following the formation of the clot, retraction occurred, with consequent expulsion of the serum from the clot. The serum and clot were then separated and tested individually via broadband spectroscopy over a broad range of frequencies (from 10 Hz to 1 MHz), using the sample-holder shown in **Figure 112-a**.

5.5 Confocal microscopy

Confocal microscope (Nikon A1r) was used to observe blood during coagulation with the aim of validating the significance of the impedance magnitude test. A solution with sodium bicarbonate (0.1M, pH 8.3) and Alexa Fluor™ 488 Conjugate, was prepared (40 $\mu\text{g}/\text{ml}$), and 5 μL of it were added to 200 μL of citrated blood. The mixture was then incubated at 37°C for 10 minutes, followed by the addition of the calcium solution in the same ratio as explained in subsection 5.2 of this chapter. A stopwatch was set as soon as calcium solution was introduced, allowing to control the delay between the addition of the coagulant and the beginning of the observation. 80 μL of blood were deposited on a closable glass bottom dish (Mattek, 35mm with 14mm glass uncoated, 1.5), to prevent the blood from drying, and observation started in a closed chamber at a controlled temperature of 37°C. Three different planes were appropriately selected to observe the coagulation process, at 0 μm , 3.28 μm , and 6.57 μm from the glass. Each 27.3 seconds an image per plane was recorded over 45 minutes. Only the pictures from the first plane (*i.e.*, the most representative of 0 μm) are reported. The objective magnification was 40x and the numerical aperture (NA) was 1.30. The emission wavelength was set at 525 nm with the excitation wavelength of 488 nm. Other setting parameters were chosen as follows: the image pixel size was 0,31 $\mu\text{m}/\text{pixel}$, the pinhole of 80 μm , the optical sectioning of 1.5 μm , and the optical resolution of 0,21 μm . The same blood observed by microscopy was then analyzed by impedance spectroscopy on a surface made of the same material of the microscope glass. Blood from the same donor was simultaneously tested at 37°C by confocal microscopy and impedance characterization, and this made it possible to link impedance markers to events that could be seen under a microscope.

5.6 Rotem® characterization

To further validate the technique developed in this study, impedance magnitude analysis combined with Rotem® test (using TOTEM delta Werfen®) were concurrently performed. Blood collected from the same donor was used during both tests, performed at 37°C. Nine tests were carried out on blood recalcified with calcium solution. For each of the nine tests the blood was drawn from a different donor. Subsequently, the extrinsic coagulation pathway was verified by performing six further tests with recalcified blood to which TF solution was added. The clotting time measured by Rotem® was then compared to the markers identified by impedance spectroscopy. A blood volume of 200 μL was used for the Rotem® analysis and the ratio of blood to clotting agents is the same mentioned in subsection 5.2 Chapter IV.

5.7 Coagulation time and wettability

Contact-induced coagulation with synthetic materials is intimately connected to surface wettability, as stated in section 2 of this chapter. The coagulation impedance test should be evaluated on a variety of surfaces with different degree of wettability in order to prove that it is suitable for the examination of contact coagulation. Therefore, four surfaces with different wettability were selected: PET, UV-ozone-treated PET (named PET UV-treated), PVDF positive and negative polarity side. Although the wettability of PET is not particularly high, UV ozone treatment can provide satisfactory wettability levels. The UV-ozone treatment is a photo-sensitized oxidation method that employs short-wavelength UV light to excite and dissociate polymer molecules. In addition, UV radiation splits oxygen into atomic oxygen and atomic oxygen reacts with polymers to make polar functional groups like peroxy, carbonyl, carboxyl and hydroxyl that increase hydrophilicity [294]. In this case the surface of PET was treated by UV-ozone for 10 minutes. PVDF, on the other hand, is a piezoelectric polymer that, when mechanically stressed, generates a positive charge on one surface and a negative charge on the opposite surface. Nevertheless, in this case the material was not mechanically stimulated during the test so the difference between surfaces' wettability was small. First, the contact angle between the blood and the surfaces with different wettability was tested by means of a Contact Angle Goniometer. Gold electrodes with the geometry presented in the subsection 5.3 Chapter IV were sputtered on each surface. Subsequently, blood from the same donor was deposited between the electrodes on the PET and UV-treated PET surfaces and two impedance measurements (voltage amplitude 0.05 V frequency 10kHz, sinusoidal shape) were taken simultaneously at 25°C. The same measurement was carried out on PVDF positive and negative side. In this instance, it was required to add extra components to the setup in order to be able to measure coagulation on two surfaces at once: an identical signal could be supplied to both samples since the two surfaces were joined by a T-connector to a single sinusoidal voltage generator; two current amplifiers—one for each sample—collected the current responses and delivered them to two distinct channels of the Dewesoft® data analyzer, which captured all the data. This arrangement made it feasible to simultaneously analyze coagulation on many surfaces. The tests were repeated 3 times on different donors' blood.

6. Results and discussion

6.1 Impedance spectroscopy

Impedance characterization of coagulating blood allowed to identify the key biomarkers related to coagulation events. First, impedance magnitude of citrate whole blood (without coagulants) was measured at a constant frequency of 10 kHz for 45 minutes. The same measurement was repeated on recalcified blood, *i.e.*, coagulating blood. **Figure 113** illustrates the time evolution of the electric impedance of bloods normalized to the first value ($|Z|/|Z_{t=0}|$). Substantial discrepancies between the whole blood and the clotting blood are observed, confirming that blood impedance spectroscopy can potentially define biomarkers to assess blood coagulation. The red curve of the whole blood is characterized by an initial

slight decrease, probably related to the formation of rouleaux¹² of red blood cells. A few minutes after, an increasing trend associated with the sedimentation of red cells on the bottom appears, leading to a phase separation between red cells and plasma. On the other hand, the black curve associated with clotting blood clearly presents a peak at around 9 minutes (the 1st possible marker), a subsequent decrease culminating in a minimum at 13 minutes (the 2nd possible marker), beyond which a sudden steep increase appears. Given the timing of the two markers, they may be related to fibrin formation and clot retraction, respectively, nonetheless further assessment is required to verify their meaning.

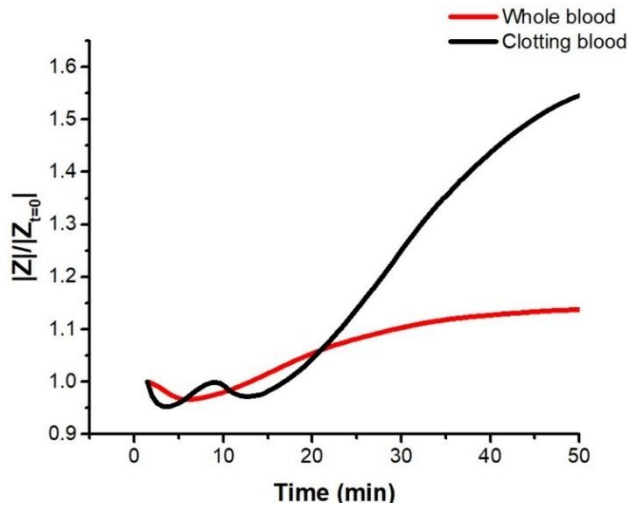


Figure 113 Time evolution of normalized impedance ($|Z|/|Z_{t=0}|$) measured at 10 kHz for the whole blood and recalcified blood.

Bioimpedance test was then conducted at a variety of frequencies between 100 Hz – 1 MHz during the whole coagulation process (45 minutes) to select the optimal frequency for detecting impedance changes related to clotting. Coagulation of citrate blood was induced by recalcification. **Figure 114** reports the evolution in time of impedance magnitude normalized at the first value at the following frequencies: 100 Hz, 1 kHz, 10 kHz, 100 kHz, and 1 MHz. The plot at 100 Hz exhibits an increase in impedance but no peak that may be connected to the beginning of fibrin production. At 1 kHz, a peak emerges between 5 and 10 minutes, followed by a minimum, then a sudden climb. These indicators are more significant between 10 and 100 kHz and subsequently become less pronounced at 1 MHz. These findings lead to the conclusion that coagulation-related impedance variations are mostly detectable between 1 kHz and 1 MHz. The frequency of 10 kHz is found to be the best for coagulation bioimpedance monitoring since it appears to display more distinct indicators, therefore is selected for impedance characterization of clotting blood. A first verification of the second marker is achieved by comparing the impedance measurements with visual inspection of the clot. The retraction of the clot is observable by naked eyes on the sample, as shown in **Figure 115-a**, where the retracting clot's serum is visibly expelled. If contraction does not occur (or is

¹² Rouleaux are stacks or aggregations of red blood cells (RBCs) that occur due to the discoid shape of vertebrate cells.

delayed beyond 45 minutes), no separation of phases is visible on the sample. As a result, the impedance curve does not manifest any increase, but ends with a plateau indicating non-retracting blood (**Figure 115-b**). This suggests that the sharp increase of impedance may be caused by a separation of clot and serum phases due to contraction of the thrombus.

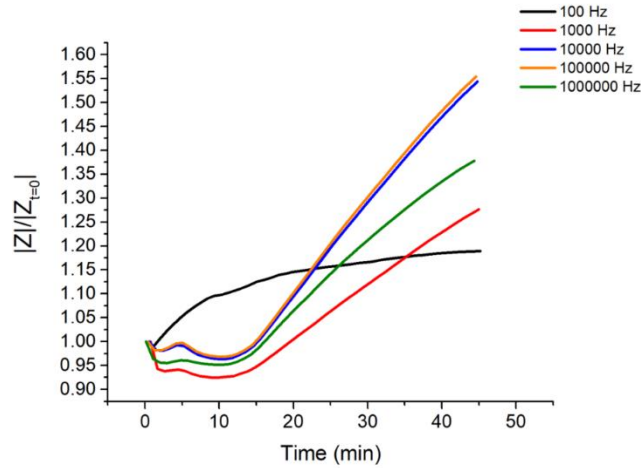


Figure 114 Evolution in time of normalized impedance magnitude during coagulation at 100 Hz, 1 kHz, 10 kHz, 100 kHz and 1 MHz.

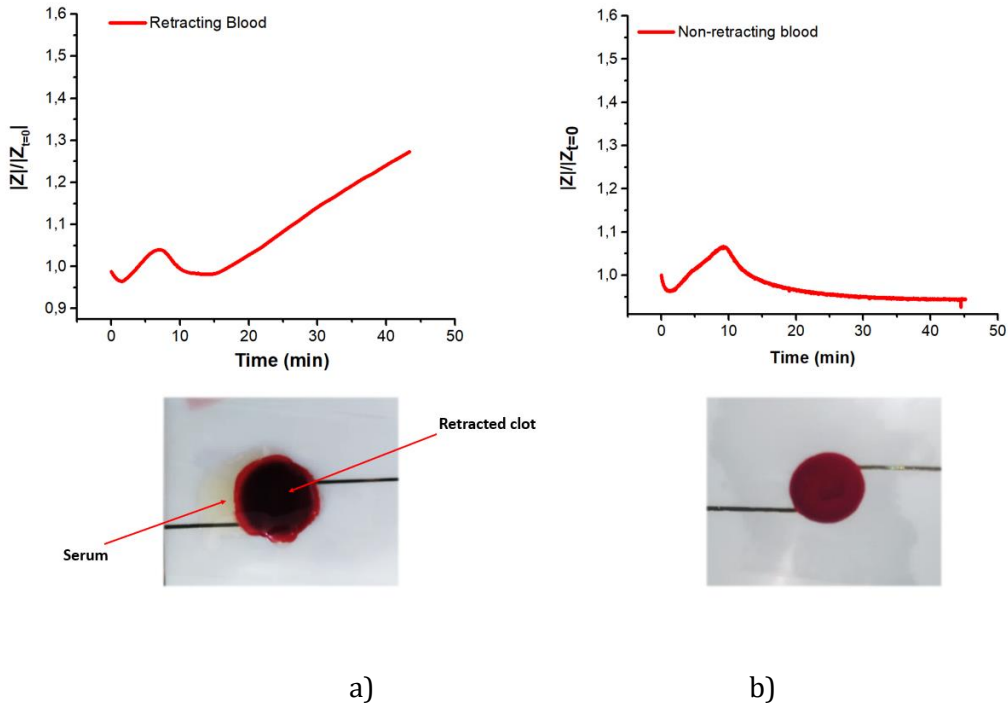


Figure 115 a) Retracting blood impedance magnitude analysis at 10 kHz with respective picture of retracted blood clot; b) non-retracting blood impedance magnitude analysis with picture of non-retracted clot.

Further assessment of the second marker is performed by measuring the impedance phase angles (Φ) using *Solartron* analyzer system. Usually, the value of Φ indicates the capacitive, resistive, or inductive behavior of a sample at a specific frequency. First, Φ at 10 kHz was measured on blood during coagulation to determine its trend over time. Then clot and serum, separated after retraction, were tested via broadband spectroscopy of Φ , over a large frequency range from 100 Hz to 1 MHz. The variation of Φ_{Blood} during coagulation follows the trend of normalized impedance magnitude, presenting the two main markers (**Figure 116-a**). Regarding the rise occurring after 13 minutes, the angle rises from $-7,3^\circ$ to -5.6° , indicating an increase in resistive behavior as 0° is associated to a perfect resistor. According to broadband spectroscopy analysis, at 10 kHz the clot has Φ_{Clot} equal to -5° while serum broadband spectroscopy reveals a Φ_{Serum} angle of -24° (**Figure 116-b**). It is therefore intuitive that an increase of resistive behavior during the coagulation may be related to a contraction of the clot with expulsion of the serum (**Figure 113-b**). We can summarize the electric changes in blood as follow: during the coagulation process, RBC aggregation results in an impedance network (increase in resistance) of the cells that are connected to one another by fibrin fibers, dramatically raising the impedance of the entire blood. After clot retraction only the clot made of fibrin, platelets and red blood cells remains between the electrodes. Further investigations are carried out in the following sections to validate the first biomarker as well as to corroborate the second one.

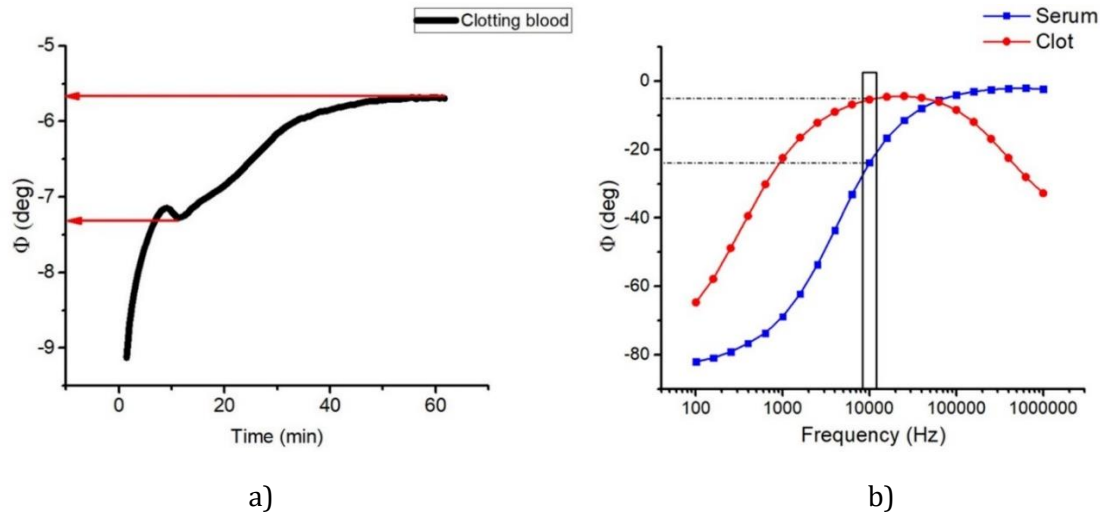
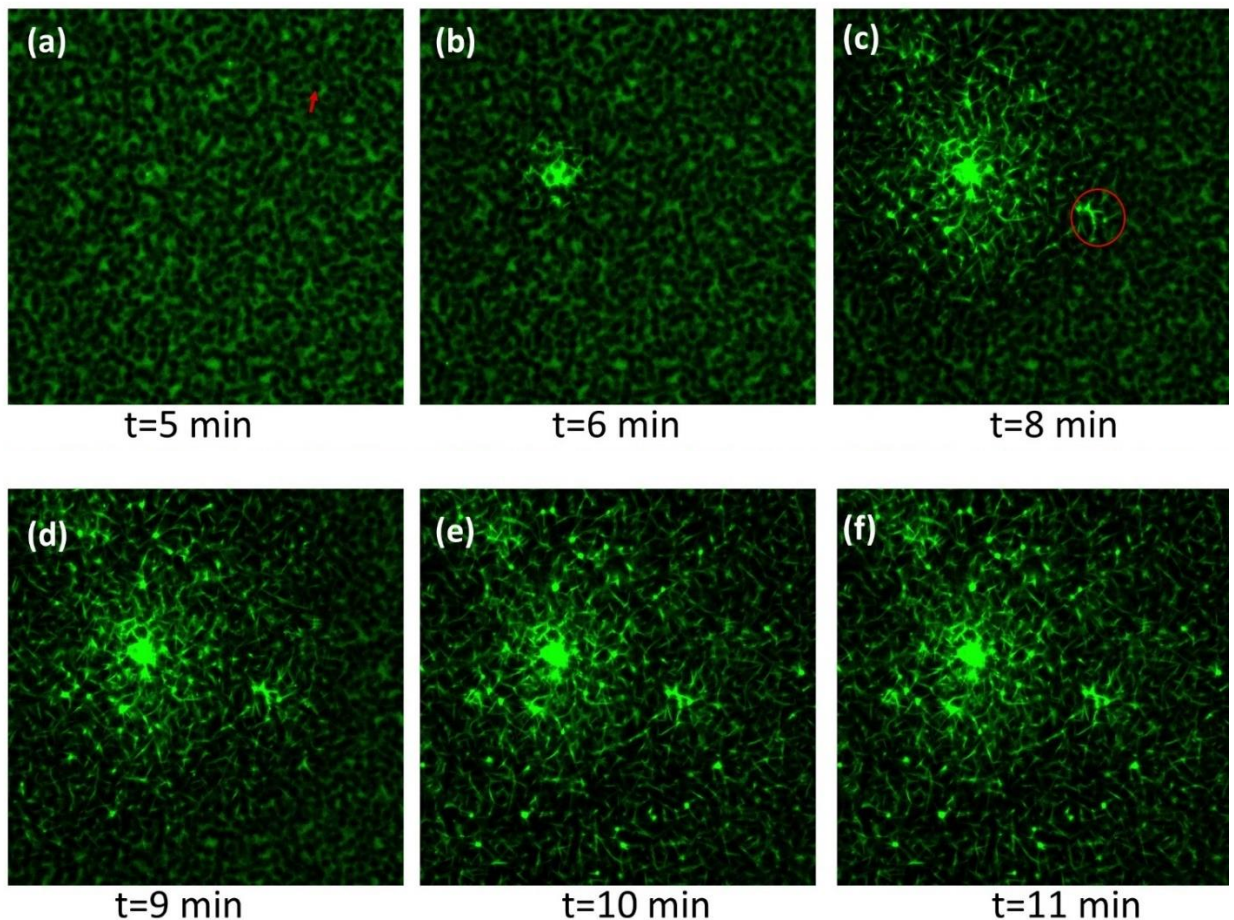


Figure 116 a) Impedance phase angle (Φ) as function of time for recalcified blood; the red arrows indicate the value of Φ before and after the steep increase. b) Impedance phase broadband spectroscopy (100 Hz-1MHz) of clot and serum separated after retraction.

6.2 Confocal microscopy

Confocal microscopy has previously been employed in several works to investigate clots and coagulating blood. One of the technique's primary advantages is the ability to track blood-related events second by second. For instance, Wallner *et al.* investigated how temperature affected platelet and coagulation activity as seen by real-time live confocal imaging [295]. The study of Kim *et al.*, who reported confocal microscopy of clot contraction, is equally

noteworthy [296]. The findings of these studies indicated that confocal imaging might be used to evaluate clotting time and clot retraction. The course of coagulation was imaged through confocal microscopy to further validate the markers found by impedance magnitude spectroscopy. A fluorescent labeling emitting in the green wavelength was added to the blood to visualize the filaments of fibrin, otherwise invisible. As explained in subsection 5.5 Chapter IV, the first image was not pictured immediately after the addition of the calcium solution, but rather 4 minutes and 40 seconds after recalcification, due to the time required to set the microscope. **Figure 117 a-l** report the results. The first image exhibits a green background with darker spots related to red blood cells, as indicated by the red arrow in **Figure 117-a**, not visible in the wavelength range analyzed, while fibrin is still not present, since no polymerization has yet occurred. When fibrinogenesis is activated, the first fibrin filament appears, at 6 minutes from recalcification (**Figure 117-b**). Fibrin begins to form from a localized area and propagates in space until it covers the entire examined area, at 11 minutes from the addition of the calcium solution, (**Figure 117-f**) (Video 1 available in supplementary support). The appearance of the fibrin indicates the clotting time (CT). A contraction of the fibrin network can be noticed in the video and in the sequence of images reported below, starting from 11-12 minutes (**Figure 117 f-g**). When contraction starts, the platelets locally pull the fibrin causing the whole clot contraction at macroscopic level [277].



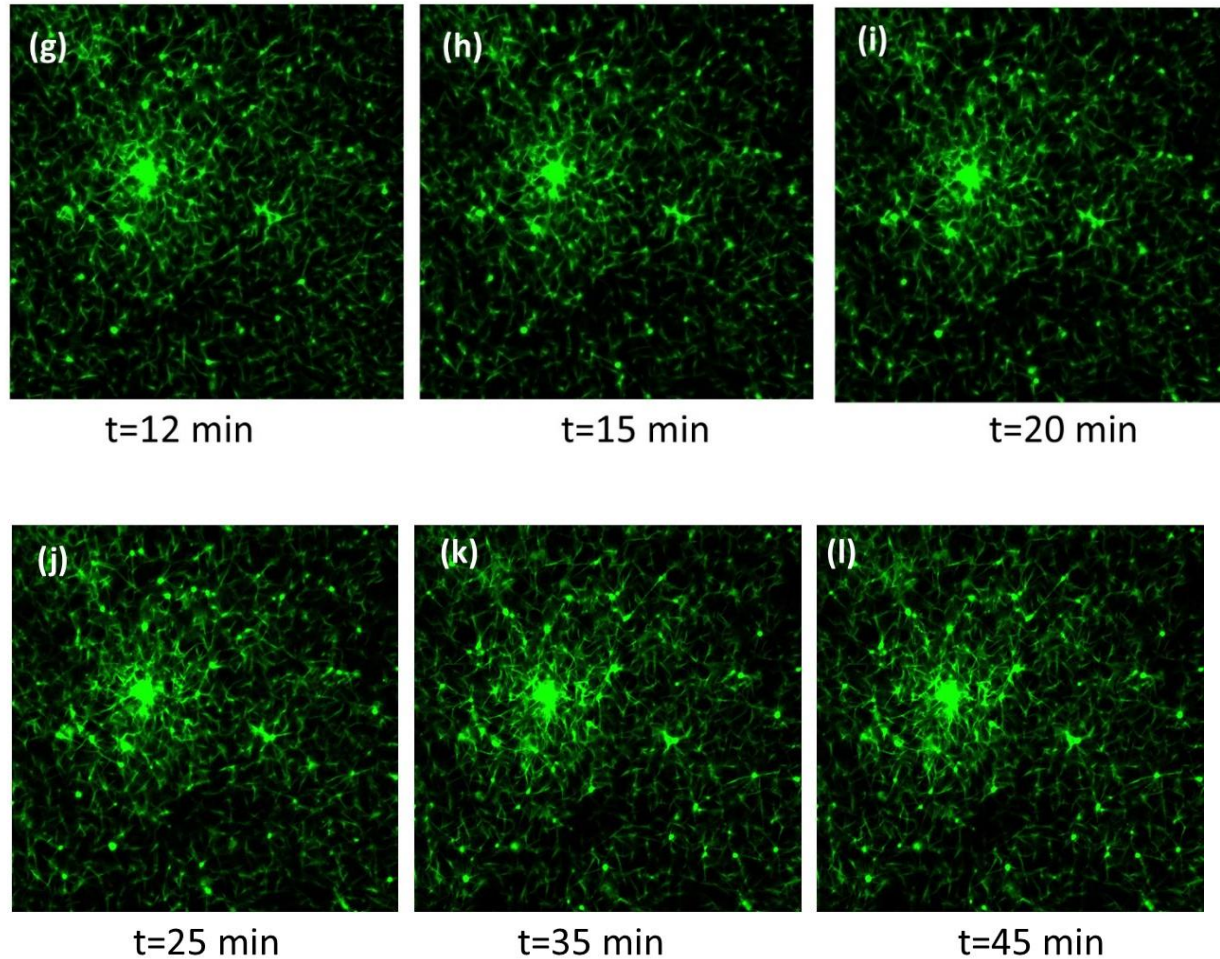


Figure 117 a)-l) Confocal microscopy frames at different times since the addition of calcium solution. The red arrow in figure a) indicates the dark shadow of a red cell. The green fibers correspond to the fibrin network labeled using fibrinogen from human plasma Alexa Fluor™ 488 conjugate.

To quantify this phenomenon, a reduced area of the whole image, circled in red in **Figure 117-c**, is analyzed. The evolution of this area as coagulation proceeds is illustrated in **Figure 118 a-l**, where the length of the filament is determined in pixels, using ImageJ®. We decided to focus on this area rather than the large agglomeration in the picture because we are observing in the x-y plane, but coagulation and contraction are also occurring in the z plane; the large clot during the observation contract is three dimensions, making it difficult to measure the variation in fibrin lengths, so we needed to identify an area that was always in the plane to properly perform the analysis. Before 11 minutes no reduction of the length of the fibrin is measured. At minute 11 the filament shortens of 10% of its initial length, indicating the starting of retraction (**Figure 118-e**), while at the end of the measurement the length reduction is of 55%. Following confocal analysis, a blood sample from the same donor was tested by impedance magnitude analysis and the markers were compared with the confocal microscopy observation. The clotting time peak (the 1st marker) and the minimum followed by a steep increase (the 2nd marker) coincide exactly with the times detected by

microscopy for CT and clot retraction, confirming what predicted in the previous subsection 6.1 Chapter IV (**Figure 119**).

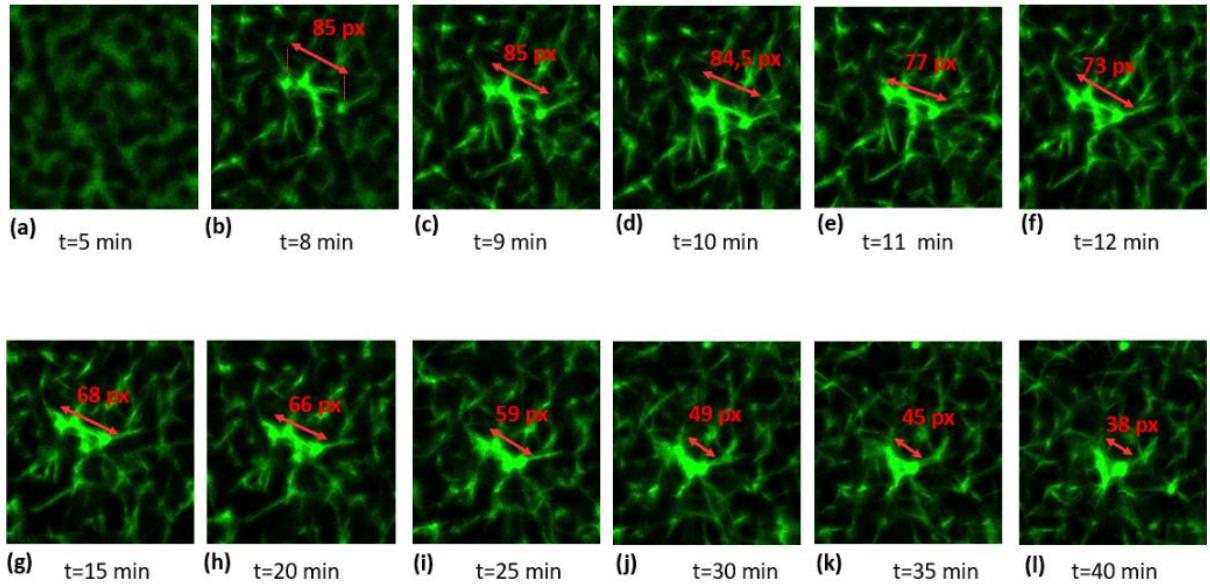


Figure 118 a)-l) Detail of a of fibrin branch from its appearance through the different moment of the contraction. On each frame the length of the fibrin is measured in pixels using ImageJ® software.

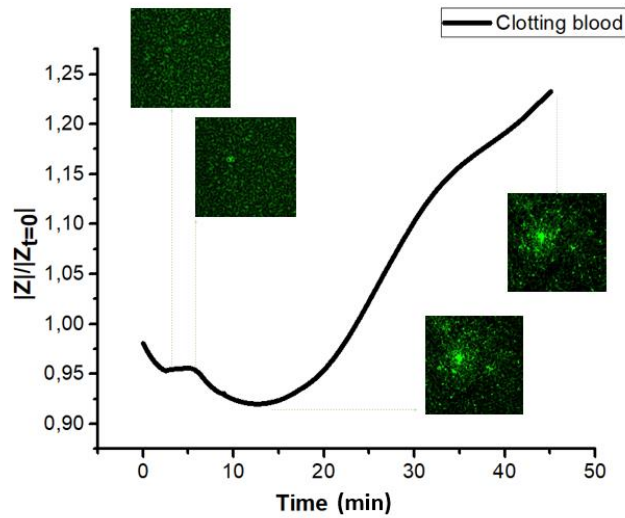


Figure 119 Impedance magnitude test of clotting blood from the same donor as that tested via confocal microscopy.

6.3 Rotem® characterization

Impedance magnitude characterization was compared to the Rotem® test, which is routinely employed in biological laboratories as the gold standard for describing the coagulation process. Blood samples were tested simultaneously with the two techniques and the collected data were compared. In a first set of tests (nine different blood samples), coagulation was

triggered only by recalcification. **Figure 120-a** displays the coagulation plot obtained by the impedance measurement of a blood sample, while **Figure 120-b** illustrates the results recorded via Rotem® for a sample from the same donor. As expected, the clotting time acquired through the impedance test (denoted $CT_{\text{Impedance}}$) is well correlated to the Rotem® one (denoted CT_{Rotem}), allowing to clarify the meaning of the first peak in the impedance plot.

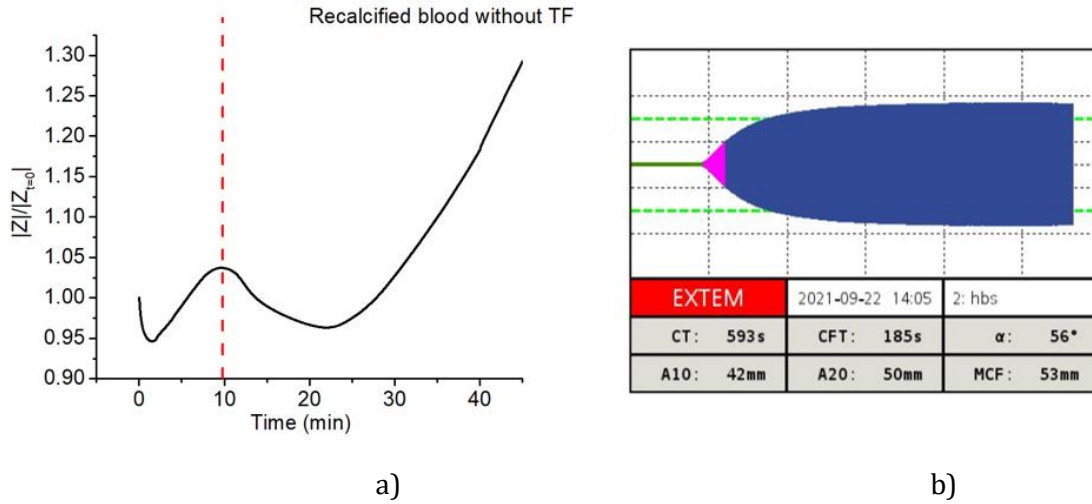


Figure 120 a) Impedance magnitude test and b) Rotem® analysis of recalcified blood from the same donor without TF.

The boxplot in **Figure 121** provides a statistical overview of the results acquired from the nine tests performed on different donors' blood, comprising locality, dispersion, and skewness of the acquired data. The numerical values are summarized in **Table 13**, where mean value, standard deviation (SD), maximum and minimum values are reported. The three quartiles (Q1, Q2 or median, and Q3) are reported as well, where Q1 is the 25th percentile, *i.e.*, the median of the lower half of the dataset, Q2 is the 50th percentile, *i.e.*, the median of the entire dataset, Q3 the 75th percentile, meaning the median of the upper half of the dataset, and IQR is the interquartile range. To better assess the variability of the data, we provide here an estimation of the quartile coefficient of dispersion (QCD, *i.e.*, given by Eq.71). The higher the QCD, the more dispersing are the observed the data.

$$QCD = \frac{Q_3 - Q_1}{Q_3 + Q_1} = \frac{IQR}{Q_3 + Q_1} \quad (71)$$

Overall, the values from the Rotem® and the Impedance spectroscopy match each other. The average discrepancy between CT_{Rotem} and $CT_{\text{Impedance}}$ is found around 11 seconds (2 %), reflecting high reliability of the impedance analysis that somehow agrees with the standard measurement. Based on Rotem® characterization, it was not possible, however, to verify the second impedance marker appearing at the beginning of the clot retraction, since this value was not accessible through the viscosity test. As a matter of fact, Rotem® allows to identify

the maximum clot firmness (MCF) that indicates the maximum strength of the clot occurring after the retraction has already begun.

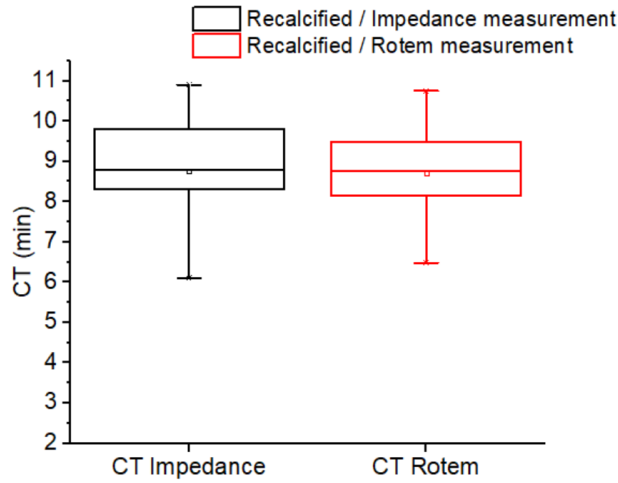


Figure 121 Box graph computed over 9 different blood samples (recalcified without TF) representing clotting time by impedance magnitude spectroscopy and Rotem® (black and red boxes, respectively).

To analyze coagulation via extrinsic pathway, a second set of tests was performed by initiating coagulation with an addition of calcium and TF solutions. Six different blood samples were characterized by Rotem® and impedance magnitude tests, simultaneously. The impedance characterization enabled to identify the clotting time and retraction markers. **Figure 120 a-b** report the results from the normalized $|Z|$ analysis and Rotem® test respectively, on blood collected from the same donor. Good coherence between CT_{Rotem} and $CT_{Impedance}$ is observed, again, confirming high accuracy of the developed protocol.

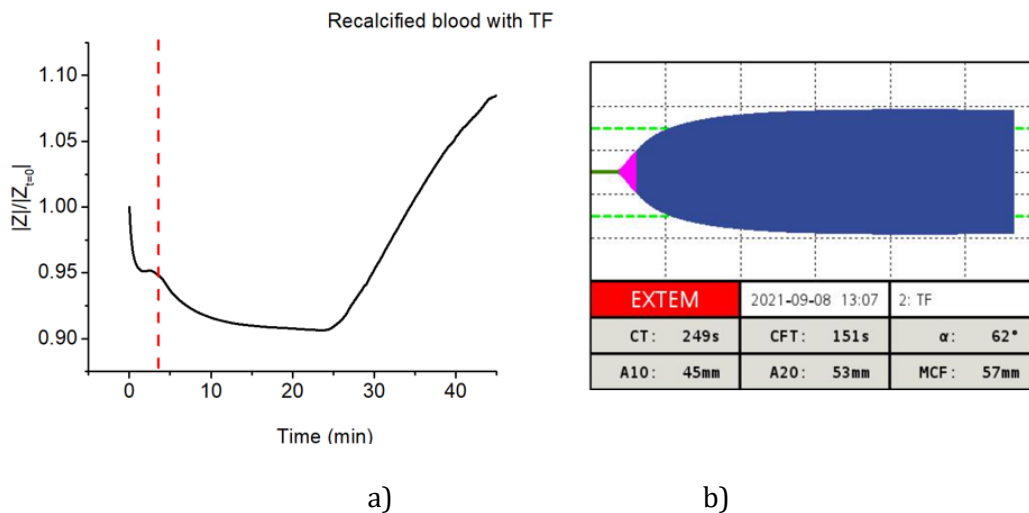


Figure 122 a) Impedance magnitude test and b) Rotem® analysis of recalcified blood from the same donor with TF.

Figure 123 displays the whisker box graph computed over all the six tests. To some extent, the clotting times measured through these two techniques are analogous. Focusing on the average value, it is 3 minutes for both impedance and Rotem® test.

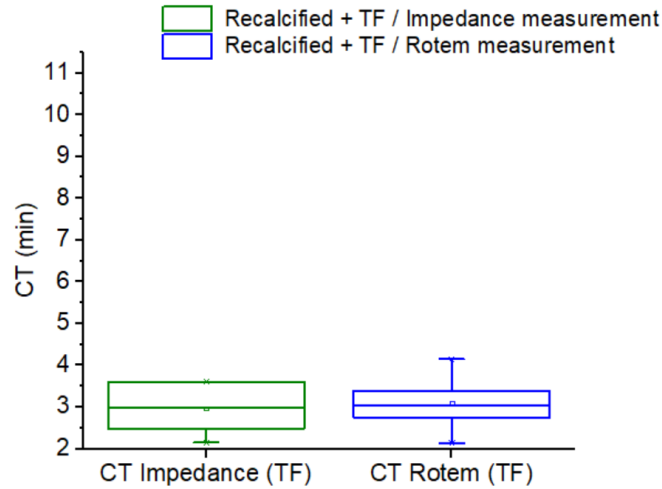


Figure 123 Box graph computed over 6 different blood samples (recalcified with TF) representing clotting time by impedance magnitude spectroscopy and Rotem® (green and blue boxes, respectively).

Table 13 reports the detailed data related to the box graph, giving an overview over the statistic of the experiments. The results lead to the following conclusion:

- Whatever the technique of measurement, recalcified blood samples with TF led to smaller value of CT.
- For all samples with or without TF, both impedance and Rotem® technique leads to similar results in terms of central tendency (mean and median values), dispersion (SD, IQR), and limit values (max, min).
- In any case, the data distributions were almost symmetrical, as the medians (horizontal lines in the whisker box) were close to the mean values (circles), thus the skewness should be near to zero.
- All observations did not show any outliers or extremes values (*i.e.*, fall below $Q1 - 1.5 \text{ IQR}$ or above $Q3 + 1.5 \text{ IQR}$), meaning that the highest and lowest occurring value were within this limit interval.
- Finner analysis regarding the data dispersion via QCD:
 - ✓ Impedance technique gave raise to somewhat higher dispersion in CT than the Rotem® one.
 - ✓ Measurement of the samples without TF results in smaller dispersion, regardless of which technique was chosen.

For all the cases, the QCD value is relatively low, confirming good repeatability of the data. Accordingly, the comparison between Rotem® and Impedance magnitude analysis confirmed the significance of the 1st biomarker in recalcified blood, either with or without TF.

Table 13 Statical data related to $CT_{Impedance}$ and CT_{Rotem} for recalcified samples with and without TF. 6.4 Wettability and blood coagulation.

Variable: CT	Impedance test		Rotem® test	
	with TF	without TF	with TF	without TF
Mean value (min)	2,96	8,76	3,08	8,71
SD (min)	0,65	1,38	0,68	1,23
Min value (min)	2,15	6,10	2,13	6,46
Max value (min)	3,60	10,90	4,15	10,75
Q1 (min)	2,50	8,30	2,73	8,13
Q2 (min)	2,99	8,80	3,04	8,76
Q3 (min)	3,60	9,80	3,41	9,50
IQR (min)	1,10	1,50	0,68	1,36
QCD (%)	18,0	8,3	11,1	7,7

The values of CT reported in this work are in good agreement with those reported in other studies where the clotting time is found from 6.5 to 10 minutes. Vrigkou *et al.* reported an average of 8.11 minutes for CT in healthy patients, showing an increase in CT for patients with chronic thromboembolic pulmonary hypertension [297]. Similar findings were presented by Sucker *et al.* where the clotting time activated by only recalcification for women was found to be 7.4 minutes, while for men 8.58 minutes [298]. Other works, such as the one performed by Ramström *et al.*, found a range of clotting times similar to the one reported in this work [299]. Additionally, the earlier CT obtained via extrinsic coagulation test is consistent with previous studies published in the literature, corroborating our findings on the involvement of TF to coagulation [298]. The results reported suggest that the procedure followed in this study in terms of storage time and temperature does not significantly affect the coagulation time, however further investigations are required on the matter.

6.4 Coagulation and wettability

After confirming the coagulation markers' validity, impedance magnitude coagulation test was examined on surfaces with varying wettability, in order to evaluate how surface energy impacted coagulation time and verify the accuracy of our test to analyze surface hemocompatibility. **Table 14** shows the blood wettability angle on untreated PET, UV-treated PET, PVDF positive side, and PVDF negative side. The blood drop on the surfaces is depicted in the **Figure 124**.

Table 14 Contact angle of blood on PET non-treated, PET UV-treated, PVDF positive and negative sides.

	PET non-treated	PET UV-treated	PVDF Positive side	PVDF Negative side
Contact angle (deg°)	77,8° ± 1°	25,7° ± 2°	68,4° ± 0.1°	65,1° ± 0.7°

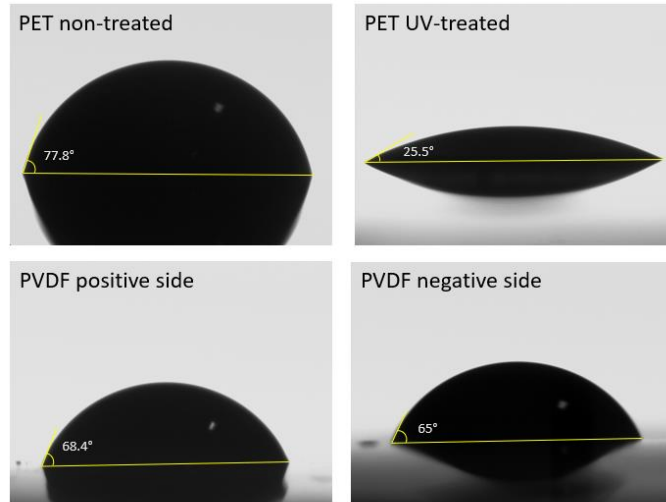


Figure 124 Drop of blood on the four different surfaces pictured by means of Contact Angle Goniometer.

As expected, UV oxidation treatment increases the wettability of the PET surface, as it promotes functional groups such as hydroxyl, carbonyl, and carboxyl groups, enhancing the hydrophilicity. Regarding the blood contact angle, PVDF's positive and negative sides are similar, given that they are examined in a static condition, which means that no stress is applied inducing surface charges. However, it appears that the negative side marginally enhances the wettability, which is reasonable given that negative charges are linked to greater hydrophilicity. **Figure 125 a-b** represent the impedance tests performed on the aforementioned surfaces. The tests are performed at 25°C thus, the timing as well as the shape differ from the test performed at 37°C and reported in the previous paragraphs, since the kinetic of coagulation is strongly related to the temperature. Although the clot contraction cannot be observed, the clotting time peak can be easily identified. It's interesting to note that the higher the wettability, the faster the coagulation; PET that has been exposed to UV ozone treatment reports a clotting time of 15 minutes, but PET non-treated has a clotting time of 25 minutes (**Figure 125-a**). On the other side, PVDF surface positive and negative sides report very similar clotting time, with a very small discrepancy of around 1 minute. These results were found on all the test performed on PVDF, suggesting good reproducibility. The results are in line with the wettability tests as PET UV-treated and non-treated exhibit an angle difference of more than 50°, which is associated with a significant difference in clotting times; However, the angle difference between the PVDF positive and negative surfaces is only a few degrees, not enough to noticeably alter the way that blood interacts with the surfaces. We can conclude that wettability strongly affects the coagulation process: as stated earlier, different proteins will adsorb on a surface based on its charge and wettability, causing the coagulation to begin either by activating *fXII* (on hydrophilic surfaces) or by adsorbing fibrinogen, which in turn promotes platelet activation (hydrophobic surfaces). It is interesting to notice that the initial slope of the bioimpedance plot varies depending on the contact angle, and this may be related to the coagulation trigger: for surfaces with poor wettability, there is an early drop in impedance magnitude, followed by an increase that peaks at the clotting time (PET non-

treated, PVDF positive/negative); This is not the case for surfaces that are highly wettable (UV-treated), as the impedance shows a sharp rise that culminates at the clotting time. This may be since on hydrophilic surfaces the kinetic of coagulation is faster than red blood cells do not have time to form rouleaux, also it could be related to the different trigger of clotting that is associated with a different layer of proteins adsorbed on the surface. Nonetheless to verify the reason behind these findings, more research is required.

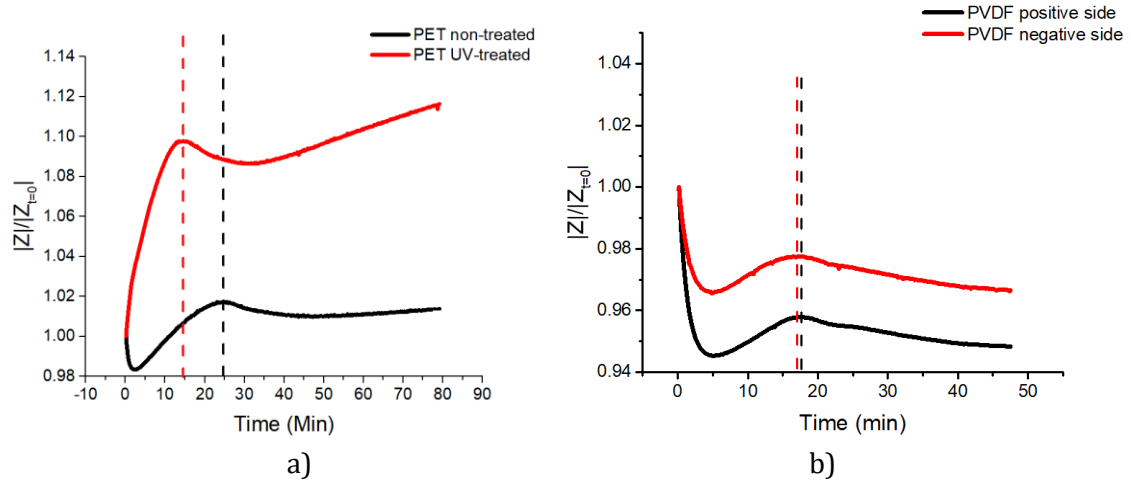


Figure 125 Coagulation impedance test at 25°C carried out simultaneously on a) PET and PET treated with UV-ozone b) PVDF positive and negative sides.

7. Conclusions and perspectives

This work reports on innovative biomarkers for assessment of blood coagulation, based on impedance spectroscopy characterization. Such approach provides a real time and comprehensive picture of all the events occurring during clotting of blood. Two significant markers are identified, *i.e.*, related to fibrin formation (the 1st marker) and clot contraction (the 2nd marker). Impedance phase (ϕ) investigation confirms the meaning of the 2nd marker, revealing an increase in the resistive behavior during the contraction caused by expulsion of serum. Next, imaging via confocal microscopy provides the onset time of the fibrin polymerization as well as the beginning of the clot contraction, enabling to further highlight the physical meaning of both test markers. In addition, $|Z|$ characterization compared with the standard Rotem[®] analysis allows to strengthen the meaning of the 1st marker. The impedance magnitude test gives an overview of the clotting time that could be useful as an effective indicator of hypo/per coagulability disorders. The test proposed in this study is not only reliable in terms of identifying clotting time, but it also provides detection of the onset of clot retraction. Indeed, if the contraction does not occur or is delayed, the test should not show the 2nd marker followed by a steep increase. This technology, relying on the electrical impedance characterization of blood, allows for a real time monitoring of coagulation which, otherwise is inaccessible with current techniques (Rotem[®] analysis). Analyses on the effect of external factors (temperature, time collecting, diseases) on coagulation are out of scope of

this paper, but nonetheless will be one of the most priorities in our future research direction. Indeed, the approach used in this study involved testing the blood 24 hours after collection, however it is not fully disclosed how much storage time may alter clotting time. In any event, the findings of this study are consistent with those of other studies conducted via Rotem® using the same coagulants, suggesting that testing within 24 hours does not significantly alter the results. A novel insight of this work involves in the development of an easy and efficient technique adaptable to various material's surfaces to analyze their interactions with blood. The proposed approach enables to study the clotting time related to the wettability. The results of a coagulation impedance test on four surfaces with variable wettability (PET, PET UV-treated, PVDF positive and negative sides) reveal that the higher the wettability, the faster the clotting time. This proves that coagulation impedance test is suitable for the determination of the thrombogenicity of materials in order to identify the most haemocompatible candidates. A study of materials' thrombogenicity is crucial because one of the main limitations of cardiovascular prostheses is their tendency to induce thrombosis once in contact with blood. Hence, there is an urgent need for materials capable to delay or avoid coagulation, to prevent patients from severe health problems such as ischemia, heart attack, or embolism. Impedance blood characterization may therefore pave the way for a new generation of smart materials that could overcome current technological lock of cardiovascular prostheses where coagulation is a serious issue. The future prospects of this study include the development of a non-contact electrode devices that can also be integrated into a real graft to perform real-time *in vivo* monitoring. Furthermore, the test should be performed under dynamic conditions, which are similar to the real human condition. Nonetheless, it is feasible to conclude that impedance blood characterization is a helpful instrument not only for studying the wellness of blood coagulation systems, but also for understanding the interaction with artificial materials.

Chapter V

A preliminary study on self-endothelialized tissue engineered vascular grafts

Summary

In this final chapter we present a preliminary study related to charge/cells interaction. As described in Chapter I, one way to improve vascular grafts while preventing body rejection and lowering the danger of thrombosis is to cover the prosthesis with endothelial cells, which are the natural cells that lid the inner layer of a human vessel. To accomplish so, innovative methods able of accelerating and improving cell culture are needed. In this chapter, we propose the employment of surfaces-charged scaffolds. The effect of charge on cells is investigated on epithelial cells, which are considerably simpler to handle than endothelial cells. Nonetheless, future works will focus on them. The charge generated by a photo-capacitive composite (ZnS:Cu/PVDF-TrFE-CFE), is driven on cell culture sample holders whose substrates are a semiconducting ITO deposited on a glass slide. Positive charged and negative charged scaffolds are compared to non-charged ones, by means of testing the cells adhesion after 6h from cells deposition. The results show that both positive and negative charges enhance the adhesion of epithelial cells. This work is mainly focused on the adhesion of the cells, future works will be focused also on the study of the charge influence on the cells' proliferation.

1. Introduction

As mentioned in Chapter I, a promising technique for the production of antithrombogenic prostheses capable of integrating into the human body is the development of tissue engineered vascular grafts (TEVGs). More specifically, the possibility of coating a prosthesis with endothelial cells before it is surgically inserted in the body would allow a total bio-integration of the prosthesis (**Figure 126**).

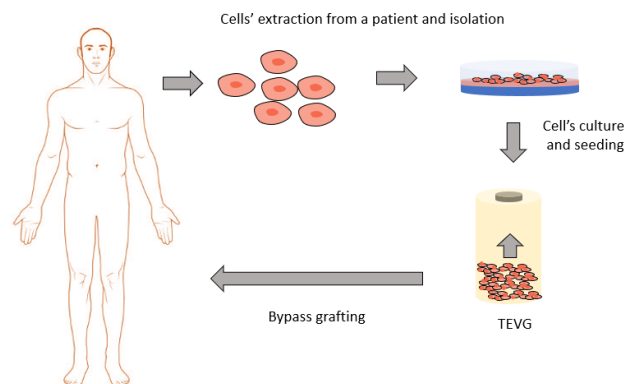


Figure 126 Concept behind tissue engineered vascular grafts covered in endothelial cells.

Cells culture includes several stages: adhesion of the cells to the substrate, growth of the cells and differentiation (**Figure 127**). This is particularly applicable for endothelial cells, which precisely differentiate from Stem cells.

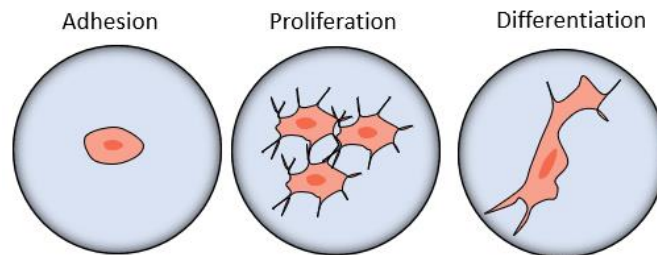


Figure 127 Stages of cells culture.

Stem cells are a class of cells able to evolve (differentiate) in more specialized cell type, involving a switch from proliferation to specialization. This entails a series of modifications to metabolic activity, membrane potential, cell shape, and response to certain signals (**Figure 128**) [300]. As result of differentiation, cells become committed to developmental lineages and acquire certain capabilities depending on the tissue they will eventually reside in. Although the idea of covering prosthetic devices with endothelial cells is promising, it is complicated to implement as the times required by the cells to adhere, proliferate and differentiate are rather long, and to fully cover a vascular prosthesis would take more than two weeks, with a very high risk of bacterial contamination [57].

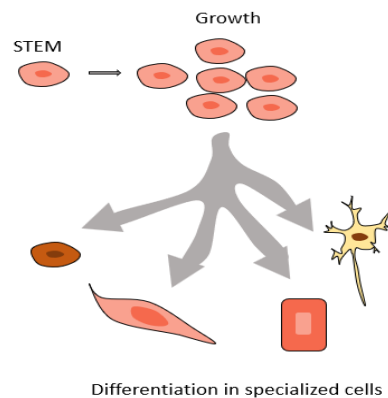


Figure 128 Typical steps of Stem cells culture.

It is thus necessary to find a solution to reduce the culture time. A way to accelerate this process may be related to the interaction with the scaffold surface. Indeed, functionalization of the substrate can govern responses of the cells, enhancing their adhesion and growth. For instance, the surface potential seems to have a strong correlation to the adhesion time and growth [301]. The objective of this pilot study is to comprehend the impact of applying a charge on the initial stage of cell culture, *i.e.*, cell adhesion on the surface scaffold. In practice, a surface charge modifies the surface potential and enables the modulation of the cell response. Depending on the type of cells involved, the charge might be positive or negative. The wettability of the surface is also influenced by its charge and may play a role in the culture

of the cells; hydrophilic surfaces have demonstrated improved compatibility with cell development [302].

In this sequence of exploratory experiments, we aimed to comprehend how positive and negative charge, as opposed to no charge (control), improved epithelial cells adhesion. Epithelial cells were chosen over endothelial cells for a variety of reasons, including the ease of handling them as opposed to Stem, their availability, and the rate of their proliferation. In future works we plan to test on Stem/endothelial cells. The study is particularly interesting for healing patches, as a faster epithelial growth enhanced by a charge on the patch could speed up the wound healing. In this work, we decided to use the charge produced by photo-capacitive composite based on (P(VDF-TrFE-CFE) terpolymer doped with 70% wt. phosphor particles ZnS:Cu. This ultra-flexible, high-performance photodetector is a light-sensitive composite material capable of generating charge surface in response to a blue light stimulus ($\lambda=470$ nm), and emit a fluorescent light if subjected to an electric field [303]. In this work, we focus on the first effect of this polymer composite embedded with phosphors, which transform into self-sensitive structures. The sample is coating on an ITO/glass slide (Indium Tin Oxide layer), so that the ITO is in contact with it. The other surface of the composite is gold sputtered. The cell adhesion test, however, is not performed directly on the material surface; rather, after light excitation of the composite, the charge is collected using conductor cables and sent to other slides coated with the semiconductor ITO, which serve as the substrate for the scaffolds. A silicone mold is glued onto them to contain the medium with the cells. When lit with blue light, the photo-capacitive produces positive charged surface on one side and negative charged on the other, and the charges are driven on the ITO surfaces. The charged ITO is in contact with medium and cells, making it possible to examine how positive or negative charge affects adhesion. The decision not to use the composite directly, but rather to conduct its charge on transparent conducting glass is based on the following reasons: first, we wanted to separate the effect of the charge from any other effect, such as surface roughness or light; and second, the use of transparent glass allowed for optical microscope observations to be made in light transmission.

In the next sections a brief overview of the charge/cell interaction will be presented as well as the photodetectors developed in this work. Then the material and methods involved in this preliminary study will be introduced as well as results and conclusion of this work.

2. Cell-surface charge interaction

The surface charge of a substrate is without a doubt one of the elements affecting how cells and the substrate interact. According to various studies, surface charge regulates the dynamics of adhesion, proliferation, and differentiation. However, depending on their composition, structural geometry, and size, not all cells react to an external charge in the same manner. To begin, the surface charge influences the amount and nature of protein adsorbed, as well as the degree of refolding, just as discussed in Chapter IV with regard to blood/material interaction. The layer of adsorbed proteins influences cell adhesion indirectly [301]. Cai *et al.*, for instance, describe a beneficial effect of charge on the adsorption of integrins, which are essential regulators of cell adhesion [304]. Additionally, the electrostatic

interaction between the substrate charge and the cell's membrane charge has a significant impact on adhesion. Each cell has a cell membrane that separates the intracellular fluid from the extracellular matrix. The presence of ions in the extracellular and intracellular matrix generates an electric potential across the membrane. Typically, a cell shows a negative surface (membrane) potential between -10 and -90 mV, depending on its nature. The electrical potential of neuronal cells, for instance, has been measured as -60 mV by Fairless *et al.* [305]. As cell adhesion is the foundation for cell survival, proliferation, and mobilization, it is important to maximize it. Non-adherent cells ultimately perish. Positive charges might also be useful for affecting the proliferation step [302]. The beneficial impact of employing charges, both positive and negative, on cell culture has been effectively described in several studies; for instance, according to Chang *et al.*, a negative surface potential reduces electrostatic repulsion between negatively charged membranes and the surface, increasing the adherence of epithelial cells (HEK293T and HepG2¹³) and fibroblasts (NIH3T3¹⁴) [306]. Yet, their research shows that compared to fibroblasts, positive charge has a stronger impact on epithelial cell attachment. Other research has emphasized the significance of surface charge density in cell adhesion, demonstrating a strong correlation between cell adhesion and proliferation with the amount of charge [307,308]. Other studies, such as that reported by Thevenot *et al.* claim that a negative charge can positively influence the adsorption of proteins that are essential for promoting adhesion [309]. Indeed, negative charges induce hydrophilicity, and this has been related to improved adhesion. As a matter of fact, the wettability (hydrophobicity and hydrophilicity) of surfaces affects protein adsorption on the surface, and it appears that cells are more prone to cling to hydrophilic surfaces. Wei *et al.*, for instance, found that osteoblast adhesion decreased when the contact angle increased from 0° to 106°[310]. It is evident from all the experimental findings reported in the literature that each combination of surface/cell has a unique interaction and distinctive properties. Other parameters such as roughness, microporosity, mechanical characteristics, and bio-coating impact adhesion proliferation and differentiation, however in this study we focus on the effect of charge, which is particularly intriguing in connection to electroactive materials.

3. Photo-capacitive ZnS:Cu/Terpolymer

The combination of the semiconducting ZnS:Cu filler with the ferro-relaxor (PVDF-TrFE-CFE) matrix allows for the development of a composite able to emit light under external electric field (Mokni *et al.* [303]), and to generate charge on its surface due to light exposition, making it suitable for use as both a photodetector and a light emitter. This behavior is correlated with both filler and matrix properties. ZnS bulk doped with Cu ions is a common inorganic photoluminescent material used in light-emitting diodes [311]. Since the middle of the previous century, the photoluminescence and electroluminescence of ZnS:Cu have been extensively researched. The material belongs to the phosphors p-type semiconductors class. Phosphors are typically created by combining a suitable host material with an activator. Copper-activated zinc sulphide (ZnS) and silver-activated zinc sulphide (ZnS) are the most

¹³ HEK293T= Embryonic kidney; HepG2 = human hepatocellular carcinoma

¹⁴ mouse embryofibroblast

well-known kinds (silver zinc sulphide). Cu-doped ZnS is gaining popularity as a blue-green emitting active layer for a variety of optoelectronics applications [303]. The photo-luminescence properties are related to its semi-conductivity: when a light beam with photon energy beyond the bandgap hit the material it excites the electrons from the valence to a higher energy state, in the conduction band [312]. Recently phosphor particles have been coupled with different classes of polymers to develop all sorts of devices, especially in the field of photoemitting diodes. For instance Huang *et al.* developed polymer based ZnS:Cu composites capable of emitting blue light under a threshold voltage of 4 V [311]. Choi *et al.* developed photodetectors made of ZnS:CU/silicone elastomer highly photo-responsive, which exhibit dielectric changes in response to an external light [313]. Similarly, Jun *et al.* developed ZnS:Cu/Polyvinyl butyral with a capacitance extremely sensitive to irradiation of light with wavelength in the range of 350-450 nm [312]. In our case phosphor fillers are combined with a dielectric ferro-relaxor matrix. The composite was already proven to be highly photosensitive in our previous works [303]. This behavior can be related to Maxwell-Wagner-Sillars effect at particle-polymer interfaces [312]. Under light excitation with high energy photons, the semi-conducting filler generates charges which accumulate at interface matrix/filler, causing polarization of the matrix chains [303,313]. This results in an increase in dielectric properties of the composite, hence capacitance. When the dipoles are oriented, there is an electric field across the thickness, which also means the presence of surface charge. This behavior will be further verified in the experimental section of this chapter. In conclusion our filler/matrix combination generates a material that once exposed to an external light excitation alters its electrical properties, inducing an increase of capacitance and surface charges. On the other hand, as already proven, if exposed to an alternating current field, it could generate visible radiation whose intensity varies with the applied voltage and frequency [303]. The polymer itself has a unique semicrystalline structure that, as a result of the nano-polar regions in the crystal domains, causes dramatically elevated polarization levels when it is exposed to an external electric field. There are no traces of polarization left once the electric field is discharged. Similarly, the matrix gets strongly polarized when the light reaches the sample, and the polarization will turn to zero in absence of light, hence in absence of charges from the polymer. We can conclude that in this material the polarization of the chains is so heavily reliant on the light.

4. Materials and methods

4.1 Material development

The new light polymeric composite photoreceiver was prepared using a solution casting method. The commercial fluorinated terpolymer powder (purchased from Piezotech S.A.S, Arkema group, Lyon, France) P(VDF-TrFE-CFE) 56.2%-36.3%-7.5 was dissolved with butanone, also known as methyl ethyl ketone (MEK) in a fraction of 14%wt. When the solution achieved a homogenous state, phosphor powder (ZnS:Cu) purchased from Shanghai Dongzhou Industrial Co., LTD with a diameter in the range of 3-10 μm was filled into the terpolymer solution with a content of 70% wt. This ratio was chosen for achieving the best trade between the photo-capacitive performance and the dispersion of the sample. The blend

was mixed via magnetic stirring for 24h. The prepared mixture was then casted on a conductive thin ITO/GLASS substrate of 1mm thickness and surface $25 \times 75 \text{ mm}^2$ (Indium Tin Oxide coated on transparent glass slides), which was purchased from Sigma Aldrich®. The ITO-coated glass film was chosen due to its high conductivity and optical transmission. The thermal treatment of the films was the following: first the temperature was increased from 25°C to 110°C in 2h, then 110°C plateau was kept for 2h, finally, the cooling down from 110°C to 25°C lasted 20h. With this thermal treatment the material was adherent to the surface, without any detachment. For surface charge test of the photo-capacitive composite, samples were sputtered on the top with 2 cm diameter circular surface gold electrode using a Crossington Sputter Coater (208 HR) that helped to deposit a very thin (25 nm) Au layer. For wettability and cell adhesion tests a $2 \times 5 \text{ cm}^2$ rectangular gold surface was sputtered. The thickness of the film was $\sim 90 \pm 10 \text{ }\mu\text{m}$ -thick. The architecture of a flexible terpolymer/phosphor is illustrated in **Figure 129 a-b**.

a)



b)

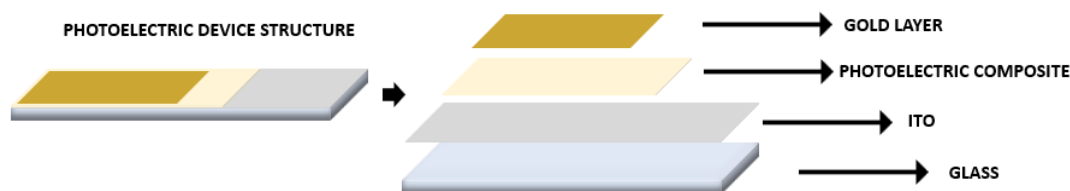


Figure 129 a) Picture of the photo-capacitive sample based on ZnS:Cu/PVFD-TrFE-CFE; b) architecture of the photo-capacitive device developed.

4.2 Electrical characterization

Figure 130 illustrates the design used to examine the charge produced on the sample's surface when exposed to blue light (470 nm). The light irradiated the sample from the glass side, as the opposite face was coated with gold, and it would prevent light transmission to the sample. The distance between the light and the sample was 5 cm. In the first test the charge developed on the surface directly illuminated was evaluated by connecting the ITO electrode to a charge meter, while the gold electrode was grounded. The charge meter (KISTLER, Type 5015) measured the charge (high pass filter 0.16 Hz, 1V, 500 pC V^{-1}), which was displayed on an oscilloscope (MSOX3014A Keysight / Agilent oscilloscope). Then the gold electrode was connected to the charge meter while the ITO was grounded, to measure the charge on the side not directly illuminated by light. The findings are presented in terms of charge per unit area (pC cm^{-2}). The characterization was repeated three times per side. This test was necessary to

understand which was the positive side and negative side, as well as the amount of charge produced per unit of surface. Then the capacitance changes of the sample without and with light excitation (5 cm of distance) were examined using a capacitance meter (Agilent 4278A) at 1kHz and 1V. Both charge and capacitance measurements were performed at room temperature. Finally dielectric broadband spectroscopy at 25°C from 0.1 to 10⁶ Hz was performed on the sample with and without light exposition (5 cm of distance) using a broadband spectroscopy analyzer (Solartron 1260A).

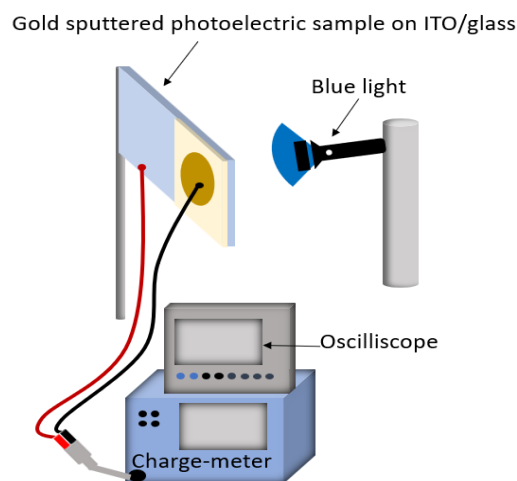


Figure 130 Set-up used to examine the charge produced by the sample when exposed to blue light. In this image, the connection is made in a way to measure the charge developed on the surface directly enlightened.

4.3 Wettability test

The set-up shown in **Figure 131** was used to study the effect of charge on the wettability of the ITO surface, in view of the cell adhesion test. Initially, a drop of demineralized water (3 μ L by volume) was placed on a bare uncharged ITO/glass slide, *i.e.*, not connected to any photo-sensing device. The contact angle between the water and the ITO surface was measured using a USB -microscope (Dinolight®). Subsequently, the ITO/glass slide was connected to the ITO electrode of a second slide where the photo-capacitive sample was deposited, *i.e.*, it was connected to the side directly illuminated by the light (positive charged side), and the same contact angle measurement was carried out. Finally, the ITO/glass was connected to the sputtered gold surface on the photo-capacitive sample, *i.e.*, the surface opposite to the light (negative charged side) and the effect of the charge on wettability was measured as in the two previous cases. Two different ITO/glass slides were tested and on each one three different tests per “charge condition” (zero, positive and negative) were performed. All the tests were performed at room temperature.

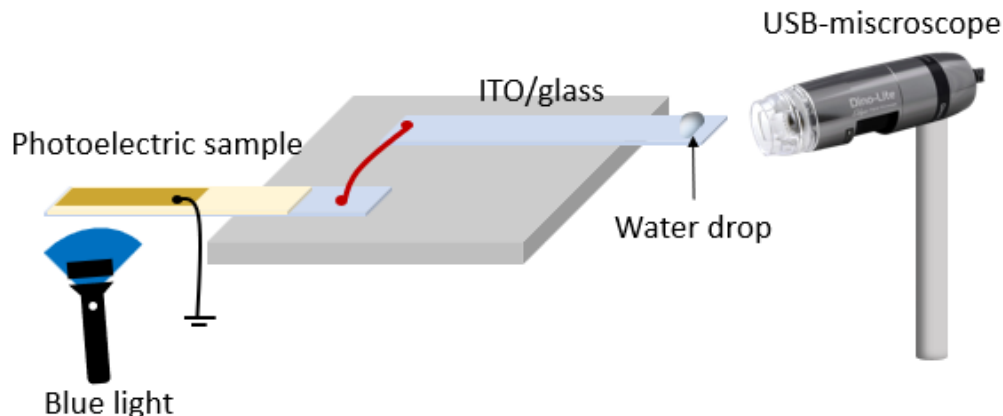


Figure 131 Set-up used for water/ITO contact angle. In this drawing we report the case where ITO is positively charged.

4.4 Cells preparation

Human epithelial cells (HBEpC-p Human Bronchial Epithelial Cells) were purchased from Promocell® in proliferating conditions in a 25 cm² flask. On arrival, they were left to stand for three hours in an incubator at 37°C. Subsequently, the medium (Airway Epithelial Cell Growth medium) was completely removed and 10 mL of new medium was added to the flask. The cells were removed from the flask the day after when a surface confluency was >70%, determined by optical microscopy. The medium was removed, the flask was rinsed with 2.5 ml Hepes (PBS). After, the Hepes was removed and 2.5 ml of trypsin were added to the flask and left for 7 minutes at 25°C, during which time the sides of the flask were gently tapped to promote cell detachment. After 7 minutes, 2.5 ml of trypsin inhibitor was added. The total of 5 ml was placed in a 15 ml sterile centrifuge tube, and the whole was centrifuged at 220 g for 3 minutes. All pipetting was carried out with sterile pipettes and the whole procedure was performed under a class II hood (class II ADS air laminar sterile dust collector PPS 12) (**Figure 132**), under sterile conditions. The cells were at the bottom of the tube after centrifugation, and the top liquid was discarded. 1 ml of new prewarmed medium was added. The cells were homogeneously mixed with the medium by pipetting up and down. 100 µl of the mixture was placed in a fresh flask with 10 ml of pre-warmed medium for the next tests. 150 µl of the mixture were placed in three separate sample holders (50 µl each one) designed for the adhesion/charge investigation and discussed in the next section, where 1.5 ml of prewarmed medium were already placed.



Figure 132 Class II hood used to perform all the cells manipulation.

4.5 Charge stimulated epithelial cells adhesion test

Three sample holders were created in order to perform the study of the influence of charge on epithelial cells adhesion. The **Figure 133** depicts the structure of the samples. The base substrate was an ITO/glass slide. A Polydimethylsiloxane mold (Sylgard® 184) was glued onto the substrate using a thin PDMS layer and cured 10 minutes on a hot plate at 150°C. This structure was used to contain medium and cells (geometry shown in the **Figure 133**). The first sample, named control, was not connected to anything, and the charge on its surface was zero. A second and third samples were connected to two photo-capacitive samples, both illuminated by blue light (470 nm). The former was connected to the positively charged surface and the latter to the negatively charged surface. The three sample holders were sprayed with 70% alcohol, which was left to dry under a ventilated fume hood type II for 24 hours. 1.5 ml of medium heated to 37°C was added to each sample holder under the hood and 50 µl of medium and cells taken from the centrifugation tube (see previous section) were injected into each sample. Once the medium and cells were inserted, the three sample holders were placed in an incubator at 37°C for 6h. After 6h, the three surfaces were observed under a light microscope. 20 photos per sample at 10x of magnification were collected to cover most of the cell-containing area and using ImageJ® the cells were counted, and the three samples compared. The same experiment was then performed, increasing the amount of charge on the samples: the positive charge sample was coupled with two, three, and four photo-capacitive samples, and the results of cell adhesion were compared to no-charged samples. The identical procedure was subsequently carried out with the negatively charged sample. In this way the number of cells adhered was evaluated depending on the sign and amount of charge and on the ITO glass.

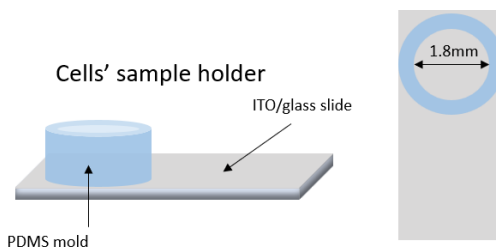


Figure 133 Drawing of the cells sample holder with detail of the geometry.

5. Results and discussion

5.1 Electrical characterization and wettability investigation

Figure 134 displays the charge developed by the Terpolymer/phosphor sample per unit of surface, when enlightened by a blue light. The black curve is the charge coming from the side that is directly facing the light, named “glass side” in the graph, while the red one is coming from the opposite side, *i.e.*, the gold sputtered one. The total charge collected per side was 300 pC, over a circular sputtered surface (diameter 2 cm). The charge developed per unit of surface was $|90 \text{ pC cm}^{-2}|$ and the side directly facing the light was producing a positive charge, while the side opposite to the light a negative charge. According to us, when the sample is enlightened, the polymer gets polarized by the excited phosphors and an electric field develops across thickness, leading to a change in capacitance. The charge trend is decreasing in time due to the measurement instrument, which integrates the results over time, leading to a fictitious drop of the charge, however the charge in the sample is not dropping.

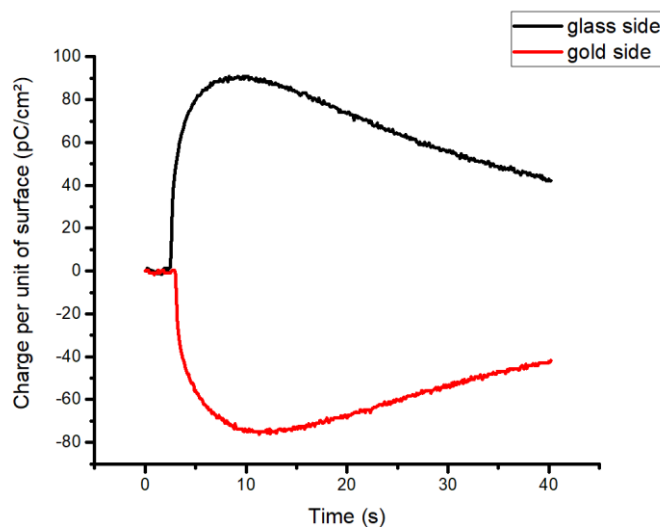


Figure 134 Charge per unit of surface when the photo-capacitive sample is lit by a blue light. The black curve is the positive charge coming from the face that is directly facing the light, while the negative one is described by the red curve and is the side not facing the light.

Table 15 Capacitance for the photo-capacitive samples without and with light excitement.

	No light	Light
Capacitance (pF)	705 ± 10	987 ± 15

Table 15 reports the capacitance values with and without the effect of the light measured across the sample. The capacitance variation and the charge associated to it is computed according to Eq.72-74, where V is the voltage applied by the capacitance meter, C the capacitance, Q the charge and A is the surface of the sputtered sample. The light on the sample induces a 40% increase of the capacitance ($\Delta C=288$ pF). The charge associated is ~ 90 pC cm⁻², matching the charge meter results. This test allowed us to understand the level of charge produced by the sample as well as which was the positive and negative side, so that we could distinguish them when testing cells' adhesion. The distance between the light and the material is an important parameter. In our previous studies we already proved the dependence of the capacitance change on the distance between the sample and the light [303].

$$\Delta Q = V * \Delta C + C * \Delta V \quad (72)$$

At constant voltage of 1V:

$$\Delta Q = V * \Delta C \quad (73)$$

The charge developed per unit of surface is computed as follow

$$\Delta Q/S = V * \Delta C/S \quad (74)$$

Finally dielectric broadband spectroscopy allowed us to collect the values of permittivity real and dielectric losses in absence and presence of enlightenment (**Figure 135**): the increase of permittivity due to light excitation is $\sim 35\%$, close to the capacitance one reported previously. The small difference may be related to uncertainties in the thickness measurements. Interestingly there is only a small increase in dielectric losses, probably due to leakages, meaning that the sample remains somewhat capacitive, and thus it does not turn in semi-conductive composite.

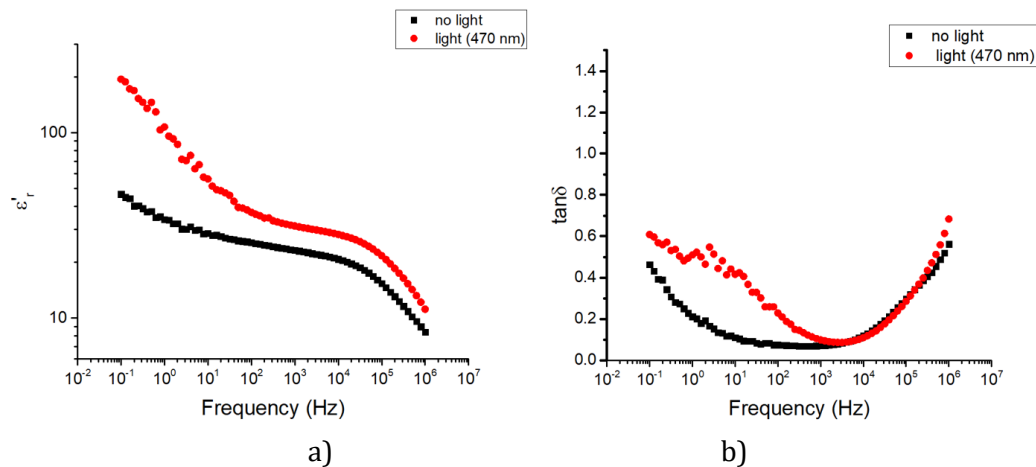


Figure 135 a) Relative permittivity real part vs. frequency and b) dielectric losses ($\tan\delta$) vs. frequency (0.1-10⁶Hz) at 25°C without (black curve) and with light (red curve).

The contact angle between demineralized pure water and ITO substrate was tested in three different conditions: without any charge applied on ITO, negative charge and positive charge. The results of the contact angle for two set of tests carried out on two different ITO are reported in **Table 16** and **Figure 136** and **Figure 137**. The percentage of contact angle variation with respect to the uncharged surface are reported in **Figure 136**. The addition of a negative charge, as expected, increases the hydrophilicity of the surface, with a $\sim 20\%$ drop of contact angle. Positive charge as well affects the wettability of the material, with a $\sim 15\%$ drop of contact angle with respect to no charge condition.

Table 16 Water contact angle ($^{\circ}\text{deg}$) with ITO in absence of charge and with negative and positive charge.

	No Charge	Negative Charge	Positive Charge
Contact angle ($^{\circ}\text{deg}$)	$73 \pm 3^{\circ}$	$60^{\circ} \pm 2^{\circ}$	$63 \pm 3^{\circ}$

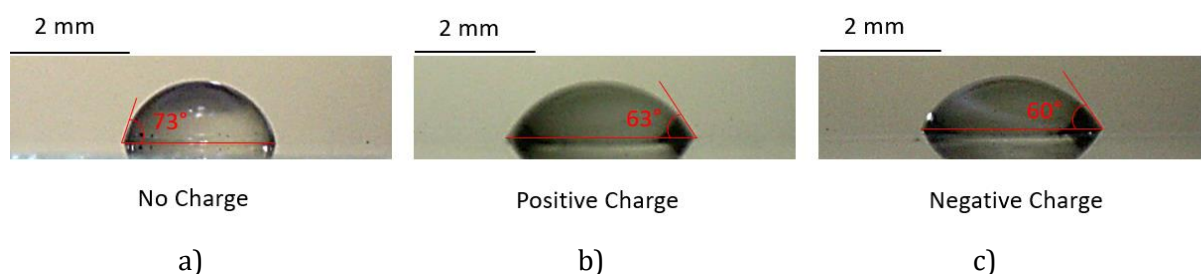


Figure 136 Drop of pure water on ITO a) uncharged, b) positively charged and c) negatively charged.

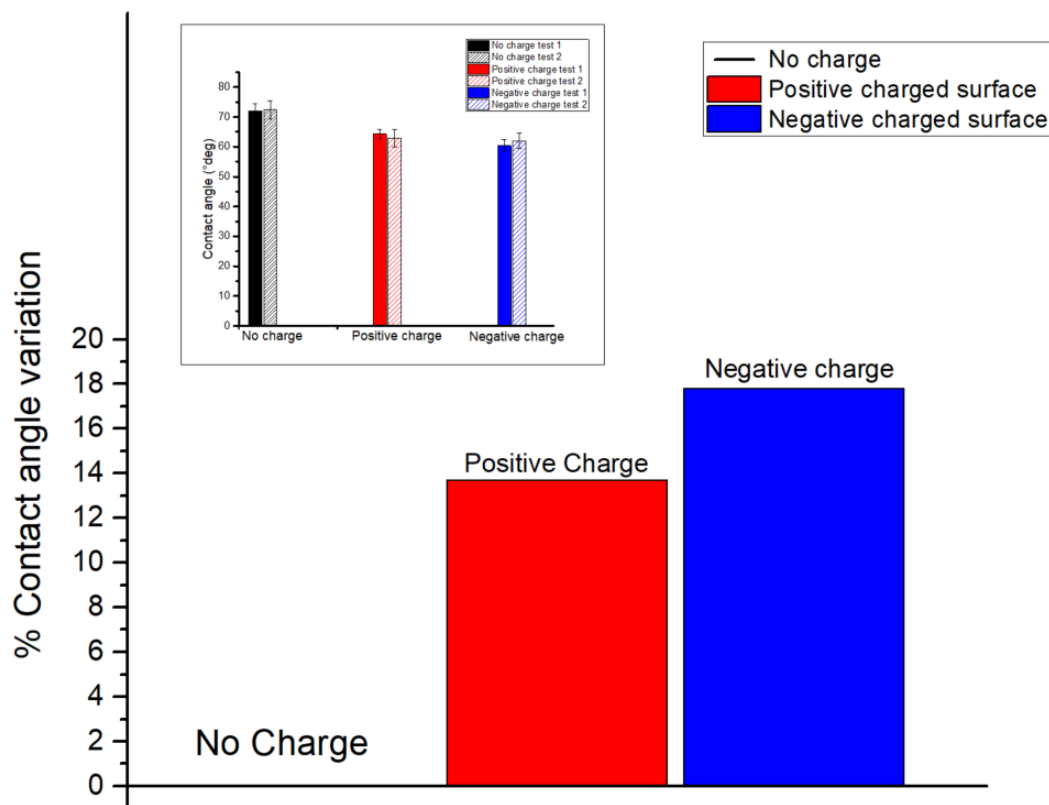


Figure 137 Normalized Contact angle ($^{\circ}\text{deg}$) of pure water in contact with ITO in three different situations: 1) no charge; 2) negative surface charge; 3) positive surface charge. The real value for the contact angle is reported in the graph at the top of the picture; the test is repeated on two different slides of ITO/glass (test 1 and test 2).

From these results we can confirm that the light generated a separation of charge across the sample of Terpolymer/phosphor, which could be transferred to ITO/glass slides and affect their wettability.

5.2 Cell's adhesion on charged surfaces

Figure 138 reports the variation (%) of cells number for positive charged and negative charged surfaces with respect to the uncharged one (control) depending on the amount of charge per unit of surface, for the tests on HBEPc-p epithelial cells. The analysis, performed via optical microscope, was done after 6h of incubation, to verify the number of cells adhered on the surface. The values of surfaces charge tested were 32, 53 and 106 $\text{pC}\cdot\text{cm}^{-2}$ for the positive charged samples, and 32, 53, 106 and 160 $\text{pC}\cdot\text{cm}^{-2}$ for the negative charged samples. The positive charge increases the number of cells adhered at each value of charge on the surface, however the maximum improvement is at 53 $\text{pC}\cdot\text{cm}^{-2}$ with a 150% improvement with respect to the sample control (no charge). At 106 $\text{pC}\cdot\text{cm}^{-2}$ the effect of the positive charge is still effective, however it is reduced to a 50% improvement. These results suggest that the interaction of the cells with the positive charge is beneficial to the adhesion, as there may be an electrostatic attraction between the negative membrane of the cells and the positive charge of the surface. Nonetheless we observe that after a certain value there is a drop in the

improvement. The positive charge may be repelling a protein called integrin, which is positively charged in our particular medium (pH 7.8)[301]. It is well known that integrin is a fundamental mediator of adhesion. The negative charge on the other side presents a quasi-monotonic improvement increasing the amount of charge per surface. At each value of surface charge there is a higher number of cells adhered to the surface with respect to uncharged sample. The maximal improvement is reached at $160 \text{ pC}\cdot\text{cm}^{-2}$ with a 115% of improvement. In this case this may be related to a favorable interaction between the negative charge and the positive integrin. We believe that two phenomena are counterbalancing each other, *i.e.*, the charge has an impact on both the cell membrane and integrin, and the quantity of charge has a different effect. Nonetheless, in both circumstances, there is an enhancement in the number of cells attached to the substrate. **Figure 139** reports the results related to the test for cells adhered on positive charge ($106 \text{ pC}\cdot\text{cm}^{-2}$) (**Figure 139 a-c**), negative ($160 \text{ pC}\cdot\text{cm}^{-2}$) (**Figure 139 d-f**) and control (no charge) (**Figure 139 g-i**). Three pictures per sample are reported, representative of the cells adhered on the sample holder. It is quite clear that positive and negative charge are beneficial to the adhesion. **Figure 140 a-b** reports the optical microscopy of human bronchial epithelial cells with high confluency from the literature, meaning cells that have adhered and growth. Comparing those pictures with pictures with our results in terms of cells shaped suggest good adhesion.

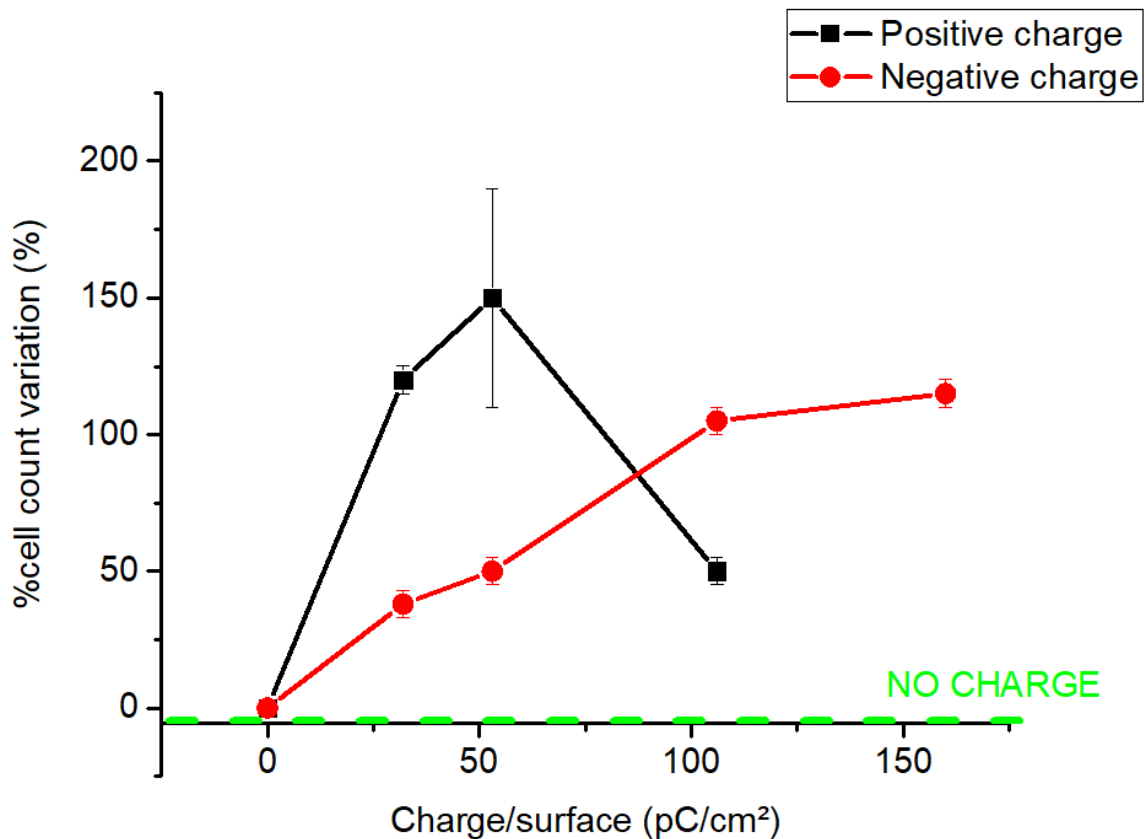


Figure 138 Percentage of HBEpC-p cells variation adhered on ITO substrate charge positively, negatively with respect to uncharged sample (control) depending on the amount of charge per unit of surface. The test analysis performed via optical microscope, was done after 6h of incubation at 37°C.

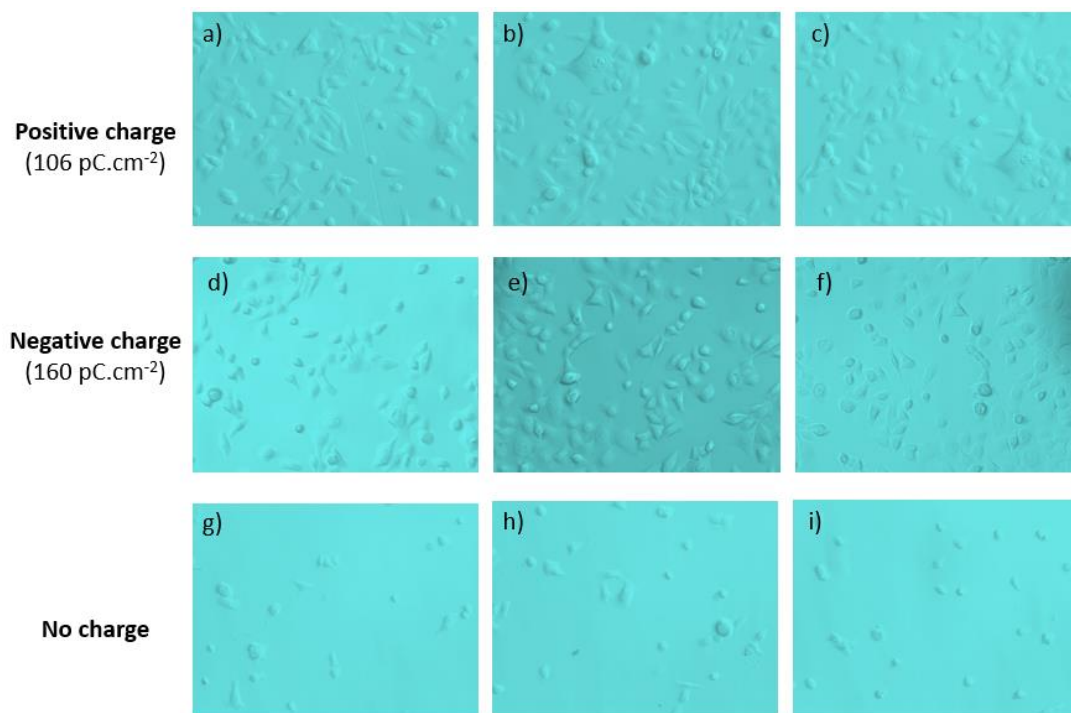


Figure 139 Epithelial cells (HBEpC-p) adhered onto a)-c) ITO positively charged (106 pC.cm^{-2}), d)-f) ITO negatively charged (160 pC.cm^{-2}), g)-i) ITO without charge. The imaging, taken via optical microscopy in light transmission was carried out after 6h of incubation.

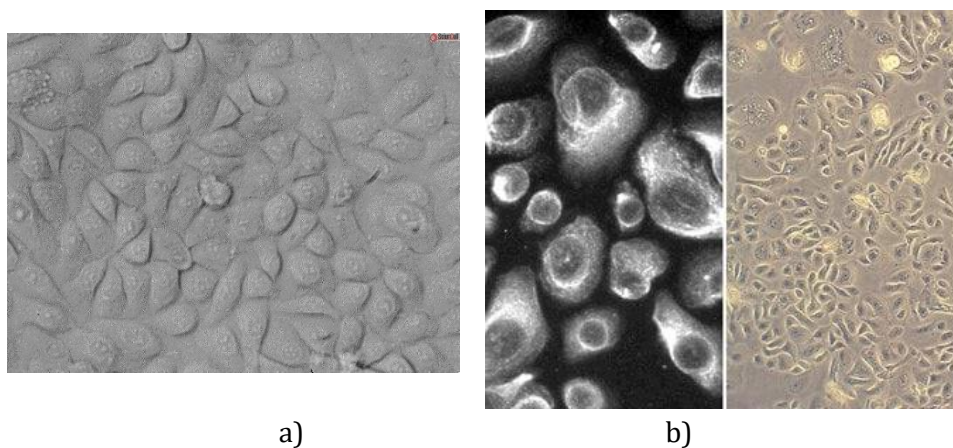


Figure 140 Human bronchial epithelial cells from a) Biotrend® [314] and b) Sigma Aldrich® [315].

6. Conclusions

In this preliminary study, we investigated the influence of charge on epithelial cell adherence to a substrate. Thanks to this pilot investigation we were able to gather early data on the charge/human cells interaction. The interest in this issue stems from the fact that human prostheses, particularly the vascular prostheses at the heart of this thesis, would profit

enormously from a covering of endothelial cells, *i.e.*, the cells that line the lumen of vascular conduits. This work was performed on epithelial cells, as they were more convenient to carry out an initial series of tests, but future projects will include the study of the interaction between Stem/Endothelial cells and substrate charge. The charge was generated by photo-capacitive samples based on ZnS:Cu semiconducting fillers in P(VDF-TrFE-CFE) ferro-relaxor matrix casted on ITO/glass slides, which was able to generate surface charge in response to a light source at a wavelength of 470 nm. The lit sample underwent a 40% increase in capacitance, producing a surface charge of $|90 \text{ pC/cm}^2|$. The side of the composite illuminated by the light source generated positive charge, while negative charge was generated on the side opposite the light. Capacitance measurement and dielectric broadband spectroscopy confirm the increase in dielectric properties under light exposition. The findings of the dielectric losses indicate that the material does not transition to semi-conductivity. The photo-capacitive system (composite on ITO/glass slide) was electrically coupled to another uncovered ITO/glass slide, allowing positive or negative charges to be conveyed depending on which side was connected. Then a drop of water was poured on the uncoated ITO/glass slide and a wettability assay was done in absence of charge and in presence of it (positive/negative). When there was a positive charge, the water drop reported a $\sim 15\%$ reduction in contact angle compared to the uncharged ITO/glass, whereas the reduction was $\sim 20\%$ with a negative charge, indicating the influence of the charge on the surface. Finally, epithelial adhesion assays on charged plus, charged minus, and uncharged surfaces revealed that positive and negative charges outperformed the sample without charges. Therefore, it appears that both positive and negative charge may be used to accelerate adhesion. These results are promising, nonetheless the impact of charge on growth (test time $>24\text{h}$) requires more testing. Additionally, in this study, a photo-capacitive material triggers charge, which is intriguing for the creation of, for instance, wound healing patches; in addition, it might be utilized to induce *ex vivo* the proliferation of endothelial cells on vascular prosthesis before they are implanted in the body. On the other hand, the employment of piezoelectric materials as charge generator may also show promise. In reality, the materials created in Chapter II may function ambivalently as sensors and as adhesion/growth stimulants for *in vivo* cells culture. Clearly, further studies are needed in this regard, but this preliminary work opens the door to a developing field of research.

Chapter VI

Conclusions and Perspectives

This research aimed to develop novel vascular prosthetic technologies that would enable *in vivo* monitoring of the device and full integration with the human body. This thesis was structured in four main sections, each of which involved knowledge and research in several scientific domains such as materials engineering, biomedical, electrical, and bioelectronics, the combination of which allowed for innovation in the field of cardiovascular devices. To draw conclusions and define perspectives, the established objectives and the results achieved will be outlined point by point.

As was covered in detail in **Chapter I**, vascular grafts are placed into the vascular system through bypass grafting in order to reroute blood flow when the patient's veins or arteries are clogged or damaged. Synthetic grafts are frequently required, however, they do not fully integrate into the biological environment, leading to strong response from the body that is hosting them; among the body's primary unfavorable reactions are blood clotting and thrombus development, intimal hyperplasia, and infection. There is a hazardous decrease in blood flow due to blockage in the event of thrombi or intimal hyperplasia, which can be deadly if not recognized promptly. Therefore, a first step in this research was to develop vascular grafts that could monitor blood flow and transmit the data via wireless systems to point-of-care devices. We set out to develop pressure sensors capable of monitoring blood pressure. The choice of sensor type steered us towards piezoelectric composites, due to a number of advantages these provide over many other materials. These materials belong to the class of electroactive materials, which are capable to produce an electrical charge in response to an external mechanical stimulus. As a result, they do not require the use of sophisticated electrical circuits to accomplish the measurement and are exceptionally reliable and reactive because of their intrinsic sensitivity. The choice of piezocomposites rather than piezoelectric ceramics or electroactive polymers stems from the fact that these can be modulated in matrix and filler to achieve a combination of unique properties tailored to the application. In this instance, the sensors needed to be both extremely piezoelectric and flexible to precisely detect blood pressure without stiffening the prosthesis.

In **Chapter II**, we therefore focused on the development of biocompatible and highly sensitive piezoelectric composites. This was the first stage of this work. Two different classes of composites were developed, the first with BaTiO₃ particles in PDMS matrix (BT/PDMS) and the second with NaNbO₃ fibers and particles in PDMS matrix (NN_MF/PDMS and NN_MP/PDMS). By structuring the composites with an electric field both before and during polymerization (Dielectrophoresis-structuring), we were able to increase the connectivity of the fillers along one direction, by driving them to form columnar structures across the material's thickness. Due to this, the piezoelectric values increased but the Young's modulus remained low.

First, the effect of DEP-structuring on BT/PDMS was investigated. The influence of the structuring electric field's frequency and amplitude was examined, allowing optimal values (1Hz, 3 V μm^{-1}) to be chosen. The BT/PDMS was then manufactured in three different volumetric contents (2.4%v, 12%v, and 24%v), with 0-3 and *quasi* 1-3 connectivity (DEP-structured connectivity). From 0-3 to *quasi* 1-3 connectivity, dielectric and piezoelectric properties revealed a considerable improvement (nearly 2-fold for ϵ'_r and g_{33} , while 3.5 times for d_{33} at 24%v). The dielectric losses increased in 1-3 composites with respect to 0-3, although they remained modest. The filler redistributed itself under the effect of an external electric field, inducing anisotropy in the composite, which is why there was such an improvement along the structuring axis, without any increase of the volume content. The development of densely aligned columns improved impedance matching between matrix and fillers, allowing for more effective polarization on the one hand and better piezoelectric characteristics on the other. These findings were supported by FE analysis and physical models. Study on the thermal stability of d_{33} and XRD analysis in temperature allowed to verify that the composite kept good piezoelectric response until 100°C. The thermal rearrangement of the dipoles caused a 20% loss at 100°C, and total losses happened at 130°C, which is the filler's curie temperature. The mechanical behavior of 0-3 and 1-3 composites could be evaluated using DMA, which revealed that at a structuring-induced rise in Y of from 6 to 9 MPa at 24%v. Finally, DSC enabled evaluation of the influence of DEP-structuring over polymerization. This analysis gave us unexpected and interesting information: the addition of fillers leads to a reduction in the amount of amorphous phase in favor of the appearance of a crystalline one, liquid at room temperature, indicating that high volume contents (24%v) partially prevent crosslinking of the chains. This applies to both 0-3 and 1-3 connectivity. In 1-3 this effect is greatly amplified and is already present at 12%v. At 24%v in 1-3 ones, a second, more rigid glass transition appears at slightly higher temperatures, which may be the reason for the rise in Young's modulus. There is unquestionably a strong interaction between the filler and the matrix, which is amplified in 1-3 connectivities since the fillers are considerably closer along a certain direction. This study allowed us to understand the effect of dielectrophoresis on different properties of the composite with medium-high volumetric content and particle filler. Dielectric Broadband spectroscopy in temperature, in particular $\tan\delta$ vs. Temperature in the range 100mHz – 1MHz, allowed to confirm the observation made via DSC. Future studies using DMA in temperature could give more information regarding the mobility of the chains and are therefore planned for the future as the main perspective of this work.

The same study was then conducted on composites containing NaNbO_3 in PDMS. Here, our attention was on the aspect ratio of the fillers and how it impacted the outcomes of the DEP-structuring. Hydrothermal synthesis was used to manufacture NaNbO_3 fibers and particles, which were then used to create composite materials with connectivity of 0-3 and *quasi* 1-3. By using fibers, it was feasible to improve the filler dimension-to-interparticle distance ratio, named r . 1-3 composites with fibers increased substantially the piezoelectric sensitivity at extremely low volumetric contents (5%v) without affecting the mechanical properties, ensuring the composite's flexibility. In addition, the selected filler has an ϵ'_r 20 times lower than barium titanate, which allows for higher voltages in response to external stress, as g_{33}

remains high. Overall, the permittivity of 1-3 fiber-based composite (NN_MF/PDMS) was 70% superior to its counterpart with 0-3 connectivity and 16% to the structured particle-based (NN_MP/PDMS). Similarly, d_{33} for 1-3 fiber composite was 7-fold higher than 0-3 one and ~ 3 times higher than the structured one with NN particles. Even though the piezoelectric constant of NaNbO_3 is 5 times lower than that of BaTiO_3 and the volumetric content of fibers is ~ 5 times lower (5%v vs. 24%v), it is interesting to note that a d_{33} of up to 9.5 pC N^{-1} is attained, which is close to the value found for BT/PDMS. As a result, we may infer that DEP-structuring of high form factor fillers allows for substantially greater improvement than particles-alignment. Our findings were validated by FE analysis. DMA did not identify significant variations in Young's modulus amongst the composites since the filler content was exceedingly low and the results closely fitted the Halpin-Tsai models for short fibers composites. Finally, unlike the BT composite, DSC showed no discernible changes between 0-3 and 1-3 or between fibers and particles. The findings clearly reveal that NN_MF/PDMS with a filler of 5%v displays the best trade-off between piezoelectric characteristics ($\sim 10 \text{ pC N}^{-1}$) and stretchability ($Y \sim 4.5 \text{ MPa}$). The composite might be improved by combining fibers and particles. This would allow for a structure as close possible to a fully 1-3. This work does not examine the biocompatibility of the two composites; it is generally known that PDMS is highly biocompatible, having been used in *in vivo* implants for decades; similarly, various studies have reported on the biocompatibility of BaTiO_3 and NaNbO_3 . However, longer-term biocompatibility and integrity tests are planned in the future.

Overall, the two composites prepared, *quasi* 1-3 BT/PDMS 24%v and *quasi* 1-3 NN_MF/PDMS 5%v, seem very suitable for blood pressure sensors, thus they were tested on specific vascular devices in **Chapter III**, which introduced to the second stage of the work. 1-3 BT/PDMS 24%v was investigated as a blood pressure sensor in FFR devices, which are vascular catheters used to identify the severity of a vessel occlusion based on the blood pressure. Systole/diastole changes and blood pressure may both be accurately measured by the sensor, when inserted in a vascular simulator thanks to the piezoelectric behavior of the sample. The second sensor designed, NN MF/PDMS 5%v 1-3, was then included into a vascular graft and placed within a cardiovascular simulator where occlusions (*i.e.*, thrombi) were simulated. First, by monitoring of the sensor's charge, we were able to spot occlusion-related changes in signal amplitude (thrombi), as well as systolic and diastolic pressure fluctuations. Additionally, by coupling the sensor with an RFID inductor, we could track the resonance frequency of the filter, whose shift denoted a change in pressure, or an obstruction. Due to the wireless signal connection of RFID technology, this device in the future may provide *in vivo* measurements throughout the lifespan of the prosthesis. Using a piezoelectric composite implies lower energy costs, less electronics, and a passive measurement method. This paves the way for a new class of intelligent, self-monitoring prostheses that interact with a point-of-care device without requiring intrusive patient procedures. There are undoubtedly many measures still to take to optimize the device. First, in the near future, wireless testing will be conducted, and in this context, the resonance frequency of the filter will be optimized to have low signal absorption by the human body and adjust tag/receiver distance. In order to avoid interfering with the functionality of the prosthesis, the sensor's shape and insertion into the grafts must be properly designed. It will also be important to comprehend how sterilizing might affect the

piezoelectric properties. To understand how it functions in a real vascular system, *in vivo* investigations are required. Nevertheless, this study opens the door for a class of smart and innovative prostheses able to detect thrombosis.

The third phase of this research, described in **Chapter IV**, entailed studying blood coagulation and designing devices to study its interactions with different materials. This is relevant to develop anti-thrombogenic devices. We were able to define two coagulation markers by investigating the impedance magnitude of coagulating blood, the first pertaining to clot start and the second relating to clot contraction. These two markers were initially verified using confocal microscopy, a special type of microscopy that allowed us to see fibrin from its appearance through its contraction. Then, a second confirmation of the first marker was possible thanks to the gold standard visco-thromboelastography method employing Rotem®. Impedance phase angle analysis was finally used to further corroborate the second marker. This method, which is based on the electrical impedance of blood, enables for real-time monitoring of coagulation, which is otherwise impossible with existing approaches (Rotem® analysis), which for example do not really provide a data point at the onset of contraction. Furthermore, our approach is based on the use of coplanar electrodes that can be placed to any surface, allowing us to analyze coagulation on a variety of materials. In this regard, Surfaces with varying wettability were tested concurrently, revealing varying coagulation times as a function of blood contact angle. This outcome was expected since the wettability and surface energy influence the protein layers absorbed and consequently the coagulation triggers. This demonstrates that the bioimpedance test is a very effective technique for evaluating the hemocompatibility required to build antithrombogenic prostheses. This technology will be upgraded in the future to produce non-contact electrodes and isolate blood contact to the mere surface under examination. Secondly, the system will be tested under dynamic conditions, so as to understand how it might respond to a flow of blood. Finally, the device might be incorporated into vascular devices to monitor blood coagulation in real time. This approach, in conjunction with the one outlined in Chapter III, might allow for comprehensive graft monitoring and thrombosis detection.

The last stage of this project, the endothelialization of vascular grafts—that is, development of coating of endothelial cells—is covered in **Chapter V**. As these cells are the natural inner layer of the vascular vessels, their coverage would allow for improved tolerance of the prosthesis in the body and would prevent coagulation to occur. Indeed, thrombosis in prosthetics is triggered by the artificial surface. In this exploratory investigation, we intended to construct cell scaffolds capable of speeding up cell growth, as time is one of its key limits. The aim was to test adhesion on an electrically charged substrate. We developed photo-capacitive composites based on ZnS:Cu/PVDF-TrFE-CFE, which are able to develop a surface charge in the presence of a light source. This was accomplished by the combined action of the semiconductor filler and the ferro-relaxor matrix. When irradiated with blue light (470nm), the material produced 90 pC cm^{-2} , and $\sim 40\%$ increase in capacitance. This charge, which was positive on the lit face and negative on the opposite face, was transmitted through electrodes onto the charged substrate of the scaffolds, which were ITO-coated glasses. A 6-hour adhesion test was conducted on neutral, positively and negatively charged substrates. The

investigation was conducted on epithelial cells rather than endothelial cells since they are simpler to manipulate but it allowed us to confirm that both positive and negative charged substrates promote cell attachment. These encouraging findings pave the way for a more in-depth investigation to be conducted in the future. The link between charge amount and adhesion speed will be studied in more detail, as will the influence of charge on cells growth. The same investigation will subsequently be performed on endothelial cells to determine the time necessary to coat a prosthesis. The charge used to accelerate culture might also be derived from a piezoelectric material, but further research is needed to fully grasp the link between mechanical action with adherence and growth.

Finally, we can state that we have accomplished significant progress in several directions, all with the objective of making vascular grafts safer and more efficient, with special focus on the occurrence of thrombosis. This study paves the way for future research and serves as a foundation for the development of new technologies for self-monitoring tissue engineered vascular grafts.

Bibliography

- [1] W.H. ORGANIZATION, Cardiovascular diseases (CVDs), (n.d.). [https://www.who.int/news-room/fact-sheets/detail/cardiovascular-diseases-\(cvds\)](https://www.who.int/news-room/fact-sheets/detail/cardiovascular-diseases-(cvds)) (accessed May 5, 2022).
- [2] E.G. Nabel, Cardiovascular Disease, *N. Engl. J. Med.* 349 (2003) 60–72. <https://doi.org/10.1056/NEJMra035098>.
- [3] T.A. Gaziano, Cardiovascular Disease in the Developing World and Its Cost-Effective Management, *Circulation.* 112 (2005) 3547–3553. <https://doi.org/10.1161/CIRCULATIONAHA.105.591792>.
- [4] H. Thomas, J. Diamond, A. Vieco, S. Chaudhuri, E. Shinnar, S. Cromer, P. Perel, G.A. Mensah, J. Narula, C.O. Johnson, G.A. Roth, A.E. Moran, Global Atlas of Cardiovascular Disease 2000–2016: The Path to Prevention and Control, *Glob. Heart.* 13 (2018) 143. <https://doi.org/10.1016/j.ghheart.2018.09.511>.
- [5] World Health Organization, (n.d.). [https://www.who.int/news-room/fact-sheets/detail/cardiovascular-diseases-\(cvds\)#:~:text=What are the risk factors,and harmful use of alcohol](https://www.who.int/news-room/fact-sheets/detail/cardiovascular-diseases-(cvds)#:~:text=What are the risk factors,and harmful use of alcohol).
- [6] P. Libby, P. Theroux, Pathophysiology of Coronary Artery Disease, *Circulation.* 111 (2005) 3481–3488. <https://doi.org/10.1161/CIRCULATIONAHA.105.537878>.
- [7] S. Roll, J. Müller-Nordhorn, T. Keil, H. Scholz, D. Eidt, W. Greiner, S.N. Willich, Dacron® vs. PTFE as bypass materials in peripheral vascular surgery – systematic review and meta-analysis, *BMC Surg.* 8 (2008) 22. <https://doi.org/10.1186/1471-2482-8-22>.
- [8] M.L.P. Portegies, P.J. Koudstaal, M.A. Ikram, Cerebrovascular disease, in: 2016: pp. 239–261. <https://doi.org/10.1016/B978-0-12-802973-2.00014-8>.
- [9] et al Gaziano T, Reddy KS, Paccaud F, Cardiovascular disease, in: *Dis. Control. Priorities Dev. Ctries.*, 2006: pp. 1–53.
- [10] Cardiovascular Diseases, (n.d.). https://www.who.int/health-topics/cardiovascular-diseases#tab=tab_1, (n.d.). (accessed April 1, 2022).
- [11] E. Marijon, M. Mirabel, D.S. Celermajer, X. Jouven, Rheumatic heart disease, *Lancet.* 379 (2012) 953–964. [https://doi.org/10.1016/S0140-6736\(11\)61171-9](https://doi.org/10.1016/S0140-6736(11)61171-9).
- [12] K. Williams, J. Carson, C. Lo, Genetics of Congenital Heart Disease, *Biomolecules.* 9 (2019) 879. <https://doi.org/10.3390/biom9120879>.
- [13] S. Pashneh-Tala, S. MacNeil, F. Claeysens, The Tissue-Engineered Vascular Graft—Past, Present, and Future, *Tissue Eng. Part B Rev.* 22 (2016) 68–100. <https://doi.org/10.1089/ten.teb.2015.0100>.
- [14] W.C. Johnson, K.K. Lee, A comparative evaluation of polytetrafluoroethylene, umbilical vein, and saphenous vein bypass grafts for femoral-popliteal above-knee revascularization: A prospective randomized Department of Veterans Affairs cooperative study, *J. Vasc. Surg.* 32 (2000) 268–277. <https://doi.org/10.1067/mva.2000.106944>.

- [15] P.B. Kreienberg, R.C. Darling, B.B. Chang, B.J. Champagne, P.S.K. Paty, S.P. Roddy, W.E. Lloyd, K.J. Ozsvath, D.M. Shah, Early results of a prospective randomized trial of spliced vein versus polytetrafluoroethylene graft with a distal vein cuff for limb-threatening ischemia, *J. Vasc. Surg.* 35 (2002) 299–306. <https://doi.org/10.1067/mva.2002.121208>.
- [16] P. Klinkert, A. Schepers, D.H.C. Burger, J.H. van Bockel, P.J. Breslau, Vein versus polytetrafluoroethylene in above-knee femoropopliteal bypass grafting: Five-year results of a randomized controlled trial, *J. Vasc. Surg.* 37 (2003) 149–155. <https://doi.org/10.1067/mva.2002.86>.
- [17] R.D. Sayers, S. Raptis, M. Berce, J.H. Miller, Long-term results of femorotibial bypass with vein or polytetrafluoroethylene, *Br. J. Surg.* 85 (2003) 934–938. <https://doi.org/10.1046/j.1365-2168.1998.00765.x>.
- [18] K. Hu, Y. Li, Z. Ke, H. Yang, C. Lu, Y. Li, Y. Guo, W. Wang, History, progress and future challenges of artificial blood vessels: a narrative review, *Biomater Transl.* 3 (2022) 81–98.
- [19] S.J. Head, M. Milojevic, D.P. Taggart, J.D. Puskas, Current Practice of State-of-the-Art Surgical Coronary Revascularization, *Circulation.* 136 (2017) 1331–1345. <https://doi.org/10.1161/CIRCULATIONAHA.116.022572>.
- [20] M. Pellicano, B. De Bruyne, G.G. Toth, F. Casselman, W. Wijns, E. Barbato, Fractional flow reserve to guide and to assess coronary artery bypass grafting, *Eur. Heart J.* (2016) ehw505. <https://doi.org/10.1093/eurheartj/ehw505>.
- [21] M. Desai, A.M. Seifalian, G. Hamilton, Role of prosthetic conduits in coronary artery bypass grafting, *Eur. J. Cardio-Thoracic Surg.* (2011). <https://doi.org/10.1016/j.ejcts.2010.11.050>.
- [22] R. Fitridge, M. Thompson, Graft Materials Past and Future, in: *Mech. Vasc. Dis. A Ref. B. Vasc. Spec.*, 2011.
- [23] S. Post, T. Kraus, U. Müller-Reinartz, C. Weiss, H. Kortmann, A. Quentmeier, M. Winkler, K. Husfeldt, J. Allenberg, Dacron vs Polytetrafluoroethylene Grafts for Femoropopliteal Bypass: a Prospective Randomised Multicentre Trial, *Eur. J. Vasc. Endovasc. Surg.* 22 (2001) 226–231. <https://doi.org/10.1053/ejvs.2001.1424>.
- [24] L.P. Jensen, M. Lepäntalo, J.E. Fossdal, O.C. Røder, B.S. Jensen, M.S. Madsen, O. Grenager, H. Fasting, H.O. Myhre, N. Bækgaard, O.M. Nielsen, U. Helgstrand, T.V. Schroeder, Dacron or PTFE for Above-knee Femoropopliteal Bypass. A Multicenter Randomised Study, *Eur. J. Vasc. Endovasc. Surg.* 34 (2007) 44–49. <https://doi.org/10.1016/j.ejvs.2007.01.016>.
- [25] M.R. Prager, T. Hoblaj, J. Nanobashvili, E. Sporn, P. Polterauer, O. Wagner, H.-J. Böhmig, H. Teufelsbauer, M. Ploner, I. Huk, Collagen- versus gelatine-coated Dacron versus stretch PTFE bifurcation grafts for aortoiliac occlusive disease: Long-term results of a prospective, randomized multicenter trial, *Surgery.* 134 (2003) 80–85. <https://doi.org/10.1067/msy.2003.179>.
- [26] L. XUE, H.P. Greisler, Biomaterials in the development and future of vascular grafts, *J. Vasc. Surg.* 37 (2003) 472–480.

- [27] D.N. Ku, R.C. Allen, *Vascular Grafts*, Biomed. Eng. Handb. (1995) 1871–1878.
- [28] R.Y. Kannan, H.J. Salacinski, P.E. Butler, G. Hamilton, A.M. Seifalian, Current status of prosthetic bypass grafts: A review, *J. Biomed. Mater. Res. Part B Appl. Biomater.* 74B (2005) 570–581. <https://doi.org/10.1002/jbm.b.30247>.
- [29] S. Ravi, E.L. Chaikof, *Biomaterials for vascular tissue engineering*, *Regen. Med.* 5 (2010) 107–120. <https://doi.org/10.2217/rme.09.77>.
- [30] A.D. Whittemore, K.C. Kent, M.C. Donaldson, N.P. Couch, J.A. Mannick, What is the proper role of polytetrafluoroethylene grafts in infrainguinal reconstruction?, *J. Vasc. Surg.* 10 (1989) a14116. <https://doi.org/10.1067/mva.1989.14116>.
- [31] I.H. Jaffer, J.C. Fredenburgh, J. Hirsh, J.I. Weitz, Medical device-induced thrombosis: What causes it and how can we prevent it?, *J. Thromb. Haemost.* 13 (2015) S72–S81. <https://doi.org/10.1111/jth.12961>.
- [32] Albograft(R) Polyester Vascular Grafts, (n.d.). <https://www.lemaitre.com/products/albograft-polyester-vascular-grafts> (accessed September 1, 2022).
- [33] D.W. Friedman, P.J. Orland, R.S. Greco, *Biomaterials: an historical perspective*, *Implant. Biol. Host Response Biomed. Devices.* (1994) 1–12.
- [34] C.D. Campbell, D.H. Brooks, M.W. Webster, H.T. Bahnson, The use of expanded microporous polytetrafluoroethylene for limb salvage: a preliminary report, *Surgery.* (1976) 485–91.
- [35] M. Contreras, W.C. Quist, F.W. Logerfo, Effect of porosity on small-diameter vascular graft healing, *Microsurgery.* 20 (2000) 15–21.
- [36] M. Prager, P. Polterauer, H.-J. Böhmig, O. Wagner, A. Fögl, G. Kretschmer, M. Plohner, J. Nanobashvili, I. Huk, Collagen versus gelatin-coated Dacron versus stretch polytetrafluoroethylene in abdominal aortic bifurcation graft surgery: Results of a seven-year prospective, randomized multicenter trial, *Surgery.* 130 (2001) 408–414. <https://doi.org/10.1067/msy.2001.115904>.
- [37] D.L. Akers, Y.H. Du, R.F. Kempczinski, The effect of carbon coating and porosity on early patency of expanded polytetrafluoroethylene grafts: An experimental study, *J. Vasc. Surg.* 18 (1993) 10–15. <https://doi.org/10.1067/mva.1993.41708>.
- [38] K. Daenens, S. Schepers, I. Fourneau, S. Houthoofd, A. Nevelsteen, Heparin-bonded ePTFE grafts compared with vein grafts in femoropopliteal and femorocrural bypasses: 1- and 2-year results, *J. Vasc. Surg.* 49 (2009) 1210–1216. <https://doi.org/10.1016/j.jvs.2008.12.009>.
- [39] L. Yu, E.R. Newton, D.C. Gillis, K. Sun, B.C. Cooley, A.N. Keith, S.S. Sheiko, N.D. Tsihliis, M.R. Kibbe, Coating small-diameter ePTFE vascular grafts with tunable poly(diols-co-citrate-co-ascorbate) elastomers to reduce neointimal hyperplasia, *Biomater. Sci.* 9 (2021) 5160–5174. <https://doi.org/10.1039/D1BM00101A>.
- [40] M.R. Kibbe, J. Martinez, D.A. Popowich, M.R. Kapadia, S.S. Ahanchi, O.O. Aalami, Q. Jiang, A.R. Webb, J. Yang, T. Carroll, G.A. Ameer, Citric acid-based elastomers provide a biocompatible interface for vascular grafts, *J. Biomed. Mater. Res. Part A.* 9999A (2009)

- NA-NA. <https://doi.org/10.1002/jbm.a.32537>.
- [41] C.S. Jørgensen, W.P. Paaske, Physical and mechanical properties of ePTFE stretch vascular grafts determined by time-resolved scanning acoustic microscopy, *Eur. J. Vasc. Endovasc. Surg.* 15 (1998) 416–422. [https://doi.org/10.1016/S1078-5884\(98\)80203-7](https://doi.org/10.1016/S1078-5884(98)80203-7).
- [42] K. Kottke-Marchant, J.M. Anderson, A. Rabinovitch, The platelet reactivity of vascular graft prostheses: an in vitro model to test the effect of preclotting, *Biomaterials.* 7 (1986) 441–448. [https://doi.org/10.1016/0142-9612\(86\)90032-3](https://doi.org/10.1016/0142-9612(86)90032-3).
- [43] B|BRAUN, VascuGraft ePTFE, (n.d.). <https://www.bbraun.ch/fr/products/b/vascugraft-eptfe.html> (accessed September 2, 2022).
- [44] Z. Zhang, Y. Marois, R.G. Guidoin, P. Bull, M. Marois, T. How, G. Laroche, M.W. King, Vasculgraft® polyurethane arterial prosthesis as femoro-popliteal and femoro-peroneal bypasses in humans: pathological, structural and chemical analyses of four excised grafts, *Biomaterials.* 18 (1997) 113–124. [https://doi.org/10.1016/S0142-9612\(96\)00054-3](https://doi.org/10.1016/S0142-9612(96)00054-3).
- [45] J.P. Santerre, R.S. Labow, D.G. Duguay, D. Erfle, G.A. Adams, Biodegradation evaluation of polyether and polyester-urethanes with oxidative and hydrolytic enzymes, *J. Biomed. Mater. Res.* 28 (1994) 1187–1199. <https://doi.org/10.1002/jbm.820281009>.
- [46] A. Eberhart, Z. Zhang, R. Guidoin, G. Laroche, L. Guay, D. De La Faye, M. Batt, M.W. King, A new generation of polyurethane vascular prostheses: Rara Avis or Ignis Fatuus?, *J. Biomed. Mater. Res.* 48 (1999) 546–558. [https://doi.org/10.1002/\(SICI\)1097-4636\(1999\)48:4<546::AID-JBM22>3.0.CO;2-V](https://doi.org/10.1002/(SICI)1097-4636(1999)48:4<546::AID-JBM22>3.0.CO;2-V).
- [47] H. Jalaie, J. Steitz, M. Afify, M.E. Barbati, K. Hoeft, M.A.M. Assar, B. Hermanns-Sachweh, R.H. Tolba, M.J. Jacobs, K. Schleimer, In vivo endothelialization and neointimal hyperplasia assessment after angioplasty of sheep carotid artery with a novel polycarbonate polyurethane patch, *J. Biomater. Appl.* 34 (2019) 208–218. <https://doi.org/10.1177/0885328219849368>.
- [48] Y. Matsuzaki, K. John, T. Shoji, T. Shinoka, The Evolution of Tissue Engineered Vascular Graft Technologies: From Preclinical Trials to Advancing Patient Care, *Appl. Sci.* 9 (2019) 1274. <https://doi.org/10.3390/app9071274>.
- [49] C.S. Ong, X. Zhou, C.Y. Huang, T. Fukunishi, H. Zhang, N. Hibino, Tissue engineered vascular grafts: current state of the field, *Expert Rev. Med. Devices.* 14 (2017) 383–392. <https://doi.org/10.1080/17434440.2017.1324293>.
- [50] J. Hirai, Venous reconstruction using hybrid vascular tissue composed of vascular cells and collagen: Tissue regeneration process, *Cell Transplant.* 5 (1996) 93–105. [https://doi.org/10.1016/0963-6897\(95\)02002-0](https://doi.org/10.1016/0963-6897(95)02002-0).
- [51] H.P. Greisler, E.D. Endean, J.J. Klosak, J. Ellinger, J.W. Dennis, K. Buttle, D.U. Kim, Polyglactin 910/polydioxanone bicomponent totally resorbable vascular prostheses, *J. Vasc. Surg.* 7 (1988) av0070697. <https://doi.org/10.1067/mva.1988.av0070697>.
- [52] H.P. Greisler, C.W. Tattersall, J.J. Klosak, E.A. Cabusao, J.D. Garfield, D.U. Kim, Partially

- bioresorbable vascular grafts in dogs, *Surgery*. (1991) 645–54.
- [53] M.A. Rodríguez-Soto, C.A. Polanía-Sandoval, A.M. Aragón-Rivera, D. Buitrago, M. Ayala-Velásquez, A. Velandia-Sánchez, G. Peralta Peluffo, J.C. Cruz, C. Muñoz Camargo, J. Camacho-Mackenzie, J.G. Barrera-Carvajal, J.C. Briceño, Small Diameter Cell-Free Tissue-Engineered Vascular Grafts: Biomaterials and Manufacture Techniques to Reach Suitable Mechanical Properties, *Polymers (Basel)*. 14 (2022) 3440. <https://doi.org/10.3390/polym14173440>.
- [54] S. Wise, M.J. Byrom, A. Waterhouse, P. Bannon, A. Weiss, M.K. Ng, A multilayered synthetic human elastin/polycaprolactone hybrid vascular graft with tailored mechanical properties. , , , *Acta Biomater.* 7 (2011) 295–303.
- [55] I.-Y. Kim, S.-J. Seo, H.-S. Moon, M.-K. Yoo, I.-Y. Park, B.-C. Kim, C.-S. Cho, Chitosan and its derivatives for tissue engineering applications, *Biotechnol. Adv.* 26 (2008) 1–21. <https://doi.org/10.1016/j.biotechadv.2007.07.009>.
- [56] C.-H. Lin, K. Hsia, H. Ma, H. Lee, J.-H. Lu, In Vivo Performance of Decellularized Vascular Grafts: A Review Article, *Int. J. Mol. Sci.* 19 (2018) 2101. <https://doi.org/10.3390/ijms19072101>.
- [57] V.A. Kumar, L.P. Brewster, J.M. Caves, E.L. Chaikof, Tissue Engineering of Blood Vessels: Functional Requirements, Progress, and Future Challenges, *Cardiovasc. Eng. Technol.* 2 (2011) 137–148. <https://doi.org/10.1007/S13239-011-0049-3>.
- [58] J. Shu, G. Santulli, Update on peripheral artery disease: Epidemiology and evidence-based facts, *Atherosclerosis*. 275 (2018) 379–381. <https://doi.org/10.1016/j.atherosclerosis.2018.05.033>.
- [59] J. No Young, S.K. Patel, *Peripheral Vascular Bypass*, 2022.
- [60] H. Lau, S.W. Cheng, Is the Preferential Use of ePTFE Grafts in Femorofemoral Bypass Justified?, *Ann. Vasc. Surg.* 15 (2001) 383–387. <https://doi.org/10.1007/s100160010085>.
- [61] F. Sala, R. Hassen-Khodja, A. Lecis, P.-J. Bouillanne, S. Declémy, M. Batt, Long-term Outcome of Femoral Above-knee Popliteal Artery Bypass Using Autologous Saphenous Vein Versus Expanded Polytetrafluoroethylene Grafts, *Ann. Vasc. Surg.* 17 (2003) 401–407. <https://doi.org/10.1007/s10016-003-0019-9>.
- [62] M. Deutsch, J. Meinhart, T. Fischlein, P. Preiss, P. Zilla, Clinical autologous in vitro endothelialization of infrainguinal ePTFE grafts in 100 patients: a 9-year experience., *Surgery*. 126 (1999) 847–55.
- [63] A. Neufang, C. Espinola-Klein, S. Savvidis, W. Schmiedt, A. Poplawski, C.F. Vahl, B. Dorweiler, External polytetrafluoroethylene reinforcement of varicose autologous vein grafts in peripheral bypass surgery produces durable bypass function, *J. Vasc. Surg.* 67 (2018) 1778–1787. <https://doi.org/10.1016/j.jvs.2017.09.039>.
- [64] Y.B.J. Aldenhoff, F.H. van der Veen, J. ter Woorst, J. Habets, L.A. Poole-Warren, L.H. Koole, Performance of a polyurethane vascular prosthesis carrying a dipyrindamole (Persantin) coating on its luminal surface, *J. Biomed. Mater. Res.* 54 (2001) 224–233. [https://doi.org/10.1002/1097-4636\(200102\)54:2<224::AID-JBM9>3.0.CO;2-E](https://doi.org/10.1002/1097-4636(200102)54:2<224::AID-JBM9>3.0.CO;2-E).

- [65] L. Melly, G. Torregrossa, T. Lee, J.-L. Jansens, J.D. Puskas, Fifty years of coronary artery bypass grafting, *J. Thorac. Dis.* 10 (2018) 1960–1967. <https://doi.org/10.21037/jtd.2018.02.43>.
- [66] F.W. Hehrlein, M. Schlepper, F. Loskot, H.H. Scheld, P. Walter, J. Mulch, The use of expanded polytetrafluoroethylene (PTFE) grafts for myocardial revascularization, *J Cardiovasc Surg.* 25 (1984) 549–53.
- [67] D. Radke, W. Jia, D. Sharma, K. Fena, G. Wang, J. Goldman, F. Zhao, Tissue Engineering at the Blood-Contacting Surface: A Review of Challenges and Strategies in Vascular Graft Development, *Adv. Healthc. Mater.* 7 (2018) 1701461. <https://doi.org/10.1002/adhm.201701461>.
- [68] M.A. Cleary, E. Geiger, C. Grady, C. Best, Y. Naito, C. Breuer, Vascular tissue engineering: The next generation, *Trends Mol. Med.* 18 (2012) 394–404. <https://doi.org/10.1016/J.MOLMED.2012.04.013>.
- [69] Y. Jeong, Y. Yao, E.K.F. Yim, Current understanding of intimal hyperplasia and effect of compliance in synthetic small diameter vascular grafts, *Biomater. Sci.* 8 (2020) 4383–4395. <https://doi.org/10.1039/D0BM00226G>.
- [70] Z. Qu, E.L. Chaikof, Prosthetic Grafts, in: *Rutherford's Vasc. Surg.*, Elsevier, 2010: pp. 1335–1349. <https://doi.org/10.1016/B978-1-4160-5223-4.00088-3>.
- [71] E.L. Schwarz, J.M. Kelly, K.M. Blum, K.N. Hor, A.R. Yates, J.C. Zbinden, A. Verma, S.E. Lindsey, A.B. Ramachandra, J.M. Szafron, J.D. Humphrey, T. Shin'oka, A.L. Marsden, C.K. Breuer, Hemodynamic performance of tissue-engineered vascular grafts in Fontan patients, *Npj Regen. Med.* 6 (2021) 38. <https://doi.org/10.1038/s41536-021-00148-w>.
- [72] E. Zetrenne, B.C. McIntosh, M.H. McRae, R. Gusberg, G.R. Evans, D. Narayan, Prosthetic vascular graft infection: a multi-center review of surgical management, *Yale J Biol Med.* 80 (2007) 113–21.
- [73] K. Lachapelle, A.M. Graham, J.F. Symes, Antibacterial activity, antibiotic retention, and infection resistance of a rifampin-impregnated gelatin-sealed Dacron graft, *J. Vasc. Surg.* 19 (1994) 675–682. [https://doi.org/10.1016/S0741-5214\(94\)70041-9](https://doi.org/10.1016/S0741-5214(94)70041-9).
- [74] S. Sarkar, K.M. Sales, G. Hamilton, A.M. Seifalian, Addressing thrombogenicity in vascular graft construction, *J. Biomed. Mater. Res. - Part B Appl. Biomater.* 82 (2007) 100–108. <https://doi.org/10.1002/jbm.b.30710>.
- [75] S.R. Hanson, E.I. Tucker, R.A. Latour, *Blood Coagulation and Blood–Material Interactions*, Fourth Edi, Elsevier, 2020. <https://doi.org/10.1016/b978-0-12-816137-1.00052-0>.
- [76] S.A. Smith, R.J. Travers, J.H. Morrissey, How it all starts: Initiation of the clotting cascade, *Crit. Rev. Biochem. Mol. Biol.* 50 (2015) 326–336. <https://doi.org/10.3109/10409238.2015.1050550>.
- [77] R. Chaudhry, S. Usama, H. Babiker, *Physiology, Coagulation Pathways.*, (2021). <https://www.ncbi.nlm.nih.gov/books/NBK482253/>.
- [78] D. GAILANI, T. RENNÉ, The intrinsic pathway of coagulation: a target for treating

- thromboembolic disease?, *J. Thromb. Haemost.* 5 (2007) 1106–1112. <https://doi.org/10.1111/j.1538-7836.2007.02446.x>.
- [79] C. Sperling, M.F. Maitz, S. Grasso, C. Werner, S.M. Kanse, A Positively Charged Surface Triggers Coagulation Activation Through Factor VII Activating Protease (FSAP), *ACS Appl. Mater. Interfaces.* 9 (2017) 40107–40116. <https://doi.org/10.1021/acsami.7b14281>.
- [80] D. Labarre, Improving blood-compatibility of polymeric surfaces, *Trends Biomater. Artif. Organs.* 15 (2001) 1–3.
- [81] P.F. Sánchez, E.M. Brey, J.C. Briceño, Endothelialization mechanisms in vascular grafts, *J. Tissue Eng. Regen. Med.* 12 (2018) 2164–2178. <https://doi.org/10.1002/term.2747>.
- [82] G.A. Villalona, B. Udelsman, D.R. Duncan, E. McGillicuddy, R.F. Sawh-Martinez, N. Hibino, C. Painter, T. Mirensky, B. Erickson, T. Shinoka, C.K. Breuer, Cell-seeding techniques in vascular tissue engineering, *Tissue Eng. - Part B Rev.* 16 (2010) 341–350. <https://doi.org/10.1089/TEN.TEB.2009.0527>.
- [83] H.J. Lee, S. Zhang, Y. Bar-Cohen, S. Sherrit, High temperature, high power piezoelectric composite transducers, *Sensors (Switzerland).* 14 (2014) 14526–14552. <https://doi.org/10.3390/s140814526>.
- [84] I. Babu, Piezoelectric composites: design, fabrication and performance analysis, Technische Universiteit Eindhoven, 2013. <https://doi.org/https://doi.org/10.6100/IR760468>.
- [85] S. Braune, R.A. Latour, M. Reinthaler, U. Landmesser, A. Lendlein, F. Jung, In Vitro Thrombogenicity Testing of Biomaterials, *Adv. Healthc. Mater.* 8 (2019). <https://doi.org/10.1002/adhm.201900527>.
- [86] A.J. Melchiorri, L.G. Bracaglia, L.K. Kimerer, N. Hibino, J.P. Fisher, In Vitro Endothelialization of Biodegradable Vascular Grafts Via Endothelial Progenitor Cell Seeding and Maturation in a Tubular Perfusion System Bioreactor, *Tissue Eng. - Part C Methods.* 22 (2016) 663–670. <https://doi.org/10.1089/TEN.TEC.2015.0562>.
- [87] J. Tressler, S. Alkoy, R.E. Newnham, Piezoelectric Sensors and Sensor Materials, *J. Electroceramics.* 2 (1998) 257–272.
- [88] K.S. Ramadan, D. Sameoto, S. Evoy, A review of piezoelectric polymers as functional materials for electromechanical transducers, *Smart Mater. Struct.* 23 (2014) 033001. <https://doi.org/10.1088/0964-1726/23/3/033001>.
- [89] B.S. and C.J. Jean-Mistral C, Comparison of electroactive polymers for energy scavenging applications, *Smart Mater. Struct.* 190850123. (2010).
- [90] J.P. Roberts, P. Popper, *Piezoelectric Ceramics*, 1971.
- [91] J. Tichý, J. Erhart, E. Kittinger, J. Přívratká, *Fundamentals of Piezoelectric Sensorics*, Springer Berlin Heidelberg, Berlin, Heidelberg, 2010. <https://doi.org/10.1007/978-3-540-68427-5>.
- [92] H. Jaffe, *Piezoelectric Ceramics*, *J. Am. Ceram. Soc.* 41 (1958) 494–498. <https://doi.org/10.1111/j.1151-2916.1958.tb12903.x>.

- [93] J.-F. Capsal, E. Dantras, L. Laffont, J. Dandurand, C. Lacabanne, Nanotexture influence of BaTiO₃ particles on piezoelectric behaviour of PA 11/BaTiO₃ nanocomposites, *J. Non. Cryst. Solids*. 356 (2010) 629–634. <https://doi.org/10.1016/j.jnoncrysol.2009.06.050>.
- [94] P. Piezoelectricity, Chapter 2 Characteristics of Ferroelectric Pzt Ceramics, (n.d.) 7–26.
- [95] H. Li, C. Tian, Z.D. Deng, Energy harvesting from low frequency applications using piezoelectric materials, *Appl. Phys. Rev.* 1 (2014) 041301. <https://doi.org/10.1063/1.4900845>.
- [96] S. Mishra, L. Unnikrishnan, S.K. Nayak, S. Mohanty, Advances in Piezoelectric Polymer Composites for Energy Harvesting Applications: A Systematic Review, *Macromol. Mater. Eng.* 304 (2019) 1800463. <https://doi.org/10.1002/mame.201800463>.
- [97] P. Ueberschlag, PVDF piezoelectric polymer, *Sens. Rev.* 21 (2001) 118–126. <https://doi.org/10.1108/02602280110388315>.
- [98] J.L. Wang, X.J. Meng, J.H. Chu, New Properties and Applications of Polyvinylidene-Based Ferroelectric Polymer, in: *Ferroelectr. Mater. - Synth. Charact.*, InTech, 2015. <https://doi.org/10.5772/60946>.
- [99] F. Mokhtari, B. Azimi, M. Salehi, S. Hashemikia, S. Danti, Recent advances of polymer-based piezoelectric composites for biomedical applications, *J. Mech. Behav. Biomed. Mater.* 122 (2021) 104669. <https://doi.org/10.1016/j.jmbbm.2021.104669>.
- [100] J.Y.-H. Kim, A. Cheng, Y.-C. Tai, Parylene-C as a piezoelectric material, in: 2011 IEEE 24th Int. Conf. Micro Electro Mech. Syst., IEEE, 2011: pp. 473–476. <https://doi.org/10.1109/MEMSYS.2011.5734464>.
- [101] G.M. Atkinson, R.E. Pearson, Z. Ounaies, C. Park, J.S. Harrison, J.A. Midkiff, Piezoelectric polyimide tactile sensors, in: *Proc. 15th Bienn. Univ. Ind. Microelectron. Symp. (Cat. No.03CH37488)*, IEEE, n.d.: pp. 308–311. <https://doi.org/10.1109/UGIM.2003.1225750>.
- [102] G. Wu, O. Yano, T. Soen, Dielectric and Piezoelectric Properties of Nylon 9 and Nylon 11, *Polym. J.* 18 (1986) 51–61. <https://doi.org/10.1295/polymj.18.51>.
- [103] F. Bernard, L. Gimeno, B. Viala, B. Gusarov, O. Cugat, Direct Piezoelectric Coefficient Measurements of PVDF and PLLA under Controlled Strain and Stress, in: *Proc. Eurosensors 2017, Paris, Fr. 3–6 Sept. 2017*, MDPI, Basel Switzerland, 2017: p. 335. <https://doi.org/10.3390/proceedings1040335>.
- [104] J. Hafner, M. Teuschel, M. Schneider, U. Schmid, Origin of the strong temperature effect on the piezoelectric response of the ferroelectric (co-)polymer P(VDF70-TrFE30), *Polymer (Guildf)*. 170 (2019) 1–6. <https://doi.org/10.1016/j.polymer.2019.02.064>.
- [105] D.A. van den Ende, B.F. Bory, W.A. Groen, S. van der Zwaag, Improving the d₃₃ and g₃₃ properties of 0-3 piezoelectric composites by dielectrophoresis, *J. Appl. Phys.* 107 (2010) 024107. <https://doi.org/10.1063/1.3291131>.
- [106] Z. Wang, F. Narita, Corona Poling Conditions for Barium Titanate/Epoxy Composites and their Unsteady Wind Energy Harvesting Potential, *Adv. Eng. Mater.* 21 (2019) 1900169. <https://doi.org/10.1002/adem.201900169>.

- [107] X. Zhang, J. Villafuerte, V. Consonni, J.-F. Capsal, P.-J. Cottinet, L. Petit, M.-Q. Le, Characterizing and Optimizing Piezoelectric Response of ZnO Nanowire/PMMA Composite-Based Sensor, *Nanomaterials*. 11 (2021) 1712. <https://doi.org/10.3390/nano11071712>.
- [108] E. Carvalho, L. Fernandes, C.M. Costa, S. Lanceros-Méndez, Piezoelectric Polymer Composites for Sensors and Actuators, in: *Encycl. Mater. Compos.*, Elsevier, 2021: pp. 473–486. <https://doi.org/10.1016/B978-0-12-819724-0.00005-7>.
- [109] A. Mayeen, N. Kalarikkal, Development of ceramic-controlled piezoelectric devices for biomedical applications, in: *Fundam. Biomater. Ceram.*, Elsevier, 2018: pp. 47–62. <https://doi.org/10.1016/B978-0-08-102203-0.00002-0>.
- [110] M.G. Broadhurst, G.T. Davis, Piezo- and pyroelectric properties, in: 1980: pp. 285–319. https://doi.org/10.1007/3540173358_13.
- [111] C. Brown, R. Kell, R. Taylor, L. Thomas, Piezoelectric Materials, A Review of Progress, *IRE Trans. Compon. Parts*. 9 (1962) 193–211. <https://doi.org/10.1109/TCP.1962.1136768>.
- [112] G. Sa-Gong, A. Safari, S.J. Jang, R.E. Newnham, Poling flexible piezoelectric composites, *Ferroelectr. Lett. Sect.* 5 (1986) 131–142. <https://doi.org/10.1080/07315178608202472>.
- [113] I. Coondoo, N. Panwar, A. Kholkin, Lead-free piezoelectrics: Current status and perspectives, *J. Adv. Dielectr.* 03 (2013) 1330002. <https://doi.org/10.1142/S2010135X13300028>.
- [114] K.V. Galloway, N.M. Sammes, FUEL CELLS – SOLID OXIDE FUEL CELLS | Anodes, in: *Encycl. Electrochem. Power Sources*, Elsevier, 2009: pp. 17–24. <https://doi.org/10.1016/B978-044452745-5.00251-3>.
- [115] P. Kour, S. Kishore Pradhan, Perovskite Ferroelectric, in: *Multifunct. Ferroelectr. Mater.*, IntechOpen, 2021. <https://doi.org/10.5772/intechopen.98382>.
- [116] P.K. Panda, Review: environmental friendly lead-free piezoelectric materials, *J. Mater. Sci.* 44 (2009) 5049–5062. <https://doi.org/10.1007/s10853-009-3643-0>.
- [117] T. Hoshina, S. Wada, Y. Kuroiwa, T. Tsurumi, Composite structure and size effect of barium titanate nanoparticles, *Appl. Phys. Lett.* 93 (2008) 2006–2009. <https://doi.org/10.1063/1.3027067>.
- [118] J.P. Ball, B.A. Mound, J.C. Nino, J.B. Allen, Biocompatible evaluation of barium titanate foamed ceramic structures for orthopedic applications, *J. Biomed. Mater. Res. Part A*. 102 (2014) 2089–2095. <https://doi.org/10.1002/jbm.a.34879>.
- [119] J.B. Park, G.H. Kenner, S.D. Brown, J.K. Scott, Mechanical Property Changes of Barium Titanate (Ceramic) After in Vivo and in Vitro Aging, *Biomater. Med. Devices. Artif. Organs*. 5 (1977) 267–276. <https://doi.org/10.3109/10731197709118677>.
- [120] G. D'Ambrogio, O. Zahhaf, Y. Hebrard, M.Q. Le, P.-J. Cottinet, J.-F. Capsal, Micro-Structuration of Piezoelectric Composites Using Dielectrophoresis: Toward Application in Condition Monitoring of Bearings, *Adv. Eng. Mater.* (2020) adem.202000773. <https://doi.org/10.1002/adem.202000773>.

- [121] H. Search, C. Journals, A. Contact, M. Iopscience, I.P. Address, Piezoelectric properties of ferroelectric PZT – polymer composites, 487 (2001).
- [122] A.B. Kounga, T. Granzow, E. Aulbach, M. Hinterstein, J. Rödel, High-temperature poling of ferroelectrics, *J. Appl. Phys.* 104 (2008) 024116. <https://doi.org/10.1063/1.2959830>.
- [123] G.H. Haertling, Ferroelectric Ceramics: History and Technology, *J. Am. Ceram. Soc.* 82 (1999) 797–818. <https://doi.org/10.1111/j.1151-2916.1999.tb01840.x>.
- [124] F.-Z. Yao, K. Wang, W. Jo, J.-S. Lee, J.-F. Li, Effect of poling temperature on piezoelectricity of CaZrO₃-modified (K, Na)NbO₃-based lead-free ceramics, *J. Appl. Phys.* 116 (2014) 114102. <https://doi.org/10.1063/1.4895774>.
- [125] C. Kittel, Theory of Antiferroelectric Crystals, *Phys. Rev.* 82 (1951) 729–732. <https://doi.org/10.1103/PhysRev.82.729>.
- [126] C.A. Randall, Z. Fan, I. Reaney, L. Chen, S. Trolier-McKinstry, Antiferroelectrics: History, fundamentals, crystal chemistry, crystal structures, size effects, and applications, *J. Am. Ceram. Soc.* 104 (2021) 3775–3810. <https://doi.org/10.1111/jace.17834>.
- [127] Z. Zhou, Q. Yang, M. Liu, Z. Zhang, X. Zhang, D. Sun, T. Nan, N. Sun, X. Chen, Antiferroelectric Materials, Applications and Recent Progress on Multiferroic Heterostructures, *SPIN.* 05 (2015) 1530001. <https://doi.org/10.1142/S2010324715300017>.
- [128] M.-H. Zhang, L. Fulanović, S. Egert, H. Ding, P.B. Groszewicz, H.-J. Kleebe, L. Molina-Luna, J. Koruza, Electric-field-induced antiferroelectric to ferroelectric phase transition in polycrystalline NaNbO₃, *Acta Mater.* 200 (2020) 127–135. <https://doi.org/10.1016/j.actamat.2020.09.002>.
- [129] L.A. Reznitchenko, A. V Turik, E.M. Kuznetsova, V.P. Sakhnenko, Piezoelectricity in NaNbO₃ ceramics, *J. Phys. Condens. Matter.* 13 (2001) 3875–3881. <https://doi.org/10.1088/0953-8984/13/17/308>.
- [130] P. Taylor, Poling flexible piezoelectric composites, (n.d.) 37–41. <https://doi.org/10.1080/07315178608202472>.
- [131] M. Alexandre, C. Bessagnet, C. David, E. Dantras, C. Lacabanne, Piezoelectric properties of polymer/lead-free ceramic composites, *Phase Transitions.* 89 (2016) 708–716. <https://doi.org/10.1080/01411594.2016.1206898>.
- [132] V.Y. Topolov, C.R. Bowen, Piezo- Particulate Composites, n.d.
- [133] M.Q. Le, F. Ganet, D. Audigier, J.-F. Capsal, P.-J. Cottinet, Printing of microstructure strain sensor for structural health monitoring, *Appl. Phys. A.* 123 (2017) 354. <https://doi.org/10.1007/s00339-017-0970-x>.
- [134] K. Uchino, Piezoelectric composite materials, *Adv. Piezoelectric Mater. Sci. Technol.* (2010) 318–346. <https://doi.org/10.1533/9781845699758.1.318>.
- [135] S. Duan, J. Wu, J. Xia, W. Lei, Innovation Strategy Selection Facilitates High-Performance Flexible Piezoelectric Sensors, *Sensors.* 20 (2020) 2820. <https://doi.org/10.3390/s20102820>.

- [136] H. Wei, H. Wang, Y. Xia, D. Cui, Y. Shi, M. Dong, C. Liu, T. Ding, J. Zhang, Y. Ma, N. Wang, Z. Wang, Y. Sun, R. Wei, Z. Guo, An overview of lead-free piezoelectric materials and devices, *J. Mater. Chem. C.* 6 (2018) 12446–12467. <https://doi.org/10.1039/C8TC04515A>.
- [137] M.A. Barique, H. Ohigashi, Annealing effects on the Curie transition temperature and melting temperature of poly(vinylidene fluoride/trifluoroethylene) single crystalline films, *Polymer (Guildf)*. 42 (2001) 4981–4987. [https://doi.org/10.1016/S0032-3861\(00\)00937-X](https://doi.org/10.1016/S0032-3861(00)00937-X).
- [138] J.-F. Capsal, C. David, E. Dantras, C. Lacabanne, Piezoelectric sensing coating for real time impact detection and location on aircraft structures, *Smart Mater. Struct.* 21 (2012) 055021. <https://doi.org/10.1088/0964-1726/21/5/055021>.
- [139] C. David, J.-F. Capsal, L. Laffont, E. Dantras, C. Lacabanne, Piezoelectric properties of polyamide 11/NaNbO₃ nanowire composites, *J. Phys. D. Appl. Phys.* 45 (2012) 415305. <https://doi.org/10.1088/0022-3727/45/41/415305>.
- [140] J.-F. Capsal, E. Dantras, J. Dandurand, C. Lacabanne, Electroactive influence of ferroelectric nanofillers on polyamide 11 matrix properties, *J. Non. Cryst. Solids*. 353 (2007) 4437–4442. <https://doi.org/10.1016/j.jnoncrysol.2007.01.097>.
- [141] D. Carponcin, E. Dantras, L. Laffont, J. Dandurand, G. Aridon, F. Levallois, L. Cadiergues, C. Lacabanne, Integrated piezoelectric function in a high thermostable thermoplastic PZT/PEEK composite, *J. Non. Cryst. Solids*. 388 (2014) 32–36. <https://doi.org/10.1016/j.jnoncrysol.2014.01.020>.
- [142] F. Dominici, D. Puglia, F. Luzi, F. Sarasini, M. Rallini, L. Torre, A Novel Class of Cost Effective and High Performance Composites Based on Terephthalate Salts Reinforced Polyether Ether Ketone, *Polymers (Basel)*. 11 (2019) 2097. <https://doi.org/10.3390/polym11122097>.
- [143] N.K. James, D. van den Ende, U. Lafont, S. van der Zwaag, W.A. Groen, Piezoelectric and mechanical properties of structured PZT–epoxy composites, *J. Mater. Res.* 28 (2013) 635–641. <https://doi.org/10.1557/jmr.2012.428>.
- [144] V.-C. Nguyen, M.-Q. Le, A. Fimbel, S. Bernadet, Y. Hebrard, J.-F. Mognotte, J.-F. Capsal, P.-J. Cottinet, Printing smart coating of piezoelectric composite for application in condition monitoring of bearings, *Mater. Des.* 215 (2022) 110529. <https://doi.org/10.1016/j.matdes.2022.110529>.
- [145] K.-I. Park, M. Lee, Y. Liu, S. Moon, G.-T. Hwang, G. Zhu, J.E. Kim, S.O. Kim, D.K. Kim, Z.L. Wang, K.J. Lee, Flexible Nanocomposite Generator Made of BaTiO₃ Nanoparticles and Graphitic Carbons, *Adv. Mater.* 24 (2012) 2999–3004. <https://doi.org/10.1002/adma.201200105>.
- [146] S. Xu, Y. Yeh, G. Poirier, M.C. McAlpine, R.A. Register, N. Yao, Flexible Piezoelectric PMN–PT Nanowire-Based Nanocomposite and Device, *Nano Lett.* 13 (2013) 2393–2398. <https://doi.org/10.1021/nl400169t>.
- [147] D. Grinberg, S. Siddique, M. Le, R. Liang, J. Capsal, P. Cottinet, 4D Printing based piezoelectric composite for medical applications, *J. Polym. Sci. Part B Polym. Phys.* 57 (2019) 109–115. <https://doi.org/10.1002/polb.24763>.

- [148] Y. Tang, L. Chen, Z. Duan, K. Zhao, Z. Wu, Graphene/barium titanate/polymethyl methacrylate bio-piezoelectric composites for biomedical application, *Ceram. Int.* 46 (2020) 6567–6574. <https://doi.org/10.1016/j.ceramint.2019.11.142>.
- [149] K.K. Sappati, S. Bhadra, Flexible Piezoelectric 0–3 PZT-PDMS Thin Film for Tactile Sensing, *IEEE Sens. J.* 20 (2020) 4610–4617. <https://doi.org/10.1109/JSEN.2020.2965083>.
- [150] P. Eltouby, I. Shyha, C. Li, J. Khaliq, Factors affecting the piezoelectric performance of ceramic-polymer composites: A comprehensive review, *Ceram. Int.* 47 (2021) 17813–17825. <https://doi.org/10.1016/j.ceramint.2021.03.126>.
- [151] X. Zhang, M.-Q. Le, V.-C. Nguyen, J.-F. Mogniotte, J.-F. Capsal, D. Grinberg, P.-J. Cottinet, L. Petit, Characterization of micro-ZnO/PDMS composite structured via dielectrophoresis – Toward medical application, *Mater. Des.* 208 (2021) 109912. <https://doi.org/10.1016/j.matdes.2021.109912>.
- [152] L. Durai, S. Badhulika, A Wearable PVA Film Supported TiO₂ Nanoparticles Decorated NaNbO₃ Nanoflakes-Based SERS Sensor for Simultaneous Detection of Metabolites and Biomolecules in Human Sweat Samples, *Adv. Mater. Interfaces.* 9 (2022) 2200146. <https://doi.org/10.1002/admi.202200146>.
- [153] D.P. Skinner, R.E. Newnham, L.E. Cross, Flexible Composite transducers, 13 (1978) 599–607.
- [154] S. Mahmud, Y. Long, M. Abu Taher, Z. Xiong, R. Zhang, J. Zhu, Toughening polylactide by direct blending of cellulose nanocrystals and epoxidized soybean oil, *J. Appl. Polym. Sci.* 136 (2019) 48221. <https://doi.org/10.1002/app.48221>.
- [155] C.K. Wong, F.G. Shin, Effect of electrical conductivity on poling and the dielectric, pyroelectric and piezoelectric properties of ferroelectric 0-3 composites, *J. Mater. Sci.* 41 (2006) 229–249. <https://doi.org/10.1007/s10853-005-7243-3>.
- [156] A. Victor, J. Ribeiro, F. F. Araújo, Study of PDMS characterization and its applications in biomedicine: A review, *J. Mech. Eng. Biomech.* 4 (2019) 1–9. <https://doi.org/10.24243/JMEB/4.1.163>.
- [157] R. Guinovart-Díaz, J. Bravo-Castillero, R. Rodríguez-Ramos, F.J. Sabina, R. Martínez-Rosado, Overall properties of piezocomposite materials 1-3, *Mater. Lett.* 48 (2001) 93–98. [https://doi.org/10.1016/S0167-577X\(00\)00285-8](https://doi.org/10.1016/S0167-577X(00)00285-8).
- [158] D.A. Van den Ende, *Structured Piezoelectric Composites*, 2012.
- [159] L.E.C. R.E.Newman, D.P.Skinner, Connectivity and piezoelectric-pyroelectric composites, 13 (1978) 377–389.
- [160] S.A. Wilson, G.M. Maistros, R.W. Whatmore, Structure modification of 0-3 piezoelectric ceramic/polymer composites through dielectrophoresis, *J. Phys. D. Appl. Phys.* 38 (2005) 175–182. <https://doi.org/10.1088/0022-3727/38/2/001>.
- [161] A. Safari, A. Halliyal, L.J. Bowen, R.E. Newnham, Flexible Composite Transducers, *J. Am. Ceram. Soc.* 65 (1982) 207–209. <https://doi.org/10.1111/j.1151-2916.1982.tb10405.x>.

- [162] H.L.W.H.L.W. Chan, J. Unsworth, Simple Model for Piezoelectric Ceramic/Polymer 1–3 Composites Used in Ultrasonic Transducer Applications, *IEEE Trans. Ultrason. Ferroelectr. Freq. Control.* 36 (1989) 434–441. <https://doi.org/10.1109/58.31780>.
- [163] H. Khanbareh, S. van der Zwaag, W.A. Groen, Effect of dielectrophoretic structuring on piezoelectric and pyroelectric properties of lead titanate-epoxy composites, *Smart Mater. Struct.* 23 (2014) 105030. <https://doi.org/10.1088/0964-1726/23/10/105030>.
- [164] C.P. Bowen, R.E. Newnham, C.A. Randall, Dielectric properties of dielectrophoretically assembled particulate-polymer composites, *J. Mater. Res.* 13 (1998) 205–210. <https://doi.org/10.1557/JMR.1998.0027>.
- [165] T. Yamada, T. Ueda, T. Kitayama, Piezoelectricity of a high-content lead zirconate titanate/polymer composite, *J. Appl. Phys.* 53 (1982) 4328–4332. <https://doi.org/10.1063/1.331211>.
- [166] I. Babu, G. De With, Highly flexible piezoelectric 0 – 3 PZT – PDMS composites with high filler content, *Compos. Sci. Technol.* 91 (2014) 91–97. <https://doi.org/10.1016/j.compscitech.2013.11.027>.
- [167] D.P. Skinner, R.E. Newnham, L.E. Cross, D.P.S. and L.E.C. R.E. Newnham, Connectivity and piezoelectric-pyroelectric composites, *Mat. Res. Bull.* Vol. 13, Pp. 525-536, 1978. Pergamon Press. Inc. Print. United States. 13 (1978) 599–607.
- [168] M.A. Gutiérrez, H. Khanbareh, S. van der Zwaag, Computational modeling of structure formation during dielectrophoresis in particulate composites, *Comput. Mater. Sci.* 112 (2016) 139–146. <https://doi.org/10.1016/j.commatsci.2015.10.011>.
- [169] M. Farshad, A. Benine, Magnetoactive elastomer composites, *Polym. Test.* 23 (2004) 347–353. [https://doi.org/10.1016/S0142-9418\(03\)00103-X](https://doi.org/10.1016/S0142-9418(03)00103-X).
- [170] Z. Varga, G. Filipcsei, M. Zrínyi, Magnetic field sensitive functional elastomers with tuneable elastic modulus, *Polymer (Guildf)*. 47 (2006) 227–233. <https://doi.org/10.1016/j.polymer.2005.10.139>.
- [171] B. Techaumnat, B. Eua-Arporn, T. Takuma, Electric field and dielectrophoretic force on a dielectric particle chain in a parallel-plate electrode system, *J. Phys. D. Appl. Phys.* 37 (2004) 3337–3346. <https://doi.org/10.1088/0022-3727/37/23/017>.
- [172] R. Pethig, How does Dielectrophoresis Differ from Electrophoresis?, *Dielectrophoresis.* (2017) 31–48. <https://doi.org/10.1002/9781118671443.ch2>.
- [173] R. Pethig, Y. Huang, X.B. Wang, J.P.H. Burt, Positive and negative dielectrophoretic collection of colloidal particles using interdigitated castellated microelectrodes, *J. Phys. D. Appl. Phys.* 25 (1992) 881–888. <https://doi.org/10.1088/0022-3727/25/5/022>.
- [174] C.P. Bowen, T.R. Shrout, R.E. Newnham, C.A. Randall, A study of the frequency dependence of the dielectrophoretic effect in thermoset polymers, *J. Mater. Res.* 12 (1997) 2345–2356. <https://doi.org/10.1557/JMR.1997.0311>.
- [175] T.B. Jones, *Electromechanics of Particles*, Cambridge University Press, 1995. <https://doi.org/10.1017/CBO9780511574498>.

- [176] M. Citeau, O. Larue, E. Vorobiev, Electric (Electro/Dielectro-Phoretic)—Force Field Assisted Separators, in: *Prog. Filtr. Sep.*, Elsevier, 2015: pp. 325–397. <https://doi.org/10.1016/B978-0-12-384746-1.00008-2>.
- [177] C.P. Bowen, T.R. ShROUT, R.E. Newnham, C.A. Randall, Tunable Electric Field Processing of Composite Materials, *J. Intell. Mater. Syst. Struct.* 6 (1995) 159–168. <https://doi.org/10.1177/1045389X9500600203>.
- [178] R. TAO, ORDER PARAMETERS AND PHASE TRANSITIONS IN ELECTORRHEOLOGICAL FLUIDS, *Int. J. Mod. Phys. B.* 06 (1992) 2635–2649. <https://doi.org/10.1142/S0217979292001341>.
- [179] O. Zahhaf, G. D’Ambrogio, M.-Q. Le, G. Coativy, F. Grasland, P.-J. Cottinet, J.-F. Capsal, Dielectrophoretic alignment of Al₂O₃/PDMS composites: Enhancement of thermal and dielectric properties through structural sedimentation analysis, *Mater. Des.* 211 (2021) 110134. <https://doi.org/10.1016/j.matdes.2021.110134>.
- [180] A.P. Gast, C.F. Zukoski, Electrorheological fluids as colloidal suspensions, *Adv. Colloid Interface Sci.* 30 (1989) 153–202. [https://doi.org/10.1016/0001-8686\(89\)80006-5](https://doi.org/10.1016/0001-8686(89)80006-5).
- [181] R.E. Park, C., Robertson, Aligned microstructure of some particulate polymer composites obtained with an electric field, *J. Mater. Sci.* 33 (1998) 3541–3553. <https://doi.org/https://doi.org/10.1023/A:1004638825477>.
- [182] C.A. Randall, C.P. Bowen, T.R. ShROUT, G.L. Messing, R.E. Newnham, Dielectrophoretic assembly: A novel concept in advanced composite fabrication, in: *Electrorheological Fluids*, 1993: p. 516.
- [183] I.D. Johnston, D.K. McCluskey, C.K.L.L. Tan, M.C. Tracey, Mechanical characterization of bulk Sylgard 184 for microfluidics and microengineering, *J. Micromechanics Microengineering.* 24 (2014) 035017. <https://doi.org/10.1088/0960-1317/24/3/035017>.
- [184] B.D. Ratner, S.J. Bryant, Biomaterials: Where We Have Been and Where We Are Going, *Annu. Rev. Biomed. Eng.* 6 (2004) 41–75. <https://doi.org/10.1146/annurev.bioeng.6.040803.140027>.
- [185] M.L. Scarpello, D. Kurup, H. Rogier, D. Vande Ginste, F. Axisa, J. Vanfleteren, W. Joseph, L. Martens, G. Vermeeren, Design of an Implantable Slot Dipole Conformal Flexible Antenna for Biomedical Applications, *IEEE Trans. Antennas Propag.* 59 (2011) 3556–3564. <https://doi.org/10.1109/TAP.2011.2163761>.
- [186] R.A. Green, N.H. Lovell, G.G. Wallace, L.A. Poole-Warren, Conducting polymers for neural interfaces: Challenges in developing an effective long-term implant, *Biomaterials.* 29 (2008) 3393–3399. <https://doi.org/10.1016/j.biomaterials.2008.04.047>.
- [187] C. Hassler, T. Boretius, T. Stieglitz, Polymers for neural implants, *J. Polym. Sci. Part B Polym. Phys.* 49 (2011) 18–33. <https://doi.org/10.1002/polb.22169>.
- [188] I. Babu, G. de With, Highly flexible piezoelectric 0-3 PZT-PDMS composites with high filler content, *Compos. Sci. Technol.* 91 (2014) 91–97. <https://doi.org/10.1016/j.compscitech.2013.11.027>.

- [189] S.Z.-U.N.D. Firmenbezeichnung, SYLGARD (R) 184 SILICONE ELASTOMER KIT (CURING AGENT information is below) SYLGARD (R) 184 SILICONE ELASTOMER KIT (CURING AGENT information is below), (2006) 1–7.
- [190] D. Meyerhofer, Transition to the Ferroelectric State in Barium Titanate, *Phys. Rev.* 112 (1958) 413–423. <https://doi.org/10.1103/PhysRev.112.413>.
- [191] A. Karvounis, F. Timpu, V. V. Vogler-Neuling, R. Savo, R. Grange, Barium Titanate Nanostructures and Thin Films for Photonics, *Adv. Opt. Mater.* 8 (2020) 2001249. <https://doi.org/10.1002/adom.202001249>.
- [192] M. Acosta, N. Novak, V. Rojas, S. Patel, R. Vaish, J. Koruza, G.A. Rossetti, J. Rödel, BaTiO₃-based piezoelectrics: Fundamentals, current status, and perspectives, *Appl. Phys. Rev.* 4 (2017) 041305. <https://doi.org/10.1063/1.4990046>.
- [193] A. von Hippel, Ferroelectricity, Domain Structure, and Phase Transitions of Barium Titanate, *Rev. Mod. Phys.* 22 (1950) 221–237. <https://doi.org/10.1103/RevModPhys.22.221>.
- [194] J. Macutkevic, A. Molak, J. Banyš, Dielectric Properties of NaNbO₃ Ceramics, *Ferroelectrics*. 479 (2015) 48–55. <https://doi.org/10.1080/00150193.2015.1011916>.
- [195] H. Guo, H. Shimizu, Y. Mizuno, C.A. Randall, Domain configuration changes under electric field-induced antiferroelectric-ferroelectric phase transitions in NaNbO₃-based ceramics, *J. Appl. Phys.* 118 (2015) 054102. <https://doi.org/10.1063/1.4928153>.
- [196] H. Zhu, Z. Zheng, X. Gao, Y. Huang, Z. Yan, J. Zou, H. Yin, Q. Zou, S.H. Kable, J. Zhao, Y. Xi, W.N. Martens, R.L. Frost, Structural Evolution in a Hydrothermal Reaction between Nb₂O₅ and NaOH Solution: From Nb₂O₅ Grains to Microporous Na₂Nb₂O₆ · 2/3 H₂O Fibers and NaNbO₃ Cubes, *J. Am. Chem. Soc.* 128 (2006) 2373–2384. <https://doi.org/10.1021/ja056301w>.
- [197] P. Li, Y. Zhang, R. Zang, P. Liu, X. Yuan, X. Wang, Cu-Loaded NaNbO₃ Three-Dimensional Networks for CO₂ Photoreduction to C₂ Species, *Energy & Fuels*. (2022). <https://doi.org/10.1021/acs.energyfuels.2c01394>.
- [198] S.L. Skjærvø, G.K. Ong, O.G. Grendal, K.H. Wells, W. van Beek, K. Ohara, D.J. Milliron, S. Tominaka, T. Grande, M.-A. Einarsrud, Understanding the Hydrothermal Formation of NaNbO₃: Its Full Reaction Scheme and Kinetics, *Inorg. Chem.* 60 (2021) 7632–7640. <https://doi.org/10.1021/acs.inorgchem.0c02763>.
- [199] C.S. Smith, Macroscopic Symmetry and Properties of Crystals, in: 1958: pp. 175–249. [https://doi.org/10.1016/S0081-1947\(08\)60727-4](https://doi.org/10.1016/S0081-1947(08)60727-4).
- [200] J.-F. Capsal, C. Pousserot, E. Dantras, J. Dandurand, C. Lacabanne, Dynamic mechanical behaviour of polyamide 11/Barium titanate ferroelectric composites, *Polymer (Guildf)*. 51 (2010) 5207–5211. <https://doi.org/10.1016/j.polymer.2010.09.011>.
- [201] L. Seveyrat, M. Lemercier, B. Guiffard, L. Lebrun, D. Guyomar, Temperature dependence of macroscopic and microscopic PZT properties studied by thermo-mechanical analysis, dielectric measurements and X-ray diffraction, *Ceram. Int.* 35 (2009) 45–49.

<https://doi.org/10.1016/j.ceramint.2007.09.010>.

- [202] G. D'Ambrogio, O. Zahhaf, M.-Q. Le, J.-F. Capsal, P.-J. Cottinet, Dielectrophoresis Structurization of PZT/PDMS Micro-Composite for Elastronic Function: Towards Dielectric and Piezoelectric Enhancement, *Materials (Basel)*. 14 (2021) 4071. <https://doi.org/10.3390/ma14154071>.
- [203] F. Kremer, A. Schönhal, *Broadband Dielectric Spectroscopy*, Springer Berlin Heidelberg, Berlin, Heidelberg, 2003. <https://doi.org/10.1007/978-3-642-56120-7>.
- [204] A.C. Patsidis, Barium titanate/polydimethylsiloxane nano/microcomposites fabrication, morphology, dielectric response and functionality, *IET Nanodielectrics*. 3 (2020) 14–19. <https://doi.org/10.1049/iet-nde.2019.0043>.
- [205] L. Wang, J. Yang, W. Cheng, J. Zou, D. Zhao, Progress on Polymer Composites With Low Dielectric Constant and Low Dielectric Loss for High-Frequency Signal Transmission, *Front. Mater.* 8 (2021). <https://doi.org/10.3389/fmats.2021.774843>.
- [206] S. Nayak, T.K. Chaki, D. Khastgir, Development of Flexible Piezoelectric Poly(dimethylsiloxane)–BaTiO₃ Nanocomposites for Electrical Energy Harvesting, *Ind. Eng. Chem. Res.* 53 (2014) 14982–14992. <https://doi.org/10.1021/ie502565f>.
- [207] H. Wu, F. Zhuo, H. Qiao, L. Kodumudi Venkataraman, M. Zheng, S. Wang, H. Huang, B. Li, X. Mao, Q. Zhang, Polymer-/Ceramic-based Dielectric Composites for Energy Storage and Conversion, *ENERGY Environ. Mater.* 5 (2022) 486–514. <https://doi.org/10.1002/eem2.12237>.
- [208] H. Khanbareh, V.Y. Topolov, C.R. Bowen, *Piezo-Particulate Composites*, Springer International Publishing, Cham, 2019. <https://doi.org/10.1007/978-3-030-19204-4>.
- [209] J. Le Rouzic, P. Delobelle, P. Vairac, B. Cretin, Comparison of three different scales techniques for the dynamic mechanical characterization of two polymers (PDMS and SU8), *Eur. Phys. J. Appl. Phys.* 48 (2009) 11201. <https://doi.org/10.1051/epjap/2009124>.
- [210] F. Cordero, Quantitative evaluation of the piezoelectric response of unpoled ferroelectric ceramics from elastic and dielectric measurements: Tetragonal BaTiO₃, *J. Appl. Phys.* 123 (2018) 094103. <https://doi.org/10.1063/1.5018746>.
- [211] J. Benz, C. Bonten, F. Paolo, L. Mantia, J.A. Covas, S. Thomas, M. Gahleitner, Rigid Amorphous Fraction as an Indicator for Polymer-Polymer Interactions in Highly Filled Plastics, *Polym.* 2021, Vol. 13, Page 3349. 13 (2021) 3349. <https://doi.org/10.3390/POLYM13193349>.
- [212] Y. Xiong, G. Chen, S. Guo, The preparation of core-shell CaCO₃ particles and its effect on mechanical property of PVC composites, *J. Appl. Polym. Sci.* 102 (2006) 1084–1091. <https://doi.org/10.1002/app.24262>.
- [213] S.K. Sharma, H. Gaur, M. Kulkarni, G. Patil, B. Bhattacharya, A. Sharma, PZT–PDMS composite for active damping of vibrations, *Compos. Sci. Technol.* 77 (2013) 42–51. <https://doi.org/10.1016/j.compscitech.2013.01.004>.
- [214] G. Hu, D. Yu, Tensile, thermal and dynamic mechanical properties of hollow polymer particle-filled epoxy syntactic foam, *Mater. Sci. Eng. A*. 528 (2011) 5177–5183.

- <https://doi.org/10.1016/j.msea.2011.03.071>.
- [215] N. Bosq, N. Guigo, J. Persello, N. Sbirrazzuoli, Melt and glass crystallization of PDMS and PDMS silica nanocomposites, *Phys. Chem. Chem. Phys.* 16 (2014) 7830–7840. <https://doi.org/10.1039/C4CP00164H>.
- [216] M. Doumeng, F. Berthet, K. Delbé, O. Marsan, J. Denape, F. Chabert, Effect of size, concentration, and nature of fillers on crystallinity, thermal, and mechanical properties of polyetheretherketone composites, *J. Appl. Polym. Sci.* 2022 (n.d.) 51574. <https://doi.org/10.1002/app.51574i>.
- [217] A. Chien, R.S. Maxwell, S. Deteresa, L. Thompson, R. Cohenour, B. Balazs, Effects of filler–polymer interactions on cold-crystallization kinetics in crosslinked, silica-filled polydimethylsiloxane/polydiphenylsiloxane copolymer melts, *J. Polym. Sci. Part B Polym. Phys.* 44 (2006) 1898–1906. <https://doi.org/10.1002/POLB.20848>.
- [218] M.I. Aranguren, Crystallization of polydimethylsiloxane: effect of silica filler and curing, 39 (1998) 4897–4903.
- [219] T. DOLLASE, H.W. SPIESS, M. WILHELM, Y. YAGEN, R. YERUSGALMI-ROZEN, M. GOTTLIEB, Effect of Interfaces on the Crystallization Behavior of PDMS, *Interface Sci.* 11 (2003) 199–209. <https://doi.org/10.1023/A:1022174712707>.
- [220] G.Z. Papageorgiou, D.S. Achilias, D.N. Bikiaris, G.P. Karayannidis, Crystallization kinetics and nucleation activity of filler in polypropylene/surface-treated SiO₂ nanocomposites, *Thermochim. Acta.* 427 (2005) 117–128. <https://doi.org/10.1016/J.TCA.2004.09.001>.
- [221] P.A. Klonos, Crystallization, glass transition, and molecular dynamics in PDMS of low molecular weights: A calorimetric and dielectric study, *Polymer (Guildf.)* 159 (2018) 169–180. <https://doi.org/10.1016/j.polymer.2018.11.028>.
- [222] G. D’Ambrogio, O. Zahhaf, M. Bordet, M.Q. Le, N. Della Schiava, R. Liang, P.-J. Cottinet, J.-F. Capsal, Structuring BaTiO₃ /PDMS nanocomposite via dielectrophoresis for fractional flow reserve measurement, *Adv. Eng. Mater.* (2021) adem.202100341. <https://doi.org/10.1002/adem.202100341>.
- [223] Q. Tao, M. Jiang, G. Li, Simulation and Experimental Study of Nanowire Assembly by Dielectrophoresis, *IEEE Trans. Nanotechnol.* 13 (2014) 517–526. <https://doi.org/10.1109/TNANO.2014.2308300>.
- [224] D.A. van den Ende, S.E. van Kempen, X. Wu, W.A. Groen, C.A. Randall, S. van der Zwaag, Dielectrophoretically structured piezoelectric composites with high aspect ratio piezoelectric particles inclusions, *J. Appl. Phys.* 111 (2012) 124107. <https://doi.org/10.1063/1.4729814>.
- [225] K. Zhu, Y. Cao, X. Wang, L. Bai, J. Qiu, H. Ji, Hydrothermal synthesis of sodium niobate with controllable shape and structure, *CrystEngComm.* 14 (2012) 411.
- [226] K. Goc, K. Gaska, K. Klimczyk, A. Wujek, W. Prendota, L. Jarosinski, A. Rybak, G. Kmita, C. Kapusta, Influence of magnetic field-aided filler orientation on structure and transport properties of ferrite filled composites, *J. Magn. Mater.* 419 (2016) 345–353. <https://doi.org/10.1016/j.jmmm.2016.06.046>.

- [227] V.L. Stuber, D.B. Deutz, J. Bennett, D. Cannel, D.M. de Leeuw, S. van der Zwaag, P. Groen, Flexible Lead-Free Piezoelectric Composite Materials for Energy Harvesting Applications, *Energy Technol.* 7 (2019) 177–185. <https://doi.org/10.1002/ente.201800419>.
- [228] S. Mortazavian, A. Fatemi, Effects of fiber orientation and anisotropy on tensile strength and elastic modulus of short fiber reinforced polymer composites, *Compos. Part B Eng.* 72 (2015) 116–129. <https://doi.org/10.1016/j.compositesb.2014.11.041>.
- [229] T. Sharma, S.-S. Je, B. Gill, J.X.J. Zhang, Patterning piezoelectric thin film PVDF-TrFE based pressure sensor for catheter application, *Sensors Actuators A Phys.* 177 (2012) 87–92. <https://doi.org/10.1016/j.sna.2011.08.019>.
- [230] T. Furukawa, K. Ishida, E. Fukada, Piezoelectric properties in the composite systems of polymers and PZT ceramics, *J. Appl. Phys.* 50 (1979) 4904–4912. <https://doi.org/10.1063/1.325592>.
- [231] C. Carbone, M. Benwadih, G. D'Ambrogio, M.-Q. LE, J.-F. Capsal, P.-J. Cottinet, Influence of Matrix and Surfactant on Piezoelectric and Dielectric Properties of Screen-Printed BaTiO₃/PVDF Composites, *Polymers (Basel)*. 13 (2021) 2166. <https://doi.org/10.3390/polym13132166>.
- [232] M.A. Mangi, R. Kahloon, A. Elzanaty, F. Zafrullah, E. Eltahawy, The Use of Fractional Flow Reserve for Physiological Assessment of Indeterminate Lesions in Peripheral Artery Disease, *Cureus*. 11 (2019). <https://doi.org/10.7759/CUREUS.4445>.
- [233] Z. Ruzsa, S. Róna, G.G. Tóth, P. Sótónyi, O.F. Bertrand, B. Nemes, B. Merkely, K. Hüttl, Fractional flow reserve in below the knee arteries with critical limb ischemia and validation against gold-standard morphologic, functional measures and long term clinical outcomes, *Cardiovasc. Revascularization Med.* 19 (2018) 175–181. <https://doi.org/10.1016/J.CARREV.2017.07.007>.
- [234] William E. Webler, System and method for FFR guidewire recovery, US 10,080,872 B2, 2018.
- [235] C. Spadaccio, D. Glineur, E. Barbato, A. Di Franco, K.G. Oldroyd, G. Biondi-Zoccai, F. Crea, S.E. Fremes, D.J. Angiolillo, M. Gaudino, Fractional flow reserve-based coronary artery bypass surgery: current evidence and future directions, *JACC. Cardiovasc. Interv.* 13 (2020) 1086. <https://doi.org/10.1016/J.JCIN.2019.12.017>.
- [236] N.H.J. Pijls, B. De Bruyne, “Coronary pressure measurement and fractional flow reserve”, *Heart*. 80 (1998) 539–542.
- [237] N.H.J. Pijls, B. de Bruyne, K. Peels, P.H. van der Voort, H.J.R.M. Bonnier, J. Bartunek, J.J. Koolen, Measurement of Fractional Flow Reserve to Assess the Functional Severity of Coronary-Artery Stenoses, *N. Engl. J. Med.* 334 (1996) 1703–1701.
- [238] M.J. Kern, A.H. Seto, FFR-Guided CABG, *Circ. Cardiovasc. Interv.* 11 (2018). <https://doi.org/10.1161/CIRCINTERVENTIONS.118.006827>.
- [239] W.F. Fearon, B. Bornschein, P.A.L. Tonino, R.M. Gothe, B. De Bruyne, N.H.J. Pijls, U. Siebert, Economic Evaluation of Fractional Flow Reserve-Guided Percutaneous Coronary Intervention in Patients With Multivessel Disease, *Circulation*. 122 (2010)

- 2545–2550. <https://doi.org/10.1161/CIRCULATIONAHA.109.925396>.
- [240] G. Toth, B. De Bruyne, F. Casselman, F. De Vroey, S. Pyxaras, L. Di Serafino, F. Van Praet, C. Van Mieghem, B. Stockman, W. Wijns, I. Degrieck, E. Barbato, Fractional Flow Reserve–Guided Versus Angiography-Guided Coronary Artery Bypass Graft Surgery, *Circulation*. 128 (2013) 1405–1411. <https://doi.org/10.1161/CIRCULATIONAHA.113.002740>.
- [241] M. Albayati, A. Patel, D. Perera, T. Donati, S. Patel, L. Biasi, H. Zayed, B. Modarai, Measurement of Fractional Flow Reserve Predicts the Functional Significance of Peripheral Arterial Lesions in the Ischaemic Leg, *Eur. J. Vasc. Endovasc. Surg.* 58 (2019) e363–e364. <https://doi.org/10.1016/J.EJVS.2019.06.991>.
- [242] T. Sharma, K. Aroom, S. Naik, B. Gill, J.X.J. Zhang, Flexible Thin-Film PVDF-TrFE Based Pressure Sensor for Smart Catheter Applications, *Ann. Biomed. Eng.* 41 (2013) 744–751. <https://doi.org/10.1007/s10439-012-0708-z>.
- [243] X. Xia, J. Zhang, G. Lu, W.C. Lai, S.K. Krishnan, T.K. Hsiai, Q. Zhou, A.H. Nguyen, H. Cao, Intravascular sensors to assess unstable plaques and their compositions: a review, *Prog. Biomed. Eng.* 2 (2019) 012001. <https://doi.org/10.1088/2516-1091/AB5418>.
- [244] A. Kärkkäinen, J. Saarilahti, J. Kyynäräinen, H. Kuisma, New MEMS Pressure Sensor Element and Concept for Coronary Catheter, *Procedia Eng.* 168 (2016) 76–79. <https://doi.org/10.1016/J.PROENG.2016.11.151>.
- [245] F. Stam, H. Kuisma, F. Gao, J. Saarilahti, D. Gomes Martins, A. Kärkkäinen, B. Marrinan, S. Pinal, Integration of a capacitive pressure sensing system into the outer catheter wall for coronary artery FFR measurements, *Bio-MEMS Med. Microdevices III*. 10247 (2017) 1024703. <https://doi.org/10.1117/12.2263779>.
- [246] M. KERN, Comparing FFR Tools: New Wires and a Pressure Microcatheter, *Clin. Ed. Corner*. 24 (2016).
- [247] K. Totsu, Y. Haga, M. Esashi, Ultra-miniature fiber-optic pressure sensor using white light interferometry, *J. Micromechanics Microengineering*. 15 (2005) 71–75. <https://doi.org/10.1088/0960-1317/15/1/011>.
- [248] B. Scientific, COMET™ II Pressure Guidewire, (n.d.). <https://www.bostonscientific.com/en-US/products/ffr-ivus-systems/comet-pressure-guidewire.html> (accessed June 4, 2022).
- [249] St Jude Medical’s New FFR Measuring PressureWire with Agile Tip Wins U.S. Clearance, (2012). <https://www.medgadget.com/2012/04/boston-scis-new-ffr-measuring-pressurewire-with-agile-tip-wins-u-s-clearance.html> (accessed June 5, 2022).
- [250] IntraSense, 1-French Wire-Connected Pressure Sensor, (n.d.). <https://www.amsys-sensor.com/downloads/data/intrasense-uncalibrated-amsys-datasheet.pdf>.
- [251] NovaSensor P162 | Medical Pressure Sensor Die, (n.d.). <https://amphenol-sensors.com/en/novasensor/pressure-sensor-die/3164-p162>.
- [252] N. Wu, Y. Tian, X. Zou, Y. Zhai, K. Barringhaus, X. Wang, A miniature fiber optic blood pressure sensor and its application in in vivo blood pressure measurements of a swine model, *Sensors Actuators B Chem.* 181 (2013) 172–178.

<https://doi.org/10.1016/j.snb.2013.02.002>.

- [253] P. Meimoun, S. Sayah, A. Luycx-Bore, J. Boulanger, F. Elmkies, T. Benali, H. Zemir, L. Doutrelan, J. Clerc, Comparison Between Non-Invasive Coronary Flow Reserve and Fractional Flow Reserve to Assess the Functional Significance of Left Anterior Descending Artery Stenosis of Intermediate Severity, *J. Am. Soc. Echocardiogr.* 24 (2011) 374–381. <https://doi.org/10.1016/j.echo.2010.12.007>.
- [254] M. Ionescu, B. Winton, D. Wexler, R. Siegele, A. Deslantes, E. Stelcer, A. Atanacio, D.D. Cohen, Enhanced biocompatibility of PDMS (polydimethylsiloxane) polymer films by ion irradiation, *Nucl. Instruments Methods Phys. Res. Sect. B Beam Interact. with Mater. Atoms.* 273 (2012) 161–163. <https://doi.org/10.1016/j.nimb.2011.07.065>.
- [255] L. Durai, S. Badhulika, A facile, solid-state reaction assisted synthesis of a berry-like NaNbO_3 perovskite structure for binder-free, highly selective sensing of dopamine in blood samples, *New J. Chem.* 43 (2019) 11994–12003. <https://doi.org/10.1039/C9NJ02282A>.
- [256] J.M. Rosso, E.A. Volnistem, I.A. Santos, T.G.M. Bonadio, V.F. Freitas, Lead-free NaNbO_3 -based ferroelectric perovskites and their polar polymer-ceramic composites: Fundamentals and potentials for electronic and biomedical applications, *Ceram. Int.* 48 (2022) 19527–19541. <https://doi.org/10.1016/j.ceramint.2022.04.089>.
- [257] H.J. Salacinski, S. Goldner, A. Giudiceandrea, G. Hamilton, A.M. Seifalian, A. Edwards, R.J. Carson, The Mechanical Behavior of Vascular Grafts: A Review, *J Biomater Appl.* 15 (2001) 241. <https://doi.org/10.1106/NA5T-J57A-JTDD-FD04>.
- [258] M. Federmann, O.M. Hess, Differentiation between Systolic and Diastolic Dysfunction, *Eur. Heart J.* 15 (1994) 2–6. https://doi.org/10.1093/eurheartj/15.suppl_D.2.
- [259] Hao Jiang, Junmin Zhang, Di Lan, K.K. Chao, Shysheng Liou, H. Shahnasser, R. Fechter, S. Hirose, M. Harrison, S. Roy, A Low-Frequency Versatile Wireless Power Transfer Technology for Biomedical Implants, *IEEE Trans. Biomed. Circuits Syst.* 7 (2013) 526–535. <https://doi.org/10.1109/TBCAS.2012.2220763>.
- [260] S. Suresh, G. Chakaravathi, RFID technology and its diverse applications: A brief exposition with a proposed Machine Learning approach, *Measurement.* 195 (2022) 111197. <https://doi.org/10.1016/j.measurement.2022.111197>.
- [261] S.A. Weis, RFID (radio frequency identification): Principles and applications, *System.* 2 (2007) 1–23.
- [262] B. Dahlbäck, Blood coagulation, *Lancet.* 355 (2000) 1627–1632. [https://doi.org/10.1016/S0140-6736\(00\)02225-X](https://doi.org/10.1016/S0140-6736(00)02225-X).
- [263] Primary and Secondary Hemostasis: Normal Mechanisms, Disease States, and Coagulation Tests: Assessment, Analysis, and Associated Dental Management Guidelines, in: *Dent. Guid. to Med. Cond. Medicat. Complicat.*, John Wiley & Sons, Ltd, Chichester, UK, 2017: pp. 229–242. <https://doi.org/10.1002/9781119421450.ch15>.
- [264] A.J. Gale, Continuing Education Course #2: Current Understanding of Hemostasis, *Toxicol. Pathol.* 39 (2011) 273–280. <https://doi.org/10.1177/0192623310389474>.
- [265] E. Hiller, Basic Principles of Hemostasis, in: *Mod. Hematol.*, Humana Press, Totowa, NJ,

- n.d.: pp. 327–345. https://doi.org/10.1007/978-1-59745-149-9_19.
- [266] H. Rasche, Haemostasis and thrombosis: an overview, *Eur. Hear. J. Suppl.* 3 (2001) Q3-qè.
- [267] T.F. Lüscher, J. Steffel, F.R. Eberli, M. Joner, G. Nakazawa, F.C. Tanner, R. Virmani, Drug-Eluting Stent and Coronary Thrombosis, *Circulation.* 115 (2007) 1051–1058. <https://doi.org/10.1161/CIRCULATIONAHA.106.675934>.
- [268] M.A. Mcmichael, S.A. Smith, Viscoelastic coagulation testing: Technology, applications, and limitations, *Vet. Clin. Pathol.* 40 (2011) 140–153. <https://doi.org/10.1111/j.1939-165X.2011.00302.x>.
- [269] M. van Geffen, W.L. van Heerde, Global haemostasis assays, from bench to bedside, *Thromb. Res.* 129 (2012) 681–687. <https://doi.org/10.1016/j.thromres.2011.12.006>.
- [270] Y. Dargaud, R. Luddington, E. Gray, T. Lecompte, T. Siegemund, T. Baglin, J. Hogwood, V. Regnault, A. Siegemund, C. Negrier, Standardisation of thrombin generation test - which reference plasma for TGT?: An international multicentre study, *Thromb. Res.* 125 (2010) 353–356. <https://doi.org/10.1016/j.thromres.2009.11.012>.
- [271] L.T. da Luz, B. Nascimento, S. Rizoli, Thrombelastography (TEG®): practical considerations on its clinical use in trauma resuscitation, *Scand. J. Trauma. Resusc. Emerg. Med.* 21 (2013) 29. <https://doi.org/10.1186/1757-7241-21-29>.
- [272] A. Amgalan, T. Allen, M. Othman, H.K. Ahmadzia, Systematic review of viscoelastic testing (TEG/ROTEM) in obstetrics and recommendations from the women’s SSC of the ISTH, *J. Thromb. Haemost.* 18 (2020) 1813–1838. <https://doi.org/10.1111/jth.14882>.
- [273] N. Bonanos, B.C.H. Steele, E.P. Butler, J.R. Macdonald, W.B. Johnson, W.L. Worrell, G.A. Niklasson, S. Malmgren, M. Strømme, S.K. Sundaram, M.C.H. McKubre, D.D. Macdonald, G.R. Engelhardt, E. Barsoukov, B.E. Conway, W.G. Pell, N. Wagner, C.M. Roland, R.S. Eisenberg, Applications of Impedance Spectroscopy, in: *Impedance Spectrosc.*, John Wiley & Sons, Inc., Hoboken, NJ, USA, 2018: pp. 175–478. <https://doi.org/10.1002/9781119381860.ch4>.
- [274] S. Hajra, K. Mohanta, M. Sahu, V. Purohit, R.N.P. Choudhary, Studies of structural, dielectric and impedance spectroscopy of fused silica ceramics fabricated through colloidal processing, *Appl. Phys. A.* 125 (2019) 369. <https://doi.org/10.1007/s00339-019-2671-0>.
- [275] J.R. Macdonald, W.B. Johnson, Fundamentals of Impedance Spectroscopy, in: *Impedance Spectrosc.*, John Wiley & Sons, Inc., Hoboken, NJ, USA, 2018: pp. 1–20. <https://doi.org/10.1002/9781119381860.ch1>.
- [276] A.L. Samson, I. Alwis, J.A.A. Maclean, P. Priyananda, B. Hawkett, S.M. Schoenwaelder, S.P. Jackson, Endogenous fibrinolysis facilitates clot retraction in vivo, *Blood.* 130 (2017) 2453–2462. <https://doi.org/10.1182/blood-2017-06-789032>.
- [277] V. Tutwiler, H. Wang, R.I. Litvinov, J.W. Weisel, V.B. Shenoy, Interplay of Platelet Contractility and Elasticity of Fibrin/Erythrocytes in Blood Clot Retraction, *Biophys. J.* 112 (2017) 714–723. <https://doi.org/10.1016/j.bpj.2017.01.005>.

- [278] Z. Li, X. Li, B. McCracken, Y. Shao, K. Ward, J. Fu, A Miniaturized Hemoretractometer for Blood Clot Retraction Testing, *Small*. 12 (2016) 3926–3934. <https://doi.org/10.1002/sml.201600274>.
- [279] T. Lang, V. Depka, Possibilities and limitations of thromboelastometry/thromboelastography, *Hamostaseologie*. 26 (2006) S21–S29. <https://doi.org/10.1055/s-0037-1617078>.
- [280] T.K. Bera, Bioelectrical Impedance Methods for Noninvasive Health Monitoring: A Review, *J. Med. Eng.* 2014 (2014) 1–28. <https://doi.org/10.1155/2014/381251>.
- [281] R. Pradhan, A. Mitra, S. Das, Impedimetric characterization of human blood using three-electrode based ECIS devices, *J. Electr. Bioimpedance*. 3 (2012) 12–19. <https://doi.org/10.5617/jeb.238>.
- [282] T.K. Bera, Bioelectrical Impedance and The Frequency Dependent Current Conduction Through Biological Tissues: A Short Review, *IOP Conf. Ser. Mater. Sci. Eng.* 331 (2018) 012005. <https://doi.org/10.1088/1757-899X/331/1/012005>.
- [283] V. Preziosi, M. Barra, G. Tomaiuolo, P. D'Angelo, S.L. Marasso, A. Verna, M. Cocuzza, A. Cassinese, S. Guido, Organic electrochemical transistors as novel biosensing platforms to study the electrical response of whole blood and plasma, *J. Mater. Chem. B*. 10 (2022) 87–95. <https://doi.org/10.1039/D1TB01584B>.
- [284] C.F. Amaral, M. Brischwein, B. Wolf, Multiparameter techniques for non-invasive measurement of blood glucose, *Sensors Actuators B Chem.* 140 (2009) 12–16. https://www.academia.edu/17737360/Multiparameter_techniques_for_non_invasive_measurement_of_blood_glucose (accessed September 25, 2022).
- [285] A. Aghaei, M.R. Milani Hosseini, M. Najafi, A novel capacitive biosensor for cholesterol assay that uses an electropolymerized molecularly imprinted polymer, *Undefined*. 55 (2010) 1503–1508. <https://doi.org/10.1016/J.ELECTACTA.2009.09.033>.
- [286] K.H. Han, A. Han, A.B. Frazier, Microsystems for isolation and electrophysiological analysis of breast cancer cells from blood, *Biosens. Bioelectron.* 21 (2006) 1907–1914. <https://doi.org/10.1016/J.BIOS.2006.01.024>.
- [287] Y. Polevaya, I. Ermolina, M. Schlesinger, B.Z. Ginzburg, Y. Feldman, Time domain dielectric spectroscopy study of human cells: II. Normal and malignant white blood cells, *Biochim. Biophys. Acta - Biomembr.* 1419 (1999) 257–271. [https://doi.org/10.1016/S0005-2736\(99\)00072-3](https://doi.org/10.1016/S0005-2736(99)00072-3).
- [288] Y. Hayashi, I. Oshige, Y. Katsumoto, S. Omori, A. Yasuda, K. Asami, Temporal variation of dielectric properties of preserved blood, *Phys. Med. Biol.* 53 (2007) 295. <https://doi.org/10.1088/0031-9155/53/1/021>.
- [289] M. Wolf, R. Gulich, P. Lunkenheimer, A. Loidl, Broadband dielectric spectroscopy on human blood, *Biochim. Biophys. Acta - Gen. Subj.* 1810 (2011) 727–740. <https://doi.org/10.1016/J.BBAGEN.2011.05.012>.
- [290] K.R. Foster, H.P. Schwan, Dielectric properties of tissues and biological materials: a critical review, *Crit Rev Biomed Eng.* 17 (1989) 25–104.
- [291] E.J.S. Denessen, D.L. Van Den Kerkhof, M.L.J. Jeurissen, R.J.H. Wetzels, P.W.M. Verhezen,

- Y.M.. Henskens, Determining the optimal storage time and temperature for performing platelet function assays and global hemostasis assays, *Platelets*. 33 (2022) 416–424. <https://doi.org/10.1080/09537104.2021.1934666>.
- [292] J. Ichikawa, M. Kouta, M. Oogushi, M. Komori, Effects of room temperature and cold storage on the metabolic and haemostatic properties of whole blood for acute normovolaemic haemodilution, *PLoS One*. 17 (2022) e0267980. <https://doi.org/10.1371/journal.pone.0267980>.
- [293] N. Thao, *Capacitive Sensing: Water Level Application*, 2016. <https://doi.org/2016060311714>.
- [294] A. Peyvandi, S.U. Abideen, Y. Huang, I. Lee, P. Soroushian, J. Lu, Surface treatment of polymer microfibrillar structures for improved surface wettability and adhesion, *Appl. Surf. Sci.* 289 (2014) 586–591. <https://doi.org/10.1016/j.apsusc.2013.11.048>.
- [295] B. Wallner, B. Schenk, M. Hermann, P. Paal, M. Falk, G. Strapazzon, W.Z. Martini, H. Brugger, D. Fries, Hypothermia-Associated Coagulopathy: A Comparison of Viscoelastic Monitoring, Platelet Function, and Real Time Live Confocal Microscopy at Low Blood Temperatures, an in vitro Experimental Study, *Front. Physiol.* 11 (2020). <https://doi.org/10.3389/fphys.2020.00843>.
- [296] O. V. Kim, R.I. Litvinov, M.S. Alber, J.W. Weisel, Quantitative structural mechanobiology of platelet-driven blood clot contraction, *Nat. Commun.* 8 (2017) 1274. <https://doi.org/10.1038/s41467-017-00885-x>.
- [297] E. Vrigkou, A. Tsantes, D. Konstantonis, E. Rapti, E. Maratou, A. Pappas, P. Halvatsiotis, I. Tsangaris, Platelet, Fibrinolytic and Other Coagulation Abnormalities in Newly-Diagnosed Patients with Chronic Thromboembolic Pulmonary Hypertension, *Diagnostics*. 12 (2022) 1238. <https://doi.org/10.3390/diagnostics12051238>.
- [298] C. Sucker, K. Tharra, J. Litmathe, R. Scharf, R. Zotz, Rotation thromboelastography (ROTEM) parameters are influenced by age, gender, and oral contraception, *Perfusion*. 26 (2011) 334–340. <https://doi.org/10.1177/0267659111407695>.
- [299] S. Ramström, Clotting time analysis of citrated blood samples is strongly affected by the tube used for blood sampling, *Blood Coagul. Fibrinolysis*. 16 (2005) 447–452. <https://doi.org/10.1097/01.mbc.0000178827.52242.89>.
- [300] W. Zakrzewski, M. Dobrzyński, M. Szymonowicz, Z. Rybak, Stem cells: past, present, and future, *Stem Cell Res. Ther.* 10 (2019) 68. <https://doi.org/10.1186/s13287-019-1165-5>.
- [301] S. Metwally, U. Stachewicz, Surface potential and charges impact on cell responses on biomaterials interfaces for medical applications, *Mater. Sci. Eng. C*. 104 (2019) 109883. <https://doi.org/10.1016/j.msec.2019.109883>.
- [302] H.-I. Chang, Y. Wang, H.-I. Chang, Y. Wang, Cell Responses to Surface and Architecture of Tissue Engineering Scaffolds, *Regen. Med. Tissue Eng. - Cells Biomater.* (2011). <https://doi.org/10.5772/21983>.
- [303] M. Mokni, F. Pedroli, G. D'Ambrogio, M.-Q. Le, P.-J. Cottinet, J.-F. Capsal, High-Capacity, Fast-Response, and Photocapacitor-Based Terpolymer Phosphor Composite, *Polymers*

- (Basel). 12 (2020) 349. <https://doi.org/10.3390/polym12020349>.
- [304] S. Cai, C. Wu, W. Yang, W. Liang, H. Yu, L. Liu, Recent advance in surface modification for regulating cell adhesion and behaviors, *Nanotechnol. Rev.* 9 (2020) 971–989. https://doi.org/10.1515/NTREV-2020-0076/ASSET/GRAPHIC/J_NTREV-2020-0076_FIG_011.JPG.
- [305] R. Fairless, A. Beck, M. Kravchenko, S.K. Williams, U. Wissenbach, R. Diem, A. Cavalié, Membrane Potential Measurements of Isolated Neurons Using a Voltage-Sensitive Dye, *PLoS One.* 8 (2013) e58260. <https://doi.org/10.1371/JOURNAL.PONE.0058260>.
- [306] H.-Y. Chang, W.-L. Kao, Y.-W. You, Y.-H. Chu, K.-J. Chu, P.-J. Chen, C.-Y. Wu, Y.-H. Lee, J.-J. Shyue, Effect of surface potential on epithelial cell adhesion, proliferation and morphology, *Colloids Surfaces B Biointerfaces.* 141 (2016) 179–186. <https://doi.org/10.1016/j.colsurfb.2016.01.049>.
- [307] J. Ishikawa, H. Tsuji, H. Sato, Y. Gotoh, Ion implantation of negative ions for cell growth manipulation and nervous system repair, *Surf. Coatings Technol.* 201 (2007) 8083–8090. <https://doi.org/10.1016/j.surfcoat.2006.01.073>.
- [308] H. Jung, B. Kwak, H.S. Yang, G. Tae, J.-S. Kim, K. Shin, Attachment of cells to poly(styrene-co-acrylic acid) thin films with various charge densities, *Colloids Surfaces A Physicochem. Eng. Asp.* 313–314 (2008) 562–566. <https://doi.org/10.1016/j.colsurfa.2007.05.070>.
- [309] L. Tang, P. Thevenot, W. Hu, Surface Chemistry Influences Implant Biocompatibility, *Curr. Top. Med. Chem.* 8 (2008) 270–280. <https://doi.org/10.2174/156802608783790901>.
- [310] J. Wei, M. Yoshinari, S. Takemoto, M. Hattori, E. Kawada, B. Liu, Y. Oda, Adhesion of mouse fibroblasts on hexamethyldisiloxane surfaces with wide range of wettability, *J. Biomed. Mater. Res. Part B Appl. Biomater.* 81B (2007) 66–75. <https://doi.org/10.1002/jbm.b.30638>.
- [311] J. Huang, Y. Yang, S. Xue, B. Yang, S. Liu, J. Shen, Photoluminescence and electroluminescence of ZnS:Cu nanocrystals in polymeric networks, *Appl. Phys. Lett.* 70 (1997) 2335–2337. <https://doi.org/10.1063/1.118866>.
- [312] S. Jun, S. Bin Choi, C.J. Han, Y.T. Yu, C.R. Lee, B.K. Ju, J.W. Kim, Fabrication and Characterization of a Capacitive Photodetector Comprising a ZnS/Cu Particle/Poly(vinyl butyral) Composite, *ACS Appl. Mater. Interfaces.* 11 (2019) 4416–4424. https://doi.org/10.1021/ACSAMI.8B20136/SUPPL_FILE/AM8B20136_SI_001.PDF.
- [313] S. Bin Choi, C.J. Lee, C.J. Han, J.W. Kang, C.R. Lee, J.W. Kim, Self-Healable Capacitive Photodetectors with Stretchability Based on Composite of ZnS:Cu Particles and Reversibly Crosslinkable Silicone Elastomer, *Adv. Mater. Technol.* 5 (2020) 2000327. <https://doi.org/10.1002/ADMT.202000327>.
- [314] 3210-SC | Human Bronchial Epithelial Cells (HBEPiC) (put into cell), (n.d.). <https://www.biotrend.com/cellules-bronchiques-humaines-395/human-bronchial-epithelial-cells-2001417.html> (accessed October 15, 2022).

- [315] Human Bronchial Epithelial Cell line, (n.d).
<https://www.sigmaaldrich.com/FR/fr/technical-documents/protocol/cell-culture-and-cell-culture-analysis/primary-cell-culture/human-bronchial-epithelial-cells>
(accessed October 15, 2022).



FOLIO ADMINISTRATIF

THESE DE L'INSA LYON, MEMBRE DE L'UNIVERSITE DE LYON

NOM : D'Ambrogio

DATE de SOUTENANCE : 15/12/2022

(avec précision du nom de jeune fille, le cas échéant)

Prénoms : Giulia

TITRE : Multiphysics coupling for cardiovascular surgery application

NATURE : Doctorat

Numéro d'ordre : 2022ISAL0122

Ecole doctorale : Mécanique, Energétique, Génie civil et acoustique ED 162 MEGA

Spécialité : Acoustique

RESUME :

Le projet de thèse s'inscrit dans le cadre d'une collaboration entre le LGEF et le service Cardiovasculaire des Hospices Civil de Lyon (Pr. Lermusiaux, Pr. Million, Dr. Della Schiava), la problématique de fond concerne l'utilisation des matériaux fonctionnels pour l'aide à la chirurgie. L'objectif de cette thèse est de développer des dispositifs vasculaires intelligents capables de s'intégrer dans le corps humain sans susciter de réactions indésirables, notamment des thromboses. Le point de départ concerne les matériaux électroactifs, qui réalisent une conversion électromécanique "directe" de l'énergie au sein même de la matière, démontrant peu à peu leurs potentiels d'innovation technologique face à de nombreux secteurs d'application. Outre l'idée qu'ils pourraient à terme supplanter dans certains cas les procédés de transduction classiques (capteurs et actionneurs), les nouvelles possibilités offertes par ces matériaux en termes de performances et de fonctionnalités de couplage multiphysique constituent une puissante motivation pour aborder et résoudre des problématiques issues de domaines émergents. Le domaine du médical est particulièrement concerné par ces ruptures technologiques potentielles. Les capacités d'intégration fonctionnelle et structurelle dont disposent par principe les systèmes électroactifs, semblent en effet constituer une réponse prometteuse à la mise au point de matériels performants, discrets et de moins en moins invasifs. Mais pour arriver au développement de ces systèmes qualifiés d'intelligents, certains points restent à développer pour démontrer le potentiel applicatif de cette technologie. C'est autour de cette problématique que une grande partie de ce travail de recherche vont puiser leur source. En outre, ce projet se concentre sur l'étude de l'interaction entre les matériaux biologiques (sang, cellules) avec les matériaux artificiels (prothèses vasculaires et cardiaques), dans le but de comprendre les mécanismes et de développer de nouvelles prothèses pouvant être adaptées au corps humain.

MOTS-CLÉS : Smart Graft, Piezoelectric Sensor, Electroactive composites, Dielectrophoresis, Thrombosis, Bioimpedance, Biosensor, Tissue Engineering, Piezoelectric composite.

Laboratoire (s) de recherche : Laboratoire de Génie Electrique et Ferroélectricité (LGEF) INSA Lyon Directeur de thèse: COTTINET, Pierre-Jean Maître de Conférence HDR INSA-LYON

Président de jury :

GUIFFARD, Benoit

Composition du jury : BARRAU Sophie; COLIN Annie; LIANG Zhiyong (Richard); CAPSAL Jean-Fabien ; COTTINET Pierre-Jean